AN OPTICAL CLOCK BASED ON A HIGHLY CHARGED ION

Von der QUEST-Leibniz-Forschungsschule der

Gottfried Wilhelm Leibniz Universität Hannover

zur Erlangung des akademischen Grades

Doktor der Naturwissenschaften
Dr. rer. nat.

genehmigte Dissertation von

Lukas Josef Spieß, M. Sc.

2023

AN OPTICAL CLOCK BASED ON A HIGHLY CHARGED ION

Lukas Josef Spieß

Referent:	Prof. Dr. Piet O. Schmidt
	Gottfried Wilhelm Leibniz Universität Hannover
	Physikalisch-Technische Bundesanstalt, Braunschweig
Korreferent:	Priv.-Doz. Dr. Ekkehard Peik
	Physikalisch-Technische Bundesanstalt, Braunschweig
Korreferent:	Prof. Dr. David Leibrandt
	National Institute of Standards and Technology, Boulder, USA
	University of California, Los Angeles, USA
Tag der Disputation:	02. Mai 2023

ABSTRACT

Optical clocks have demonstrated the lowest uncertainties among all experimental devices with applications in time keeping as well as for tests of fundamental physics. Their exceptional accuracy is realised by referencing their frequency to an electronic transition in either neutral or singly-charged atoms. The achieved uncertainties are often limited by external perturbations shifting the measured transition frequency. Highly charged ions (HCI) are intrinsically less sensitive to external-field perturbations, making them interesting candidates for such an application. The construction of a HCI-based optical clock was for along time prohibited by the megakelvin temperatures at which HCI are produced. Only in recent years, isolation and sympathetic cooling of individual HCI in a Paul trap has been achieved, which enables the application of quantum logic spectroscopy (QLS), resolving a narrow transition with Hz-level accuracy.

In this thesis, the first optical clock based on a HCI is presented. For this, QLS is used to coherently excite the $^2P_{1/2}$-$^2P_{3/2}$ transition at 441 nm in Ar^{13+}. The large charge-to-mass ratio mismatch between the employed ions ($^{40}Ar^{13+}$, $^9Be^+$), leads to challenges for cooling of some of the motional modes. This is overcome by employing a novel algorithmic cooling protocol, leading to the lowest temperature reported for a HCI. A detailed evaluation of the experimental setup yields a systematic uncertainty of 2×10^{-17} comparable to many optical clocks in operation. A path to an uncertainty below 10^{-18} is discussed and can be achieved with technical improvements. An optical clock comparison was performed and the derived absolute frequency of the clock transition improves its uncertainty by eight orders of magnitude. A nine orders of magnitude improvement of the isotope shift ($^{40}Ar^{13+}$-$^{36}Ar^{13+}$) resolves the quantum electrodynamical nuclear recoil, an effect not previously observed in a many-electron system.

The Ar^{13+} clock is limited by its statistical uncertainty, which can be overcome by employing species offering transitions with narrower linewidth. However, their experimental determination remains challenging in the absence of data from fluorescence measurements. To aid with this, an optical dipole force technique is demonstrated, which is initial-state preserving and achieves broader linewidths than conventional Rabi interrogation. This will allow a plethora of clock transitions in HCI to be experimentally identified before employing them in optical clocks.

Keywords: optical atomic clock, systematic frequency shifts, highly charged ion, frequency metrology, fundamental physics

ZUSAMMENFASSUNG

Optische Uhren sind die Versuchsaufbauten mit der geringsten Unsicherheit. Dadurch finden sie Anwendung sowohl in der Zeitmessung als auch bei Test der Grundlagenphysik. Ihre außerordentliche Genauigkeit wird erreicht, in dem ihre Frequenz auf einen elektronischen Übergang in neutralen oder einfach geladenen Atomen referenziert wird. Die erzielten Ungenauigkeiten sind häufig limitiert durch externe Störungen, die die Übergangsfrequenz verschieben. Hochgeladene Ionen (HCI) sind intrinsisch weniger sensitive auf Störungen durch externe Felder, was sie zu interessanten Kandidaten für solche eine Anwendung machen. Der Bau einer optischen Uhr basierend auf einem HCI war lange nicht möglich, da sie bei Megakelvin Temperaturen erzeugt werden. Erst in den letzten Jahren, wurde die Isolation und das sympathetische Kühlen einzelner HCI in einer Paul Falle erreicht, was Quantenlogik Spektroskopie (QLS) mit Hz-Genauigkeit ermöglicht.

In dieser Arbeit wird die erste optische Uhr basierend auf einem HCI präsentiert. Hierzu wurde QLS verwendet um den $^2P_{1/2}$-$^2P_{3/2}$ Übergang bei 441 nm in Ar^{13+} koheränt anzuregen. Der große Unterschied im Ladungs-zu-Mass Verhältnis der verwendeten Ionen ($^{40}Ar^{13+}$, $^9Be^+$) führt zu Schwierigkeiten beim Kühlen bestimmter Bewegungsmoden. Dies wird gelöst, in dem eine neue algorithmische Kühlmethode verwendet wird, wobei die niedrigste je berichtete Temperatur für ein HCI erreicht wird. Eine detaillierte Untersuchung des experimentellen Aufbaus liefert eine systematische Unsicherheit von 2×10^{-17}, was vergleichbar ist mit anderen optischen Uhren. Ein Uhrenvergleich wurde durchgeführt und die daraus abgeleitede Übergangsfrequenz verbessert deren Genauigkeit um acht Größenordnungen. Die Isotopieverschiebung ($^{40}Ar^{13+}$-$^{36}Ar^{13+}$) wird um neun Größenordnungen genauer gemessen, was den quantenelektrodynamischen Kernrückstoß auflöst, ein Effekt der zuvor nicht in einem Mehrelektronen System beobachtet wurde.

Die Ar^{13+} Uhr ist limitiert durch ihre statistische Unsicherheit. Dies kann überwunden werden in dem ein System mit einem Übergang mit schmallerer Linienbreite verwendet wird. Deren experimenteller Nachweis bleibt schwiering solange keine Daten aus Fluroszensmessung vorliegen. Um dies zu verbessern, wird eine optische Dipolkraft demonstriert, welche zustandserhaltend ist und eine größere Linienbreite erreicht als konventionelle Rabi-Anregung. Dies ermöglichte es eine Vielzahl von Uhrenübergängen in HCI experimentell zu identifizieren, bevor sie in optischen Uhren genutzt werden.

Schlagworte: Optische Atomuhr, systematische Frequenverschiebungen, hochgeladene Ionen, Frequenzmetrologie, fundamentale Physik

CONTENTS

LIST OF FIGURES

LIST OF TABLES

ABBREVIATIONS

ADC	analog-digital converter
AOM	accusto-optical modulator
BBR	blackbody radiation
BSB	blue-sideband
DBR	distributed Bragg reflector
dc	direct current
DDS	direct digital synthesizer
DIO	digital in- and output
$E1$	electric-dipole
$E2$	electric-quadrupole
$E3$	electric-octupole
EBIT	electron beam ion trap
EMM	excess micromotion
FPGA	field-programmable gate array
FWHM	full width at half maximum
HCI	highly charged ion
IMM	intrinsic micromotion
IP	in-phase
IR	infrared
LI	logic ion
$M1$	magnetic-dipole
MM	micromotion
OADEV	overlapping Allan deviation
ODF	optical-dipole force

OP	out-of-phase
PI	photoionisation
PID	proportional–integral–derivative
PLL	phase lock loop
PMT	photomultiplier tube
PPKTP	periodically poled Potassium titanyl phosphate
PTB	Physikalisch-Technische Bundesanstalt
Q	quality factor
QED	quantum electrodynamics
QLS	quantum logic spectroscopy
QPN	quantum projection noise
RAP	rapid adiabatic passage
rf	radio-frequency
RSB	red-sideband
SFG	sum frequency generation
SHG	second harmonic generation
SI	spectroscopy ion
WCR	weakly-coupled radial
XUV	extreme ultraviolet

MATHEMATICAL SYMBOLS

Γ_{h}	anomalous heating rate
J_n	Bessel function of the first kind
Z	charge state
ϵ_0	dielectric constant
Z_a	effective charge state
m_{e}	electron mass
e	elementary charge
α	fine-structure constant
t_{p}	interrogation time
t_π	interrogation time to achieve a π rotation
q	ion charge
m	ion mass
η	Lamb-Dicke parameter
ω_{l}	laser frequency
$\bar{n}$	mean phonon number
β	modulation index
Z_{n}	nuclear charge state
Ω	on-resonant Rabi frequency
Θ	quadrupole moment
$\lambda\!\!\!^{-}_C$	reduced Compton wavelength

c	speed of light
Ω_{rf}	trap drive frequency
$\vec{k}_{\mathrm{l}}$	wavevector

Part I

INTRODUCTION

1 INTRODUCTION

In the first section of the introductory chapter, the concept of optical atomic clocks is introduced. The current state-of-the art among optical clocks and inconsistencies in clock comparisons are discussed. In the second section, highly charged ions (HCI) are addressed which are interesting candidates for optical clocks and might help resolve open issues.

1.1 OPTICAL ATOMIC CLOCKS

Time keeping is a fundamental feature of society and allows for coordination and synchronisation of objectives and activities. The unit of time is the second which was initially based on the average length of the day or year though it was soon realised that these definitions are not ideal due to the lack of reproducibility and a limited precision. Instead atomic transitions were recognised as universal frequency standards as they can be well controlled and reproduced anywhere.

In 1955, the first atomic frequency standard was realised in the microwave-regime using the hyperfine-states in ^{133}Cs (Essen et al., 1955). It was immediately understood that their accuracy had the potential to surpass the astronomical standards which were used to define the second at this point (Bullard, 1955). The General Conference on Weights and Measures (French: Conférence Générale des Poids et Mesures, CGPM) decided in 1967 to switch to an microwave, atomic standard based on ^{133}Cs. Since then the second is defined as 9 192 631 770 times the transition frequency of the hyperfine levels in ^{133}Cs (CGPM, 1967). This defined the second unambiguously and the knowledge of it became a matter of experimental uncertainty.

Contrary, to microwave clocks, optical clocks were not realised for a long time as the oscillations of optical frequencies could not directly be counted. The first direct measurements of optical frequencies required long phase-locked frequency chains which reference optical light to an radio-frequency (rf) signal (Schnatz et al., 1996). Building such a device is expensive, impractical for everyday use, and needs to be tailored to a specific wavelength. This was overcome by the invention of the frequency comb, where a mode-locked laser allows downconversion of optical frequencies directly to rf signals (Udem et al., 2002), making optical clocks practical.

The working principle of an optical clock is illustrated in Fig. 1.1. A local oscillator, in form of a laser, interrogates an atomic reference with

a suitable optical transition. Based on the response of the reference, the local oscillators frequency is steered towards the atomic resonance and therefore stabilised to the reference. Its frequency is measured by down converting it to an rf frequency using a frequency comb. The rf signal can directly be counted and provides a time standard. These devices have since become the experimental setups with the lowest uncertainties across physics.

The uncertainty of an atomic clock can broadly be separated into statistical and systematic uncertainty. The former is how well the frequency can be estimated given a certain amount of measured frequency data, which usually is limited by the amount of data that is gathered. The latter is caused by perturbations of the atomic transition which need to be estimated.

To assess the statistical uncertainty of a clock, it is compared to another clock and their frequency ratio y_i is averaged for a time interval τ. By analysing the distribution of the gathered frequency samples, their uncertainty and the dominant noise process at varying averaging times τ can be estimated. Mathematically, this is expressed by the so-called Allan deviation. It describes the frequency instability σ for an averaging time τ through (Allan, 1987; Riley, 2008)

$$\sigma(\tau) = \sqrt{\frac{1}{2(M-1)} \sum_{i=1}^{M-1} [y_{i+1} - y_i]^2} \tag{1.1}$$

where M is the number of frequency samples y_i. The averaging over a time interval τ is performed in discrete sets for the standard Allan deviation, i.e. the underlying data for y_i and y_j ($i \neq j$) is non-overlapping. The estimated uncertainty on σ can be improved by allowing for overlap between the datasets which increase the sample size and yields the so-called overlapping Allan deviation (OADEV). This increases the confidence of the result (Riley, 2008) but introduces correlations between the frequency samples, necessitating a more involved uncertainty estimation (Howe et al., 1981)[1].

The statistical uncertainty of atomic clocks is limited by quantum projection noise (QPN) (Itano et al., 1993). This describes the quantum-mechanical nature of the measurement process, where each measurement projects the state into an eigenstate destroying any superposition. Therefore, to estimate the excitation probability P_{exc} after interrogation, N measurements are necessary to estimate the state distribution. For uncorrelated measurements, the uncertainty from QPN is described by

$$\Delta P_{\text{exc}} = \sqrt{\frac{P_{\text{exc}}\,(1 - P_{\text{exc}})}{N}}. \tag{1.2}$$

1 All OADEVs within this thesis were calculated using Stable32 (Riley, 2016) which provides an automatic error estimation.

For a QPN-limited frequency measurement, the instability can be written as (Riehle, 2004)

$$\sigma(\tau) \propto \frac{\Delta\nu}{\nu_0}\frac{1}{\sqrt{N}}\sqrt{\frac{T_c}{\tau}} \tag{1.3}$$

where ν_0 is the transition frequency, $\Delta\nu$ its linewidth, T_c the total cycle time needed to prepare and interrogate the atoms per frequency sample.

Experimental progress for ^{133}Cs microwave clocks yields instabilities no better than $3 \times 10^{-14}/\sqrt{\tau}$ (Guena et al., 2012; Heavner et al., 2014; Levi et al., 2014; Szymaniec et al., 2016; Weyers et al., 2018). This is significantly worse than what has been achieved for optical clocks, which primarily gain through their four to five orders of magnitude higher transition frequency ν_0 (Eq. (1.3)). Their achievable instability depends on the number of emitters and can be separated into two types of systems. Firstly, ion clocks which interrogate a single ion trapped in a Paul trap. This leads to instabilities of $1 \times 10^{-15}/\sqrt{\tau}$ (Brewer et al., 2019; Sanner et al., 2019). Secondly, optical lattice clocks employ $N = 10^4$ neutral atoms (or more) trapped in an optical lattice. The larger number of emitters permits instabilities down to $5 \times 10^{-17}/\sqrt{\tau}$ (Bothwell et al., 2019; Schwarz et al., 2020).

The systematic uncertainty of a clock is related to shifts of the measured transition frequency relative to the unperturbed transition frequency. There are various sources for this, e.g. external electromagnetic fields which couple to the internal states. Often these fields are caused by lasers used for trapping and interrogation, or the blackbody radiation of the thermal environment. Other shifts are caused by the atoms motion, which leads to a first- and second-order Doppler shift, which are often relevant even for temperatures below 1 mK. The uncertainties of those shifts are limited by incomplete knowledge of the experimental setup, atomic state, or atomic parameters, fundamentally limiting the precision of any given clock. The magnitude of the shifts depends strongly on the employed atomic system and transition, and it therefore needs to be chosen carefully.

For ^{133}Cs microwave clocks, a state-of-the-art fractional systematic uncertainties of mid to low 10^{-16} has been achieved (Guena et al., 2012; Heavner et al., 2014; Levi et al., 2014; Szymaniec et al., 2016; Weyers et al., 2018). While this already is among the most precise experimental devices, they are behind what has been demonstrated for optical clocks. Those have reached state-of-the-art systematic fractional uncertainties at 10^{-18} (Huntemann et al., 2016; McGrew et al., 2018; Ushijima et al., 2015) and below (Brewer et al., 2019).

Overall have optical clocks surpassed the ^{133}Cs primary standard in statistical and systematic uncertainty which poses the question if an optical transition should become the primary standard (Gill, 2011; Riehle, 2015).

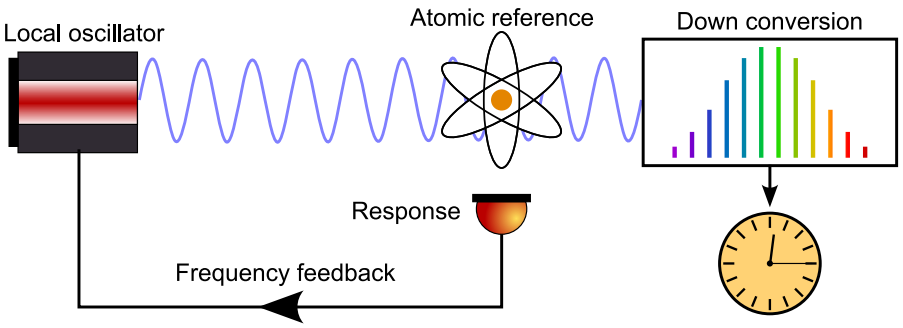

Figure 1.1: Principle of an optical clock. A local oscillator produces laser light which is used to interrogate an atomic reference. The response of the atomic reference is detected and used to stabilise the frequency of the local oscillator. The stabilised frequency is down converted to a rf frequency using a frequency comb. The oscillations of the rf frequency are counted and provide a time standard. Some graphical components were adapted from Franzen, 2006.

As a step towards a potential redefinition, it is imperative to demonstrate consistency of optical clocks at the claimed systematic uncertainties. This needs to be realised locally, i.e. within an institute, but also across independent setups to verify the results. Various such measurements at or below a fractional uncertainties of 5×10^{-18} need to occur, which is two orders of magnitude below the uncertainty of ^{133}Cs clocks (Riehle et al., 2018).

As a first step, frequency comparisons between the primary standard and a state-of-the-art optical clock are performed. The primary standard is usually either a local ^{133}Cs microwave clock or International Atomic Time distributed via satellites, which derives its frequency from multiple atomic clocks around the world. The measured absolute frequency can easily be shared and compared between institutes. This comes at the disadvantage that their uncertainty is limited to a fractional uncertainty of 10^{-16} by the primary standard. At this level, various measured transition frequencies showed good agreement in independent setups for multiple atomic species (Lange et al., 2021; McGrew et al., 2019; Schwarz et al., 2020). Though in other systems large deviations have been reported, beyond the statistical and systematic uncertainties of the involved experimental setups (Huang et al., 2016; Jian et al., 2022; Steinel et al., 2022).

More precise comparisons can be performed by directly comparing optical clocks. In this way, claimed systematic fractional uncertainties below 10^{-16} can be tested. In many cases, frequency ratio measurements have been performed within an institute, where independent setups employing the same atomic species were compared. Some of these have shown consistency with the systematic uncertainty at a fractional uncertainty of 10^{-17} (Chou et al., 2010a) and below (Huang et al., 2022; Sanner et al., 2019; Ushijima et al., 2015; Zhiqiang et al., 2022).

Despite this, the two most precise interspecies comparisons performed locally, showed frequency ratios that were less stable than expected from the uncertainties of the involved clocks. In the measurements of Dörscher et al., 2021, a $^{171}Yb^{+}$ single ion clock and a ^{87}Sr lattice clock were compared with a combined evaluated systematic uncertainty around 2×10^{-17}. Repeated measurements over seven years, showed an excess long term instability which corresponds to an unknown uncertainty of 1.8×10^{-17} with no identified cause. In another experiment, the BACON Collaboration, 2021 compared a ^{87}Sr lattice clock, a ^{171}Yb lattice clock and a single ion $^{27}Al^{+}$ clock with systematic uncertainties at and below 5×10^{-18}. The comparisons yielded a similar statistical uncertainty, but found an excess uncertainty of $5\,\% - 20\,\%$ for the measured frequency ratios. It was not possible to unambiguously decide which clock showed the excess instability, due to the statistically limited amount of overlapping data from all involved clocks (BACON Collaboration, 2021), leaving it also as an open issue.

Remote comparisons of optical clocks at different institutes are of interest as these setups are built by independent groups, where different approaches might be employed. The frequency transfer over such distances ($> 1000\,\mathrm{km}$) is performed through satellite based techniques (Droste et al., 2015; Hachisu et al., 2014; Piester et al., 2008) or optical fibre links (Lisdat et al., 2016). The former are easier to implement experimentally as it is based on already existing satellites. This comes at the cost of a significant uncertainty contribution from the frequency link itself. Such comparisons have shown agreement at the low 10^{-16}-level, though unexpected systematic uncertainties have been discovered at this level as well (Riedel et al., 2020). The use of optical fibre links provides a lower link uncertainty but requires a direct fibre link of institutes, which is not available everywhere. Nonetheless, it has been used to show an agreement at 5×10^{-17} between independent clocks (Lisdat et al., 2016).

To resolve discrepancies, additional optical clocks with systematic uncertainties below 5×10^{-18} are helpful to allow for ring-closure measurements. Employing atomic systems different from the so far investigated ones, provides an appealing prospect, as they have other properties and limiting uncertainties to the established neutral and singly charged atoms. In particular, optical clocks based on the nuclear transition in ^{229}Th and HCIs have come to attention in recent years.

The candidate for a nuclear clock, ^{229}Th, (Beeks et al., 2021; Peik et al., 2003) has an unusually low transition energy of the isomeric state ^{229m}Th with the corresponding wavelength close to 150 nm (Kraemer et al., 2022; Seiferle et al., 2019; Sikorsky et al., 2020). This makes it the only known nuclear transition in the laser accessible range. A nuclear transition will in general exhibit very different properties then the usually utilized electronic transitions. A particular advantage is

the low sensitivity to external-field perturbations. For a ^{229}Th clock based on a single ion, a systematic uncertainty of 1×10^{-19} has been estimated (Campbell et al., 2012), making it an interesting supplement to established optical clocks.

1.2 HIGHLY CHARGED IONS

Highly charged ions (HCI) are ions where a significant amount of electrons are missing. This leaves them strongly positively charged and with the outer electrons experiencing large internal fields. Their extreme properties makes them interesting candidates to test fundamental physics and as references for optical clocks (Kozlov et al., 2018). In the following section, the availability of optical transitions in HCI is discussed. In the second section, experimental challenges and achievements paving the way towards an optical clock based on an HCI are detailed.

1.2.1 Optical transitions

An effect of the high charge state is that the energy of electronic transitions increases. Thus most transitions, including all electric-dipole ($E1$) transitions, lie in the extreme ultraviolet (XUV) range far outside the laser accessible range. Nonetheless, narrow optical transitions can be found in HCI in certain cases. The first type of optical transitions are based on fine-structure or hyperfine-structure transitions which become optical for various charge states (Yudin et al., 2014). The hyperfine-structure becomes optical in high charge states, e.g. in Pb^{81+} at 1020 nm (Seelig et al., 1998). Such high charge states, require large energies to be produced, due to the increasing ionisation potential, which necessitates large, complex devices for production (Knapp et al., 1993; Stöhlker et al., 1997). Alternatively, fine-structure transitions can become optical for much lower charge states $Z \approx 5 - 20$, e.g. in Ar^{13+}, Ca^{14+} or Ni^{12+} (Draganić et al., 2003; Rehbehn et al., 2021; Yu et al., 2018). Such charge states require lower energies to be produced which is possible in table-top devices (Micke et al., 2018).

Another option for $E1$-forbidden optical transitions in HCI are level crossings, which occur along an isoelectronic sequence when the level ordering changes and electronic levels are almost degenerate (Berengut et al., 2012a). Despite being rare, such transitions have been proposed to be studied in optical clocks (Berengut et al., 2011; Porsev et al., 2020). Recently, the first level crossing transition in the optical regime has been experimentally identified in Pr^{9+} (Bekker et al., 2019) paving the way for further studies. Level crossings transitions are particularly interesting for their large sensitivity to variation of the

Shift	Scaling
Second-order Stark shift	$Z_a{}^{-4}$
Polarisability	$Z_a{}^{-4}$
Second-order Zeeman shift	suppressed
Electric quadrupole shift	$Z_a{}^{-2}$

Table 1.1: Scaling of some external-field shifts in HCI. Many frequency shifts due the external field scale inversely with the effective charge state Z_a. The effective charge is used instead of the charge state Z as it includes the partial screening of the outer electron and it scales nearly linearly with Z. The second-order Zeeman shift is in general suppressed though its size depends on the specific level structure. Adapted from Berengut et al., 2012a.

fine-structure constant α, which can be orders of magnitudes larger then transitions in neutral or singly charged atoms (Berengut et al., 2011). Nonetheless, level crossings usually involve complex states and theoretical predictions come with large uncertainties, which makes experimental identification difficult.

Regardless of the chosen transition, a low sensitivity to external-field perturbations has been predicted for an increasing charge state (Berengut et al., 2012a; Gillaspy, 2001; Schiller, 2007). A summary of some relevant shifts is given in Tab. 1.1. The decreased sensitivity comes from the larger internal fields that the outer electrons experiences, a compact wavefunction, and the sparsity of states in the optical energy range. Many of these shifts are relevant for optical clocks, making HCI interesting candidates for such an application. In principle, this should enable lower uncertainties for external-field perturbations and less stringent requirements when assessing the perturbing fields. Other shifts are not suppressed by the charge state, in particular motional shifts, and require careful investigation.

Many optical transitions in HCI have been proposed to be used in optical clocks (for a recent review see Kozlov et al., 2018), including many of the above mentioned once. In some cases, systematic uncertainties below 10^{-18} have been estimated (Barontini et al., 2022; Derevianko et al., 2012). So far though, no experimental realisation has been achieved.

1.2.2 Laboratory studies

Historically, HCI have been investigated in astronomical studies due to their abundance in the universe. For example, many optical lines in the Sun's corona have been identified as transitions in HCI (Edlén, 1943; Grotian, 1939).

Laboratory studies of HCI have in the past mostly been performed in storage rings or electron beam ion traps (EBIT) where the HCI are stored in a plasma. There, transitions ranging from the optical

(e.g. Ullmann et al., 2017; Windberger et al., 2015) to the XUV regime (e.g. Beiersdorfer et al., 1998; Epp et al., 2007) have been examined. The uncertainty of optical transition frequencies measured in such an environment is limited by the megakelvin (MK) temperatures within the plasma to no better than 100 MHz (Draganić et al., 2003; Mäckel et al., 2011). This is more than nine orders of magnitude worse than what is achievable in optical clocks. Therefore, the first step towards high-precision spectroscopy of HCI required isolation of single or few HCI and transfer from a source, e.g. an EBIT, to a better controlled environment like a Penning or Paul trap (Kozlov et al., 2018), where some form of cooling needs to be employed.

A particular problem of HCI is the lack of optical $E1$ transitions which makes direct laser cooling impossible. Therefore, direct cooling is only possible with some form of electronic or evaporative cooling. An alternative is to co-trap a second ion which can be laser cooled and sympathetically cools the HCI. A refinement of this is quantum logic spectroscopy (QLS) (Wineland et al., 2002), where the second ion, the so-called logic ion (LI), is also used to detect the internal state. This was first demonstrated for $^{27}Al^+$ (Schmidt et al., 2005) and was shortly after suggested to be used for HCI (Schiller, 2007). This technique is also employed within this thesis, with additional information on QLS given in Sec. 2.2.3.

The transfer of HCI to Penning traps has been achieved earlier than to Paul traps (Schneider et al., 1994). In Penning traps, sympathetic cooling using $^9Be^+$ (Gruber et al., 2001), evaporative cooling (Hobein et al., 2011), and negative feedback cooling (Egl et al., 2019) afforded temperatures down to 1 K. Subsequent spectroscopy of an optical transition has been demonstrated with an uncertainty of 6 MHz (Egl et al., 2019). Fundamentally though, the application of ions trapped in a Penning trap for high-precision spectroscopy is hindered by the high magnetic field necessary for trapping. This does not allow for systematic uncertainties similar to established optical clocks (Riehle, 2004).

The second option, Paul traps, are already in use for optical atomic clocks and quantum information processing. This provides a large toolbox of established techniques, including QLS, making it the preferred choice for high-precision spectroscopy of HCI. The injection of individual HCI into a Paul trap has first been demonstrated by Schmöger et al., 2015a. There, HCI are extracted from a plasma in an EBIT and transferred through an ion-optical beamline to a cryogenic linear Paul trap (Schwarz et al., 2012). After injection into the Paul trap laser-cooled $^9Be^+$ is used to sympathetically cool the HCI until one or multiple co-crystallise reaching temperature in the mK regime (Schmöger et al., 2015b). This corresponds to reduction of the HCI's temperature by nine orders of magnitude since production.

In a new experimental setup at the Physikalisch-Technische Bundesanstalt (PTB) (Leopold et al., 2019; Micke et al., 2019) this was repeated, based on the earlier gained experience. It was furthered by reducing the amount of ions in the Paul trap to a Ar^{13+}-$^{9}Be^{+}$ two-ion crystal. Then, QLS was employed, enabling interrogation of the HCI's internal state through the $^{9}Be^{+}$ (Micke et al., 2020). This yielded linewidths of 50 Hz for an magnetic-dipole transition in Ar^{13+}, making it the best resolved optical line of any HCI by six orders of magnitude and bringing it into the regime where optical clock interrogation becomes feasible.

In this work, it is built on this by establishing control over all motional degrees of freedom of Ar^{13+}-$^{9}Be^{+}$ two-ion crystal in Chapter 4. The systematic shifts of the system are investigated in detail in Chapter 5. This provides the first such experimental investigation for an HCI, revealing a systematic uncertainty similar to many operational optical clocks. The long-sought realisation of an optical clock based on a HCI is demonstrated by stabilising a laser to the dipole-forbidden optical transition in Ar^{13+} and comparing it to an established optical clock at PTB in Chapter 6. To demonstrate the potential of HCI based optical clocks, the isotope shift ($^{40}Ar^{13+}$ vs $^{36}Ar^{13+}$) is measured and compared to recently improved *ab initio* calculations. Further a technique to ease searches for narrow optical lines in HCI is demonstrated in Chapter 7. Finally, prospects of a HCI based optical clock with an uncertainty competitive to the state-of-the art based on the experimental findings are discussed.

2 THEORY

This chapter discusses the theoretical backgrounds for trapping, manipulation, and spectroscopy of ions. Section 2.1 introduces the motion of a single ion trapped in a linear Paul trap, which is expanded to the case of a two-ion crystal. Such a system is used for the most part in this thesis. The following Sec. 2.2 discuss atom-light interaction of trapped ions, which allows to manipulate their electronic and motional state. In Sec. 2.3 laser-cooling protocols employed in this thesis are introduced. The final Sec. 2.4 introduces the isotope shift, an atomic property that can be calculated by theory and is measured for an optical transition in Ar^{13+} within this thesis.

2.1 ION MOTION IN A LINEAR PAUL TRAP

The ions interrogated in this work were harmonically trapped using a linear Paul trap. Understanding the motion of the ions in such a trap is critical to control them and to assess motion-induced shifts. In the following, a summary of the most important concepts of trapping a single ion is introduced and the interaction of two co-trapped ions is discussed.

2.1.1 Single ion motion

Ion trapping using pure static electric fields is not possible due to Earnshaw's theorem (Werth et al., 2009). It states that such fields are associated with a potential φ that cannot have local extrema as this would violet the Laplace equation $\nabla\varphi = 0$. Therefore, a Paul trap uses a combination of rf and static electric fields to trap ions. Extensive information on the working principle and applications can be found in the literature (e.g. Berkeland et al., 1998; Ghosh, 1995; Leibfried et al., 2003; Wineland et al., 1998). Here only a short description will be given.

A sketch of the electrode configuration for the linear Paul trap used in this work is shown in Fig. 2.1. Within this thesis, two distinct coordinate systems are used. Firstly $\vec{x} = (x, y, z)$ is aligned with the electrodes of the Paul trap. Relative to this, the laboratory frame $\vec{x}_{\text{lab}} = (x_{\text{lab}}, y_{\text{lab}}, z_{\text{lab}})$ is rotated by 45° around z (Fig. 2.1).

For trapping in radial (x and y) direction of a linear Paul trap, an rf voltage is applied (Fig. 2.1(a)). This generates a quadrupole

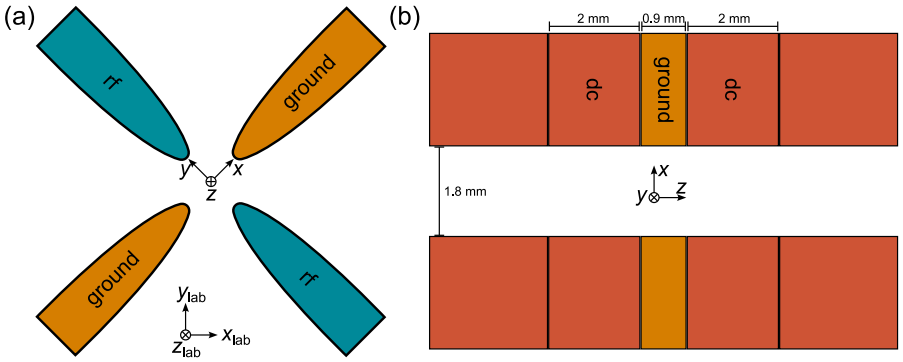

Figure 2.1: Sketch of segmented linear Paul trap. (a) Radial (x and y) confinement is provided by a rf voltage applied to opposing blades, while the other set of blades is kept at ground voltage leading to a quadrupole field. The radial motional modes of a trapped ion are rotated by 45° with respect to the laboratory frame, as detailed in the main text. (b) Along the axial (z) direction, confinement is achieved by a segmentation of the dc blades. The central segments are kept at ground voltage, while the outer electrodes are at positive voltages, trapping the ions.

potential with vanishing rf electric field in its centre defining the axial (z) axis. An additional direct current (dc) voltage is applied along the z-direction for axial confinement (Fig. 2.1(b)), leading to a deconfinement in radial direction. The corresponding electrical potential close to the trap centre is given by

$$\varphi(x,y,z) = \frac{V_{\mathrm{ac}}}{2}\cos\left(\Omega_{\mathrm{rf}}t\right)\left[1+\frac{x^2-y^2}{r_0^2}\right]+\frac{\kappa V_{\mathrm{dc}}}{z_0^2}\left[z^2-\frac{1}{2}\left(x^2+y^2\right)\right] \tag{2.4}$$

where Ω_{rf} is the trap drive frequency and V_{DC} and V_{AC} are the amplitude of the applied dc and rf voltage. The geometry of the trap enters through z_0 and r_0, which are characteristic distances of the trap electrodes and $\kappa < 1$ is a geometric factor (Berkeland et al., 1998).

The ion motion in the radial direction is then described by the so-called Mathieu equations given by

$$\frac{d^2u}{dt^2}+\frac{\Omega_{\mathrm{rf}}}{4}\left(a_u-2q_u\cos(\Omega_{\mathrm{rf}}t)\right)u=0 \qquad u\in\{x,y\} \tag{2.5}$$

with the so-called stability parameters given by

$$a_u = -\frac{4\kappa q V_{\mathrm{dc}}}{z_0^2 m\Omega_{\mathrm{rf}}^2} \tag{2.6}$$

$$q_u = \mp\frac{2qV_{\mathrm{ac}}}{r_0^2 m\Omega_{\mathrm{rf}}^2} \tag{2.7}$$

where q and m are the ion charge and ion mass of the trapped ion respectively.

In most cases, $|a_u| \ll |q_u|^2 \ll 1$ and the motion of a single ion is solved from Eq. (2.5) to first order by

$$u(t) = A_u \cos(\omega_u t + \phi_u) \left[1 + q_u \cos(\Omega_{\mathrm{rf}} t)\right] \tag{2.8}$$

where A_u and ϕ_u are amplitude and phase, which depend on the initial conditions, and

$$\omega_u = \frac{\Omega_{\mathrm{rf}}}{2} \sqrt{a_u + \frac{1}{2} q_u^2}. \tag{2.9}$$

The first term in the bracket of Eq. 2.8 describes the so-called secular motion, which is a harmonic motion at frequency ω_u. Thus, the ion oscillates around the z-axis and is periodically exposed to the rf field which only vanishes at $z = 0$. This leads to the second term describing the so-called intrinsic micromotion (IMM), which is a driven motion at frequency Ω_{rf}. Importantly, the amplitude of IMM is directly linked to the secular motions amplitude A_u and therefore cooling of the secular motion will also directly reduce the amplitude of IMM.

The confinement along the z-axis is provided by the dc voltages applied as shown in Fig. 2.1(b). For this, the electrodes are segmented. The central segment is kept at ground while the outer segments are set to the voltage V_{dc}. This produces, to first order, a harmonic potential with the motional frequency

$$\omega_z^2 = \frac{2\kappa V_{\mathrm{dc}}}{z_0^2 m}. \tag{2.10}$$

For cooling of the motional modes, it is favourable to lift the degeneracy of the radial modes by breaking radial symmetry. Thus, the trap used for the presented experiments differs from the general case as the dc voltage is only applied on the blades lying along the x-axis, instead of both blades. Simulations indicate that the dc voltage only affects one of the radial modes, while the other is unaffected, which is particular for our trap geometry. Experimentally, this is confirmed as the motional frequency in x-direction (ω_x) does not depend on the applied dc potential. The motional frequency in this work is thus given by (Leopold, 2018)

$$\begin{aligned} \omega_x^2 &= 2 \left(\frac{q V_{\mathrm{ac}}}{r_0^2 m \Omega_{\mathrm{rf}}} \right)^2 \\ \omega_y^2 &= 2 \left(\frac{q V_{\mathrm{ac}}}{r_0^2 m \Omega_{\mathrm{rf}}} \right)^2 - \frac{2\kappa q V_{\mathrm{dc}}}{z_0^2 m}. \end{aligned} \tag{2.11}$$

where the dc blades lie along the x-direction and the rf blades lie along the y-direction (Fig. 2.1). The geometric orientation of the defocused motional mode with frequency ω_y was previously incorrectly given to

lie along the axis connecting the dc blades (Leopold et al., 2019; Micke, 2020).

2.1.2 Excess micromotion

In an ideal trap the rf electric field vanishes along $z = 0$. In real traps, imperfections of the geometry produce a residual rf field at the ion position which leads to a driven motion at frequency Ω_{rf}. This is called excess micromotion (EMM) which can partially be compensated by moving the ion position with in the trapping potential but not in all cases. The following discussion is based on Berkeland et al., 1998 and Keller et al., 2015, where further informations on EMM can be found.

The velocity of EMM be given by $\vec{v}(t) = \vec{v}_{\mathrm{EMM}} \cos(\Omega_{\mathrm{rf}} t)$. Then, a narrow laser at laser frequency ω_{l} probing an internal transition of the ion is modulated in the reference frame of the ion due to the Doppler effect. The electric field E in this frame is described by

$$|E(\omega_{\mathrm{l}} \pm n\Omega_{\mathrm{rf}})| \propto J_n(\beta) \qquad n \in \mathbb{N}_0 \tag{2.12}$$

where J_n is the Bessel function of the first kind, and β is the so-called modulation index defined by

$$\beta = \frac{\vec{k}_{\mathrm{l}} \cdot \vec{v}_{\mathrm{EMM}}}{\Omega_{\mathrm{rf}}}, \tag{2.13}$$

where $\vec{k}_{\mathrm{l}}$ is the wavevector of the laser. Equation (2.12) shows that a transition probed with the laser will have sidebands at frequencies at multiples of Ω_{rf} and with their strength depending on β. By measuring the on-resonant Rabi frequencies of the carrier (Ω_{Car}) and the first-order sideband (Ω_{MM}) (see Sec. 2.2) the modulation index can be derived using

$$\frac{\Omega_{\mathrm{MM}}}{\Omega_{\mathrm{Car}}} = \frac{J_1(\beta)}{J_0(\beta)} \approx \frac{\beta}{2}. \tag{2.14}$$

The given approximation holds for $\beta \ll 1$. The measurement is useful as it is directly relates to $\vec{v}_{\mathrm{EMM}}$ and therefore estimates the related kinetic energy and the induced second-order Doppler shift.

2.1.3 Two-ion crystal

Above the case of a single trapped ion has been discussed. In this work, a two-ion crystal consisting of a single $^9Be^+$ and a single Ar^{13+} is mainly used and investigated. When the two ions are trapped in a linear Paul trap and cooled to sufficiently low temperatures, they are described by two independent harmonic oscillators coupled by the Coulomb interaction. The theoretical description is studied in various

publications (e.g. James, 1998a; Kielpinski et al., 2000; Wübbena et al., 2012). Here, a short summary of the important features is given.

The system consists of two ions with masses m_i, and charge states Z_i that are harmonically trapped with a motional frequency $\omega_{u,i}$ in the three dimensions $u \in \{x, y, z\}$ with i denoting one of the two ions. The potential $\mathcal{V}$ for this system is given by

$$\mathcal{V} = \sum_{u=x,y,z} \left[\frac{1}{2} m_1 \omega_{u,1}^2 u_1(t)^2 + \frac{1}{2} m_2 \omega_{u,2}^2 u_2(t)^2 \right] + \frac{Z_1 Z_2 e^2}{4\pi\epsilon_0} \frac{1}{r} \tag{2.15}$$

where the sum runs over the spatial dimensions, u_i are the coordinates of the two ions, ϵ_0 is the dielectric constant, and e the elementary charge. The bracketed term in the sum describes the harmonic trapping of the two ions. The last term describes the Coulomb interaction of the two ions which is related to the ion-ion distance

$$r = \sqrt{(x_1 - x_2)^2 + (y_1 - y_2)^2 + (z_1 - z_2)^2}. \tag{2.16}$$

For sufficiently high trap frequencies in x- and y-directions and small kinetic energy, the ions will align along the z-axis at the equilibrium position u_i^0 which can be calculated by demanding $\partial\mathcal{V}/\partial u_i|_{\vec{u}^0} = 0$ (James, 1998a; Kielpinski et al., 2000) as,

$$x_i^0 = y_i^0 = 0 \tag{2.17}$$

$$z_1^0 = \sqrt[3]{\frac{Z_1 Z_2 e^2}{4\pi\epsilon_0 m_1 \omega_{z,1}^2 \left(1 + \frac{Z_1}{Z_2}\right)^2}} \tag{2.18}$$

$$z_2^0 = -\sqrt[3]{\frac{Z_1 Z_2 e^2}{4\pi\epsilon_0 m_2 \omega_{z,2}^2 \left(1 + \frac{Z_2}{Z_1}\right)^2}}. \tag{2.19}$$

It is convenient to define the ion-ion distance at equilibrium

$$d = \sqrt{(x_1^0 - x_2^0)^2 + (y_1^0 - y_2^0)^2 + (z_1^0 - z_2^0)^2}. \tag{2.20}$$

The dynamics of the systems when displaced from the equilibrium position, can be derived from the Lagrangian,

$$\mathcal{L} = \sum_{u=x,y,z} \left[\frac{1}{2} m_1 \dot{u}_1(t)^2 + \frac{1}{2} m_2 \dot{u}_2(t)^2 \right] - \mathcal{V}. \tag{2.21}$$

A particular problem of this formulation is the non-linear Coulomb interaction term, which is $\propto 1/r$. At equilibrium the first-order Taylor expansion vanishes and therefore the dynamics, for a sufficiently small amplitude, is described by the second order expansion (James, 1998a). Experimentally this is a good approximation if sufficiently low

temperatures of the ions are reached. The Coulomb interaction can then be approximated around the equilibrium position as

$$\frac{Z_1 Z_2 e^2}{4\pi\epsilon_0}\frac{1}{r} \approx \frac{Z_1 Z_2 e^2}{4\pi\epsilon_0}\left[\frac{1}{d} - \frac{(x_1 - x_2)^2}{2d^3} - \frac{(y_1 - y_2)^2}{2d^3}. \right. \\ \left. + \frac{(z_1 - z_2)^2}{d^3} + \mathcal{O}(u^3)\right]. \tag{2.22}$$

The terms $\propto u_i^2$ modify the harmonic potential of each ion, while terms $\propto u_1 u_2$ describe the coupling of the motional modes. The eigenmodes of the system are thus not restricted to each ion but have contributions from both ions.

To describe the motion of the ions, the motional eigenmodes of Eq. (2.21) with the approximation in Eq. (2.22) can be found (Kielpinski et al., 2000). This yields (Kozlov et al., 2018; Wübbena et al., 2012):

$$u_1(t) = \left[A_{\mathrm{IP}} b^1_{\mathrm{IP}} \sin\left(\omega_{\mathrm{IP}} t + \phi_{\mathrm{IP}}\right) \right. \\ \left. + A_{\mathrm{OP}} b^1_{\mathrm{OP}} \sin\left(\omega_{\mathrm{OP}} t + \phi_{\mathrm{OP}}\right)\right] / \sqrt{m_1} \tag{2.23}$$

$$u_2(t) = \left[A_{\mathrm{IP}} b^2_{\mathrm{IP}} \sin\left(\omega_{\mathrm{IP}} t + \phi_{\mathrm{IP}}\right) \right. \\ \left. - A_{\mathrm{OP}} b^2_{\mathrm{OP}} \sin\left(\omega_{\mathrm{OP}} t + \phi_{\mathrm{OP}}\right)\right] / \sqrt{m_2}. \tag{2.24}$$

The motion of each ion consists of an in-phase (IP) and an out-of-phase (OP) component, where the phase refers to the relative phase of the two ions motion. Each motional mode has an oscillation frequency ω_k, a phase ϕ_k ($k \in \mathrm{IP}, \mathrm{OP}$) and an amplitude A_k. The contribution of each ion to the motion is described by the so-called eigenvector of the system $\vec{b}_k = (b^1_k, b^2_k)$ with $\vec{b}_k \cdot \vec{b}_k = 1$, which can be calculated analytically or numerically based on the ion (Z_i, m_i) and trapping ($\omega_{u,i}$) parameters (James, 1998a; Kielpinski et al., 2000).

In general, for similar charge-to-mass ratio of the two ions the eigenvector components are similar in magnitude and the modes will be considered strongly coupled. For a large mismatch like in an Ar^{13+}-$^9Be^+$ crystal, this is not necessarily the case and modes exist where only of the two ions has a significant amplitude (Kozlov et al., 2018). This has implications for cooling of specific modes, which requires a significant amplitude of the cooled ion in that mode and is further discussed in Chapter 4.

2.1.4 Quantum harmonic oscillator

At low temperatures, a classical description of the ion motion is insufficient and needs to be replaced by a quantum mechanical one.

Each independent motional mode at frequency ω_u is then described by the Hamiltonian

$$\hat{\mathcal{H}}^{(\mathrm{m})} = \frac{\hat{p}^2}{2m} + \frac{1}{2} m\omega_u^2 \hat{z}^2 \tag{2.25}$$

where the momentum operator $\hat{p}$ and position operator $\hat{z}$ are introduced. It is convenient to rewrite the equation in terms of the creation and annihilation operators (Cohen-Tannoudji et al., 1977)

$$\hat{a} = \sqrt{\frac{m\omega_u}{2\hbar}} \left(\hat{z} + \frac{i}{m\omega_u} \hat{p} \right) \tag{2.26}$$

$$\hat{a}^\dagger = \sqrt{\frac{m\omega_u}{2\hbar}} \left(\hat{z} - \frac{i}{m\omega_u} \hat{p} \right) \tag{2.27}$$

such that

$$\hat{\mathcal{H}}^{(\mathrm{m})} = \hbar\omega_u (\hat{a}^\dagger \hat{a} + \frac{1}{2}). \tag{2.28}$$

The energy eigenstates can be found by solving the corresponding Schrödinger equation and are given by

$$E = \hbar\omega_u \left(n + \frac{1}{2} \right) \qquad n \in \mathbb{N}_0, \tag{2.29}$$

where n is the so-called Fock state number. It is important to note that the energy is quantised and can therefore be used for quantum information applications, e.g. quantum logic spectroscopy (Schmidt et al., 2005).

Another useful parameter is the extension of the wavefunction for a Fock state $|n\rangle$ given by

$$z_n = \sqrt{\langle n | \hat{z}^2 | n \rangle} = \sqrt{\left(n + \frac{1}{2} \right) \frac{\hbar}{m\omega_u}}. \tag{2.30}$$

Notably, the extension of the ground-state wavefunction z_0 is non-vanishing.

2.2 ATOM–LIGHT INTERACTION

Laser light is commonly used to address the internal state of an atom, enabling spectroscopy. Further, it can couple to the ions motion which allows for laser cooling with various techniques. In this section, a short quantum-mechanical description of it is given (Leibfried et al., 2003; Riehle, 2004; Wineland et al., 1998).

For the simplest approximation, assume the atoms internal state to be a two-level system consisting of a ground state $|\mathrm{g}\rangle$ and an excited

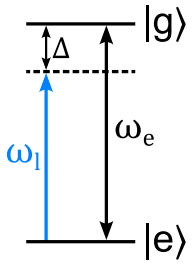

Figure 2.2: Two-level system. In many cases, the atom-light interaction can be approximated by a two-level system consisting of the ground state $|\mathrm{g}\rangle$ and the excited state $|\mathrm{e}\rangle$ with an energy difference of $\hbar\omega_\mathrm{e}$. A light field with frequency ω_l, which is detuned by $\Delta = \omega_\mathrm{e} - \omega_l$ couples the states.

state $|\mathrm{e}\rangle$ separated by an energy $\hbar\omega_\mathrm{e}$ (Fig. 2.2). The wave function of the internal state is described by

$$\Phi(t) = c_\mathrm{g}(t)\,|\mathrm{g}\rangle + c_\mathrm{e}(t)\,|\mathrm{e}\rangle \tag{2.31}$$

where c_g and c_e are the (complex) population in $|\mathrm{g}\rangle$ and $|\mathrm{e}\rangle$ respectively with the normalisation $|c_\mathrm{g}|^2 + |c_\mathrm{e}|^2 = 1$. Let this system be interacting with a light field with frequency ω_l, e.g. a narrow laser which couples $|\mathrm{g}\rangle$ and $|\mathrm{e}\rangle$ (Fig. 2.2). Assuming the system is initially prepared in the ground state $|\mathrm{g}\rangle$ ($c_g(0) = 1$), yields the time evolution of the excited-state population (Riehle, 2004)

$$|c_\mathrm{e}(t)| = \left(\frac{\Omega}{\Omega_\mathrm{R}}\right)^2 \sin^2\left(\frac{\Omega_\mathrm{R} t}{2}\right) \tag{2.32}$$

where Ω is the so-called on-resonant Rabi frequency which describes the coupling strength for $\omega_\mathrm{l} = \omega_\mathrm{e}$. It depends on the transition type and for a magnetic-dipole ($M1$) transition it is given by

$$\Omega = \frac{\left|\langle \mathrm{e}|\,\hat{\vec{\mu}}\cdot\vec{B}\,|\mathrm{g}\rangle\right|}{\hbar} \tag{2.33}$$

where $\hat{\vec{\mu}}$ is the magnetic dipole operator and $\vec{B}$ is the magnetic field associated with the light field. The generalised Rabi frequency Ω_R is defined by $\Omega_\mathrm{R} = \sqrt{\Omega^2 + \Delta^2}$ where Δ is the laser detuning from resonance $\Delta = \omega_\mathrm{e} - \omega_\mathrm{l}$. Equation 2.32 describes Rabi oscillations between $|\mathrm{g}\rangle$ and $|\mathrm{e}\rangle$ and shows that for $\Delta = 0$ a full transfer of population from the ground to the excited state is possible. This occurs for an interaction time of $t_\pi = \pi/\Omega$ which is the interrogation time to achieve a π rotation.

In spectroscopy experiments, rectangular pulses of length t_p are commonly used, and in this case, the excitation probability as a function of detuning Δ is given by

$$|c_\mathrm{e}(t)| = \left(\frac{\Omega t_\mathrm{p}}{2}\right)^2 \mathrm{sinc}^2\left(\frac{\Omega_\mathrm{R} t_\mathrm{p}}{2}\right) \tag{2.34}$$

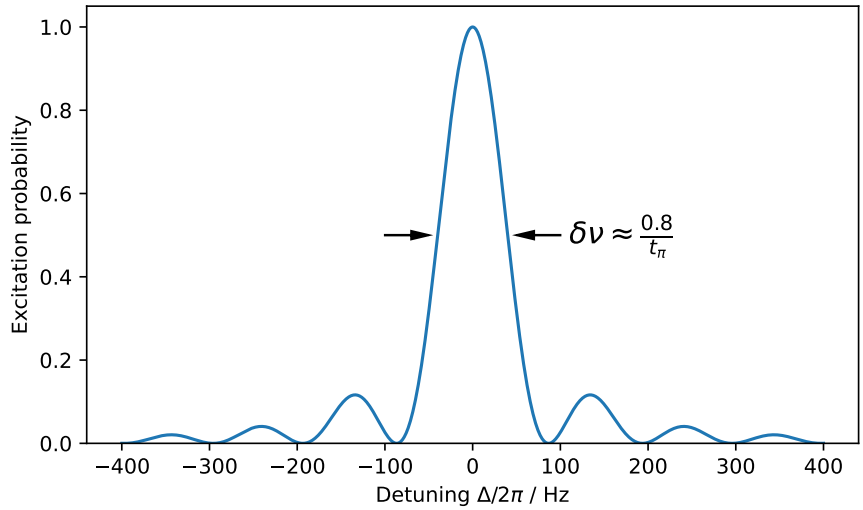

Figure 2.3: Rabi lineshape. Example for an ideal Rabi excitation with pulse length $t_\mathrm{p} = t_\pi = 10$ ms. Notable are the sidelobes which lead to a significant excitation probability even far from resonance.

with the unnormalised sinc function $\mathrm{sinc}(x) = \sin(x)/x$. The lineshape is shown in Fig. 2.3 for $t_\mathrm{p} = t_\pi$ where the linewidth is approximately given by

$$\delta\nu_\mathrm{R} \approx \frac{0.8}{t_\pi}. \tag{2.35}$$

The used two-level approximation is justified for real atomic systems if the detuning of the light from the transition $\Delta = \omega_\mathrm{l} - \omega_\mathrm{e}$ is small compared to the detuning to any other transition. Further, Eq. (2.32) and (2.34) only hold under ideal condition. In real experiments laser noise, finite temperature, excited-state lifetime and similar imperfections lead to a reduced contrast and limited coherence time.

2.2.1 Coupling to motion

Besides coupling to the electronic state, atom-light-interaction can be used to address the motional states of trapped ions. In the following, assume a single ion harmonically trapped in a Paul trap with a two-level system describing the internal electronic state. The wavevector of the light $\vec{k}$ is chosen such that it aligns with the z-axis. The internal state Hamiltonian is given by

$$\hat{\mathcal{H}}^{(\mathrm{e})} = \frac{1}{2}\hbar\omega_\mathrm{e}\hat{\sigma}_z \tag{2.36}$$

with σ_i $(i \in \{x, y, z\})$ being the Pauli matrices.

The total Hamiltonian is

$$\hat{\mathcal{H}} = \hat{\mathcal{H}}^{(\mathrm{m})} + \hat{\mathcal{H}}^{(\mathrm{e})} + \hat{\mathcal{H}}^{(\mathrm{i})} \tag{2.37}$$

where $\hat{\mathcal{H}}^{(\mathrm{m})}$ describes the motion and is given in Eq. (2.28). The interaction Hamiltonian from the laser, which couple internal and motional state is described by (Leibfried et al., 2003)

$$\hat{\mathcal{H}}^{(\mathrm{i})} = \frac{\hbar\Omega}{2}\left(\hat{\sigma}_+ + \hat{\sigma}_-\right)\left(e^{i(k\hat{z}-\omega_1 t+\phi)} + e^{-i(k\hat{z}-\omega_1 t+\phi)}\right) \tag{2.38}$$

where a phase ϕ and the operators $\hat{\sigma}_\pm = \left(\hat{\sigma}_x \pm \hat{\sigma}_y\right)/2$ were introduced. Transforming to the interaction picture and applying the rotating-wave approximation yields the interaction Hamiltonian

$$\hat{\mathcal{H}}_{\mathrm{int}}(t) = \frac{\hbar\Omega}{2}\hat{\sigma}_+ \exp\left(i\left\{\phi + \eta\left[\hat{a}e^{-i\omega_z t} + \hat{a}^\dagger e^{i\omega_z t}\right] - \Delta t\right\}\right) + \mathrm{H.c.} \tag{2.39}$$

where H.c. stands for the Hermitian conjugate and the Lamb-Dicke parameter $\eta = kz_0$ was introduced. Here, $z_0 = \sqrt{\hbar/2m\omega_z}$ is the extension of the ground-state wavefunction of the particle (Eq. (2.30)). The so-called Lamb-Dicke regime is defined as the regime where the wave package of a motional state $|\Psi_{\mathrm{m}}\rangle$ is much smaller than the wavelength, i.e.

$$\langle\Psi_{\mathrm{m}}|\, k^2\hat{z}^2\, |\Psi_{\mathrm{m}}\rangle \ll 1. \tag{2.40}$$

For a specific Fock state $|n\rangle$ this can be evaluated using Eq. (2.30), yielding $\eta\sqrt{2n+1} \ll 1$. In the Lamb-Dicke regime, Eq. (2.39) can be expanded to first order in η:

$$\hat{\mathcal{H}}_{\mathrm{int}}(t) \approx \frac{\hbar\Omega}{2}\sigma_+\left\{1 + i\eta\left(\hat{a}e^{-i\omega_z t} + \hat{a}^\dagger e^{i\omega_z t}\right)\right\}e^{i(\phi-\Delta t)} + \mathrm{H.c.} \tag{2.41}$$

The first term describes the Carrier transition $|\mathrm{g},n\rangle \to |\mathrm{e},n\rangle$ at $\Delta \approx 0$ where the motional mode remains unaffected. The other two terms are called the first-order red-sideband (RSB) and blue-sideband (BSB), which give rise to the transitions $|\mathrm{g},n\rangle \to |\mathrm{g},n-1\rangle$ at $\Delta \approx -\omega_z$ and $|\mathrm{g},n\rangle \to |\mathrm{e},n+1\rangle$ at $\Delta \approx +\omega_z$, respectively. The Rabi frequency of the $|\mathrm{g},n\rangle \to |\mathrm{e},n\pm1\rangle$ is given by

$$\Omega_{n,n\pm1} = \Omega\eta\sqrt{n_>} \tag{2.42}$$

where $n_>$ is the larger value of n and $n \pm 1$.

For large η and outside of the Lamb-Dicke regime, higher order expansions in η become relevant. Terms appear that allow for higher-order sideband transitions of the type $|\mathrm{g},n\rangle \to |\mathrm{e},n+l\rangle$ with $l \in \mathbb{Z}_0$ at $\Delta \approx l\omega_z$. The Rabi frequency for these is given by

$$\Omega_{n,n+l} = \Omega_{n+l,n} = \Omega e^{-\eta^2/2}\eta^{|l|}\sqrt{\frac{n_<!}{n_>!}}L_{n_<}^{|l|}(\eta^2) \tag{2.43}$$

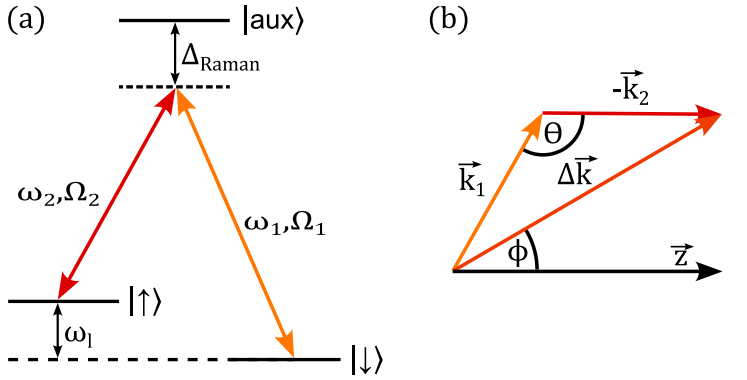

Figure 2.4: Scheme of a stimulated Raman transition. (a) Involved electronic states and lasers. A transition between $|\uparrow\rangle$ and $|\downarrow\rangle$ can be driven by two lasers at frequency ω_i with their difference equaling the transition frequency $\omega_l = \omega_2 - \omega_1$. It is mediated by an auxiliary state $|\text{aux}\rangle$ which each laser couples to with an on-resonant Rabi frequency Ω_i. The detuning Δ_{Raman} is sufficiently large that the population in $|\text{aux}\rangle$ is negligible. (b) The orientation of the wavevectors $\vec{k}_i$, the difference $\Delta\vec{k} = \vec{k_1} - \vec{k_2}$ and the direction of an addressed motional mode $\vec{z}$ define the angles Θ and ϕ (Leopold, 2018). These influence the Lamb-Dicke parameter (Eq. (2.47)).

where $n_>$ and $n_<$ stand for the larger and smaller value of n and $n+l$ respectively. The generalised Laguerre polynomial $L_n^\alpha(x)$ are described by

$$L_n^\alpha(x) = \sum_{m=0}^{n} (-1)^m \frac{(n+\alpha)!}{(n-m)!(\alpha+m)!m!} x^m. \tag{2.44}$$

The appearance of L_n^α in Eq. (2.43) leads to zero-crossings of the Rabi frequency for specific combinations of Fock states n and sideband order l. This needs to be taken into account when addressing these transitions for example for ground-state cooling of an ion (Wan et al., 2015). Some ways of using the coupling to the motion for laser cooling are addressed in Sec. 2.3.

2.2.2 Raman transition

Addressing of an individual motional sideband requires a transition with a linewidth $\Gamma \ll \omega_z$ and a non-vanishing Lamb-Dicke parameter η. In $^9Be^+$, this is realised through a two-photon process coupling long-lived hyperfine-structure states (see Sec. 3.1). A stimulated Raman transition is used to drive this transition. In the following an introduction to this is given following Leibfried et al., 2003.

The electronic states and lasers involved in a stimulated Raman transition between the $|\downarrow\rangle$ and $|\uparrow\rangle$ are shown in Fig. 2.4(a). Two lasers at frequencies ω_1 and ω_2 couple each state to an auxiliary state $|\text{aux}\rangle$ with an on-resonant Rabi frequency $\Omega_{1,2}$. Their detuning Δ_{Raman} is chosen to be much larger than the linewidth of the transitions, leading to negligible population in $|\text{aux}\rangle$. By setting the frequency difference

of the lasers to be equal to the transition frequency $\omega_1 = \omega_2 - \omega_1$, a stimulated Raman transition between $|\downarrow\rangle$ and $|\uparrow\rangle$ is driven. The effective on-resonant Rabi frequency for this is

$$\Omega_{\text{Raman}} = \frac{\Omega_1 \Omega_2}{4\Delta_{\text{Raman}}}. \tag{2.45}$$

To address a motional sideband, the Lamb-Dicke parameter η needs to be non-vanishing (Sec. 2.2.1). For a stimulated Raman transition, it can be identified that

$$\eta = \Delta\vec{k} \cdot \vec{z} z_0 \tag{2.46}$$

where $\vec{z}$ is the normalised vector describing the direction of the motional mode, z_0 is the extension of the wavefunction (Eq. (2.30)), and $\Delta\vec{k} = \vec{k}_1 - \vec{k}_2$ is the difference of the wavevectors $\vec{k}_{1,2}$ of the two lasers. The coupling therefore depends on the geometric alignment of the beams relative to each other and relative to the motional mode. Denote the angle between the wavevectors $\vec{k}_1$ and $\vec{k}_2$ as Θ, and the angle between $\Delta\vec{k}$ and $\vec{z}$ as ϕ (Fig. 2.4(b)). Then, the Lamb-Dicke parameter is expressed as (Leopold, 2018)

$$\eta = 2kz_0 \sin\left(\frac{\Theta}{2}\right) \cos(\phi), \tag{2.47}$$

where it was assumed that $\omega_1 \approx \omega_2$ and therefore $k = \left|\vec{k}_1\right| \approx \left|\vec{k}_2\right|$. This is for example the case for the here employed transition in $^9Be^+$ (Sec. 3.1). The angle dependence allows selectively addressing of motional modes in one direction while being insensitive to others. This is utilised in the experimental setup by using a combination of Raman beams that only address the axial modes or radial modes (Sec. 3.6.4).

2.2.3 Quantum logic spectroscopy

To build an optical clock based on a single ion, a specific level structure is required. It needs to provide the option of laser cooling, detection of the internal state, and a narrow clock transition with all required laser wavelengths within the technically accessible range. The combination of these requirements is realised in only a few atomic systems, such as the alkali-like ions (Be^+, Mg^+, Ca^+, Sr^+, Ba^+, Ra^+), Yb^+ or Hg^+. To extend the range of ion species that can be used in an optical clock, QLS was invented (Wineland et al., 2002). It combines two ions, the so-called logic ion (LI) and the spectroscopy ion (SI), to provide all the necessary tools for high-precision spectroscopy.

The LI is coolable and possesses two internal states which can efficiently be manipulated, detected and distinguished. Typically ions that are well understood and often find applications in quantum in-

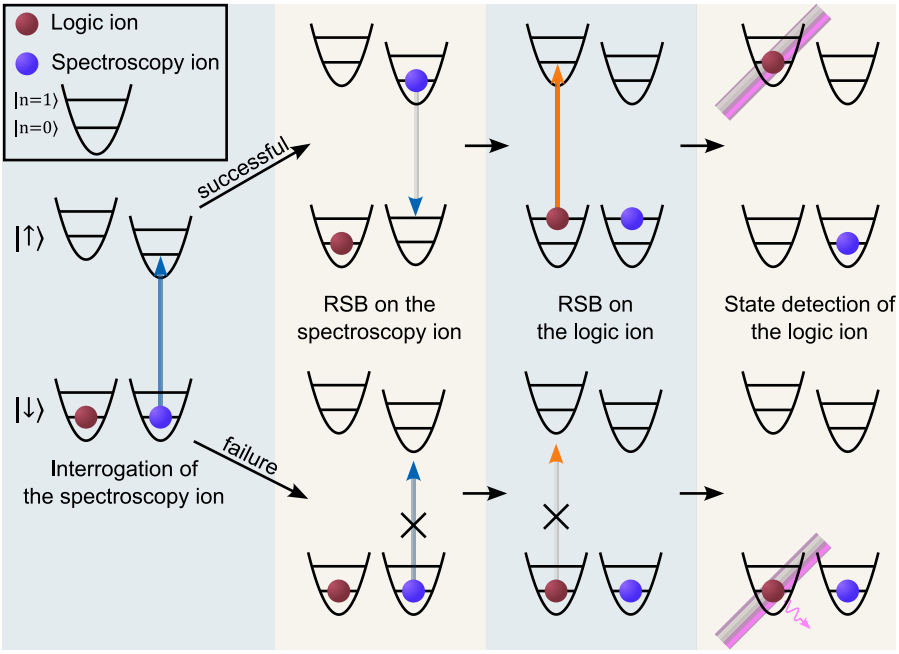

Figure 2.5: Quantum logic spectroscopy (QLS) scheme. A logic ion (LI) and spectroscopy ion (SI) are co-trapped in a harmonic potential. Through the strong Coulomb interaction they have a shared motional mode $|n\rangle$ given a sufficiently low temperature. Both ions have an electronic ground state $|\downarrow\rangle$ and a long-lived excited state $|\uparrow\rangle$. For the LI, the two states can experimentally be distinguished as being either bright or dark, respectively. For QLS, the ions are prepared in the electronic and motional ground state. The SI is interrogated on its $|\downarrow\rangle_{\mathrm{SI}} \rightarrow |\uparrow\rangle_{\mathrm{SI}}$ carrier transition. A RSB transition on the SI is used to map the success of the initial interrogation onto the shared motional mode. Then a RSB transition on the LI is used to map the motional excitation to the electronic transition of the LI which is then detected. The result (bright or dark) depends on the success of the initial interrogation of the SI's $|\downarrow\rangle_{\mathrm{SI}} \rightarrow |\uparrow\rangle_{\mathrm{SI}}$ transition (Schmidt et al., 2005).

formation processing such as $^{9}Be^{+}$ (Micke et al., 2020; Schmidt et al., 2005), Mg^{+} (Chou et al., 2010a; Wolf et al., 2016), or Ca^{+} (Hannig et al., 2019; Lin et al., 2020) are used. The SI is chosen only for spectroscopic interest and needs none of the other necessary features to be interrogated. After co-trapping, LI and SI are strongly coupled through the Coulomb force, which allows for sympathetic cooling of the SI using the LI.

The scheme for QLS is depicted in Fig. 2.5. After preparing the two-ions in their shared motional ground state and the individual electronic ground states, the SI is interrogated. A series of laser pulses is then applied to transfer internal state information from the SI to the LI through the quantised motional state (Fig. 2.5). The transferred information can then efficiently be detected on the LI.

The initial use of QLS was to perform spectroscopy of optical transitions in otherwise inaccessible systems (Wineland et al., 2002). It was first demonstrated for $^{27}Al^{+}$ (Schmidt et al., 2005) and the subsequent

optical clock based on $^{27}Al^+$ is the first to reach a fractional uncertainty below 10^{-18} (Brewer et al., 2019). Recently, QLS of an HCI was demonstrated in the here presented setup, where a dipole-forbidden transition was resolved with a linewidth of 50 Hz (Micke et al., 2020). This paved the way to build an optical clock based on a HCI using many of the established techniques employed for $^{27}Al^+$.

Besides spectroscopy, QLS has also found more general applications. For example optical pumping of internal states (Chou et al., 2017; Micke et al., 2020) or cooling of inaccessible motional modes (King et al., 2021 and Sec. 4.2), making it a versatile tool.

2.3 LASER COOLING

The first step to control individual atoms is to efficiently cool them. In this work, two well-known techniques are applied to the $^9Be^+$ ion to cool the trapped Ar^{13+}-$^9Be^+$ crystal. In a first step, Doppler cooling is used which is very efficient even for high ion temperatures. However, the achievable temperature ($\approx$ mK) is limited by the stochastic nature of the dissipation process. Further cooling to the motional state is performed using resolved sideband cooling, which allows to reach the motional ground state. Details are introduced in the following sections.

2.3.1 Doppler cooling

Doppler cooling is a well established method to cool atoms. It uses that an atom's motion leads to a Doppler shift, allowing for a velocity depended absorption. This is followed by spontaneous emission dissipating the energy. Here, Doppler cooling will be discussed following Leibfried et al., 2003. Further details can be found in the literature (e.g. Lett et al., 1989; Wineland et al., 1987).

For simplicity, consider a trapped ion in one dimension, which moves harmonically with a motional frequency ω_z and possesses an internal transition with linewidth Γ. Classically, the ions velocity is described by $v = v_0 \cos(\omega_z t)$. A laser with wavevector k and a detuning of Δ from resonance of the internal state is applied along the direction of motion. Due to the first-order Doppler shift, the effective detuning is given by $\Delta - kv$ and absorption happens predominantly when $\Delta \approx kv$. Each absorption event leads to a momentum transfer of $\Delta p = \hbar k$ and excites the electronic state. The excited state can then decay spontaneously which in general is an isotropic process and therefore does not transfer momentum when averaged over many absorption-emission cycles.

In the case $\omega_z \ll \Gamma$, the ion will absorb and emit many photons per oscillation period and the interaction can be described by an effective

force. The rate of absorption-emission events is the product of the excited state probability ρ_{ee} and the decay rate, which is equal to the linewidth Γ. The average force is then described by

$$F \approx \hbar k \Gamma \rho_{ee} \tag{2.48}$$

with

$$\rho_{ee} = \frac{s/2}{1 + s + (2(\Delta - kv)/\Gamma)^2}. \tag{2.49}$$

where $s = 2|\Omega|^2/\Gamma^2$ is the saturation parameter, and Ω is the on-resonant Rabi frequency.

For small velocities, i.e. $|kv| \ll \Delta$ and $|kv| \ll \Gamma$, Eq. (2.48) can be linearised in v and is given by

$$F \approx \frac{\hbar k \Gamma s/2}{1 + s + (2\Delta/\Gamma)^2} \left(1 + \frac{8k\Delta/\Gamma^2}{1 + s + (2\Delta/\Gamma)^2} v\right). \tag{2.50}$$

Equation (2.50) consists of a velocity independent term, which displaces the ion from the trap centre and does not directly affect the dynamics. Neglecting this, the force can be written as

$$F \approx -\beta v \tag{2.51}$$

with

$$\beta = \frac{-4\hbar k^2 s \Delta/\Gamma}{((1 + s) + (2\Delta/\Gamma)^2)^2}. \tag{2.52}$$

For $\Delta < 0$, this describes a frictional force which cools the ion. Within the used approximations, no bound to the achievable temperature is apparent. In reality though, the absorption-emission cycles do not cease for $v = 0$ as $\rho_{ee}(v = 0) \neq 0$. Therefore while $\langle \Delta p \rangle = 0$, there is a diffusion process $\langle \Delta p^2 \rangle \neq 0$, where $\langle \cdot \rangle$ denotes the time average. The minimal attainable temperature due to this is

$$T_{\min} = \frac{\hbar \Gamma \sqrt{1 + s}}{4 k_B} (1 + \xi) \tag{2.53}$$

where k_B is the Boltzmann constant. The factor $\xi = \mathcal{O}(1)$ was introduced to account for the emission pattern of the transition, which is not necessarily isotropic, as typically electric dipole transitions are used for Doppler cooling.

Giving the Doppler limit as a temperature requires a definition of the temperature of a single ion. For this, the temperature of the ion after cooling is understood as being in thermal equilibrium with a reservoir at temperature T (Stenholm, 1986). Then, the probability to find it in a Fock state $|n\rangle$ follows a Boltzmann distribution. To determine the temperature, a single experimental realisation of the system is insufficient. Instead, the ion is repeatedly allowed to thermalise with

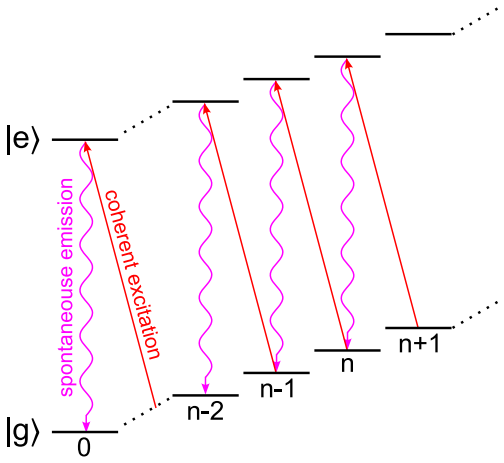

Figure 2.6: Scheme for resolved-sideband cooling. The trapped atom has the electronic states $|g\rangle$ and $|e\rangle$. The trapping adds the Fock states $|n\rangle$as an additional dimension. A coherent RSB transition is used to map motional excitation to the electronic excitation. The electronic excitation is dissipated through spontaneous emission, effectively removing a phonon. This process can be repeated until the motional ground state is reached.

its reservoir and each time the Fock state $|n\rangle$ is determined, yielding the mean phonon number $\bar{n}$. The associated temperature is

$$T = \frac{\hbar\omega_z}{k_B \ln\left(\frac{\bar{n}+1}{\bar{n}}\right)}. \tag{2.54}$$

Therefore, the temperature is to be understood as an ensemble average of a mixed state where the population distribution follows

$$P(n,\bar{n}) = \frac{1}{1+\bar{n}}\left(\frac{\bar{n}}{1+\bar{n}}\right)^n. \tag{2.55}$$

Doppler cooling is often used as a first step of cooling since the cooling efficiency can easily be adjusted by varying Δ. This allows to cool atoms even with high initial temperatures and to bring them close to $T_{\min}$ by successively lowering Δ and s. In ion trapping, this typically leads to a mean phonon number $\bar{n} \approx 1 - 20$ with a thermal distribution (Stenholm, 1986). Such temperatures are sufficiently low to further employ resolved-sideband cooling (or other techniques) to cool the ions to the motional ground state, which is discussed in the following section.

2.3.2 Resolved-sideband cooling

Cooling of ions beyond the Doppler limit is required for QLS and to reduce the second-order Doppler shift of the optical clock. One method for this is resolved-sideband cooling (Itano et al., 1995; Monroe et al., 1995) where a narrow optical transition is used to drive transitions between different Fock states. This allows it to map motional excitation onto the electronic state where it is dissipated through spontaneous emission.

The scheme for pulsed resolved-sideband cooling is shown in Fig. 2.6. The trapped atom consists of the internal electronic ground ($|\mathrm{g}\rangle$) and excited ($|\mathrm{e}\rangle$) state. Additionally, the Fock states $|n\rangle$ span a second dimension with an energy spacing much smaller than the electronic transition. By applying a RSB transition, the motional excitation is mapped onto the electronic excitation via $|\mathrm{g}, n\rangle \rightarrow |\mathrm{e}, n-1\rangle$. By pumping the $|\mathrm{e}\rangle$ population to a fast-decaying state, spontaneous emission to $|\mathrm{g}\rangle$ can occur making the process irreversible. For a sufficiently small Lamb-Dicke parameter η, the decay happens pre-dominantly on the $|\mathrm{e}, n\rangle \rightarrow |\mathrm{g}, n\rangle$ transition, dissipating the motional energy. Repeating these steps reduces the mean phonon number until $\bar{n} \approx 0$ is reached where the RSB can not be driven again. Various processes can limit the achievable temperature, e.g. decoherence, off-resonant scattering and heating rates.

A problem of this method is that the on-resonant Rabi frequency Ω depends on the motional state $|n\rangle$ which has zero-crossings (see Eq. (2.43)). There population can become trapped. Higher-order sidebands can be employed to mitigate this (Che et al., 2017; Wan et al., 2015) though it can still lead to non-thermal distributions which are difficult to assess (Chen et al., 2017; Rasmusson et al., 2021). Nonetheless, with resolved-sideband cooling $\bar{n} \ll 1$ has been achieved for single ions (Diedrich et al., 1989; Leopold, 2018) and two-ion crystals (Chen et al., 2017; Wan et al., 2015).

For efficient resolved-sideband cooling, a small Lamb-Dicke parameter η is necessary to suppress the recoil of the spontaneous decay used for dissipation (Wan et al., 2015). Though, if η is nearly vanishing, resolved-sideband cooling becomes impractical as the Rabi frequency of the RSB transition vanishes (Eq. (2.42)), requiring impractical laser powers to counteract this. Such a situation occurs in two-ion crystals with a large charge-to-mass ratio mismatch like the Ar^{13+}-$^{9}Be^{+}$ crystal investigated in this thesis. For some motional modes, one of the two ions has a vanishing amplitude (Sec. 2.1.3). Thus, as resolved-sideband cooling is only possible on the logic ion $^{9}Be^{+}$, some motional modes cannot be cooled this way. Therefore, other cooling protocols are necessary, which is further discussed in Chapter 4.

2.4 ISOTOPE SHIFT

The isotope shift describes the shift of the transition frequency for a given transition on the probed isotope. It occurs due to the dependence of the electronic wavefunction on the mass of the nucleus M, and its finite charge radius R (Breit, 1958; King, 1963). Through this, it is used to gain experimental access to nuclear parameters. Further, theoretical calculations achieve a much higher precision for the isotope shift than for the transition frequency itself. This allows probing of the

underlying theories. Few-electron systems, like HCI, are particularly appealing, as their calculation is less complicated, which enables accurate predictions (Soria Orts et al., 2006).

The transition frequency difference between two isotopes A and B is denoted by the isotope shift $\Delta\nu_{A,B}$. To first-order it can be described by (Yerokhin et al., 2020)

$$\Delta\nu_{A,B} = \left(\frac{m_\mathrm{e}}{M_A} - \frac{m_\mathrm{e}}{M_B}\right) K + \left(\frac{R_A^2}{\lambda\!\!\!^{-2}_C} - \frac{R_B^2}{\lambda\!\!\!^{-2}_C}\right) F, \tag{2.56}$$

where m_e is the electron mass and $\lambda\!\!\!^{-}_C = \hbar/m_\mathrm{e}c$ is the reduced Compton wavelength. The dimensionless mass shift (K) and field shift (F) constants depend only on the element and the transition but not the isotope. This assumes that higher-order contributions, which scale with $(m_\mathrm{e}/M)^2$ and $(R/\lambda\!\!\!^{-})^4$, are negligible. For a light atom (like Argon) the isotope shift is dominated by the mass shift component, while the field shift contributes less. In heavy atoms this is reversed and the field shift is dominant.

The calculation of the mass shift constant K is usually performed up to order $(Z_\mathrm{n}\alpha)^4$ within the so-called Breit approximation. Here, α is the fine-structure constant and Z_n is the nuclear charge state. In this approximation the mass shift is induced by the relativistic recoil operator given by (Yerokhin et al., 2020)

$$\hat{\mathcal{H}}_\mathrm{rec} = \frac{1}{2}\sum_{i,j}\left[\hat{\vec{p}}_i \cdot \hat{\vec{p}}_j - \frac{Z_\mathrm{n}\alpha}{r_i}\left(\hat{\alpha}_i + \frac{\left(\vec{\alpha}_i \cdot \hat{\vec{r}}_i\right)\hat{\vec{r}}_i}{r_i^2}\right) \cdot \hat{\vec{p}}_j\right] \tag{2.57}$$

where i and j denote the electrons, $\hat{\vec{p}}$ is the momentum operator, $\hat{\vec{r}}$ is the position operator, and $\vec{\alpha}$ is the vector of Dirac matrices. As common in literature, relativistic units ($\hbar = 1$, $c = 1$) are used in this section. This allows to calculate the relativistic mass shift constant as the expectation value $K = \langle\hat{\mathcal{H}}_\mathrm{rec}\rangle$ using the Dirac wavefunction. Corrections to K in higher orders of $Z_\mathrm{n}\alpha$ occur due to quantum-electrodynamical (QED) effects (King et al., 2022; Shabaev, 1998). This correction is therefore called QED nuclear recoil, which so far has only been observed in He (Delaunay et al., 2017a) and hydrogen-like Ne^{9+} (Sailer et al., 2022).

The field shift constant F is calculated as the expectation value of the derivative of the nuclear charge potential V_nuc with respect to the nuclear charge radius (Zubova et al., 2016):

$$F = \left\langle \sum_i \frac{\mathrm{d}V_\mathrm{nuc}(r_i)}{\mathrm{d}(R/\lambda\!\!\!^{-})^2} \right\rangle, \tag{2.58}$$

where i sums over all electrons. Similar to the mass shift constant, QED corrections to F are necessary to achieve accurate results (King et al., 2022; Zubova et al., 2016).

In this thesis, the isotope shift in Ar^{13+} is measured (Chapter 6), which is dominated by the mass shift. This allows to test theoretical predictions and to resolve the QED nuclear recoil for the first time in a many-electron system.

3 EXPERIMENTAL SETUP

In this work two ions are used: $^9Be^+$ is used as the logic ion (LI) which possesses a well-controllable electronic structure. As the spectroscopy ion (SI), Ar^{13+} is investigated, which is a well-studied HCI and therefore an ideal test bed.

In the first two sections of this chapter the level structures of the two ion species is introduced. In Sec. 3.3 the scheme for HCI production and transfer to a linear Paul trap are shortly described. Then, the cryogenic environment of the linear Paul trap and improvements to the HCI lifetime are discussed in Sec. 3.4. The magnetic field stabilisation is introduced in Sec. 3.5 and the laser systems necessary to control the two ions are described in Sec. 3.6. The final section address the newly implemented experimental control scheme.

The experimental setup has been described in detail in previous theses (Leopold, 2018 and Micke, 2020) as well as various publications (Leopold et al., 2019; Micke et al., 2018, 2019). This chapter will only give a short introduction of the most relevant parts and changes that have been implemented compared to previous descriptions.

3.1 LOGIC ION $^9BE^+$

The employed LI is $^9Be^+$, which is a well studied and commonly used ion in quantum information processing. The level structure composes of a $^2S_{1/2}$ ground state and the $^2P_{1/2}$ and $^2P_{3/2}$ excited states and is shown in Fig. 3.1. All states are split due to a hyperfine interaction with the nuclear spin ($I = 3/2$). Notable features are a closed, fast cycling transition between $\left|^2S_{1/2}, F = 2, m_F = 2\right\rangle$ (denoted as $|\downarrow\rangle$) and $\left|^2P_{3/2}, F = 3, m_F = 3\right\rangle$, and the long-lived qubit state $\left|^2S_{1/2}, F = 1, m_F = 1\right\rangle$ (denoted as $|\uparrow\rangle$).

The $|\downarrow\rangle \rightarrow \left|^2P_{3/2}, F = 3, m_F = 3\right\rangle$ transition, the *cooling transition*, is a closed, $E1$-allowed transition which is used for Doppler cooling by driving it with a σ^+-polarised beam. Due to imperfections of the polarisation, decay from the excited state to $|\uparrow\rangle$ and $\left|^2S_{1/2}, F = 2, m_F = 1\right\rangle$ is possible which are dark to the cooling laser. This is avoided by applying a repumper laser coupling them to $\left|^2P_{1/2}, F = 2, m_F = 2\right\rangle$. From there spontaneous decay to $|\downarrow\rangle$ is possible, closing the cooling cycle. Repumping through the $^2P_{1/2}$ state is preferred over the $^2P_{3/2}$ state as it has a lower off-resonant excitation rate from the cooling transitions when the ion is in $|\downarrow\rangle$. Additionally, it avoids the so-called

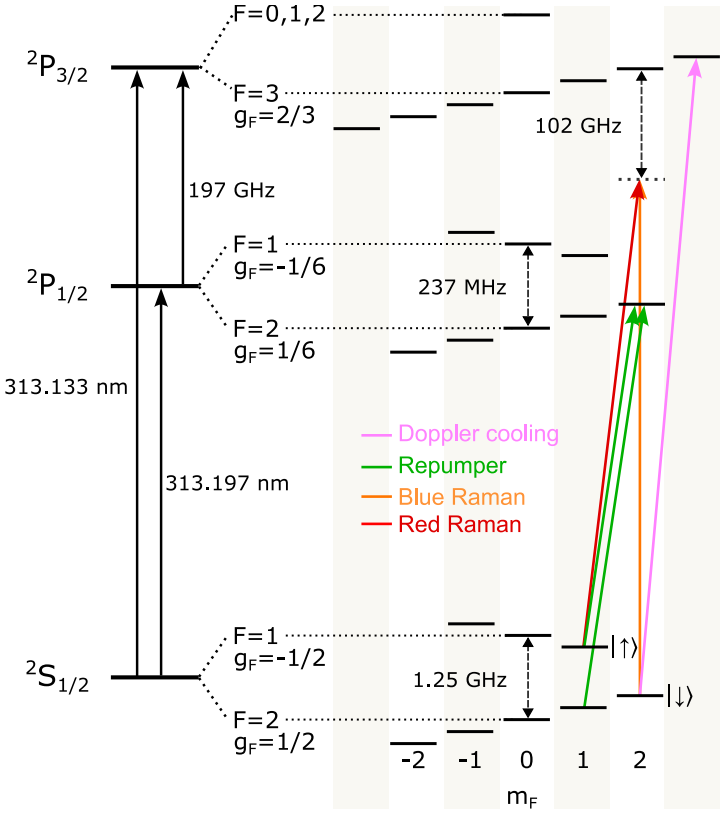

Figure 3.1: Level scheme of $^9Be^+$ and addressed transitions. The Doppler cooling transition is used for cooling and state detection of ion where the $|^2S_{1/2}, F = 2, m_F = 2\rangle := |\downarrow\rangle$ appears bright while $|^2S_{1/2}, F = 1, m_F = 1\rangle := |\uparrow\rangle$ appears dark. The $|\uparrow\rangle \rightarrow |\downarrow\rangle$ transition is driven through a Raman transition. Repumping of the $|\uparrow\rangle$ to the $|\downarrow\rangle$ is performed via the $^2P_{1/2}$ state. Details are given in the main text.

coherent population trapping where $|^2P_{3/2}, F = 3, m_F = 3\rangle$ is a dark state if the transition amplitude from the cooling and repumper laser interfere destructively (Morigi, 2003). Therefore, repumping through the $^2P_{1/2}$ state allows the $|\downarrow\rangle$ to be prepared with higher fidelity and improves resolved-sideband cooling (Leopold, 2018).

The qubit transition $|\uparrow\rangle \rightarrow |\downarrow\rangle$ can be driven by a microwave at 1.25 GHz, which can be used to measure the magnetic field strength. Alternatively, it is driven by a stimulated Raman transition (Sec. 2.2.2). This allows for addressing of motional sidebands and therefore is used for ground-state cooling and quantum logic operations (see 2.2.1). The detuning of the Raman beams from the $^2P_{3/2}$ and $^2P_{1/2}$ state is chosen to be roughly equally detuned from both states to minimise off-resonant scattering and to allow for cancelling of the a.c. Stark shift by adjusting the polarisation of the Raman beams (Leopold, 2018).

State detection, which discriminates $|\uparrow\rangle$ and $|\downarrow\rangle$, is performed on the cooling transition where $|\uparrow\rangle$ corresponds to the *dark* and $|\downarrow\rangle$ to the *bright* state. For this, the Doppler transition is driven for about 200 µs

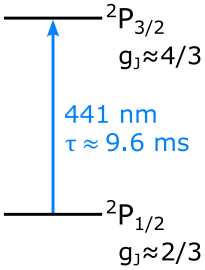

Figure 3.2: Simplified level structure of Ar^{13+}. The interrogated magnetic-dipole transition at 441 nm is between the fine-structure states $^2P_{1/2}$ and $^2P_{3/2}$. The excited-state lifetime of 9.6 ms (Lapierre et al., 2006) corresponds to a natural linewidth of around 17 Hz.

with no repumper applied and the scattered photons are detected with a photomultiplier tube (PMT). A threshold discrimination is used to assign 0 and 1 photons to the dark state, while > 1 photons are considered to be the bright state (Leopold, 2018). As mentioned above, this transition is not fully closed when the repumper is not applied due to polarisation impurities, limiting the state detection efficiency of the bright state to $\approx 99.5\,\%$. The detection efficiency of the dark state is limited to $\approx 98\,\%$ by off-resonant scattering of the $^2P_{3/2}$ state (Leopold, 2018).

3.2 BORON-LIKE ARGON

The HCI of interest is Ar^{13+}, which has previously been investigated in this experimental setup. It is a five-electron system and has therefore a Boron-like electronic structure shown in Fig. 3.2. The ground state is $^2P_{1/2}$ ($1s^2 2s^2 2p$) with the lowest lying excited state $^2P_{3/2}$ connected to it by a $M1$ transition at 441 nm. The excited-state lifetime is 9.6 ms (Lapierre et al., 2006). The next lowest lying transitions from either of these low-lying states states have wavelengths of less than 50 nm. Within this thesis, only even isotopes, ^{40}Ar and ^{36}Ar, with no nuclear spin ($I = 0$) are studied. This system was chosen due to its simple electronic structure and because the optical transition is one of the most accurately known in HCI. This reduced the time needed to find the transition when scanning with a narrow laser (Micke et al., 2020).

The optical transition in $^{40}Ar^{13+}$ has historically been studied in plasmas using an EBIT where grating spectroscopy (Draganić et al., 2003; Soria Orts et al., 2007) and laser spectroscopy (Mäckel et al., 2011, 2013) reached an uncertainty of about 150 MHz. This was predominantly limited by the megakelvin temperature in a plasma leading to large Doppler broadening. In a recent experiment, $^{40}Ar^{13+}$ was trapped in a Penning trap and cooled using negative-feedback and adiabatic cooling, reaching temperatures down to about 1 K. By applying the continuous Stern-Gerlach effect, the optical transition frequency was measured with an uncertainty of about 6 MHz (Egl et al., 2019), making it by far the best known optical transition in a HCI.

The simple electronic structure of Ar^{13+} allows for accurate *ab initio* atomic structure calculations, yielding theoretical predictions with

uncertainties beyond what is possible in atomic systems with more electrons. The ground-state g-factor has been measured with a relative uncertainty of 1.4×10^{-9} in a Penning trap, while calculations reach a relative uncertainty of 9×10^{-7} where electron correlation, nuclear effects, and quantum electrodynamics (QED) contributions were taken into account (Arapoglou et al., 2019). The excited-state g-factor has previously been measured in the system of this work with a relative uncertainty of 4×10^{-6} (Micke et al., 2020) while independently being calculated with a relative uncertainty of 1×10^{-6} (Agababaev et al., 2019). Another interesting property is the $^{40}Ar^{13+}$-$^{36}Ar^{13+}$ isotope shift which was experimentally determined with an uncertainty of 100 MHz using an EBIT (Soria Orts et al., 2006), while theoretical predictions reached an uncertainty of 11 MHz (Zubova et al., 2016).

In parallel with the here presented work, improvements of the predicted isotope shift reached an uncertainty of 4 MHz (King et al., 2022). These calculations were performed blind to the presented experiments and resolve for the first time the QED nuclear recoil in Ar^{13+} (see Sec. 2.4). This makes the QED nuclear recoil experimentally accessible in a many-electron system.

3.3 HIGHLY CHARGED ION PRODUCTION AND TRANSFER

A compact EBIT is employed for production and initial storage of HCI (Micke et al., 2018). It features an electron beam of about 10 mA which ionises injected atoms through electron impact ionisation. The beam is focused using a magnetic field with a flux density of about 0.86 T at the trap centre. The negative space charge of the electron beam as well as the magnetic field provide confinement to the ionised HCI in the directions transverse to the electron beam. Static dc fields are used to confine the ions in direction of the electron beam. The generated plasma has a typical temperature of around 1 MK.

From there HCI can be extracted and are transferred through an ion-optical beamline to a linear Paul (Schmöger et al., 2015a). The extracted ion beam is steered by multiple electro-optical elements and a pulsed drift tube is used to decelerate the ion bunch (Schmöger, 2013). In the beamline different charge-to-mass ratios separate in time-of-flight, which allows for selection of a specific charge state by switching a single electrode at the correct timing. When reaching the Paul trap the ions have a residual energy of about 130 V/charge. This requires the Paul trap to be put on an elevated ground of similar value leaving the ions at a residual energy of 5–10 eV per charge. In the trap approximately 100 laser-cooled $^{9}Be^{+}$ are present and the entering HCI collides with the $^{9}Be^{+}$ crystal until enough energy is dissipated for co-crystallisation (Micke et al., 2020; Schmöger et al., 2015b). Following

this, excess $^{9}Be^{+}$ is removed by switching off the Doppler cooling laser and applying parametric excitation. To implement the parametric excitation, the trap drive frequency is modulated at the single $^{9}Be^{+}$ ion axial motional frequency ($\approx 500\,\mathrm{kHz}$) which selectively removes $^{9}Be^{+}$ until only a single $^{9}Be^{+}$ and a single HCI are left (Micke et al., 2020).

In this thesis, $^{40}Ar^{13+}$ and $^{36}Ar^{13+}$ were investigated. $^{40}Ar^{13+}$ has a natural abundance of 99.6 % and is obtained from a Argon gas source with this abundance through a leak valve into the trap centre of the EBIT. The natural abundance of $^{36}Ar^{13+}$ is only 0.33 % and it is therefore an isotopically enriched source is used which has a dedicated injection system. The difference in mass between the two isotopes necessitates small changes to the timings of the switched electrodes to slow and trap the desired HCI.

3.4 CRYOGENIC PAUL TRAP

The Paul trap used within this thesis has previously been described in Leopold et al., 2019 and Leopold, 2018. It is a segmented linear Paul trap, with a sketch of the geometry given in Fig. 2.1. In the radial directions (x and y) a quadrupole field is generated by applying an rf voltage to opposing electrodes while keeping the dc blades on a fixed voltage. The dc electrodes are segmented in axial (z) direction, allowing for confinement by applying a dc voltage to the outer electrodes while keeping the central electrode at ground voltage. The degeneracy of the radial motional frequencies is broken by applying dc voltage only on the pair of electrodes in x-direction (Leopold, 2018).

The Paul trap is installed in a cryogenic system (Micke et al., 2019) which keeps the trap and the surrounding area at a temperature close to 4 K. This reduces the background gas pressure because most gases freeze and the large surfaces cryogenically pump impinging gas particles. It allows for extended storage lifetime of HCI which are susceptible to charge exchange collisions. For optical access and HCI injection, various ports of the room temperature vacuum chamber to the 4 K stage are available. Compared to the previous descriptions (Micke et al., 2019), eight of these optical ports were additionally closed by installing windows on the 4 K stage (see Fig. 3.3). The windows are coated with standard antireflective coatings[1] to increase light transmission efficiency. The installed windows are wedged 0.5° to prevent etaloning within the individual windows which could affect interrogation of the ions.

The window installation reduces the in-flux of atoms from the room temperature stage. This decreases ion loss from ballistic gas, which passes through the optical ports that lead directly to the trap centre. It

1 A and UV-coating from Thorlabs Inc.

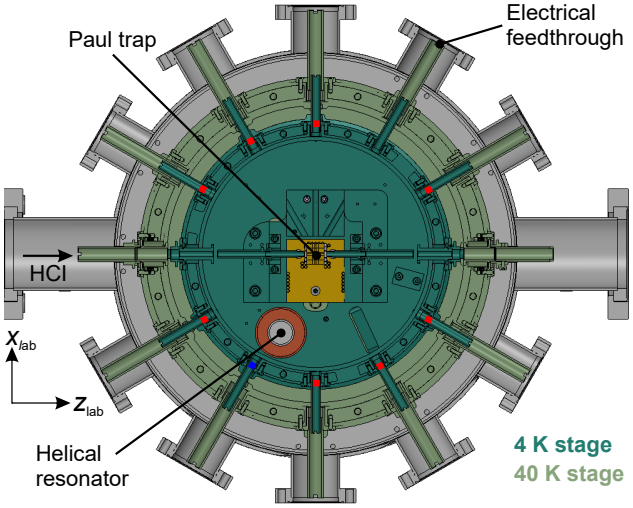

Figure 3.3: Windows installed into optical ports at 4 K from top view. The 4 K stage (dark green) contains the Paul trap and is mounted inside the 40 K stage (light green) which itself is mounted inside a room temperature vacuum chamber (grey). The protruding tubes are for optical access of the trap centre and were previously open. The red markings indicate newly installed wedged windows which improve isolation of the 4 K stage from the room temperature vacuum chamber. Of the in-plane ports, only the axial ports for HCI injection and the port for the electrical feedthrough remained open. There are four additional out-of plane ports at an angle of $\pm 15°$ where only one is closed by a mirror previously used for vibration measurements (Micke et al., 2019). The blue marked port is closed by a similar mirror. Details are given in the main text.

also reduces the intake of H_2 which accumulates and slowly degrades the vacuum as H_2 is the dominant background gas at 4 K (Micke et al., 2019). If the ion lifetimes are significantly reduced, a so-called warm up is performed where the cryocooler is turned off and the 4 K stage is allowed to warm up by about 20 K to degas H_2 (Leopold, 2018).

To assess the change in residual pressure, charge exchange collisions of HCI with background gas particles are used. For this, the lifetime of 235 HCI was recorded when performing various experiments. The distribution of lifetimes after installation of the windows is shown in Fig. 3.4(a) with all data being taken during the first four weeks following a warm up. The observed $1/e$ lifetime is $84(8)$ min, which is about double the previously measured value of $43(4)$ min (Micke et al., 2019). This is consistent with the approximately 57 % reduction in solid angle of the room temperature stage visible to the trap centre. Figure 3.4(b) shows the lifetimes of all recorded HCI as well as the mean lifetime as a function of time since the last warm up. The ion lifetime steadily decreases for the first three weeks, before a step-like decrease in the fourth week. This is attributed to in-flux of H_2 which saturates the surfaces of the cold stage at cryogenic temperatures. To counteracted this, a warm up can be performed after three to four weeks of operation.

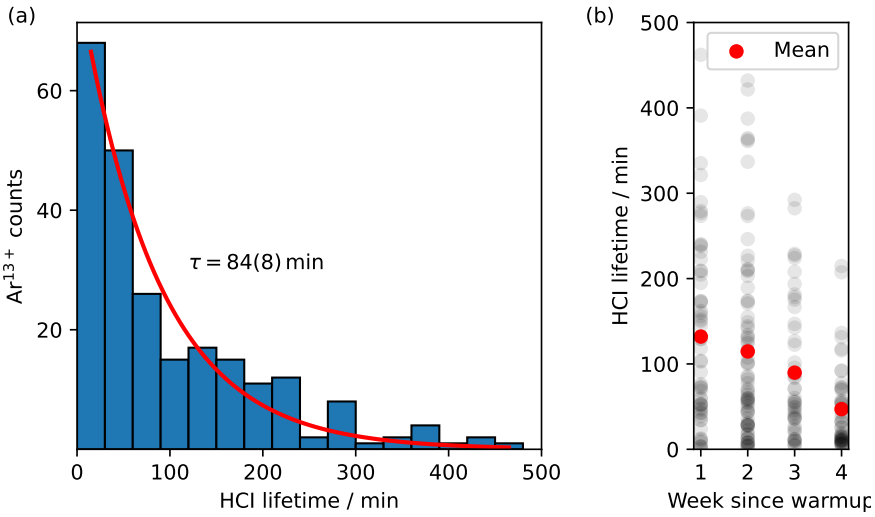

Figure 3.4: Lifetime of Ar^{13+} after installation of windows in the cold stage. (a) Recorded lifetime of 235 HCI binned in 30 min intervals. The red curve is an unweighted fit of an exponential function with time constant τ =84(8) min. This is an improvement by about a factor of two compared to results obtained without windows (Micke et al., 2019). (b) Individual lifetime of all recorded HCI (shaded black) as well as their mean (red) as a function of weeks since the last warm up. A steady decline of the lifetime is visible for the initial three weeks with a sharper drop in the fourth week. The estimated lifetimes in both graphs are likely to be underestimated due to the way the data was recorded (see main text).

Recording of HCI lifetimes was performed in parallel with other experimental measurements leading to biases. Ions that lived for long time were often removed from the trap at the end of the day when shutting down the experiment. Thus the lifetime of these ions is truncated and then recorded, leading to an underestimation of the lifetime. Another issue is that it takes several minutes from successful loading and trapping of an HCI to unambiguous detection of the charge state through the motional mode frequency. This means that lifetimes below a few minutes cannot be unambiguously recorded. For example, Ar^{12+} was detected in rare cases after loading, and it is possible that this resulted from a short-lived Ar^{13+}. Such events are not included in the presented data. Other issues, like accidental dumping of the ions from the trap due to laser or electrical issues might also bias the data.

A downside of the window installation was that the laser polarisation at the ion position became strongly dependent on the beam alignment. This is attributed to birefringence of the wedged windows. This could be further amplified by additional stress during cooldown which induces a position dependent birefringence. This made additional polarising components necessary. A time dependence of the

laser polarisation was also observed (see Sec. 5.2.5) though this was not unambiguously attributed to the windows.

3.5 MAGNETIC FIELD

A magnetic field is used to define the quantisation axis and to lift the degeneracy of the Zeeman sub-states. It has a magnetic flux density of around 23 µT, which is smaller than the previously used 160 µT. The reduction improved the separation of the carrier and sideband transitions from the various Zeeman components of Ar^{13+} and $^{9}Be^{+}$, reducing the off-resonant excitation rate. Experimentally an approximately 10 % improvement of contrast for spectroscopic signals of an Ar^{13+}-$^{9}Be^{+}$ two-ion crystals was observed.

The magnetic field is generated by three pairs of orthogonal coils and the setup is described in detail by (Leopold et al., 2019). The coils are passively driven and stabilised by a scheme similar to Merkel et al., 2019. For the active stabilisation, a sensing resistor in series is used to measure the current and an error signal is derived from the voltage drop by comparing it to a reference voltage. A control loop shunts parts of the current through a transistor in parallel with the coils, stabilising the current through the coil. Furthermore, an additional, larger set of coils is used for active stabilisation. For this, a magnetic field sensor outside of the vacuum is used as a reference with a resolution of 150 pT. Finally, at the trap centre, the magnetic field is additionally passively stabilised by the surrounding copper from the cryogenic system, which acts as a low pass filter with a cutoff frequency at or below 0.3 Hz for all directions (Leopold et al., 2019). From data taken during the clock campaign, the magnetic field stability can be estimated, and it was found to be below 200 pT for up to several 1000 s (see Sec. 5.2.4).

3.6 LASER SYSTEMS

The control of motional and internal degrees of freedom of trapped ions is achieved through various laser systems. The necessary laser systems for $^{9}Be^{+}$ and Ar^{13+} and their delivery to the trapped ions is described in the following section.

3.6.1 Laser systems for $^{9}Be^{+}$

The laser systems to generate, cool, and address the $^{9}Be^{+}$ consist of a photoionisation (PI) laser, Doppler cooling laser, a repumper, and a Raman laser system. In this thesis, these remained unchanged compared to previous descriptions in Hahn, 2019 and Leopold, 2018. Thus it will

not be repeated here. Nevertheless, a modification to the repumper was performed and for parts of the presented experiments, the PI laser and repumper laser have been replaced, which are described here.

Previously, the two repumper laser (see Fig. 3.1) were generated from a single self-injected distributed Bragg reflector (DBR) diode at 626 nm (King et al., 2018) which was frequency doubled to 313 nm using intracavity second harmonic generation (SHG). This was split 50 : 50 using a beam splitter to generate the two required repumper. The two beams were then shifted using accusto-optical modulators (AOM) to generate the necessary 1.25 GHz frequency difference before being overlapped again. The usage of two beam splitters for separation and recombination led to a significant power reduction. This is avoided here, by replacing the setup with an electro-optic modulator, which phase modulates the initial laser beam and directly produces sidebands at the required frequency. For switching, two AOMs are employed to turn the laser off with high extinction. This setup was used for all presented experiments.

The employed DBR diodes showed a lifetime of only a few thousand hours. Then they needed to be replaced. This made the system less reliable and only provides a limited amount of laser power. Therefore, a sum frequency generation (SFG) system was setup which is an extension to the SFG already in use for the Doppler cooling and Raman lasers (Hahn, 2019). The complete setup is shown in Fig. 3.5. The previously described Raman and Doppler cooling laser are derived from a single 1050 nm laser which is sent through two separate periodically poled Potassium titanyl phosphate (PPKTP) crystals where it is combined with two individual 1550 nm lasers for SFG of 626 nm light (Hahn, 2019). For the new repumper, the 1050 nm is again recycled and sent through a third PPKTP crystal where another, separate 1550 nm is overlapped for SFG. This third stage achieved an output power of about 120 mW with an input of 2 W at 1050 nm and 5 W at 1550 nm. The low conversion efficiency is mostly due to a deformed beam profile of the 1050 nm beam after the first two SFG stages. The repumper is frequency stabilised by measuring its wavelength with a wavemeter[2] and giving feedback to the piezo of the 1550 nm laser.

The old PI laser was based on a laser diode at 940 nm which was twice frequency doubled. There the power after the first frequency doubling was split between two experiments (Hahn, 2019). To make the laboratories more independent, it was replaced by a laser diode at 470 nm which only requires a single doubling stage, reducing the work for maintenance. The new setups for PI and repumper laser were used for measurements involving $^{36}Ar^{13+}$ in Chapter 6 and the measurements in Chapter 7. All other data was taken with the old setups.

2 High Finesse WS-7-30 wavemeter

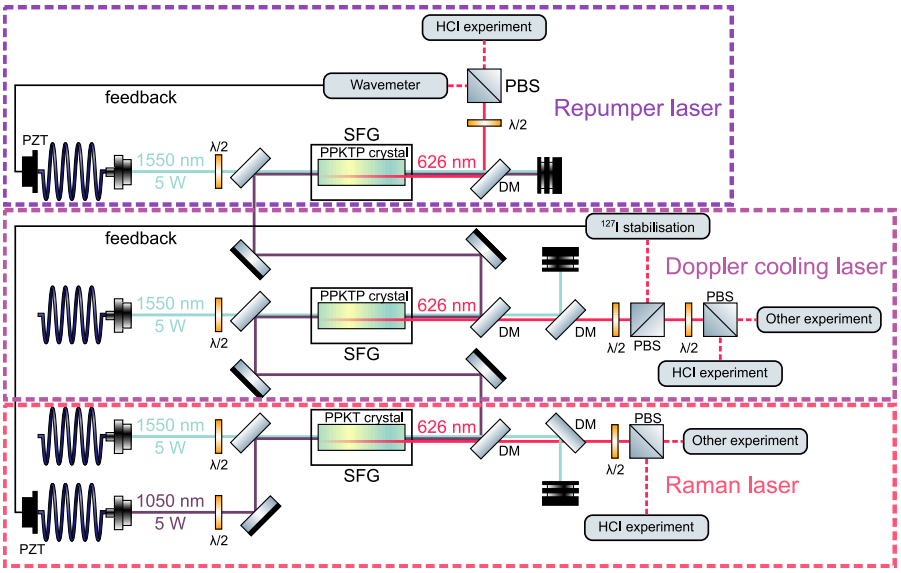

Figure 3.5: Sum frequency generation (SFG) setup. Light from high-power fibre lasers at 1050 nm and 1550 nm is overlapped inside PPKTP crystals for SFG of 626 nm light. Independent 1550 nm lasers at different frequencies are used for the Raman, Doppler cooling and repumper laser, while only a single 1050 nm laser is repeatedly employed. The light from the Raman and Doppler cooling laser are split between the HCI laboratory and another experiment, while the repumper laser is only used by the former. The Doppler cooling laser frequency is stabilised to an absorption line in iodine-127 by giving feedback to the 1050 nm laser (Stepanova, 2014). The repumper laser is frequency stabilised by measuring its frequency with a commercial wavemeter and by giving feedback to its 1550 nm laser. Various optical components were omitted. The setup for the Doppler cooling and Raman laser has previously been described in detail in Hahn, 2019. Abbreviations: DM: dichroic mirror, PBS: polarising beam splitter, PPKTP: periodically poled Potassium titanyl phosphate, PZT: piezo. Some graphical components were adapted from Franzen, 2006.

3.6.2 Ar^{13+} clock laser setup

Previously (Micke et al., 2020), the clock laser for interrogation of Ar^{13+} was only delivered along the symmetry axis of the trap to have optimal coupling to the axial motional modes. While this is sufficient to interrogate the HCI and perform quantum logic, it is not enough to fully characterise the system. Therefore, additional laser paths were built to deliver light to other ports. The increased power demand is met by using an injection-locked slave laser.

The clock laser is based on a 882 nm laser diode which is frequency doubled to generate the required 441 nm light for interrogation of the clock transition in Ar^{13+}. A schematic drawing is shown in Fig. 3.6. The master laser provides about 55 mW entering into a SHG cavity (Hannig et al., 2018) which produces about 15 mW of frequency-doubled light for clock interrogation. Most of the light is passed through a double-pass AOM which allows for frequency shifting. The light is then sent

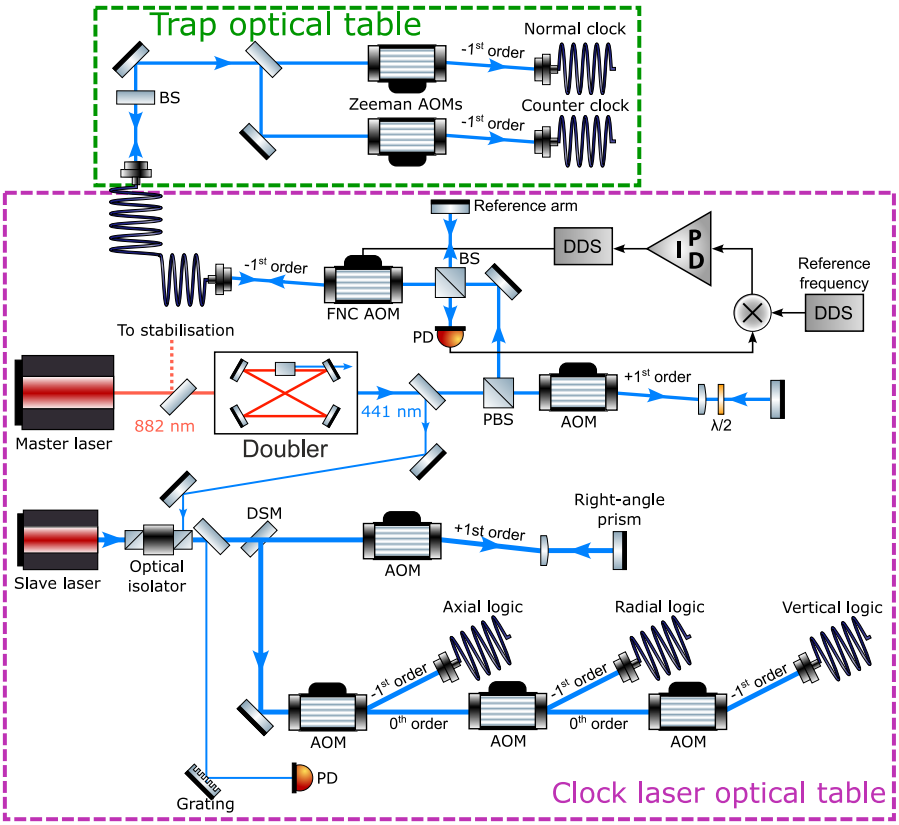

Figure 3.6: Sketch of the laser system used to address Ar^{13+}. The master laser is a diode laser at 882 nm which is stabilised with a scheme described in Sec. 3.6.3. The stabilised light is frequency doubled using intracavity second harmonic generation (SHG), and AOM and beamsplitters are separate the light for the two clock ports. Parts of the setup are built on the optical table fixed to the vacuum chamber to avoid differential movement. The length of the fibre transferring light between the tables is actively stabilised. For this, parts of the light is retro-reflected after passing the fibre and the phase noise is detected in a self-heterodyne measurement (Ma et al., 1994). Part of the frequency-doubled light is sent to a slave laser diode for injection locking. The injection lock is monitored with a grating and a photodiode (PD), which is sensitive to the level of injection. Light from the slave lasers is sent to three different ports of the vacuum chamber which can be switched separately. It is only used to perform logic operations with high Rabi frequencies. Various elements were omitted for clarity. Abbreviations: DSM: D-shaped mirror, AOM: accusto-optical modulator, BS: beam sampler, DDS: direct digital synthesizer, FNC: fibre noise cancellation, PBS: polarising beam splitter, PD: photodiode . Some graphical components were adapted from Franzen, 2006.

through a fibre to a second optical table, which has a rigid connection to the vacuum chamber and the in-vacuum Paul trap. Differential movement of these tables lead to non-negligible Doppler shifts and active fibre length stabilisation is employed to mitigate this (Ma et al., 1994). On the trap optical table, the light is split into two beams and then sent separately to the two counter-propagating optical ports for interrogation.

This setup is sufficient to interrogate the HCI's optical clock transition. Higher power is required for motional sidebands addressing with sufficiently high on-resonant Rabi frequency. For this, a slave diode with a free running wavelength around 440 nm at 30 °C is used. Its frequency is stabilised by injection-locking it to the master laser (see e.g. Hosoya et al., 2015; Pagett et al., 2016). Around 100 µW of light after the doubling cavity are picked off and injecting it into the slave diode through the rejection port of an optical isolator. The injection is monitored through a grating spectrometer which reflects light onto a photodiode with a signal depending on the injection level. While light from the slave laser is injection locked to the master and is therefore phase coherent, there remains a phase offset, which depends on the free-running and master frequency as well as their power (Siegman, 1986). If these parameters drift, a phase offset leads to an offset of the injected laser frequency from the measured master laser frequency. Additionally, it cannot be excluded that residual amplified spontaneous emission leads to an impure spectral profile. To avoid such issues having any effect on the measured transition frequency, the slave laser light is only used for logic operations addressing sidebands. The logic path includes various AOMs in double and single pass configurations to allow sending of light, to the axial, radial, and vertical ports (see Fig. 3.8).

3.6.3 Ar^{13+} clock laser stabilisation

Interrogation of the clock transition in Ar^{13+} necessitates a narrow laser, ideally with a linewidth below the natural linewidth of 16 Hz. For this, part of the fundamental light at 882 nm light is picked off (Fig. 3.6). It is sent to an optical cavity and a frequency comb for stabilisation, leading to a laser linewidth sufficiently narrow to probe the clock transition.

The stabilisation scheme is illustrated in Fig. 3.7. In the first step the laser is locked to a local pre-stabilisation cavity. This cavity has a finesse of ≈ 1000 which suppresses high frequency noise and narrows the laser linewidth to about 4 kHz. To further stabilise the laser, part of the light is sent through an optical fibre to a frequency comb. The optical path length of the fibre is actively stabilised by retro-reflecting a part of the light after passage and producing a beat signal with a reflection reference at the fibre input for phase stabilization (Ma et al., 1994). At the frequency comb, a beat signal ν_{Beat} between the laser and a comb tooth is generated. To improve the signal-to-noise ratio, a tracking oscillator[3] amplifies the beat signal. To transfer the beat from the frequency comb laboratory to the HCI laboratory, the beat signal is mixed with a fixed rf frequency to generate a 10.76 MHz signal. This is frequency mixed with a reference frequency ν_{Ref} to

3 Design from Department 4.3 Quantum Optics and Unit of Length at PTB.

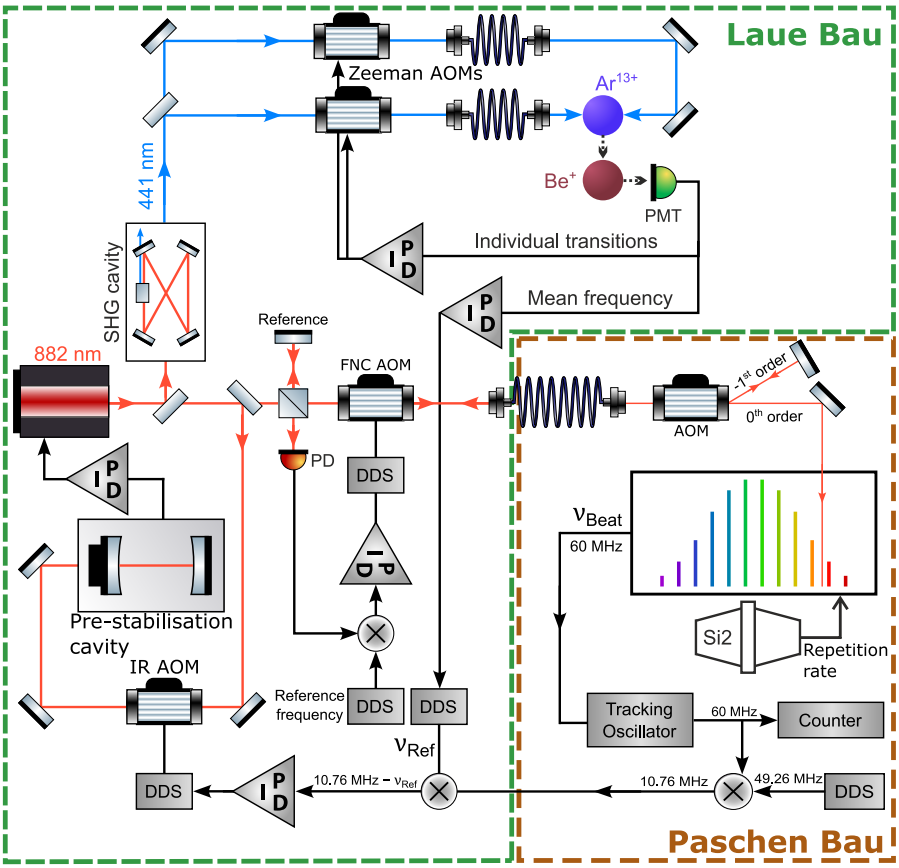

Figure 3.7: Scheme for stabilisation of the Ar^{13+} clock laser. The HCI clock is situated in the Laue Bau at PTB. On short time scales, the clock laser is stabilised to a pre-stabilisation cavity, removing high-frequency noise. For further stabilisation, light is sent to another building (Paschen Bau) at PTB. Part of the light sent through the fibre is retro-reflected to stabilise the fibre phase noise (Ma et al., 1994). There, a frequency comb locked to a laser stabilised to the ultra stable Si2 cavity (Matei et al., 2017) provides stabilisation at intermittent timescales. The such stabilised laser is employed to interrogate the individual Zeeman components. For clock operation, the laser frequency is steered to the interrogated Zeeman components using the so-called Zeeman AOMs. Additionally, the frequency measured on the frequency comb is steered towards the mean frequency by steering the offset between frequency comb and clock laser (Chapter 6). The given frequencies in the rf chain are typical values but various values were used during this work. Details are given in the main text. Abbreviations: AOM: accusto-optical modulator, DDS: direct digital synthesizer, FNC: fibre noise cancellation, IR: infrared, PD: photodiode, PMT: photomultiplier tube, SHG: second harmonic generation. Some graphical components were adapted from Franzen, 2006.

generate an error signal. Feedback is given to the drive frequency of the AOM denoted as IR AOM in-between the laser head and the pre-stabilisation cavity, stabilising ν_{Beat} (see Fig. 3.7). This phase lock loop (PLL) has a bandwidth of about 10 kHz. The repetition rate of the frequency comb itself is stabilised to the cryogenic silicon cavity Si2 (Matei et al., 2017) by another PLL. The combination of locks transfers the Si2 stability to the Ar^{13+} clock laser, suppressing laser frequency drifts to tens of Hz per day. The achieved laser linewidth for short timescales has not directly been measured which would necessitate another ultrastable laser for comparison. Data from clock comparison, and another similarly stabilised laser indicate that a linewidth of around 10 Hz at the ion position is plausible (see Appendix C). The stabilised laser is sufficient to interrogate the clock transition of Ar^{13+} with a natural linewidth of around 17 Hz.

For clock operation (Chapter 6), a frequency lock to the individual Zeeman components is performed. The derived mean frequency of the Zeeman components is used to steer the reference frequency $\nu_{\mathbb{R}}$. The time constant of this steering is much larger then the first two stabilisation steps and therefore does not interfere with the interrogation of the atomic transitions. It is implemented as part of the clock sequence and is described in Chapter 6.

3.6.4 Laser arrangement

The geometry of the laser delivery is critical to be able to perform all the required operations on the $^9Be^+$ and the Ar^{13+}. The geometry relative to the laboratory frame $\vec{x}_{\text{lab}}$ is shown in Fig. 3.8. Most beams are delivered in the $x_{\text{lab}} - y_{\text{lab}}$ plane, which also contains the quantisation axis defined by the magnetic field. In this plane, the beam angles are restricted by the vacuum chamber to multiples of 30° relative to the symmetry axis of the trap.

The $^9Be^+$ can be addressed by the Doppler cooling beam and the repumper, which are delivered along the quantisation axis. This is required to allow for pure σ^+ polarisation to have a closed transition for efficient Doppler cooling, repumping and state detection (see Fig. 3.1). Coherent operations on the $^9Be^+$ are performed using the red and blue Raman beams to drive a stimulated Raman transition on the qubit. Two different blue Raman beams are used to either address the axial or the radial motional modes by only having an effective k-vector along either axis when combined with the red Raman (Eq. 2.47). Imaging and fluorescence detection of ions is realised through a set of lenses in y_{lab} direction. More details on the orientation of the beams used for control of $^9Be^+$ can be found in Leopold, 2018.

Interrogation of the Ar^{13+} is performed by beams aligned with the coordinate system of the laboratory. Clock interrogation occurs along the x_{lab} where beams can be delivered in counter-propagating

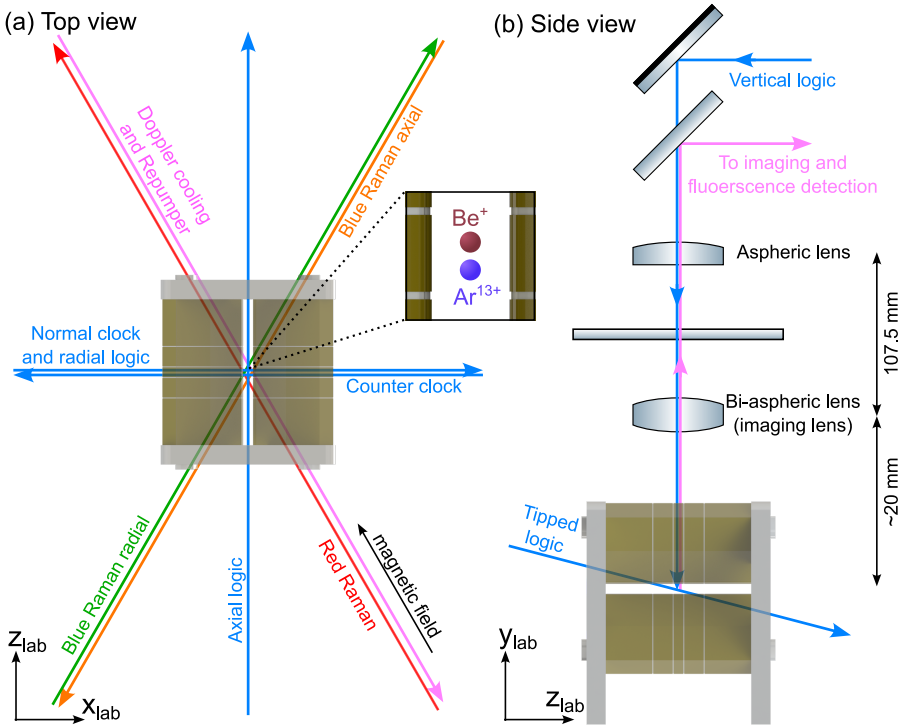

Figure 3.8: Laser orientations relative to the Paul trap. (a) Top view of the Paul trap along $-y_{\text{lab}}$. Most beams are delivered in the $x_{\text{lab}} - z_{\text{lab}}$ plane under various angles constrained by the vacuum chamber. The inset shows the orientation of a Ar^{13+}-$^{9}Be^{+}$ two-ion crystal along the symmetry axis. The magnetic field defines the quantisation axis. (b) Side view of the Paul trap along x_{lab}. Imaging and fluorescence detection of the ions is implemented in y_{lab} direction. To interrogate the HCI from outside the $x_{\text{lab}} - z_{\text{lab}}$ plane, a laser is sent backwards through the imaging system. Alternatively, a tipped beam which has angle of 15° with respect to the $x_{\text{lab}} - z_{\text{lab}}$ is available. Details are given in the main text. Some graphical components were adapted from Franzen, 2006.

directions, dubbed *normal* and *counter* clock in Fig. 3.8. Separate beam paths are used for so-called *logic* operations which address motional sidebands. Firstly, an axial logic beam is used for coupling the HCI's internal state to the axial motional modes for QLS. Secondly, a radial logic beam is used to address the weakly-coupled radial modes to perform algorithmic ground-state cooling and temperature measurements of these modes (see Sec. 4.2). Both beams are also used to measure micromotion (MM). To fully characterise MM in three dimensions, an out-of-plane beam is required, which is delivered to the trap centre through the imaging system along y_{lab} and is dubbed *vertical* logic.

Characterisation of MM requires knowledge of the laser angles and their uncertainties (Brewer et al., 2019). For the axial and radial logic beams an angle uncertainty of 3° is estimated based on geometrical constraints of the vacuum chamber and cryogenic system. The vertical beam passes through two lenses and in particular the imaging lens close to the trap has a high numerical aperture. This allows the beam

to be in principle focused onto the ion with significant angles of up to $\approx 23^\circ$ where it is limited by the aperture of the imaging lens. To assesses the angle of the vertical beam, a test setup including all the out-of-vacuum parts and a spare imaging lens was set up after the measurements concluded. The beam position on the imaging lens was measured for possible positions of the involved components within their tolerances. It was found that the beam was displaced in x_{lab} direction. From the known distance between ions and imaging lens, the estimated incident angles onto the ion of $\phi = 75(7)^\circ$ and $\theta = 90(7)^\circ$ in spherical coordinates[4] were deduced.

3.7 EXPERIMENTAL CONTROL SYSTEM

An experimental control system is critical for an optical clock as the dead time needs to be kept at a minimum while requiring flexible programming. During this work a new experimental control system has been implemented, called ARTIQ (Advanced Real-Time Infrastructure for Quantum physics) (Bourdeauducq et al., 2021).

ARTIQ provides accurate timing control through a field-programmable gate array (FPGA), which controls additional devices, like direct digital synthesizer (DDS), digital in- and output (DIO), and analog-digital converter (ADC). The DDS are primarily used to drive AOMs to shift laser frequencies. Switching of AOMs is achieved with external rf switches[5], which are triggered by the DIOs. The external rf switches provide an attenuation of at least 68 dB when switched off. Two types of DDS are available using either the AD9910 chip or the AD9912 chip[6]. The first one provides the option to amplitude or frequency modulate the pulses, at the cost of a limit frequency resolution of about 0.25 Hz. This type is primarily used for quantum logic operations performed on the $^9Be^+$ and for high-power, logic operations on the HCI as typical linewidths are much larger then the resolution. The AD9912 on the other hand provides a frequency resolution of about 8 µHz, but without the option of pulse shaping. All AOM involved in generation of the laser pulses used for clock interrogation are driven by these high-resolution DDSs to avoid aliasing effects. ADCs are used to monitor various system parameters, like the status of the laser stabilisation, cavity locks, and laser frequencies. The ARTIQ system's internal clock is running at 125 MHz which is disciplined by a 10 MHz signal generated by a Cs-fountain stabilised maser (Bauch et al., 2012).

Sequences are written in a programming language resembling Python, which is compiled on a host computer and then sent to

4 The spherical coordinates follow the convention that $\phi = 0^\circ$ and $\theta = 90^\circ$ corresponds to the x_{Lab}-axis, while $\phi = 90^\circ$ and $\theta = 90^\circ$ corresponds to the y_{Lab}-axis.

5 Mini-Circuits, ZASWA-2-50DRA+

6 https://github.com/sinara-hw/Urukul/wiki

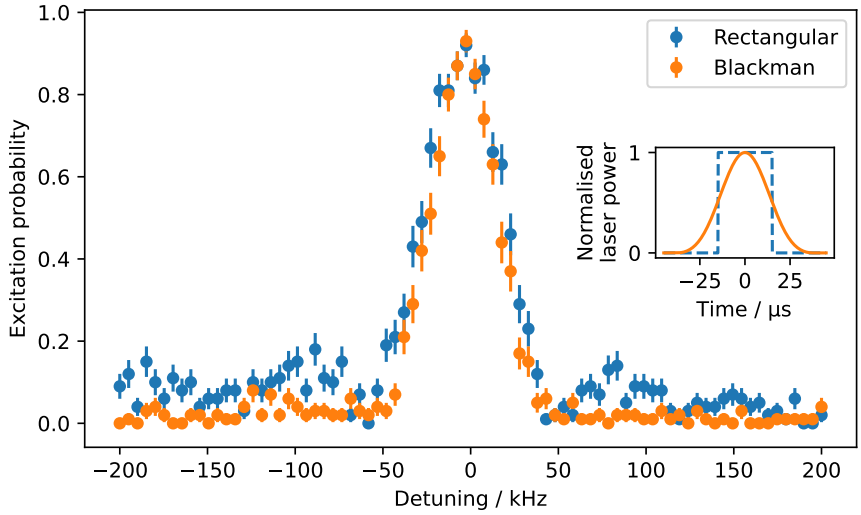

Figure 3.9: Comparison of excitation with a rectangular or Blackman-shaped pulse. The rectangular pulse shape shows the Rabi lineshape with the characteristic sidelobes, shown as the blue dots. These sidelobes are not present for the Blackman pulse shown as orange dots. The probed transition is the axial OP mode of a Ar^{13+}-$^{9}Be^{+}$ two-ion crystal after ground-state cooling. It is interrogated through a stimulated Raman transition on the $^{9}Be^{+}$. The inset shows the corresponding ideal laser pulse shapes.

the kernel device (FPGA) where it is executed. Data gathered during experiments is sent to the host computer asynchronously to the sequence and is saved without interrupting the sequence.

The laser power of the Raman beams used for $^{9}Be^{+}$ and the high power logic beams used for Ar^{13+} is actively stabilised to achieve consistent Rabi frequencies. The laser power is measured on a pulse-by-pulse basis and fed to a modified STEMlab (formerly: Red Pitaya) system in sample-and-hold configuration (Hannig et al., 2018). The integrated proportional–integral–derivative (PID) controller gives feedback to amplifiers providing the rf for driving the AOMs.

3.7.1 Pulse shaping

Coherent operations on transitions are commonly performed using "rectangular" pulses which sharply turn on and off and have a constant laser power in between. This leads to the well-known Rabi lineshape which has a non-vanishing excitation probability even far from resonance (see Fig. 2.3). This can lead to far off-resonant driving of other transitions and sidebands, reducing fidelity. To suppress this, pulse shaping can be employed where the incident laser power P is temporally modulated. Here we use the so-called Blackman shape where the

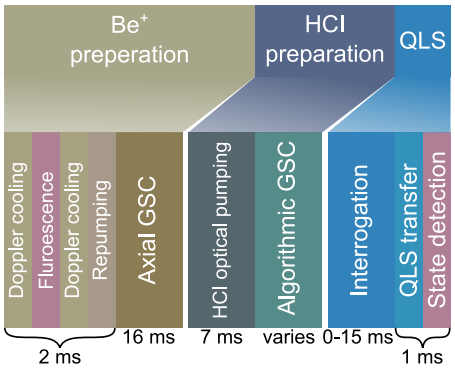

Figure 3.10: Typical experimental sequence. A typical experimental sequence interrogating the HCI consists of preparation of the $^{9}Be^{+}$, followed by preparation of the HCI. Finally, a transition is interrogated and readout using QLS. Timings are typical values that vary, in particular due to laser power changes. Details are given in the main text. Abbreviations: GSC: ground-state cooling, QLS: Quantum logic spectroscopy.

Rabi frequency $\Omega \propto \sqrt{P}$ of the pulses is modulated following (Harris, 1978)

$$\frac{\Omega(n)}{\Omega_0} = \left[\frac{1-\alpha}{2} - \frac{1}{2}\cos\left(\frac{2\pi n}{M-1}\right) + \frac{\alpha}{2}\cos\left(\frac{4\pi n}{M-1}\right)\right] \tag{3.59}$$

with $\alpha = 0.16$, M the number of discrete steps, $n \in \{0, 1, ..., M-1\}$ is the current step, and Ω_0 being the maximal Rabi frequency. Typically $M = 100$ is used to describe the waveform for pulse lengths between 5 µs and 100 µs. An example of the different excitation profiles for a rectangular pulse and a Blackman-shaped pulse is shown in Fig. 3.9 for the case of stimulated Raman transition of $^{9}Be^{+}$ in a $^{40}Ar^{13+}$-$^{9}Be^{+}$ crystal. For stimulated Raman transitions, only the blue Raman beam (see Sec. 3.6.1) is temporally shaped, while the red Raman remains rectangular. The wings of the Rabi lineshape are clearly visible for rectangular pulses while no such feature appears for the shaped pulse.

The downside of pulse shaping is that for a given peak laser power, the pulse length needs to be increased to achieve a π-rotation. Empirically, a 2.5 times longer pulse length was found to be optimal. To keep the additional time needed low, Blackman pulses are only employed for first-order sideband pulses of the stimulated Raman transition of the $^{9}Be^{+}$ and for first-order axial motional sidebands of the HCI. This led to a significant reduction of the achieved temperature as well as a slight increase in cooling rate when using resolved-sideband cooling due to lower off-resonant scattering rates. Additionally, it increased the fidelity of QLS operations.

3.7.2 Sequence

The experimental sequence varies depending on the performed experiments. In the case of an Ar^{13+}-$^{9}Be^{+}$ crystal it typically follows the scheme shown in Fig. 3.10. An experimental cycle starts by Doppler cooling the $^{9}Be^{+}$, then PMT counts are measured with the repumper enabled to check if an ion is present. The system is again Doppler cooled with decreasing power to reach a temperature close to the

Doppler limit. Then the $^9Be^+$ is prepared in $|\downarrow\rangle$ by using the repumper laser before resolved-sideband cooling on the $^9Be^+$ Raman transition cools the axial motional modes close to the ground state. First-, second- and third-order sidebands are used to avoid population trapping in Fock states with nearly vanishing Rabi frequency, due to the large Lamb-Dicke parameter ($\eta_{ax} \approx 0.5$) (Leopold et al., 2019). The employed sequence is described in Micke, 2020.

In the next step, the internal state of Ar^{13+} is prepared by optically pumping it to the desired electronic ground state using a quantum-logic like sequence of laser pulses (Micke et al., 2020). Optionally, in a final preparation step algorithmic ground-state cooling is applied to cool the radial IP modes (see Sec. 4.2). After the motional and electronic states are prepared, the desired transition, e.g. the clock transition is interrogated using QLS. The result of the interrogation is detected on the cycling transition of the $^9Be^+$ by detecting photons scattered (Leopold, 2018). Cooling, optical pumping and detection take a combined time of around 26 ms with additional time needed for algorithmic ground-state cooling (Sec. 4.2) and interrogation. The experiments are usually repeated 100 times to reduce quantum projection noise (Itano et al., 1993).

3.7.3 Monitoring

Monitoring of the experimental setup is integrated into the sequence. The first check that is performed, is the measurement of fluorescence of the $^9Be^+$ by performing state detection after preparing the bright state. To avoid scattering into the dark state due to polarisation impurities, the repumper is applied simultaneously. If no fluorescence is detected, an error is raised. This can for example indicate a loss of ion due to charge exchange collisions.

Furthermore, the status of various lasers and the trap drive stabilisation is monitored at the beginning and end of each experimental cycle by reading in various voltages using the ADC. A list of the monitored parameters is given in Tab. 3.1 separated for algorithmic ground-state cooling (Chapter 4) and clock comparison (Chapter 6). For the optical dipole force measurements (Chapter 7), the monitoring was kept the same as during the clock comparison. If any measured value is outside a specified range, an error is raised. If any error is raised, the result of the experimental cycle is discarded and the cycle is repeated. After 100 successively invalid cycles, the sequence is terminated with an error message displayed.

	Algo. GSC	Clock comp.
$^{9}Be^{+}$ laser systems		
Raman laser SHG cavity lock	X	X
Raman laser SHG cavity power	X	X
Red Raman laser power	X	X
Blue Raman laser power	X	X
Doppler cooling laser SHG cavity power	X	X
Repumper laser SHG cavity power		X
Repumper laser frequency	X	X
Ar^{13+} laser systems		
Pre-stabilisation cavity lock	X	X
Slave diode injection level	X	X
Axial logic laser power	X	X
Radial logic laser power	X	X
Miscellaneous		
Trap drive stabilisation		X

Table 3.1: Monitored systems and values during experimental cycles. Electronic signals indicating the status of the listed systems were read in using an ADC of the control system. Some parameters were added to the monitoring in between measurements of the algorithmic ground-state cooling (Chapter 4) and the clock comparison (Chapter 6).

Part II

EXPERIMENTS AND RESULTS

4 RADIAL IN-PHASE MODES

The motional modes of the two-ion crystal are described by a coupled system, as explained in Sec. 2.1.3, where the energy of each motional mode is distributed between the two ions. The coupled motional modes are derived from the single ion motional modes which interact through the Coulomb interaction. The coupling strength depends on the ion's properties in the form of the ion charge q and ion mass m as well as the trapping potential characterised through the single ion motional frequency. In the case of similar charge-to-mass ratios, the motional modes are strongly coupled and both ions exhibit considerable motion in all motional modes. In the combination of $^9Be^+$ and an HCI (e.g Ar^{13+}), this can be violated and some motional modes are only weakly coupled (Kozlov et al., 2018; Wübbena et al., 2012), i.e. there exist modes where only one of the two ions moves for practical purposes. This decoupling happens predominantly in radial direction which is more sensitive to the charge-to-mass ratio. This can be seen from the single ion motional frequency which in the radial directions scales with $\omega_{x/y} \propto q/m$ (Eq. 2.11), while in axial direction it scales with $\omega_z \propto \sqrt{q/m}$ (Eq. 2.10).

The mode coupling is characterised by the eigenvector $\vec{b}_k$, which describes the relative contribution of each ion to the total energy of a motional mode (Sec. 2.1.3). It is illustrated for one radial mode (x) and the strongly coupled axial modes in Fig. 4.1 for a Ar^{13+}-$^9Be^+$ crystal, showing that the $^9Be^+$ has only a negligible contribution to the x IP mode. Correspondingly the velocity of the $^9Be^+$ in this mode is small which leads to weak Doppler cooling (Eq. 2.51). This leads to a long time of Doppler cooling time being needed to reach the Doppler limit as is shown in Sec. 4.2. The small eigenvector components also lead to vanishing Lamb-Dicke parameters. To counteract this impractical high laser power would be necessary, making Raman sideband cooling on the $^9Be^+$ infeasible. To solve this problem, other methods to cool down the weakly-coupled radial (WCR) modes need to be employed.

In the first section of this chapter, simulations are presented which investigate methods which use static or rf electric fields to increase the cooling rate. These showed an insufficient increase in cooling rate. Thus, in the second section a quantum algorithm, dubbed *algorithmic ground-state cooling*, is demonstrated, which allows for ground-state cooling of WCR modes.

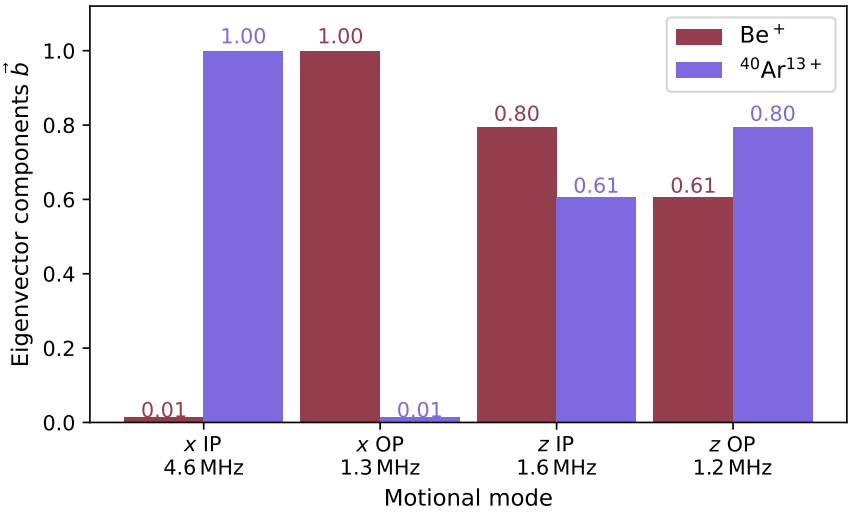

Figure 4.1: Eigenvector $\vec{b}$ components for the axial and one radial direction for typical experimental parameters. In the axial direction the two components are similar in size, i.e. the motional modes are strongly coupled. The strongly differing charge and mass, leads in the radial direction to a weak coupling between the ions and correspondingly low cooling rates for the x IP mode. The $^{9}Be^{+}$ single ion frequencies are $\omega_x/2\pi$ =1.6 MHz and $\omega_z/2\pi$ =0.78 MHz, the coupled motional mode frequencies are given in the figure.

4.1 SIMULATION

Various options for cooling the WCR modes are investigated using a classical simulation of a Ar^{13+}-$^{9}Be^{+}$ two-ion crystal's motion. The simulations are performed using a Fourth-Order Runge-Kutta integrator on the classical equations of motion, which is implemented using custom C++ code. It allows for simulations within the pseudo-potential approximation as well as simulations including the rf field and MM. Unless otherwise stated, the pseudo-potential approximation is used.

The simulations are initialised with a single $^{9}Be^{+}$ and a single $^{40}Ar^{13+}$ positioned randomly within a region of 100 µm of the trap centre. To find the equilibrium, the ions are moved along the force vector (Eq. (2.15)) with overdamping. This relaxes the ions slowly to their equilibrium positions and is continued until the residual forces reach a threshold of below 1×10^{-30} N. At the equilibrium position, the ions possess no potential energy. Therefore, to add a finite energy their velocity is set such that the corresponding kinetic energy is 10 times the Doppler limit. Doppler cooling is implemented as a frictional force acting only on the $^{9}Be^{+}$ (Eq. (2.51)), with $\beta \approx 6 \times 10^{-21}$, corresponding to a value of the saturation parameter of $s \approx 0.4$ and a laser detuning $\Delta = 0.5\Gamma$ with the linewidth Γ. The cooling force is projected onto the different axes using the experimental laser angle (Sec. 3.6.4).

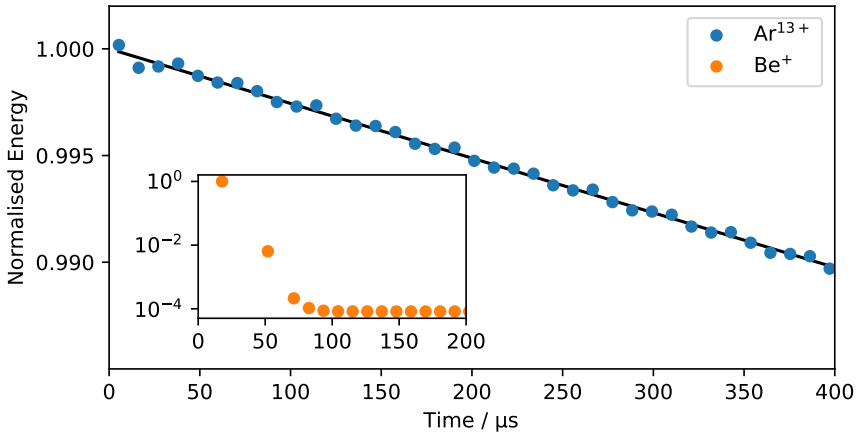

Figure 4.2: Extraction of the cooling rate γ from simulations. The peak amplitude (u_{max}) for each oscillation is extracted from the simulations for each ion separately. This is converted to an energy ($E \propto u_{max}^2$) where the energy of the WCR mode is mostly stored in the Ar^{13+} while the energy of the OP mode is in the motion of the $^9Be^+$. Laser cooling of the $^9Be^+$ reduces the energy of the Ar^{13+} slowly, as its total energy is dominated by the energy in the WCR mode. The energy of the $^9Be^+$ decays quickly, with the small residual energy coming from the WCR mode. A linear fit is used to describe the Ar^{13+} data, where the slope is taken as the cooling rate γ of the WCR mode. For illustrative purposes only the average energy of 50 successive oscillations is shown.

The simulations use a timestep of 1 ns for the pseudo-potential approximation and 0.1 ns when including the full rf potential. To check for convergence, various simulations are run with 10 times smaller timesteps and only negligible differences were observed in the extracted results. Trapping parameters were chosen such that they correspond to typical experimental values as given in Tab. 5.1. The simulated trajectories are written to an external file during the simulation. To reduce the filesize only every 10^{th} nanosecond is saved.

Cooling rates are estimated by automatically detecting the peak amplitude of each oscillation of each ion. The motional amplitude (u_{max}^2) is converted to an energy ($E \propto u_{max}^2$) and an example is shown in Fig. 4.2. The WCR mode dominates the residual motion after a short amount of time and a linear fit to the kinetic energy of the Ar^{13+} is performed where the slope is taken as a cooling rate γ of the WCR mode. The observed cooling rates are small compared to the simulated timescales allowing for the linearisation. In the case where the full rf field is simulated, the same procedure is used with the result including contributions from IMM. This does not affect the conclusions as only the relative change of the cooling rate is relevant.

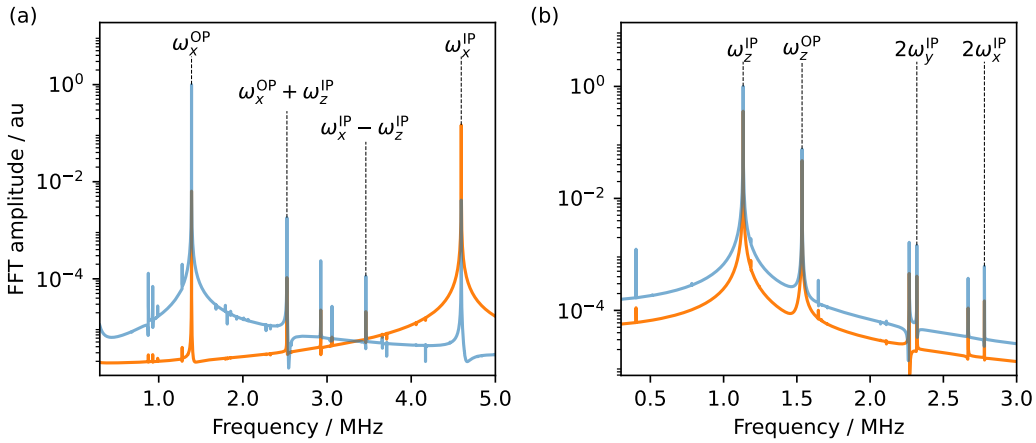

Figure 4.3: Fourier transformation of simulated Ar^{13+}-$^{9}Be^{+}$ crystal motion. Shown is the result for $^{40}Ar^{13+}$ (orange) and for $^{9}Be^{+}$ (blue) for the (a) x-direction and (b) z-direction. The dominant peaks are the secular motional eigenmodes. Additional mixture terms appear due to higher-order expansions of the Coulomb interaction (see Appendix B).

4.1.1 Motional spectrum

As a test, the motion of a Ar^{13+}-$^{9}Be^{+}$ two-ion crystal is simulated with no cooling applied. A fast Fourier transform is applied to the simulated trajectory, with the spectrum shown in Fig. 4.3 for the x- and z-axis. The largest amplitude in both directions are the frequencies of the coupled secular motion which come from the second-order expansion of the Coulomb interaction (see Sec. 2.1.3). Additional peaks are visible where some can be identified as coming from third-order terms of the Coulomb interaction (see Appendix B), which mix different dimensions. Further peaks can likely be attributed to higher-order terms.

4.1.2 Crystal tilting

Tilting of a crystal can be achieved by applying a transverse electric field. This changes the motional eigenmodes such that an increased cooling efficiency of the WCR modes can be achieved and has been used in the case of a $^{9}Be^{+}$-$^{27}Al^{+}$ two-ion crystal (Rosenband et al., 2008). Here, simulations are performed to investigate this approach for the $^{9}Be^{+}$-$^{40}Ar^{13+}$ two-ion crystal.

Assume an electric field in x-direction being applied to an axially (z) aligned two-ion crystal. Due to the different charges and masses of the two ions, they are displaced differently and the crystal will be tilted with respect to the initial configuration (see Fig. 4.4). Then the two ions are separated in z-direction by a distance Δz and by Δx in x-direction. In the following, calculations are given to estimate the

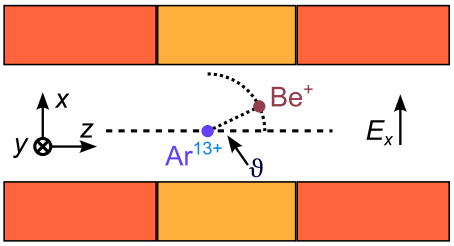

Figure 4.4: Sketch of a tilted ion crystal. By applying an electric field E_x in x-direction, the crystal is tilted by an angle ϑ with respect to the z-axis. The resulting motional mode mixing increases the cooling rate of the WCR mode in x direction. Only the displacement of $^9Be^+$ is shown, while the smaller displacement of Ar^{13+} is omitted for clarity.

increase in cooling efficiency, where only the relative scalings are of interest.

The coupling between the two ions is given by the Coulomb interaction. In the new ion positions, the coupling can be expanded similarly to Eq. (2.22) and yields

$$\begin{aligned}\frac{1}{r} \approx \frac{1}{d} &+ \frac{(3\Delta x^2 - d^2)(x_{\mathrm{Be}} - x_{\mathrm{Ar}})^2}{2d^3} - \frac{(y_{\mathrm{Be}} - y_{\mathrm{Ar}})^2}{2d^3} \\ &+ \frac{(3\Delta z^2 - d^2)(z_{\mathrm{Be}} - z_{\mathrm{Ar}})^2}{2d^5} \\ &+ \frac{3\Delta x \Delta z (x_{\mathrm{Be}} z_{\mathrm{Be}} + x_{\mathrm{Ar}} z_{\mathrm{Ar}} - x_{\mathrm{Be}} z_{\mathrm{Be}} - z_{\mathrm{Be}} x_{\mathrm{Ar}})}{d^5}. \end{aligned} \tag{4.60}$$

The total distance between the ions is $d = \sqrt{\Delta x^2 + \Delta z^2}$. It is useful to define the angle between the crystal axis and the z-axis ϑ, and $\tan(\vartheta) = \Delta x / \Delta z$. The distances Δx and Δz can be extracted from simulations. It is found that $d \approx$ const. for $0 \leq \vartheta < \pi$.

The additional coupling terms in Eq. (4.60) scaling with $\Delta x \Delta z$ and $3\Delta x^2 - d^2$ correspond to axial-radial and radial-radial coupling respectively. They are treated as perturbations because the radial modes are weakly coupled in the very beginning and can be rewritten in terms of d and ϑ as

$$\Delta x \Delta z = \frac{d^2}{2} \sin(2\vartheta) \tag{4.61}$$

$$\left(3\Delta x^2 - d^2\right) = \frac{d^2}{2} \left(1 - 3\cos(2\vartheta)\right). \tag{4.62}$$

The cooling rate γ is quadratic in the motional amplitude (Wübbena et al., 2012), and therefore the expected scaling as a function of the angle ϑ is

$$\gamma_{xz} \propto \sin^2(2\vartheta) \tag{4.63}$$

$$\gamma_{xx} \propto \left(1 - 3\cos(2\vartheta)\right)^2. \tag{4.64}$$

This shows that tilting the crystal angle will increase γ by a factor $\mathcal{O}(1)$ within the assumed approximations. Note that this implicitly

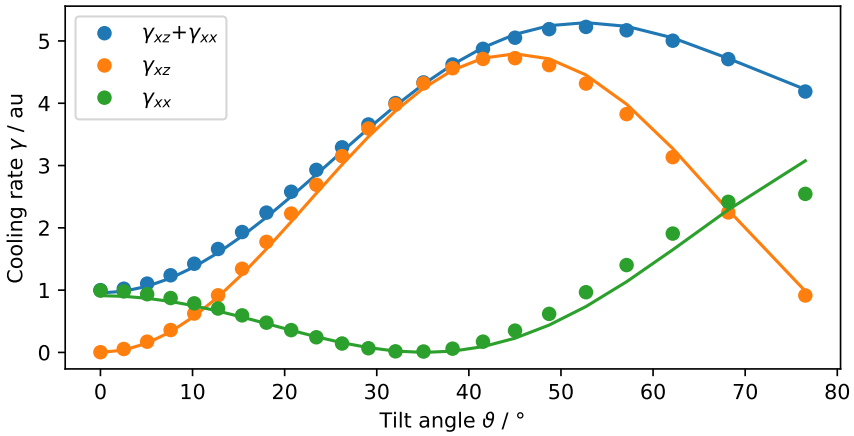

Figure 4.5: Cooling rate γ as a function of tilting angle ϑ. The cooling laser is either along the z-axis (orange), x-direction (green) or the experimentally used direction (blue) (Fig. 3.8). The cooling rates were rescaled such that the individual directions are comparable. Points show results from simulations while the lines are a single parameter fit of Eq. (4.63) and (4.64).

assumes that there is no resonantly enhanced coupling between axial and WCR modes, based on $\omega_z^{\mathrm{IP/OP}} \ll \omega_x^{\mathrm{IP}}$ [1].

To investigate this with simulations, a two-ion crystal is prepared as described above with a varying electric field in x-direction to tilt the crystal angle. Then cooling is applied either along x-, z- or the experimentally used direction (see Fig. 3.8). The achieved cooling rate as a function of ϑ is extracted and the result is shown in Fig. 4.5.

To describe the data, Eq. (4.63) and (4.64) with only the amplitude factor as degree of freedom are used to fit the data for the individual cooling directions. The weighted sum of the equations is used for the experimental cooling direction with the weights given by the relative angle. The fits agree reasonably well within the used approximations. The maximal cooling of the radial direction is achieved for $\approx 53°$, where a cooling rate increase of ≈ 5.5 is achieved. This is significantly smaller then the required factor of ≈ 100 which is needed to reach the Doppler cooling limit in a reasonable time with the current setup (see Sec. 4.2.1).

4.1.3 Parametric excitation

Parametric excitation is a process where trapping parameters are varied such that they can excite motion. It can also lead to mixture of different motional modes if the variation happens at the difference

1 In the case that $\omega_x^{\mathrm{IP}} \approx \omega_z^{\mathrm{IP/OP}}$ much larger coupling between these motional modes where observed in simulations. This makes it applicable in a $^{27}Al^+$-$^9Be^+$ two-ion crystal and might make it useful in certain $^9Be^+$-HCI systems. Further investigated was not performed here.

frequency of two motional modes allowing, in principle, for cooling of WCR modes by coupling them to other modes. In the following, the option of modulating the dc confinement or the rf trap drive to improve the cooling of the WCR modes are discussed.

4.1.3.1 DC modulation

The first option for parametric excitation is to apply an rf drive to a dc electrode to modulate the trapping potential. If the rf drive has a frequency equal to the frequency difference of two motional eigenmodes, phonons can be swapped between them. By ground-state cooling one of the motional modes while the mixing drive is applied, the other one will also be cooled. This has already been experimentally demonstrated for a single $^{40}Ca^{+}$ trapped in a surface trap by Gorman et al., 2014. The following discussion regarding the application here is based on their findings. Recently, application to a $^{9}Be^{+}$-$^{25}Mg^{+}$-$^{9}Be^{+}$ mixed ion crystal was also demonstrated (Hou et al., 2022).

When applying the rf voltage at frequency ω to a dc electrode it will primarly generate an electric field $\vec{E}$ which leads to a driven motion at frequency ω, similar to MM. The driven motion is detrimental to the cooling, as it modulates the cooling laser frequency and introduces heating effects. Secondarily, field gradients of the form $\partial E_u/\partial v \quad (u, v \in x, y, z)$ are generated, which lead to a coupling of motional modes of direction u and v. An important quantity is the ratio of $\vec{E}$ to $\partial E_u/\partial v$ which is effectively the ratio of driven motion to mode coupling. It depends strongly on the geometry of the trap and is expected to be more favourable in surface traps due to the small ion-electrode distance. In larger traps, like the blade trap used here, the electric fields are expected to be more homogeneous. Simulations[2] of the electric potentials of the employed trap showed that of all available electrodes the optimal one is the central segment with $E_r/\left(\partial E_r/\partial r\right) \approx 2500\,\mathrm{m}^{-1}$ where $r \in \{x, y\}$.

A problem of this technique stems from the $\approx 3\,\mathrm{MHz}$ frequencies that need to be applied to the electrode. This is much higher then the cut-off frequency of the low-pass filters on the central (34 Hz), inner (34 Hz), and outer endcap (34 kHz) electrodes (Leopold, 2018). With this filtering, an electric field $E_r = 0.2\,\mathrm{V\,m}^{-1}$ at the ion position is achievable for a peak input voltage of 100 V. Much higher voltages are omitted by the voltage rating of the in-vacuum wires. A reduction of the filtering is possible but also allows noise at megahertz to enter the trap. This will potentially increase anomalous heating rates Γ_h which is particularly harmful for HCI because $\Gamma_\mathrm{h} \propto Z^2$ (Brownnutt et al., 2015).

For simulations, the effect of the driven motion was neglected, and only the coupling field was included. Even in this favourable case, an

2 Based on simulations from Jan-Christoph Heip. Software: COMSOL Multiphysics from COMSOL Inc.

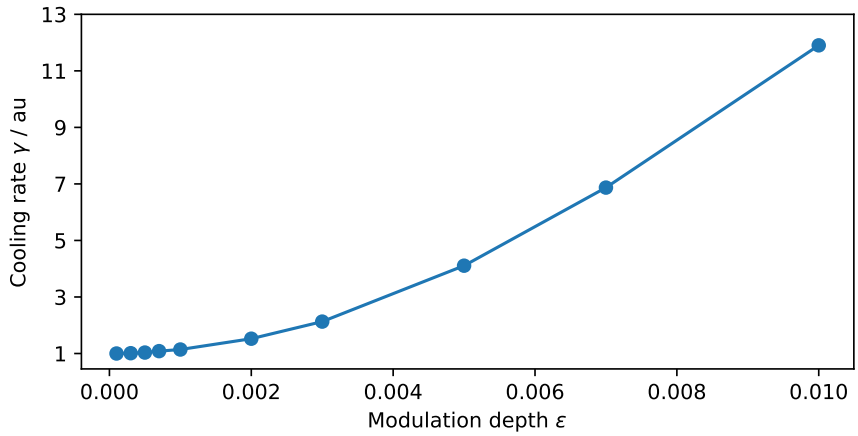

Figure 4.6: Normalised cooling rate as a function of rf modulation depth. The points show simulation results for varying modulation depth ϵ. The line is a guide to the eye. The modulation frequency is the difference frequency of the x-modes allowing for cooling of the x WCR through the strongly cooled x-OP mode. In the experimentally accessible range $\epsilon < 10^{-3}$ only a small increase can be achieved.

electric field gradient 1000 times larger then currently possible was needed to achieve a fivefold increase in cooling rate and drops of for smaller electric field gradients, being negligible for experimental achievable parameters. This makes it unlikely to be an approach with sufficient coupling strength, thus no experimental implementation was pursued here.

4.1.3.2 Trap drive modulation

Alternatively, exchange of energy through parametric excitation can be achieved by modulating the rf drive at a frequency which is equal to the frequency difference. This only allows for coupling of x- and y-modes as the z-modes are not affected by the trap drive field. The main limitation of this method is the narrow bandwidth helical resonator used to generate high voltage rf signal for ion trapping (Leopold, 2018).

To simulate the effect, the rf amplitude is modulated by an oscillatory term with amplitude ϵ and with difference frequency of the x-modes $\delta/2\pi \approx 3.3\,\mathrm{MHz}$. This requires the simulation to fully simulate the rf voltage instead of the pseudo-potential approximation. The rf voltage is described by

$$V_{\mathrm{rf}} = V_0\,[1 - \epsilon\cos(\delta t)]\cos(\Omega_{\mathrm{rf}} t) \tag{4.65}$$

where Ω_{rf} is the trap drive frequency, and V_0 is its peak amplitude. The simulation result of the cooling rate as a function of ϵ is shown in Fig. 4.6. The currently employed helical resonator has a bandwidth

of $\approx 100\,\mathrm{kHz}$ leading to a maximum modulation depth of around $\epsilon \approx 10^{-3}$ at δ. This means that cooling is only marginally increased for the experimental accessible values of $\epsilon < 10^{-3}$. Larger ϵ would require a smaller quality factor (Q) for the helical resonator which potentially increases heating rates due to worse suppression of high frequency noise. A lower Q would also require higher input power to achieve the same voltage amplitude and therefore more dissipated power in the cryogenic system, leading to an elevated temperature and worse vacuum conditions. No experimental implementation was pursued here.

4.2 ALGORITHMIC GROUND-STATE COOLING

Another approach to control the WCR modes is to use coherent operations on the $^{40}Ar^{13+}$ to transfer energy from the radial mode to the axial modes then dissipate it through the $^{9}Be^{+}$. This is the method employed during clock operation. This technique falls in the category of algorithmic cooling, where energy is transferred from one qubit to another to dissipate it there (Boykin et al., 2002). The results presented in the following have also been published in King et al., 2021.

The protocol is schematically shown in Fig. 4.7 (a). It is similar to QLS and starts by preparing the HCI and $^{9}Be^{+}$ in their electronic ground states and the motional ground states of the axial modes. A pair of RSB pulses is used to transfer the excitation of one of the WCR modes to the axial OP mode via the HCI's electronic state. Then, the energy from the WCR modes can be dissipated from the shared axial OP mode through Raman sideband cooling on $^{9}Be^{+}$. This can be achieved because $^{9}Be^{+}$ possesses a significant amplitude in both axial motional modes. By applying such a cycle, one phonon can be removed from a WCR mode while returning the HCI to its electronic ground state. It is important to note that the small amplitude of the $^{9}Be^{+}$ ion for the WCR modes suppresses reheating of this mode during the dissipation process (scattering of photons during sideband cooling).

The experimental implementation is illustrated in Fig. 4.7. To fully ground-state cool the WCR modes, initial Doppler-cooling for 200 ms is needed to bring the WCR modes close to the Doppler limit. Then the axial modes are ground-state cooled using resolved Raman sideband cooling (Sec. 2.3.2) and the internal state of the HCI is optically pumped to the required ground state (Micke et al., 2020). Then eight algorithmic cooling cycles are applied to each WCR mode in an interleaved fashion. The optimal pulse length for the WCR mode RSB population transfer increases as the mean phonon number is lowered with each cooling cycle (Wineland et al., 1998). Therefore, the pulse

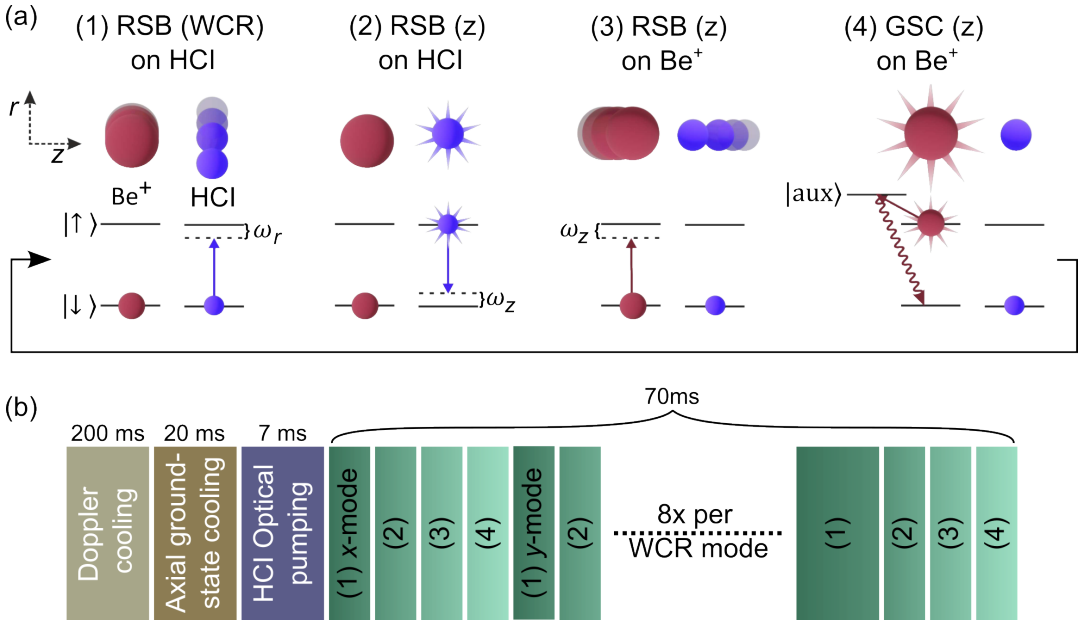

Figure 4.7: Algorithmic ground-state cooling sequence. (a) Scheme of algorithmic ground-state cooling. (1) The motional excitation of one of the WCR modes ($r = x, y$) is mapped onto the HCI's electronic state through a red-sideband (RSB) transition. (2) The electronic excitation is transferred to one of the axial (z) modes through another RSB transition. (3-4) Resolved sideband cooling on the $^9Be^+$ is used to remove the transferred motional energy and returns the $^9Be^+$ back to the electronic ground state. Dissipation is achieved by spontaneous decay of the short-lived auxiliary state $|\text{aux}\rangle$. In total, the ions are returned to their electronic ground states and a single phonon was removed from one of the WCR modes. This is repeated multiple times to reach the motional ground state of the WCR modes. (b) Experimental sequence to apply algorithmic ground-state cooling to the WCR and cool it to the ground state. Doppler cooling, axial ground-state cooling and optical pumping prepare the two ions' internal and motional states. The long Doppler cooling time of 200 ms is necessary to achieve a temperature close to the Doppler limit for the WCR modes. Algorithmic ground-state cooling is applied eight times per mode with the two modes being interleaved. Parts of the figure are adapted from King et al., 2021.

length slowly increases from $0.5t_{\pi,0}$ to $t_{\pi,0}$ during the cooling[3], where $t_{\pi,0}$ is the optimal time for the lowest achieved temperature calibrated through Rabi oscillations after ground-state cooling.

As a demonstration of the reduction in mean phonon number due to algorithmic ground-state cooling, frequency scans over the sidebands are performed with 200 ms for only Doppler cooling which is compared to the result with additional algorithmic ground-state cooling. The experimental result is shown in Fig. 4.8. For the Doppler cooled case (blue), a small asymmetry between RSB and BSB is visible, which is caused by a small fraction of the population being in $|n = 0\rangle$.

3 With in this section the relative pulse lengths $(0.5, 0.6, 0.7, 0.8, 1, 1, 1, 1)$ are used. This was later numerically optimised to $(0.4, 0.4, 0.5, 0.5, 0.6, 0.7, 0.8, 1.)$ which showed only an insignificant improvement.

After algorithmic ground-state cooling (orange), a significant part of the population is moved to $|n = 0\rangle$, leading to a strong suppression of the RSB.

To estimate the mean phonon number, sideband thermometry is employed (Turchette et al., 2000). For this, the k^{th} order RSB and BSB are probed and, assuming a thermal distribution, $\bar{n}$ is given by

$$\bar{n} = \frac{r^{1/k}}{1 - r^{1/k}} \tag{4.66}$$

where r is the ratio of the measured excitation probability of RSB and BSB. Equation (4.66) is valid for all sideband orders with the highest sensitivity reached for k close to $\bar{n}$. Therefore, for $\bar{n}$ close to the ground-state, $k = 1$ is optimal while for Doppler-cooled modes ($\bar{n} \approx 5 - 20$) larger k are employed to achieve lower uncertainties (see Sec. 5.1.2). The assumption of a thermal distribution neglects that resolved sideband cooling can produce non-thermal distributions leading to an underestimated temperature (Chen et al., 2017; Rasmusson et al., 2021). This is not the main topic of this chapter and will be discussed in more detail in Sec. 5.1.2. For the temperature measurements presented in the section below, the sidebands are probed on resonance with a probe time length chosen to give the largest contrast of both RSB and BSB excitation.

In the case of Fig. 4.8, the line centre is first estimated by fitting to the data. In the Doppler-cooled case, a thermal distribution of Fock states is occupied and a sinc^2-function is used for the fitting. After ground-state cooling, most of the population is in the ground state and the data is well fitted by the Rabi lineshape (Eq. (2.34)). For the sideband excitation probability, the experimental value closest to the fitted line centres is used, which is consistent with other temperature measurements in this thesis. This yields an $\bar{n}$ after Doppler cooling for the x- and y-mode of $3.1(13)$ and $3.3(13)$ respectively. This value is consistent with the expected Doppler limit of $\bar{n} \approx 3$. After ground-state cooling the estimated mean phonon number is $\bar{n}_x = 0.39(15)$ and $\bar{n}_y = 0.21(8)$, showing its clear reduction. This corresponds to a temperature of $T = 174(38)\,\mu\text{K}$ and $T = 121(22)\,\mu\text{K}$, assuming a thermal distribution (Eq. (2.54)). This, combined with the simultaneous axial ground-state cooling, makes these the coldest HCI ever reported.

Additionally, Rabi excitation was performed with a varying probe time on the BSB of each of the two WCR modes with and without applying algorithmic ground-state cooling. In such a measurement, all occupied Fock states contribute to the signal with a varying on-resonant Rabi frequency (Eq. (2.43)). For high temperatures, many Fock states are occupied which quickly dephase. Near the ground-state, the signal is dominated by $|n = 0\rangle$, suppressing this effect. The experimental result is given in Fig. 4.9 and shows the expected reduction in dephasing after algorithmic ground-state cooling. For fitting

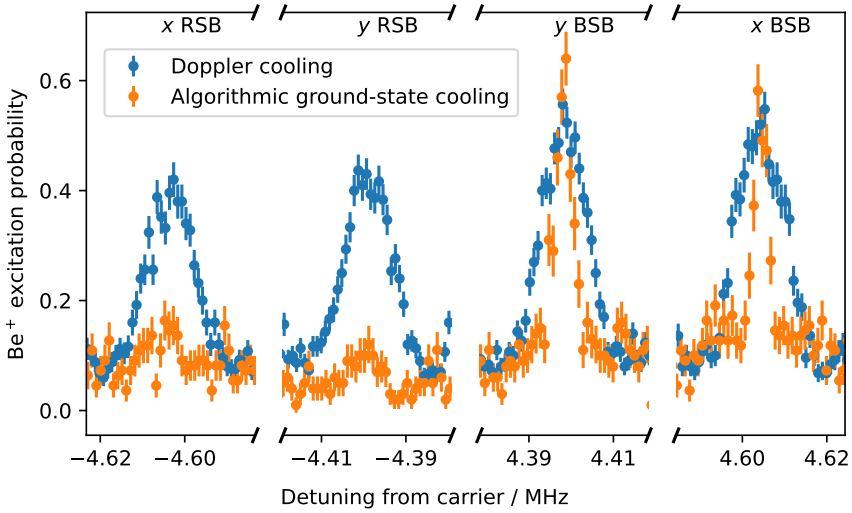

Figure 4.8: Frequency scan over the weakly coupled radial modes. After sufficiently long time of Doppler cooling (blue), a small asymmetry between red and blue sideband (RSB and BSB) is visible. With algorithmic ground-state cooling (orange), a significant population transfer to the ground state is achieved, which is indicated by the vanishing red sideband. From the asymmetry, the mean phonon numbers are estimated to be $\bar{n}_x = 0.39(15)$ and $\bar{n}_y = 0.21(8)$. Differences in linewidths are caused by different probe time lengths. Details are given in the main text.

of the data we assume a thermal state for each WCR mode with the population in each Fock state $|n\rangle$ given by Eq. (2.55).

The effective Rabi frequency of the transition depends on the initial and the final motional state even if the motional state is not changed (Eq. (2.43)). This is called the Debye-Waller effect (Wineland et al., 1998) and thus both motional modes need to be included in the excitation probability $P_\uparrow$ detected on the $^9Be^+$. For the BSB transition of one of the WCR modes, the excitation probability $P_\uparrow$ takes the form

$$P_\uparrow(t) = A \sum_{n,m} P(n,\bar{n}) P(m,\bar{m}) \sin^2\left(\Omega_{n\to n+1,m\to m} t\right) \tag{4.67}$$

where A is the maximal contrast, and the sum runs over the Fock states of the two modes with mean phonon number $\bar{n}$ and $\bar{m}$. The population distribution $P(n,\bar{n})$ is assumed to be thermal (Eq. (2.55)). The Rabi frequency $\Omega_{n\to n+1,m\to m}$ describes the coupling strength of the transition $|g,n,m\rangle \to |e,n+1,m\rangle$, where $|\mathrm{g}\rangle$ and $|\mathrm{e}\rangle$ are the electronic states (Eq. (2.43)). In general, $\Omega_{n\to n+1,m\to m}$ depends only weakly on m. Therefore, to reduce the fitting parameters the constraint $\bar{n} = \bar{m}$ is used and decoherence effects are neglected. Furthermore, the number of Fock states was limited to $n, m = 0, ..., 50$, which includes $\gg 99\,\%$ of the population and requires reasonable computational time.

Fits to experimental data using Eq. (4.67) are shown in Fig. 4.9 with the free fitting parameters A, $\bar{n}$, and Ω. For the ground-state cooled

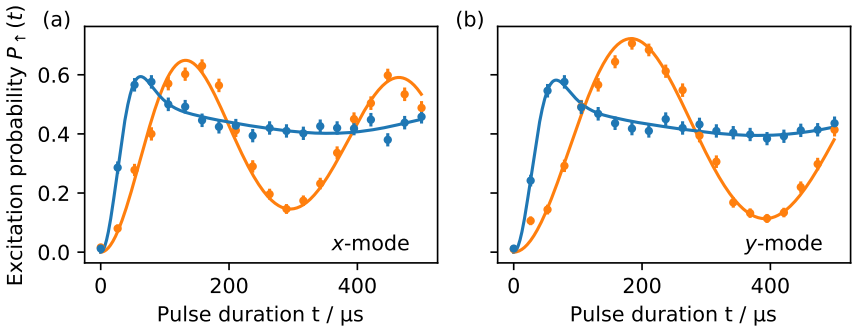

Figure 4.9: Rabi excitation of the WCR modes. The excitation probability is given for varying probe time interrogating the blue sideband of the (a) x-WCR mode and (b) y-WCR mode. An decrease in dephasing is clearly visible when comparing the Doppler cooled case (blue) to the algorithmic ground-state cooled case (orange). The solid lines are theory fits and functions are given in the main text.

case, we obtain $\bar{n}_x = 0.34(3)$ and $\bar{n}_y = 0.21(2)$, consistent with the results from the sideband thermometry above. For the Doppler-cooled case, $\bar{n}_x = 6.9(8)$ and $\bar{n}_y = 7.0(10)$ are extracted from the simulation with Eq. (4.67). It is noticed this value is different from the sideband ratio method result. This is mainly because the excitation probability becomes less sensitive to the $\bar{n}$ when the temperature is high. When fitting, this leads to a higher correlation between Rabi frequency and $\bar{n}$. Additionally, experimental uncertainties and decoherence effects are not included in Eq. (4.67). Nonetheless, the data still demonstrates the effectiveness of algorithmic cooling for the WCR modes.

The so-far described experimental implementation of algorithmic ground-state cooling requires a cooling time of several hundred milliseconds per experimental cycle. This is far too long to be used during clock operation, where the dead time needs to be minimised. Therefore, in the following sections, the heating mechanisms of the WCR modes are investigated and counteracted to reduce the cooling time.

4.2.1 Doppler heating of the WCR modes

The first heating mechanism of the WCR modes is the Doppler cooling applied to the $^9Be^+$, which drives the temperature of any given mode to the Doppler limit. For a ground-state cooled motional mode, this leads to a heating effect, dubbed Doppler heating. To demonstrate the weak coupling of the WCR modes, Doppler heating is performed where the effect on the y WCR mode is measured.

Firstly, the two WCR modes are prepared close to the ground state using algorithmic cooling. Then the Doppler cooling laser is applied with a saturation parameter of $s \approx 0.3$ (Sec. (2.3.1)) and the repumper laser is used to prevent pumping $^9Be^+$ to a dark state. A Lamb-Dicke

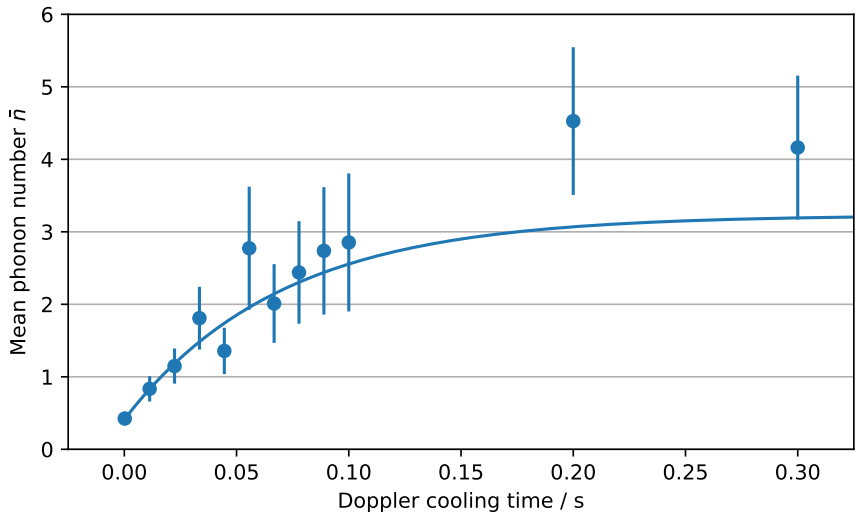

Figure 4.10: Heating of the y WCR mode due to Doppler cooling of the $^9Be^+$. The ground-state cooled motional mode is slowly heated by applying the Doppler cooling and repumper laser to the $^9Be^+$. The mean phonon number $\bar{n}$ approaches the Doppler limit for long interaction time of several hundred milliseconds due to the weak coupling. The curve is a fit of a semi-classical model, with details given in the main text.

parameter-dependent fraction of the photons scattered by the $^9Be^+$ during the cooling lead to transitions on the motional sidebands. This leads for the WCR modes to a small heating effect where the temperature asymptotically approaches the Doppler limit slowly.

To describe $\bar{n}$ as a function of interaction time t, a semi-classical model is used (Eschner et al., 2003; Stenholm, 1986):

$$\bar{n}(t) = \bar{n}_0 \exp\left(-(A_- - A_+)t\right) + \bar{n}_D \left[1 - \exp(-(A_- - A_+))\right] \quad (4.68)$$

with the rate coefficients

$$A_\pm = \frac{\Omega^2}{\Gamma}\eta^2 \left(\cos^2(\Theta) W(\Delta \mp \nu) + \alpha_d W(\Delta)\right) \quad (4.69)$$

where

$$W(\Delta) = \frac{1}{4\Delta^2/\Gamma^2 + 1}. \quad (4.70)$$

Thus, the mean phonon number $\bar{n}$ depends on the cooling laser detuning $\Delta/2\pi = -9\,\mathrm{MHz}$, and the on-resonant Rabi frequency $\Omega = \gamma\sqrt{(s/2)}$ with the linewidth $\gamma/2\pi \approx 18\,\mathrm{MHz}$. Geometrically the angle between laser and addressed motional mode $\Theta \approx 69.3°$ enters as well as $\alpha_d = 0.3125$ which takes into account the dipole emission pattern of the transition (Itano et al., 1982). Further, the frequency of the WCR mode is given by $\omega_y/2\pi = 4.41\,\mathrm{MHz}$ and η is the corresponding Lamb-Dicke parameter. For fitting, the initial mean Fock state number

$\bar{n}_0$, the asymptotic Doppler limit $\bar{n}_\mathrm{D}$, and Lamb-Dicke parameter η are kept as free parameters.

The experimental result with a fit of Eq. (4.68) is shown in Fig. 4.10. The anomalous heating rate is subtracted from the experimental data based on its independently measured value (Appendix A). A heating from the ground state is clearly visible where it takes hundreds of milliseconds to reach equilibrium. The fit describes the data well and yields $\eta = 3.7(4) \times 10^{-3} \cos(\Theta)$ as a measure for the scattering rate. This is consistent with the calculated theory value of $\eta = 3.3 \times 10^{-3} \cos(\Theta)$. The given uncertainty comes only from the fit uncertainty and does not include errors of the experimental parameters.

4.2.2 Continuous ground-state cooling

In an experimental cycle, a total of 1–2 ms of Doppler cooling, repumping and state detection are performed. In particular, at the beginning of an experimental cycle, 400 µs of Doppler cooling are used to get all the motional modes, excluding the WCR modes, close to the Doppler limit. Due to the small Lamb-Dicke parameter, the WCR modes are negligibly affected by this and the state at the beginning of the experimental cycle depends on the state it was left in after the previous cycle. This is used to keep the motional mode close to the ground state over many experimental cycles by applying algorithmic ground-state cooling once and then suppressing the dominant anomalous heating by individual cooling pulses.

To demonstrate this, 200 ms of Doppler cooling are applied and then algorithmic ground-state cooling is preformed, bringing the WCR modes close to the ground states. A varying number of "normal" experimental cycles, as used during clock operation, are performed with a duration of about 32 ms each, which includes axial ground-state cooling, optical pumping of the HCI and a 1 ms clock interrogation with quantum logic. Finally, an additional cycle is used to measure the temperature of one of the WCR modes using sideband thermometry. The temperature of the x-WCR mode is shown in Fig. 4.11 in blue as an example due to its higher heating rate being the worse case. The observed temperature increase is consistent with the anomalous heating rate $\Gamma_\mathrm{h} = 10.2(9)\,\mathrm{s}^{-1}$ measured in the Appendix A for which no laser pulses were applied during the wait time. This confirms that most operations performed during a clock cycle have a negligible effect on the WCR mode temperature.

To counteract the heating rate, a single algorithmic cooling cycle is applied during each clock cycle, increasing the cycle time from 32 ms to 41 ms. This leads to the $\bar{n}$ shown in orange in Fig. 4.11, demonstrating that the heating rate is effectively suppressed and that $\bar{n}$ remains close to the ground state across many experimental cycles with the minimal overhead of 9 ms.

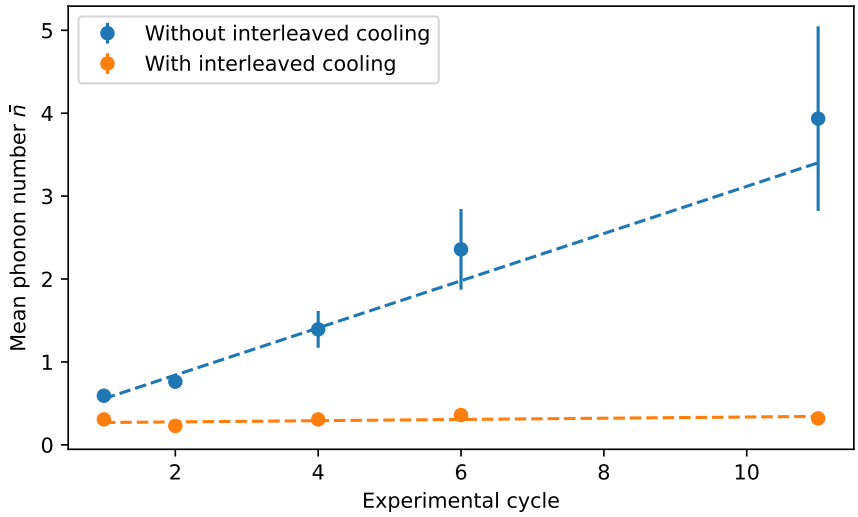

Figure 4.11: Mean phonon number ($\bar{n}$) of the x-WCR mode as a function of experimental cycles. Blue dots are experimental data of $\bar{n}$ without interleaved algorithmic ground-state cooling, and orange points are data when one algorithmic cooling cycle is added per experimental cycle. The dashed lines are linear fits, whose slope shows the respective heating rate of $8.9(16)\,\mathrm{s}^{-1}$ and $0.18(15)\,\mathrm{s}^{-1}$. The heating rate without applied cooling is consistent with the anomalous heating rate (Appendix A). The experimental cycle time with and without interleaved cooling are 41 ms and 32 ms respectively.

The limitation of this technique is the amount of cooling that a single algorithmic cooling sequence provides. For the cycle time of 42 ms used here, a maximum $\approx 25\,\mathrm{s}^{-1}$ is possible which must be larger then the heating rate. This bound can be raised by applying multiple cooling sequences per experimental cycle at the cost of an increased cycle time up to a cooling rate of about $\approx 100\,\mathrm{s}^{-1}$. While the heating rate does not pose a limitation in this system, it might be relevant in other apparatuses investigating HCI due to its scaling quadratically in the charge state.

4.3 SUMMARY

Cooling of the WCR modes has been investigated. Simulations indicate that tilting and parametric excitation of the Ar^{13+}-$^{9}Be^{+}$ crystal would not provide sufficient increase in cooling rate to be experimentally profitable. Instead, a quantum protocol, algorithmic ground-state cooling, was developed which coherently transfers energy from the WCR modes to the axial modes where it can be efficiently dissipated. With this method, a mean phonon number close to the ground state was achieved. It was also shown that the WCR modes are only marginally affected by Doppler cooling process on the $^{9}Be^{+}$. This allows to keep the WCR modes close to the ground state for extended periods of

time where only the anomalous heating rate needs to be counteracted. When this method is applied to clock operations, it only contributes a dead time of 9 ms of the total state preparation time of 40 ms per experimental cycle, making it suitable for practical applications.

5 SYSTEMATIC SHIFTS

An optical clock uses an electronic transition as a frequency reference which is perturbed by the atom's environment and the atom's motion. To correct for this, the perturbations are assessed and corrected yielding a universal frequency standard that can be reproduced anywhere. The shifts for the Ar^{13+} clock and their uncertainty are estimated in the following chapter for the two investigated isotopes, $^{40}Ar^{13+}$ and $^{36}Ar^{13+}$, separately.

In Sec. 5.1, frequency shifts induced by the ion's motion are investigated. This is followed by Sec. 5.2 discussing the shifts due to external fields. In the subsequent sections, the collisional shift, the accusto-optical modulator phase shift, the servo error and line pulling effects are evaluated. Finally, the gravitational redshift from the height difference of the clocks involved in the clock comparison (Chapter 6) is estimated. Most of the presented results have been published in King et al., 2022.

5.1 MOTIONAL SHIFTS

The motion of the ion relative to a probing laser leads to a Doppler shift depending on the ion's velocity. The measured frequency ν, relative to the unperturbed frequency ν_0, is relativistically described by

$$\frac{\nu}{\nu_0} = \gamma\left(1 - \frac{v\cos(\theta)}{c}\right) \tag{5.71}$$

where c is the speed of light, v the ion's velocity and θ the angle between v and the laser. The Lorentz factor γ is defined by $\gamma^{-1} = \sqrt{(1 - v^2/c^2)}$. A laser-cooled, trapped ion has a velocity which is much smaller than c and Eq. 5.71 can be expanded in v/c to yield (Chou et al., 2010b)

$$\frac{\nu}{\nu_0} \approx 1 - \frac{\langle v\rangle\cos(\theta)}{c} + \frac{\langle v^2\rangle}{2c^2} - \frac{\langle v\rangle^2\cos^2(\theta)}{c^2} + \mathcal{O}\left(\frac{v^3}{c^3}\right) \tag{5.72}$$

where $\langle\cdot\rangle$ denotes the time averaged value over the interrogation time of $t_p = 15\,\text{ms}$. The dominant motion of trapped ion is harmonic (Sec. 2.1) and therefore $\langle v\rangle = 0$, assuming that the oscillation period is much shorter than the interrogation time. Therefore, it will only lead to a second-order Doppler shift. In some cases, additional linear motion

can occur with $v < 1\,\mathrm{nm\,s^{-1}}$, which is sufficiently small to neglect the fourth term but not the second term.

5.1.1 First-order Doppler shift

A first order Doppler shift can arise by a constant motion of the ion relative to the interrogating laser, for example if the ion trap relaxes slowly over time along the beam direction, e.g. due to a long time constant for thermalisation of the cryogenic system. Also, charging of surfaces due to UV lasers has been observed to lead to motion correlated with the clock interrogation (Brewer et al., 2019). This might also be the case here due to the 313 nm light needed to control $^{9}Be^{+}$, though likely to be less severe than in Brewer et al., 2019, where the laser light was around 267–280 nm.

To mitigate this effect, the ion is probed with two counter-propagating lasers independently, dubbed *normal* and *counter* directions. The beams are delivered via two separate fibres and each beam is back-coupled into the opposite fibre to maximise overlap of the beams and minimize the relative angle. From data taken during a clock comparison (Chapter 6), the observed transition frequency of the normal (ν_n) and counter (ν_c) interrogating laser can be compared. This yielded the difference $\Delta\nu_\mathrm{FD} = \nu_\mathrm{n} - \nu_\mathrm{c}$ for the two investigated isotopes:

$$\Delta\nu_\mathrm{FD}\left(^{40}\mathrm{Ar}^{13+}\right) = -0.05(11)\ \mathrm{Hz} \tag{5.73}$$

$$\Delta\nu_\mathrm{FD}\left(^{36}\mathrm{Ar}^{13+}\right) = -0.13(13)\ \mathrm{Hz}. \tag{5.74}$$

Both cases are consistent with no first-order Doppler shift within the statistical uncertainty. Any first-order Doppler shift below that level is suppressed by the averaging of the two directions making it negligible.

A slight misalignment of the counter-propagating beams cannot be excluded, which leads to an unbounded uncertainty along any potential bisector (Brewer et al., 2019). To put an upper bound on this, the velocity is estimated from typical position changes of the $^{9}Be^{+}$ on the CCD camera and from changes in EMM over the course of a day. Both methods yield a velocity $\ll 1\,\mathrm{nm\,s^{-1}}$ which corresponds to a fractional frequency shift $< 10^{-18}$ rendering it negligible.

Another effect is the thermal expansion of the experimental apparatus around the HCI, which would not be detected through the counter-propagating beams. The temperature of the laboratory is stabilised to $\pm 0.25\,\mathrm{K}$ and the distance between the fibre coupler of the clock laser and ion is about 1 m. Using the thermal expansion coefficient of steel, a maximal fractional frequency shift of 5×10^{-19} is calculated for a dataset of 10 h which is further suppressed for longer datasets.

A relevant first-order Doppler shift also arises from motion with an oscillation period longer than the interrogation time, e.g. the pulse tube cryocooler induces a vibration at a frequency of 1.7 Hz (Leopold et al., 2019). This does not lead to a shift of the measured frequency as long as it is not temporally correlated with the clock interrogation and many of its oscillation periods are averaged over. Nonetheless, low-frequency vibration can lead to line broadening effects. For the cryocooler, a fractional frequency shift around 10^{-16} has been measured (Leopold et al., 2019). This is much narrower than the fractional natural linewidth of the clock transition (2.5×10^{-14}) and thus negligible.

5.1.2 Secular motion

The secular motion is the harmonic motion at a specific motional frequency, typically $\omega_u \approx 1\,\mathrm{MHz}$, in each degree of freedom (Sec. 2.1). It contributes to the Doppler shift only in second order, since its period is much smaller than the probe time. The shift is described by

$$\frac{\Delta\nu_{\mathrm{SM}}}{\nu} = -\frac{\hbar}{2mc^2}\sum_u b_u^2 \xi_u \omega_u \left(\bar{n}_u + \frac{1}{2}\right) \tag{5.75}$$

where u sums over all motional modes (see Tab. 5.1), b_u is the eigenvector component of the HCI (Sec. 2.1.3), and $\bar{n}_u$ is the mean phonon number. To account for IMM $\xi_{x,y} = 2$ and $\xi_z = 1$ is included (Sec. 2.1). A factor of $1/2$ accounts for the virial theorem stating that the energy of the quantum harmonic oscillator is equally split between potential and kinetic energy.

The mean phonon number $\bar{n}$ during the probe time t_p consists of the initial phonon number $\bar{n}_0$ at $t = 0$ and a contribution from the anomalous heating rate Γ_h:

$$\bar{n} = \bar{n}_0 + \Gamma_\mathrm{h}\frac{t_\mathrm{p}}{2}. \tag{5.76}$$

The experimentally determined values of $\bar{n}_0$ and Γ_h are summarised in Tab. 5.1 with details on the measurement methods given in the following.

Measurements of $\bar{n}$ were performed using the sideband ratio method (Eq. (4.66)). This technique is valid for thermal phonon distributions and it has been shown that the kinetic energy can be significantly underestimated for non-thermal distributions (Chen et al., 2017; Rasmusson et al., 2021). These are often a side effect of resolved sideband cooling when working far outside the Lamb-Dicke regime (Chen et al., 2017). The estimated effect of non-thermal distributions are discussed below for different motional modes individually, though no experiments were performed to assess it. In the future, further experimental data is necessary to test those estimations.

Motional Mode	$\omega/2\pi$ / MHz	$\bar{n}_0$ / phonons	Γ_h / phonons/s	Ar^{13+} amplitude / nm
$^{36}\mathbf{Ar}^{13+}$				
x_{IP}	5.26	0.8(3)	11.1(10)	5.2
x_{OP}	1.29	10.8(6)	1.57(12)	0.12
y_{IP}	5.05	0.12(7)	1.65(13)	5.3
y_{OP}	1.05	21(6)	0.54(9)	0.14
z_{IP}	1.18	0.1(3)	12.4(6)	5.9
z_{OP}	1.63	0.1(6)	7.7(5)	7.8
$^{40}\mathbf{Ar}^{13+}$				
x_{IP}	4.62	0.9(8)	9.9(10)	5.2
x_{OP}	1.29	15(2)	1.6(3)	0.13
y_{IP}	4.42	0.2(2)	2.0(2)	5.4
y_{OP}	1.03	21(3)	0.31(4)	0.15
z_{IP}	1.16	0.03(20)	10.8(5)	6.3
z_{OP}	1.57	0.04(20)	4.8(3)	7.2

Table 5.1: Motional modes of $^{36}\mathbf{Ar}^{13+}$ and $^{40}\mathbf{Ar}^{13+}$. Given are the mode frequency ω, the mean Fock state at the beginning of the clock interrogation $\bar{n}_0$, the heating rate Γ_h, and the mode amplitude of Ar^{13+}. Details are given in the main text and the Appendix A. Abbreviations: IP - in-phase, OP-out-of-phase.

The heating rate Γ_h was measured by initially cooling the motional mode of interest close to the ground state and then measuring $\bar{n}$ as a function of a variable wait time during which the system heats up (Turchette et al., 2000). This heating quickly drives the Fock state distribution towards a thermal distribution (Chen et al., 2017; James, 1998b) allowing the use of the sideband ratio method. A summary of the heating rate measurements is given in the Appendix A. For HCI, heating rates are of particular concern as (Brownnutt et al., 2015)

$$\Gamma_h \propto \frac{Z^2}{m}. \tag{5.77}$$

This necessitates a lower electric field noise than for singly-charged ions to achieve a similar fractional frequency shift for the same ion mass m.

The influence of the heating rate in the presented work is small due to the short interrogation time of 15 ms and a small value of the heating rate. With a different HCI species and a longer interrogation time this might become a dominant source of uncertainty.

5.1.2.1 Axial modes

The axial motional modes are ground-state cooled using resolved-sideband cooling on the Raman transition of the $^9Be^+$ as a pre-requisite for QLS. The estimation of $\bar{n}_0$ for these motional modes with sideband thermometry is likely inaccurate as they possess a large Lamb-Dicke parameter $\eta \approx 0.5$ for the Raman transitions. This leads to zero-crossings of the Rabi frequency of the RSB transition at non-negligible Fock states n (Chen et al., 2017; Wan et al., 2015). To counteract this, second and third order RSB transitions are employed which have zero-crossings at different Fock states than the first-order RSB transitions (Leopold et al., 2019). To investigate the remaining Fock state population, simulations based on the employed sequence were performed following the formalism by Rasmusson et al., 2021. This showed that $\bar{n}$ measured using sideband thermometry can be underestimated by up to a factor of five. With this added as an uncertainty (Tab. 5.1), the shift and its uncertainty are around 10^{-19}, which is negligible.

In the future, the axial motional modes can actively be ground-state cooled using the $^9Be^+$ during clock interrogation to counteract heating rates. This does not affect the clock transition if the polarisability is sufficiently small, which is the case for many HCI species.

5.1.2.2 Radial out-of-phase modes

The HCI only has a negligible motional amplitude in the radial OP modes (Chapter 4) leading to a suppressed shift. Ground-state cooling using resolved sideband cooling on the $^9Be^+$ can be achieved in a similar manner to the axial modes due to similar trapping frequencies

and Lamb-Dicke parameters. Simultaneous cooling of axial modes and radial OP modes can be achieved by interleaved cooling of all four motional modes and was experimentally achieved. Due to the high recoil heating when repumping (Leopold, 2018), this requires cooling times four times longer than if only the axial modes were cooled. This makes it impractical to ground-state cool the OP modes for clock operation.

Therefore, during clock operation the radial OP modes are only Doppler cooled leaving them at a temperature of about $\bar{n}_0 \approx 10 - 20$ (Tab. 5.1) with a thermal Fock state distribution (Stenholm, 1986). To measure $\bar{n}_0$, sideband thermometry on fourth or fifth order RSB is used as they are more sensitive for larger $\bar{n}$ than the first order RSB (Turchette et al., 2000). The combined fractional frequency shift on the clock transition from both motional modes combined is below 10^{-20}, rendering it negligible.

5.1.2.3 Radial in-phase modes

The radial IP mode, also called WCR in Chapter 4, are the secular motion with the largest contribution to the second-order Doppler shift due to their higher frequency and difficulty in cooling. For cooling of the IP modes, algorithmic ground-state cooling is used (Sec. 4.2). Experimentally, variations of the achieved temperature were observed due to fluctuating laser parameters and motional mode frequencies. To accurately assess the temperature during clock operation, it is measured in parallel to clock interrogation.

Similar to what has been shown in Sec. 4.2, the ions are Doppler cooled for 200 ms before algorithmic ground-state cooling is applied to the radial IP mode. Then only interleaved cooling pulses are used to keep it close to the ground state. The Fock state distribution is expected to be mostly thermal due to the relatively small Lamb-Dicke parameter ($\eta \approx 0.1$) and large contribution from heating rates which drives to a thermal distribution (James, 1998b). Measurements of the RSB and BSB of both modes are interleaved with clock operation to estimate the temperature (see Sec. 6.1).

The data is evaluated on a day by day basis. Within each day the statistical uncertainty from QPN as well as drifts in the temperature are taken into account. The estimated fractional shift and its uncertainty for $^{40}Ar^{13+}$ are shown in Fig. 5.1. Across all measurement days, the combined fractional shift of the radial IP modes is estimated to be

$$\frac{\Delta\nu^{\mathrm{IP}}_{\mathrm{SM}}}{\nu}\left(^{40}\mathrm{Ar}^{13+}\right) = 1.2(4) \times 10^{-18} \tag{5.78}$$

$$\frac{\Delta\nu^{\mathrm{IP}}_{\mathrm{SM}}}{\nu}\left(^{36}\mathrm{Ar}^{13+}\right) = 1.3(2) \times 10^{-18} \tag{5.79}$$

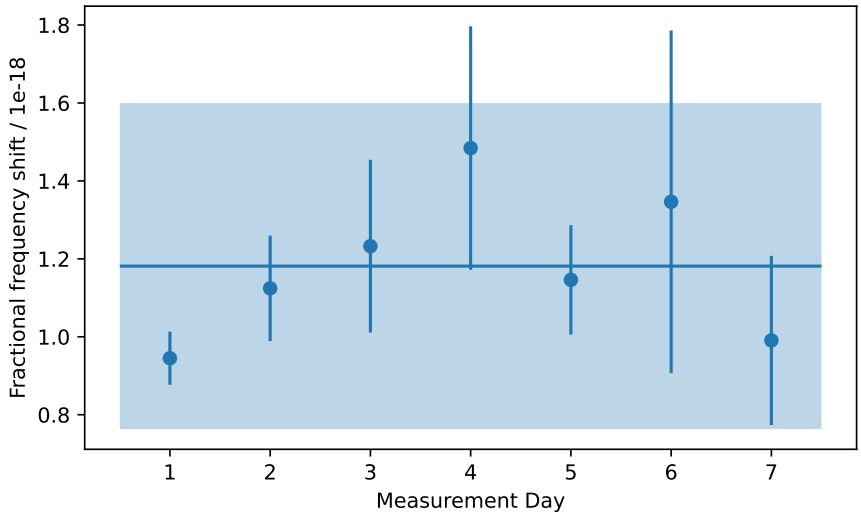

Figure 5.1: Fractional frequency shift from the radial IP modes for $^{40}Ar^{13+}$. The temperature is measured in parallel to clock operation revealing temporal variations due to fluctuating experimental parameters. The data shows the day-by-day fractional second-order Doppler shift of both modes combined. The solid line indicates the mean and the shaded area the estimated 1σ uncertainty.

The lower uncertainty of $^{36}Ar^{13+}$ is attributed to the lower total measurement time as well as the replacement of the repumper laser (see Sec. 3.6.1) improving state preparation.

The measured $\bar{n}$ of the x mode is higher than what has been achieved in Sec. 4.2. This is attributed to a longer experimental cycle time (42 ms to 52 ms) during clock operation and an larger amount of experimental cycles than have been measured in Sec. 4.2. This leads to a larger influence from heating and a overall higher temperature.

5.1.3 Excess micromotion

Excess micromotion (EMM) is a driven motion at the trap drive frequency caused by exposure of the ion to residual rf electric field which has not or cannot be compensated (Sec. 2.1.2). This motion causes a second-order Doppler shift and is by far the dominant and limiting uncertainty in the presented system. In particular, in the axial direction an unexpectedly large component is observed, which only weakly depends on the axial position (Leopold et al., 2019).

The EMM-induced shift is measured using sideband spectroscopy and Eq. (2.14) is used to derive the modulation index β. In most cases, EMM is small, meaning $\beta \ll 1$ and the approximation given in Eq. (2.14) holds. In the experiments presented here, $\beta \approx 1.2$ was

observed in the axial direction. In such a case Eq. (2.14) must be further expanded in β yielding (Leopold et al., 2019)

$$\frac{\Omega_{\mathrm{MM}}}{\Omega_{\mathrm{Car}}} = \frac{J_1(\beta)}{J_0(\beta)} = \frac{\beta}{2} + \frac{\beta^3}{16} + \frac{\beta^5}{96} + \frac{17\beta^7}{9216} + ... \tag{5.80}$$

Higher order terms beyond β^7 can also be calculated, but do not influence the results significantly. Using Eq. (5.80), the modulation index β can be calculated numerically from measurements of the on-resonant Rabi frequencies of the carrier transition Ω_{Car} and the MM sideband Ω_{MM}. For this, on-resonant Rabi excitation is used to measure the interaction time for a π-rotation , t_π, and by using that $\Omega_{\mathrm{Rabi}} = \pi/t_\pi$ (Sec. 2.2).

The fractional frequency shift of the clock transition is related to β by (Berkeland et al., 1998; Keller et al., 2016)

$$\frac{\Delta\nu_{\mathrm{EMM}}}{\nu} = -\left(\frac{\Omega_{\mathrm{rf}}}{\omega_{\mathrm{l}}}\frac{\beta}{2}\right)^2 \tag{5.81}$$

where $\Omega_{\mathrm{rf}}/2\pi$ and $\omega_{\mathrm{l}}/2\pi$ are the frequency of the trap drive and clock transition, respectively. The laser power used for probing the carrier transition and the MM sideband varies due to variations in the AOMs diffraction efficiency. To account for this the laser power is measured with a photodiode and the signal is recorded at the end of each experimental cycle by generating an additional laser pulse. The Rabi frequency is then corrected for laser power differences assuming a linear response of the used photodiodes.

Measurements of the EMM are performed from three nearly orthogonal directions (Sec. 3.6.4). For perfectly orthogonal beams the results from each direction can be treated independently. Since this is not the case here, the relative angle and its uncertainty needs to be taken into account. Additionally, a phase ambiguity between the different directions needs to be included for non-orthogonal beams. For this, an analysis similar to what has been employed by Brewer et al., 2019 is performed.

From the measurements of each beam, a projected velocity $v_{\mathrm{EMM,i}}$ along the probe laser wavevector $\vec{k}_i$ is calculated following Eq. (5.80) and (2.13) where i denotes one of the three probe directions. The velocity in the laboratory frame is written as the vector $\vec{v}^{\mathrm{lab}}$. It is calculated from the measurements through the coordinate transformation

$$\vec{v}^{\mathrm{lab}} = \mathbf{k}^{-1}\begin{pmatrix} v_{\mathrm{EMM,1}} \\ \pm v_{\mathrm{EMM,2}} \\ \pm v_{\mathrm{EMM,3}} \end{pmatrix} \tag{5.82}$$

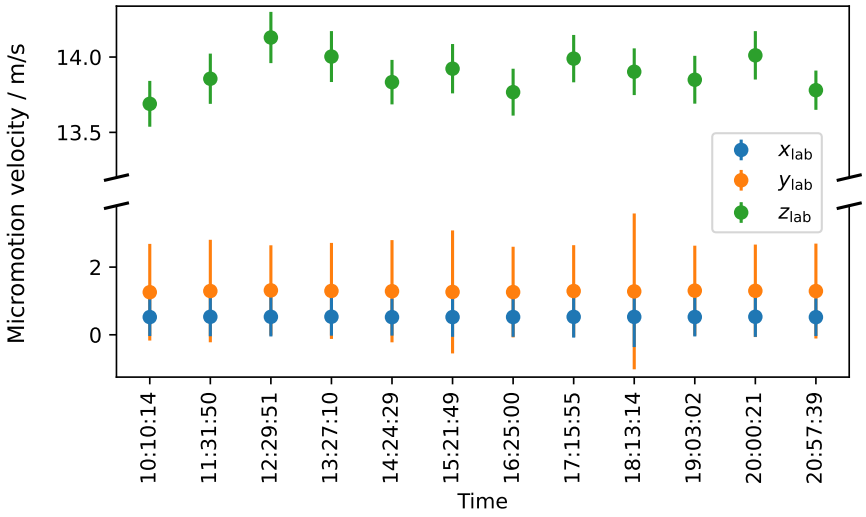

Figure 5.2: Measured excess micromotion velocity amplitude in the laboratory frame. The data was taken over the course of 11 h during the clock measurement of $^{36}Ar^{13+}$. The given time corresponds to the time when the measurement started, needing around 5 min to complete. The EMM is predominantly defined by a large component along the z_{lab} direction. The x_{lab} and y_{lab} direction show much smaller amplitudes.

where $\pm$ indicates the phase ambiguity between the different direction which is taken to be either 0 or π as the worst case scenario. The matrix $\mathbf{k}$ is defined by

$$\mathbf{k} = \begin{pmatrix} \vec{k}_1^{\mathrm{T}}/|\vec{k}_1| \\ \vec{k}_2^{\mathrm{T}}/|\vec{k}_2| \\ \vec{k}_3^{\mathrm{T}}/|\vec{k}_3| \end{pmatrix}, \tag{5.83}$$

where $\vec{k}^{\mathrm{T}}$ denotes the transpose of the vector. The necessary matrix inversion includes the angle uncertainty and is in general non-trivial. Therefore, the error estimation is performed using a Monte-Carlo simulation, where the probe angle, the relative phase, and the value for $v_{\mathrm{EMM,i}}$ are randomly chosen following a normal distribution with standard deviation equal to their uncertainties. Typically 10 000 such samples are drawn and their resulting set of $\vec{v}^{\mathrm{lab}}$ is found to closely resemble a normal distribution. The 68 % confidence interval is calculated and used as its uncertainty.

An example of the measured velocity $\vec{v}^{\mathrm{lab}}$ over the course of multiple hours is given in Fig. 5.2. It shows the large velocity in z_{lab}-direction producing the dominant shift and uncertainty due to $\delta\nu_{\mathrm{EMM}} \propto v^2$. The x_{lab}- and y_{lab}- direction show small velocities with their uncertainty predominantly limited by the angle uncertainty, leading to a finite projection onto the z_{lab}-direction.

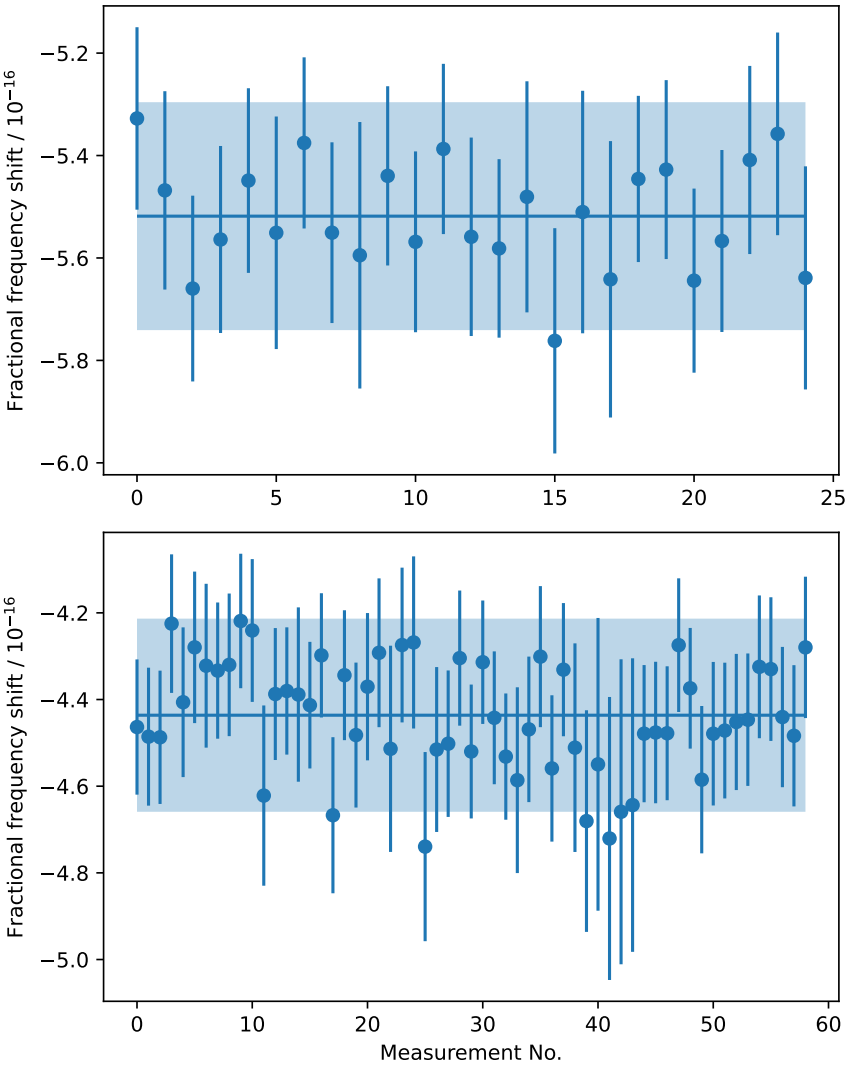

Figure 5.3: Excess micromotion induced frequency shift. Data taken during the clock measurements of $^{36}Ar^{13+}$ (top) and $^{40}Ar^{13+}$ (bottom). The solid line indicates the mean value and the shaded area the estimated 1σ uncertainty.

During the clock operation, the EMM was measured about once per hour and the measured fractional frequency shifts are shown in Fig. 5.3. The resulting shift is estimated to be

$$\frac{\Delta\nu_{\mathrm{EMM}}}{\nu}\left({}^{40}\mathrm{Ar}^{13+}\right) = -4.43(22)\times10^{-16} \tag{5.84}$$

$$\frac{\Delta\nu_{\mathrm{EMM}}}{\nu}\left({}^{36}\mathrm{Ar}^{13+}\right) = -5.50(21)\times10^{-16}. \tag{5.85}$$

The error is based on a combination of single measurement uncertainty and the observed scatter. The ratio of the two isotopes is $0.81(5)$ which is consistent with the expected inverse scaling with the mass $(36/40)^2 = 0.81$ given that the same rf fields were applied. This is by far the largest shift of the system and limits its accuracy. The source of the EMM along the symmetry axis has not unambiguously been identified though it had been suggested to be caused by misalignment of the blade electrodes (Leopold et al., 2019; Leopold, 2018).

While this is by far the dominant shift and uncertainty, it is not related to the high charge state of the HCI. This is because both the EMM and the radial trap frequencies depend only on the charge-to-mass ratio, instead of mass and/or charge separately. Therefore, the higher charge state allows to apply smaller rf electric fields to achieve sufficiently high trapping frequencies. This counteracts the increased sensitivity of the HCI to residual rf field inducing EMM.

5.2 EXTERNAL-FIELD SHIFTS

External electric and magnetic fields and their gradients perturb electronic states and therefore influence transition frequencies (Itano, 2000). Sources can be static electric and magnetic fields as well as dynamic fields from the rf trap drive, laser photons or black-body radiation. For these shifts, the choice of interrogated Zeeman components is important due to many shifts depending on the magnetic quantum number m_J. The transitions interrogated here are illustrated in Fig. 5.4 and consist of four of the six available Zeeman components. The average of the chosen transitions is free of the first-order Zeeman shift as well as the quadrupole shift, making it the preferred choice as described below.

In general, HCI are expected to exhibit small sensitivities to external-field shifts due to the high charge state and correspondingly strong internal fields (Berengut et al., 2012a). This makes many shifts that need to be precisely assessed in other optical clocks negligible. A detailed discussion of the relevant external field shifts for Ar^{13+} is given in the following section.

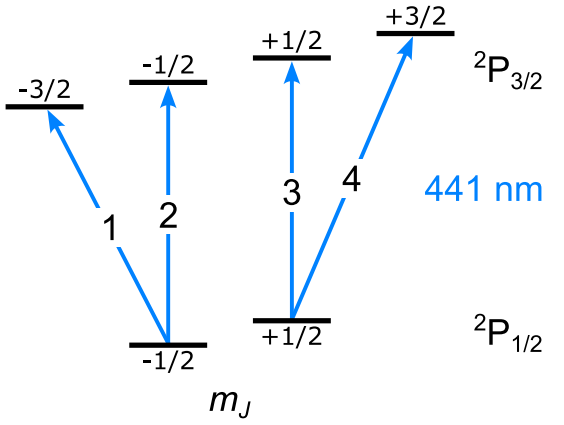

Figure 5.4: Zeeman transitions of Ar^{13+} interrogated during clock operation. The choice of transition is such that their mean frequency is free of linear Zeeman shift and quadrupole shift. Details are given in the main text.

5.2.1 A.c. Stark shift

Atom-light interaction can often be approximated using a two-level system for the driven electronic states, when all other transitions are far detuned from the perturbing field. The corrections to this approximation come from far-off resonant coupling which leads to mixture of states.

The response of an atomic state to an electric field at frequency ω is to first-order described by the scalar polarisability (Rosenband et al., 2006):

$$\alpha^{\mathrm{sc}} = \frac{e^2}{m_e} \sum_i \frac{f_i}{\omega_i^2 - \omega^2} \tag{5.86}$$

where the sum runs over all transitions connecting to the electronic state, f_i describes their oscillator strength and ω_i is the resonance frequency. The shift of an electronic transition is described by the differential scalar polarisability $\Delta\alpha^{\mathrm{sc}} = \alpha_{\mathrm{e}}^{\mathrm{sc}} - \alpha_{\mathrm{g}}^{\mathrm{sc}}$ where $\alpha_{\mathrm{e}}^{\mathrm{sc}}$ and $\alpha_{\mathrm{g}}^{\mathrm{sc}}$ are the scalar polarisabilities of the excited and ground state respectively. In the case of the Ar^{13+} clock transition, this is suppressed because the lowest lying transitions from each state involved in the clock transition are at wavelengths below 50 nm (Kramida et al., 2021) and are therefore much further detuned than what is found in neutral or singly-charged atoms.

For radiation with a frequency far below any electronic transition, resonant effects can be neglected and the induced a.c. Stark shift becomes frequency independent and is described by (Baynham et al., 2018a; Rosenband et al., 2006)

$$\Delta\nu_{\mathrm{ACS}} = -\frac{\Delta\alpha_{\mathrm{dc}}^{\mathrm{sc}}}{2h}\langle E^2\rangle \tag{5.87}$$

where $\langle E^2\rangle$ is the mean squared electric field. The so-called static differential polarisability $\Delta\alpha_{\mathrm{dc}}$ has been calculated for Ar^{13+} to be $\Delta\alpha_{\mathrm{dc}}^{\mathrm{sc}} = -3 \times 10^{-45}\,\mathrm{J\,m^2\,V^{-2}}$ (Yu et al., 2019), leading to negligible shifts in many cases. For example, the residual rf field estimated from

EMM is $E_{\mathrm{rf}} \approx 100\,\mathrm{V\,m^{-1}}$, yielding a fractional second-order Stark shift below 10^{-22}.

Additionally to above discussed scalar polarisability, a tensor polarisability of the $^2\mathrm{P}_{3/2}$ state is present. Its static value is $\alpha^{\mathrm{dc}}_{\mathrm{ten}} = 6 \times 10^{-44}\,\mathrm{J\,m^2\,V^{-2}}$, which is 20 times larger than $\Delta\alpha^{\mathrm{sc}}_{\mathrm{dc}}$ (Yu et al., 2019). It has the same m_J dependence as the quadrupole shift (see Eq. (5.90)), and is thus suppressed by the averaging technique used to cancel that (Sec. 5.2.3). This makes it negligible.

The differential polarisability of Ar^{13+} is significantly smaller than in other systems. For example, $^{27}\mathrm{Al}^+$ has one of the smallest values of all operational optical clocks with $\Delta\alpha_{\mathrm{Al}^+} \approx 7 \times 10^{-42}\,\mathrm{J\,m^2\,V^{-2}}$ (Brewer et al., 2019), which is more then three orders of magnitudes larger. The smallest value for any operational clock is in $^{176}\mathrm{Lu}^+$ with $\Delta\alpha_{\mathrm{Lu}^+} \approx 3 \times 10^{-43}\,\mathrm{J\,m^2\,V^{-2}}$ (Arnold et al., 2018), which is two orders of magnitudes larger.

5.2.2 Blackbody radiation shift

A body at a finite temperature emits blackbody radiation (BBR) with a temperature-dependent spectrum. This couples to $E1$ and $M1$ transitions, leading to an a.c. Stark and an a.c. Zeeman shift respectively. The polarisability of HCI is expected to be small as it scales with the effective charge state like ${Z_a}^{-4}$ (Berengut et al., 2012a). The effective charge state Z_a is the screened potential that the outer electron experiences and is a nearly linear function in Z.

At room temperature the peak wavelength of BBR is $\lambda \approx 10\,\mu\mathrm{m}$, which is much smaller than any relevant transition frequency in Ar^{13+} and the induced a.c. Stark shift is well described by Eq. (5.87). The mean squared electric field at a temperature T is given by $\langle E^2 \rangle = (831.9\,\mathrm{V/m})^2 (T/300\,\mathrm{K})^4$. With this the fractional shift at $T = 300\,\mathrm{K}$ is 2.5×10^{-21}. A secondary component is the a.c. Zeeman shift from BBR. This has been calculated to yield a fractional shift of -1.1×10^{-21} at 300 K (Yu et al., 2019).

Within the cryogenic system only about 10^{-3} of the 4π solid angle visible to the ion are at room temperature. The majority of the surfaces are close to 4 K which suppresses the shift further due the T^{-4} of the emitted power following the Stefan-Boltzmann law. Overall this makes the shift negligible.

5.2.3 Electric quadrupole shift

Electronic states with an angular momentum $J \geq 1$ posses a quadrupole moment Θ which couples to electric field gradients and shifts the states depending on their m_J^2. In HCI, Θ is expected to be suppressed due to scaling with the effective charge state like ${Z_a}^{-2}$ (Berengut et al., 2012a).

The electric field gradient can be calculated from the experimentally accessible trap frequencies and consists of two contributions. The primary part comes from the static electric field applied for trapping along the z-axis (Sec. 2.1). This field is described by the electric potential

$$\varphi(x,y,z) = \frac{1}{2}\frac{dE_z}{dz}\left(y^2 - y^2\right). \tag{5.88}$$

The lack of x-dependence is specific to the geometry of the employed trap (Eq. (2.11)).

The electric field gradient can thus be calculated from the axial motional frequency ω_z of a single ion with charge q and mass m through

$$\frac{dE_z}{dz} = \frac{m}{q}\omega_z^2. \tag{5.89}$$

A secondary contribution comes from the potential of the $^9Be^+$ (or other) ion (Akerman et al., 2018; Roos et al., 2006). Compared to a two-ion crystal composed of singly-charged ions, this is suppressed in an Ar^{13+}-$^9Be^+$ crystal due to the large ion-ion separation. For typical trap parameters used in the presented experiments, this leads in total to $dE_z/dz = 2\,\mathrm{V\,mm^{-2}}$.

The quadrupole shift for a electric potential given by Eq. (5.88) is described by (Itano, 2000)

$$\Delta\nu_{\mathrm{QS}}\left(m_J^2\right) = \frac{\Theta}{4h}\frac{\mathrm{d}E_z}{\mathrm{d}z}\frac{J\left(J+1\right) - 3m_J^2}{J\left(2J-1\right)}\left(3\cos^2\beta - 1 + \sin^2\beta\cos(2\alpha)\right), \tag{5.90}$$

where β=30(5)° is the angle between quantisation axis and the z-axis and α=45(5)° the angle between the y-axis and the plane spanned by the z-axis and the quantisation axis.

For the Ar^{13+} clock transition, only the $^2P_{3/2}$ excited state is affected by this shift. Theoretical calculations predict $\Theta = 0.025\,ea_0^2$ for this state (Müller, 2021; Yu et al., 2019) which leads to a shift of about $\pm 8\,\mathrm{mHz}$ for each Zeeman component of the excited state. This is significantly smaller then the achieved statistical uncertainty and therefore not resolved.

Additionally, the shift is averaged to zero by the choice of interrogated Zeeman component which are such that each excited state is interrogated equally (Fig. 5.4). According to Eq. (5.90), the mean is then free of the quadrupole shift, since $\Delta\nu_{\mathrm{QS}}\left((\pm 3/2)^2\right) = -\Delta\nu_{\mathrm{QS}}\left((\pm 1/2)^2\right)$. With this averaging technique a suppression of more than four orders of magnitude has been achieved in other experiments, e.g. employing $^{88}Sr^+$ (Dubé et al., 2013). Here only a suppression by a factor 20 is necessary to achieve a fractional shift below 10^{-18} making it negligible.

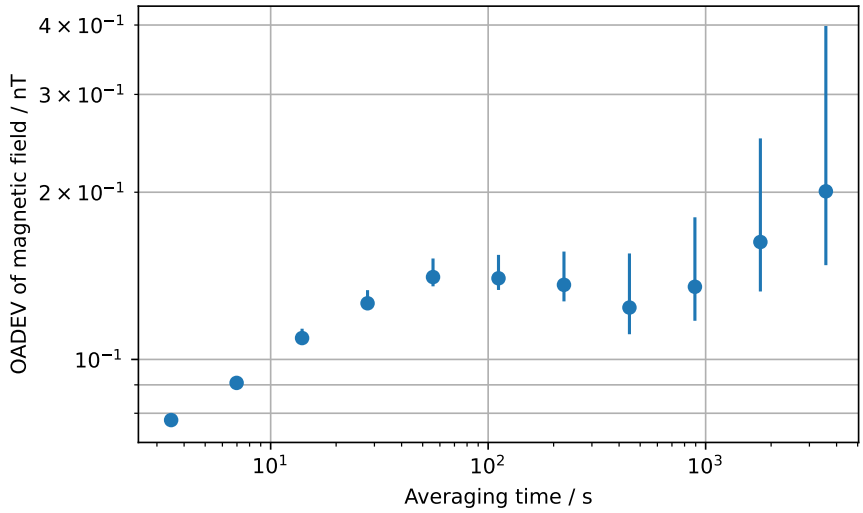

Figure 5.5: Overlapping Allan deviation of the magnetic field. A 6 h dataset from the clock campaign with minor gaps is used as the basis. The magnetic field is calculated from the most sensitive transitions (transition 1 and 4 in Fig. 5.4) using Eq. (5.91). Averaging time beyond the servo time constant of 30 s show a magnetic field stability below 0.2 nT up to 1000 s.

5.2.4 Magnetic field

The interrogated Zeeman states are highly sensitive to magnetic field changes due to a linear Zeeman shift. The most sensitive transitions change by about $23\,\mathrm{Hz\,nT^{-1}}$ compared to the linewidth of around 50 Hz. Therefore the magnetic field needs to be much more stable than 2 nT during the interrogation time to avoid line broadening. Additionally, the magnetic field shift has to be more stable than the servo instability of ≈ 30 Hz at the servo time constant of 30 s (For details see Chapter 6). This corresponds to a 1 nT stability in order to avoid additional instability when locking to these transitions.

The setup for generating the magnetic field is described in Sec. 3.5. In short, three pair of passively-driven coils generate the magnetic field in x-,y-, and z-direction. For active stabilisation an out-of-vacuum magnetic field sensor is used to give feedback to additional coils in x- and z-direction. The stability of the magnetic field is directly characterised using the first order Zeeman effect of the clock states. For this, the frequency difference between the outer Zeeman components is calculated (see Eq. (5.92) below):

$$\nu_4 - \nu_1 = (3g_{3/2} - g_{1/2})\,\mu_\mathrm{B} B \tag{5.91}$$

where g_J is the Landé-factor, μ_B is the Bohr magneton and B is the magnetic flux density. The OADEV for a 6 h dataset from clock comparison of ν_1 and ν_4 with minor gaps is given in Fig. 5.5. At short timescales, the response is dominated by the atomic servo response

locking to the clock transition. After the servo time constant of around 30 s, a magnetic field stability of <200 pT up to times of 1000 s is observed. The stability is limited by the resolution of the employed magnetic field sensor for stabilisation. This is sufficiently stable such that it does not influence clock operation (Chapter 6). Over the course of a day, variations of a few nT are observed for the magnetic field. Shorter timescales, like the typical interrogation time of 15 ms cannot be resolved due to the limited atomic servo response time. Nonetheless, no additional line broadening attributed to the magnetic field was observed, making it sufficiently stable for the presented experiments (see also Appendix C).

5.2.4.1 First-order Zeeman shift

In a magnetic field, states with $m_J \neq 0$ are shifted due to a first-order Zeeman shift following

$$\Delta\nu_Z^{(1)}(m_J) = \frac{m_J g_J}{h}\mu_B B. \tag{5.92}$$

For Ar^{13+} this affects all states of the clock transition with a summary of the shift given in Tab. 5.2 for the employed magnetic bias field of 23 µT. This shift is not suppressed in HCI and is the largest shift affecting the Zeeman substates. It is suppressed by using the symmetry of Eq. (5.92) which is $\Delta\nu_Z^{(1)}(m_J) = -\Delta\nu_Z^{(1)}(-m_J)$. The choice of probed transitions (Fig. 5.4) are such that the mean frequency is free of the linear Zeeman shift. Further, the probe order of the transitions is pseudo-randomised to suppress any shift that can come from a drift of the magnetic field between the measurements.

5.2.4.2 Second-order Zeeman shift

A second-order Zeeman shift is caused by the mixture of different electronic states due to the externally applied magnetic field. This scales inversely with the energy difference of the involved states and is therefore suppressed in HCI (Berengut et al., 2012a) similar to the a.c. Stark shift (Sec. 5.2.1).

The induced second-order Zeeman shift is described by

$$\Delta\nu_Z^{(2)}(m_J) = \frac{g_J^{(2)}(m_J)}{h}\frac{(\mu_B B)^2}{m_e c^2} \tag{5.93}$$

where $g_J^{(2)}(m_J)$ is a dimensionless expansion factor which fulfils the symmetry relationship $g_J^{(2)}(m_J) = g_J^{(2)}(-m_J)$. For Ar^{13+}, $g_J^{(2)}(m_J)$ was calculated using perturbation theory and the most precise published calculations achieve an uncertainty of about 1 % (Lindenfels, 2015). A summary of these values is given in Tab. 5.2 alongside the expected shift for each state given our employed magnetic field of about 23 µT.

	g_J	$\Delta\nu_Z^{(1)}$ / kHz	$g_J^{(2)}$ / 10^3	$\Delta\nu_Z^{(2)}$ / µHz
$^2P_{1/2}$				
$m_J = 1/2$	0.663	107	−39.66	−33
$m_J = -1/2$	0.663	−107	−39.66	−33
$^2P_{3/2}$				
$m_J = 3/2$	1.332	644	1.007	0.8
$m_J = 1/2$	1.332	215	41.20	35
$m_J = -1/2$	1.332	−215	41.20	35
$m_J = -3/2$	1.332	−644	1.007	0.8

Table 5.2: First- and second-order Zeeman shift of the Ar^{13+} clock transition. The experimentally used magnetic field strength of 23 µT is used for the calculations. The first-order Zeeman shift $\Delta\nu_Z^{(1)}$ is the largest shift of individual transitions but can be cancelled by averaging Zeeman components. The second-order Zeeman shift $\Delta\nu_Z^{(2)}$ cannot easily be cancelled but is negligible. Details are given in the main text. Uncertainties are smaller then the presented values and have been omitted for clarity. Values for g_J and $g_J^{(2)}$ are taken from Lindenfels, 2015.

The estimated fractional shift is about 10^{-19} with an even smaller uncertainty rendering it negligible.

The second-order Zeeman shift in Ar^{13+} is much smaller than what is found in other optical clock systems. For example, ^{199}Hg has the smallest second-order Zeeman shift of any employed atomic system and is one order of magnitude larger than that for Ar^{13+}. This is due to the mentioned sparsity of low-lying states, such that the dominant contributions in Ar^{13+} comes from coupling between the ground state $^2P_{1/2}$ and the excited state $^2P_{3/2}$, while higher lying states can be neglected (Lindenfels et al., 2013).

5.2.4.3 Trap drive magnetic field

An additional source for a magnetic field are the currents induced by the rf voltages applied to the trap blades. This leads to an a.c. magnetic field at the trap drive frequency Ω_{rf} which adds to the quadratic Zeeman effect (Chou et al., 2010a; Gan et al., 2018).

The magnetic field from the trap drive can be measured by comparing microwave transitions in the $^9Be^+$ with different magnetic field sensitivity and was bounded to $< 3\,\mu T^2$ along the quantisation axis for the trap in use (Leopold et al., 2019). This measurement was performed for almost up to 2.5 times larger rf voltages than used here. This means that the bound for the presented measurements is expected to be lower. Due to the geometry of the trap, the transverse components of the magnetic field are assumed to be at a similar level. The coefficient of the second-order Zeeman shift (Tab. 5.2) yields a

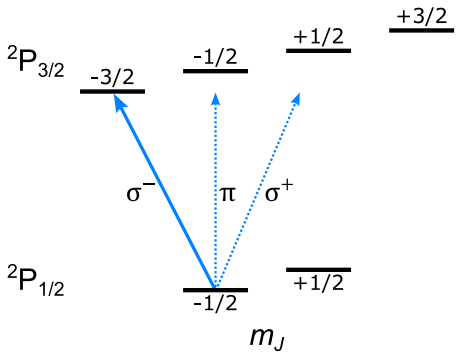

Figure 5.6: Probe laser-induced a.c. Zeeman shift. As an example the interrogation of the $|^2P_{1/2}, -1/2\rangle \rightarrow |^2P_{3/2}, -3/2\rangle$ transition is shown. It is driven by the σ^--polarised component of the light (full line). Additional polarisation components (σ^-, π) off-resonantly couple to other Zeeman components (dashed lines) and induce an a.c. Zeeman shift.

fractional shift below 10^{-21} where $3\,\mu T^2$ was taken as a conservative bound for each magnetic field component. While this is negligible for the transition frequency, it does affect the g-factor measurement by coupling different Zeeman substates within a manifold (see Sec. 6.3.1). For the future, a direct measurement of the transverse components of the trap drive magnetic field is desirable to confirm the here made assumption based on symmetry (Gan et al., 2018).

5.2.5 Probe laser-induced shift

The small differential polarisability of Ar^{13+} leads to a negligible a.c. Stark shift from the probe light (see Sec. 5.2.1). A remaining shift comes from an a.c. Zeeman shift of the probe light off-resonantly coupling the different Zeeman components of the clock transition (Fig. 5.6). A theoretical description of this effect has recently been given in an unrelated publication (Yudin et al., 2023).

During clock operation, the Rabi frequency of all interrogated components is equalised to achieve the optimal statistical uncertainty. This is achieved by adjusting the laser power for each transition to achieve similar Rabi frequencies as the achievable polarisation purity is technically limited. The induced a.c. Zeeman shift is linear in laser power analogous to the a.c. Stark shift (Kien et al., 2004). Thus, the shifted frequency ν_i of each Zeeman component i is described by

$$\nu_i = \nu_{i,0} + \kappa_{AZ,i}\Omega_i^2 \tag{5.94}$$

where $\nu_{i,0}$ is the unperturbed frequency, $\kappa_{AZ,i}$ is a coupling constant describing the shift and Ω_i is the on-resonant Rabi frequency. In this description, Ω_i is used as a measure for the laser power P in the polarisation component required to drive transition i, as $P \propto \Omega^2$. To estimate the effect, ν_i is measured at three different laser powers (denoted in the following with k) and is extrapolated to the Rabi frequency used during clock operation. The used laser powers are much larger than the ones used during clock operation, amplifying the shift. Experimentally, the on-resonant Rabi frequency is accessed through measuring the π-time $t_\pi = \pi/\Omega$ by performing Rabi oscillations (Sec. 2.2).

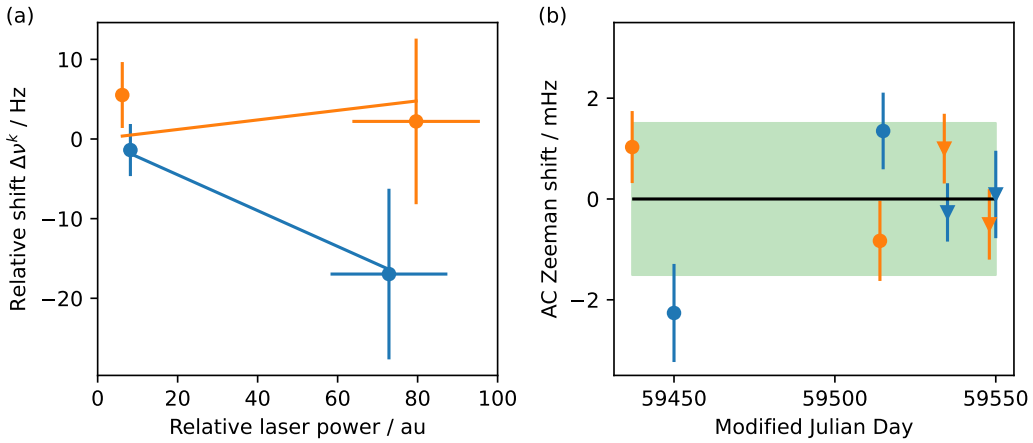

Figure 5.7: Measurement of the probe laser-induced a.c. Zeeman shift. (a) Example measurement of the shift of the mean frequency from high to low laser power for the two directions normal (blue) and counter (orange). The slope is the only degree of freedom for the linear fit. Further explanations are given in the main text. (b) Estimated a.c. Zeeman shift by extrapolation to t_π =15 ms for $^{40}Ar^{13+}$ (circles) and $^{36}Ar^{13+}$ (triangles) as a function of date. The shaded area shows the estimated 1σ uncertainty based on the scatter and uncertainties of the single measurements.

The measured ν_i at the lowest power is used as a reference to eliminate $\nu_{i,0}$ by taking the difference to the other two measured values:

$$\Delta\nu^k = \nu^k - \nu^0 = \kappa_{AZ}\left(\frac{\pi}{t_{\pi,k}} - \frac{\pi}{t_{\pi,0}}\right) \qquad k \in \{1,2\}. \tag{5.95}$$

where $k \in \{1,2\}$ denotes the laser power setting and i is omitted for clarity. This gives two differences from the three performed measurements which can be fitted using a single fit parameter κ_{AZ} as shown in Fig. 5.7 (a). Extrapolation to t_π =15(1) ms yields the shift during clock operation.

The measurement is performed, similar to clock operation (Chapter 6), by locking simultaneously to the required Zeeman components with different laser powers and corresponding probe time t_π. By measuring all the transitions in parallel, common mode noise from the magnetic field and laser frequency drift is rejected through a cycle-by-cycle evaluation. Either the shift of each Zeeman component or just the mean frequency can be analysed. Both analysis were performed with a negligible difference in shift and uncertainty of the mean frequency which is the relevant result for clock operation.

Over time, changes of the probe laser-induced shift were observed where the reason has not been identified. It could be caused by temperature variations in the laboratory affecting the waveplates used to control the polarisation, changes in the birefringence of the in-vacuum windows due to varying mounting stress, or due to variations in

beam pointing combined with a gradient of the birefringence of the in-vacuum windows.

To estimate the variation, measurements were performed before and after each clock run for both interrogation directions independently. The results of all measurements are shown in Fig. 5.7(b). Based on the measured variation, the fractional shift is estimated to be

$$\frac{\Delta\nu_{\mathrm{PL}}}{\nu} = (0 \pm 2.2) \times 10^{-18}. \tag{5.96}$$

The uncertainty of the shift is the second largest uncertainty of the system though it is an order of magnitude smaller than the dominant uncertainty from EMM (Sec. 5.1.3). In the future, the shift can be suppressed by employing generalised Ramsey interrogation schemes which suppress it (Hobson et al., 2016; Huntemann et al., 2012; Sanner et al., 2018; Yudin et al., 2010).

5.3 COLLISIONAL SHIFT

Collisions of the interrogated ions with background gas affect the measured transition frequency in two ways. Firstly, a collision adds kinetic energy to the system and therefore changes the second-order Doppler shift and also affects state readout with QLS. Secondly, a phase shift of the interrogated state can occur (Hankin et al., 2019).

The collisional shift scales linearly with the background gas pressure (Davis et al., 2019) and is fractionally at or below 1×10^{-18} in room temperature experiments (Hankin et al., 2019 and references therein). The background pressure in the presented system had been estimated to be below 1.3 pPa from the estimated lifetime of Ar^{13+} limited by charge exchange collisions (Micke et al., 2019). Since then the lifetime has approximately been doubled (see Sec. 3.4) corresponding to a reduced pressure below 0.7 pPa. With this, the pressure is around four orders of magnitude lower than what is commonly achieved in room temperature setups. Additionally, collisions with HCI are typically catastrophic as they lead to charge-exchange which is easily detected as the clock transition cannot be excited anymore. The collisional shift is negligible due to these reasons.

5.4 ACCUSTO-OPTICAL MODULATOR PHASE SHIFT

Accusto-optical modulators (AOM) are used for fast switching of light pulses and can introduce cycle-synchronous phase shifts in two ways: For short pulses of about 1 µs, ringing of the AOM electric circuit leads to a phase shift at the beginning and end of the pulse (Degenhardt et al., 2005). This effect is negligible for the pulse length of 15 ms used

here. A second effect is the thermal expansion through heating of the AOM due to the applied rf voltage and linearly depends on the applied rf power and increases for longer pulses (Degenhardt et al., 2005; Rosenband et al., 2008).

Interferometric measurements by Rosenband et al., 2008 found a frequency shift of less than 0.2 Hz at a drive power of 1 W for clock lasers for $^{199}Hg^{+}$ and $^{27}Al^{+}$ at 282 nm and 267 nm respectively. A measurement for a clock laser of $^{171}Yb^{+}$ at 467 nm by Kazda et al., 2016 found a shift of about 0.6 mHz for 50 mW drive power. In the present experiments drive powers below 5 µW are used. This is possible as the Ar^{13+} clock transition is broader than most transitions used in optical clocks and therefore requires lower laser light intensities to achieve the same line broadening for clock operation. The shift is expected to be correspondingly smaller by several orders of magnitude and therefore negligible.

5.5 SERVO ERROR

Offsets of the digital control loop (*servo*) from the actual line centres are counteracted in several ways. First, a second-order integrator is part of the control loop (Sec. 6.1) and allows for suppression of linear drifts of the clock laser and magnetic field (Peik et al., 2006), though, higher-order drifts are not suppressed by this. Additionally, the probe order of the probe points is pseudo-randomised which further suppresses linear drifts.

The first source of higher order drifts is the Si2 cavity which is used to stabilise the clock laser (Sec. 3.6.3). This is negligible though, due to its small linear drift of only tens of Hz d^{-1} with even smaller higher-order drifts.

The second, dominant source are variations of the magnetic field which leads to line shifts of the most sensitive Zeeman components of ≈ 100 Hz over the course of a day. To investigate this, the error signals were checked to be consistent with zero. Further, simplified simulations were performed with a linear (2 pT s^{-1}) and quadratic drift (2 fT s^{-2}) of the magnetic field. Both values lead to a the magnetic field instability on timescales >1000 s which is at least one order of magnitude larger than what is experimentally observed. The simulations were performed 1000 times with a length corresponding to 85 000 s. This yielded a frequency shift of ± 1 mHz for the individual Zeeman components and $0.0(2)$ mHz for the mean frequency where the effect on opposing Zeeman components cancels to a high degree. Therefore the fractional shift is expected to be below 10^{-18} and thus negligible.

5.6 LINE PULLING

5.6.1 Overlapping transitions

The Rabi lineshape (see Eq. (2.34) and Fig. 2.3) leads to a finite excitation probability far from resonance. When probing any given Zeeman components, these contributions from other transitions can lead to line distortions. The first contributions comes from other carrier transitions where the detuning is about 200 kHz compared to typical linewidths of 50 Hz. Using this, the maximal remaining overlap leads to a fractional shift around 10^{-21}, rendering it negligible.

Motional sidebands can also have a significant overlap with the carrier transition. Here, clock interrogation is performed from the radial direction and only the radial modes can be excited. Due to weak coupling of the radial motional modes (see Sec. 2.1.3), only the IP modes at ± 4.5 MHz are relevant. The large detuning and small Lamb-Dicke parameters ($\eta \approx 0.1$) render this effect also negligible.

5.6.2 Clock laser leakage

Clock interrogation of Ar^{13+} is performed with two counter-propagating beams where each direction is treated independently of the other. The beams are switched by two independent AOMs (see Fig. 3.6) which are driven at the same center frequency. Any cross talk of the rf between the AOMs could lead to additional clock light entering from the wrong direction compromising the suppression of the first-order Doppler shift.

To check for this, the ion is interrogated with one of the beams though the beam path was physically blocked. Any observed excitation would then come from the other beam path. During the probe time, the Ar^{13+}-$^{9}Be^{+}$ crystal is actively ground-state cooled to avoid anomalous heating rate affecting the QLS readout. With this, no significant excitation up to 200 ms is observed for rf powers at least an order of magnitude larger than what is used for clock operation.

Further, the DDS driving the AOMs are detuned by a random value close to 50 MHz from the nominal value when not being used for interrogation. This is in addition to being switched off by high attenuation rf switches (see Sec. 3.7) and further reduces possible effects from laser leakage.

5.6.3 Logic laser leakage

Any leakage light from any of the logic beams could lead to line distortion, similar to the clock beams in the previous section. To increase attenuation of the logic beam paths, a double-pass and a single-pass AOM (see Fig. 3.6) are switched off during the clock

interrogation. Furthermore, the DDS driving the radial and vertical logic single pass AOM are detuned by a random value close to 50 MHz from the nominal value. For the single pass AOM of the axial logic a detuning was not possible due to the employed pulse shaping (Sec. 3.7.1), which is pre-programmed onto the DDS at a fixed drive frequency. This cannot be changed without large overhead and could lead to on-resonance excitation, if leakage light reached the ion.

Similar to the previous section, leakage is checked by running a QLS sequence where the HCI is interrogated for varying probe times with the clock beams physically blocked. During the interrogation, the $^{9}Be^{+}$ is used to actively ground-state cool the axial motional modes to avoid detrimental effects from anomalous heating on QLS. No significant excitation was observed for interrogation times up to 200 ms.

5.7 GRAVITATIONAL REDSHIFT

Einstein's general theory of relativity predicts that clocks run slower when affected by a gravitational potential. When comparing optical clocks, this so-called gravitational redshift needs to be accounted for by measuring the gravitational potential at each clock position.

The frequency shift of a clock when moving it from a gravitational potential V_1 to V_2 is given by (Mehlstäubler et al., 2018)

$$\frac{\Delta\nu_{\mathrm{GRS}}}{\nu} = -\frac{V_1 - V_2}{c^2} \tag{5.97}$$

where c is the speed of light. For a local comparisons this can be simplified to

$$\frac{\Delta\nu_{\mathrm{GRS}}}{\nu} = \frac{g_{\mathrm{local}}\Delta h}{c^2} \tag{5.98}$$

where it is assumed that the gravitational acceleration g_{local} does not vary on local scales. This is justified as long as the scales are small compared to the size of the earth. At PTB, $g_{\mathrm{local}} = 9.812526312(2)$ has previously been measured (Timmen, 2018). With this, the frequency shift only depends on the height difference Δh of the involved clocks. For this, height differences of various markers across the PTB premises have been measured in the past (Denker et al., 2014).

For the Ar^{13+} clock no dedicated height marker exists. Instead a marker for the $^{27}Al^{+}$ clock four floors above is used as a reference with a height difference of 11.136(5) m to the trapped HCI (Denker et al., 2022). A similar marker exists for the $^{171}Yb^{+}$ clock, which leads in total to a height difference of the clock ions of Δh =1.496(7) m. Additional uncertainties from measurements of the relative marker

Shift	$\Delta\nu/\nu$ / 10^{-17}		σ/ν / 10^{-17}	
	$^{40}Ar^{13+}$	$^{36}Ar^{13+}$	$^{40}Ar^{13+}$	$^{36}Ar^{13+}$
Excess micromotion	-44.3	-55.0	2.2	2.1
Laser-induced a.c. Zeeman	0		0.2	
Secular motion	-0.1		< 0.1	
Quadrupole shift	0		< 0.1	
First-order Doppler	0		< 0.1	
First-order Zeeman	0		< 0.1	
Quadratic Zeeman	< 0.1		$\ll 0.1$	
Blackbody radiation	$\ll 0.1$		$\ll 0.1$	
Servo error	0		$\ll 0.1$	
AOM phase chirp	< 0.1		< 0.1	
Gravitational redshift	-		< 0.1	
Total	-44.4	-55.1	2.2	2.1

Table 5.3: Systematic shifts ($\Delta\nu$) and uncertainties (σ) of the Ar^{13+} clock. All values are given relative to the transitions frequency ν. The by far largest shift and uncertainty stem from EMM. It depends on the isotope and the difference is consistent with the differing masses. The shift and uncertainty of the gravitational redshift depends on the height difference to the clock that is compared to, with the given uncertainty applying to clock comparisons within PTB. A detailed analysis of the shifts is given in the main text.

heights and the height of the $^{171}Yb^{+}$ clock are included. This yields a total fractional shift of

$$\frac{\Delta\nu_{GRS}}{\nu} = 1.633(8) \times 10^{-16}. \tag{5.99}$$

Improvements are possible in particular to the height difference between the HCI clock and the $^{27}Al^{+}$ marker. Assuming an improvement to an uncertainty of 1 mm, gives a fractional uncertainty of about 5×10^{-19}, limited by knowledge of the relative marker heights. A similar uncertainty is also achieved for other optical clocks within PTB, which in principle allows for ring closure measurements down to this level.

5.8 SUMMARY

The summary of the investigated shifts for the Ar^{13+} clock is given in Tab. 5.3. In total, a fractional systematic uncertainty of 2×10^{-17} was achieved. This is similar to many optical clocks in operation (Baynham et al., 2018b; Huang et al., 2020; Lodewyck et al., 2016; Schwarz et al., 2020) though the best clocks reach uncertainties at the low 10^{-18} level

(BACON Collaboration, 2021; Huntemann et al., 2016; Ushijima et al., 2015) or below (Brewer et al., 2019).

The Ar^{13+} clock is predominantly limited by EMM, a shift that is not exaggerated by the large charge state but rather an intrinsic property of the trap. In other traps, a fractional EMM shift below 10^{-18} has been achieved (Brewer et al., 2019; Pyka et al., 2014) and is therefore expected to be achievable by employing an improved trap. The second largest shift, the probe laser-induced a.c. Zeeman shift, is already at the low 10^{-18} level and can easily be suppressed using advanced interrogation techniques (Hobson et al., 2016; Huntemann et al., 2012; Sanner et al., 2018; Yudin et al., 2010). All other uncertainties are already estimated to be fractionally below 10^{-18}, where many are suppressed due to the favourable properties of Ar^{13+} and HCI in general.

In the future, particular care needs to be taken of the secular motion shift, as its influence will increase for longer interrogation times. In particular the influence of non-thermal Fock state distributions needs to be investigated. Nonetheless, a fractional uncertainty of the motional shifts below 10^{-18} is achievable as has been demonstrated for the $^{27}Al^{+}$ QLS clock (Chen et al., 2017). Also, a measurement of the transverse components of the trap drive magnetic field is desirable, which is possible with established techniques (Gan et al., 2018). Overall, this leads to a clear path for an HCI based optical clock with a fractional uncertainty at or below the 10^{-18} level.

6 CLOCK COMPARISON

The operation of the experimental setup as an optical clock is achieved by stabilising the frequency of the clock laser to the frequency of the clock transition of Ar^{13+}. The frequency ratio of the laser to another clock is then measured using a frequency comb. Comparisons between an optical clock and a ^{133}Cs clock are usually limited by the instability of the ^{133}Cs clock. Therefore, comparisons between optical clocks are preferred as they provide lower statistical and systematic uncertainties. At PTB, various optical clocks are established and the $^{171}Yb^{+}$ clock (Huntemann et al., 2016) provides an ideal reference as it has a lower systematic and statistical uncertainty than the Ar^{13+} clock.

In Sec. 6.1 the laser stabilisation scheme for clock operation of the Ar^{13+} clock is discussed. This is followed by a presentation of the results of a clock comparison between the Ar^{13+} and $^{171}Yb^{+}$ clocks for the two isotopes $^{40}Ar^{13+}$ and $^{36}Ar^{13+}$ in Sec. 6.2. In the final section, the excited-state g-factor and quadrupole moment of Ar^{13+} are extracted from the clock data and compared to theoretical predictions.

The results of the following sections have been published in King et al., 2022. The presented values are from an independent analysis which was performed as a cross check. This yielded small, non-significant differences to the published values due to differences in data processing.

6.1 CLOCK OPERATION

The sequence for clock operation is illustrated in Fig. 6.5. It consists of a series of so-called *servo cycles* which take about 3.6 s each. Each of them yields an estimation of the laser frequency with respect to the four probed Zeeman components (Fig. 5.4). The interrogation of the clock transition is performed from two independent directions, totalling eight independent frequency measurements. The servo cycle begins by using algorithmic ground-state cooling to cool the WCR modes to the ground state (Sec. 4.2). With initial Doppler cooling for 200 ms, the crystal is prepared close to the Doppler limit. Then, 64 so-called *experimental cycles* are performed where the Zeeman components are interrogated (Fig. 6.5). An additional experimental cycle is used to measure the radial temperature by probing either the RSB or a BSB of one of the WCR modes (see Sec. 5.1.2.3). After the interrogation, eight independent servos give feedback to the estimated transition frequency of their associated Zeeman components based on the ion's response

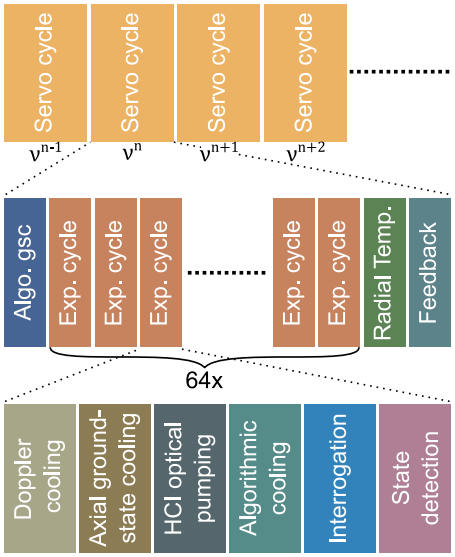

Figure 6.1: Clock sequence. Successive servo cycles i provide estimations of the transition frequencies ν_i for each Zeeman component and their mean frequency. Within a servo cycle, the various Zeeman components are probed for a total of 64 times with the result being used to give feedback to the estimated transition frequencies. Additionally, full algorithmic ground-state cooling (algo. gsc) and a measurement of the radial IP temperature are performed. Each of the 64 experimental cycles prepares and interrogates the Ar^{13+}-$^9Be^+$crystal. Details are given in the main text.

to the interrogation using the Zeeman AOMs for the two different directions (Fig. 3.7). An additional servo uses the mean frequency of the Zeeman components to steer the offset between frequency comb and clock laser. A simplified depiction of the feedback loops is shown in Fig. 6.2.

The probing of each of the Zeeman components from each direction consists of four measurements at each of the two half-maxima of the atomic transition at frequencies $\nu_i \pm \delta\nu/2$ as shown in Fig. 6.3(a). Here ν_i is the estimated mean frequency, $\delta\nu$ is the linewidth and $i \in \{1, 2, ..., 8\}$ denotes one of the eight independent servos. The linewidth $\delta\nu$ is equal for all probed transitions and is approximated by an ideal Rabi interrogation $\delta\nu \approx 0.8/t_\mathrm{p}$ (Sec. 2.2) with the probe time $t_\mathrm{p} = 15\,\mathrm{ms}$. This is justified as only small additional line broadening effects were observed (see Appendix C). An error signal e_i is generated from the difference in excitation between the probe points:

$$e_i^n = p_i^+ - p_i^- \tag{6.100}$$

with p_i^+ and p_i^- being the measured excitation probability of the higher and lower frequency probe point respectively and n the servo iteration. The resulting error signal is shown in Fig. 6.3(b). It has a zero-crossing on resonance.

A digital control loop is steering the frequency of the Zeeman AOMs by applying the correction

$$\nu_i^{n+1} = \nu_i^n + \delta\nu \left(g_1 e_i^n + g_2 \sum_{m=n-100}^{n} e_i^m \right) \tag{6.101}$$

where ν_i^n is the estimated centre frequency of the Zeeman components at servo cycle n. The response of the servo is controlled by the gain factors $g_1 \approx 0.3$ and $g_2 \approx 0.005$ controlling the response of the servo.

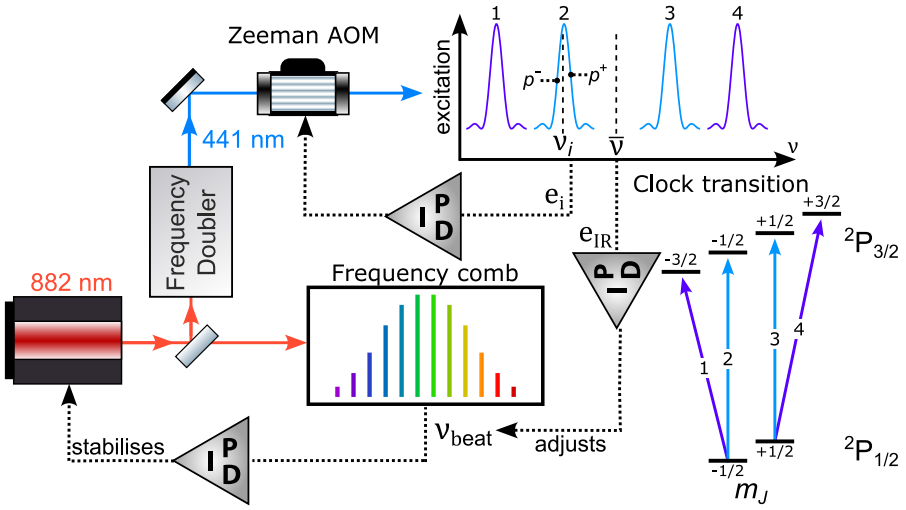

Figure 6.2: Simplified feedback scheme for clock operation. The laser at 441 nm interrogates the Zeeman components of the clock transition (bottom right). Two-point sampling (Fig. 6.3) is used to estimate the frequency ν_i of each Zeeman component relative to the laser frequency. From this the error signal is derived e_i which steers the frequency of the Zeeman AOM. The mean frequency of the Zeeman components $\bar{\nu} = \sum_i \nu_i$ is used to generate an error signal e_{IR}. This steers the setpoint of the beat frequency ν_{beat} between clock laser and frequency comb, stabilising the former. Details are provided in the main text and a detailed depiction of the setup is shown in Fig. 3.7. Some graphical components were adapted from Franzen, 2006.

The first term (right-hand side) of Eq. 6.101 corresponds to a first order integrator. With only this in place, drifts can still lead to a significant servo error (Peik et al., 2006). To mitigate this, a second-order integrator is added which acts on much longer timescales compared to the first-order integrator. In total, this servo allows stabilisation of the laser to the individual Zeeman components.

An additional servo is used to stabilise the laser frequency measured on the frequency comb to the estimated mean frequency $\bar{\nu}^n = \sum_i \nu_i^n / 8$. This servo gives feedback to the fundamental light's frequency such that $\bar{\nu}^n$ is stabilised by adjusting the offset between the clock laser and the frequency comb. The error signal for this is given by

$$e_{\mathrm{IR}}^n = \bar{\nu}^n - \nu_0 \tag{6.102}$$

where ν_0 is a fixed reference value. The choice of ν_0 is arbitrary and represents the fixed value $\bar{\nu}^n$ converges to on long timescales. For the servo to engage reliably it needs to be close to $\bar{\nu}^n$. Note that e_{IR}^n is in units of Hz. The error signal is used to steer the setpoint ν_{beat}^n of the beat between laser and frequency comb which stabilises the clock laser. The feedback is given by

$$\nu_{\mathrm{beat}}^n = \nu_{\mathrm{beat}}^0 + g_1^{\mathrm{IR}} e_{\mathrm{IR}}^n + g_2^{\mathrm{IR}} \sum_{m=0}^{n} e_{\mathrm{IR}}^m + g_3^{\mathrm{IR}} \sum_{k=0}^{n} \sum_{m}^{k} e_{\mathrm{IR}}^m. \tag{6.103}$$

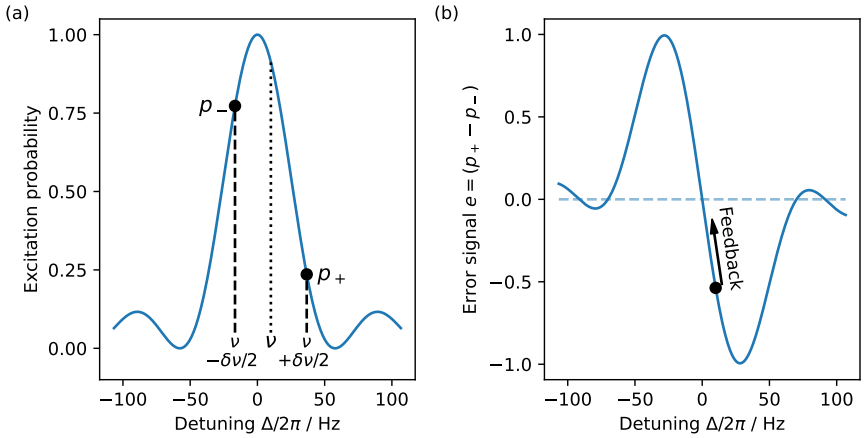

Figure 6.3: Error signal generation scheme for two-point sampling. For stabilisation to the individual Zeeman components, two-point sampling is employed (Peik et al., 2006). (a) Ideal Rabi lineshape for a probe time of $t_\mathrm{p} = t_\pi = 15\,\mathrm{ms}$ with a transition linewidth $\delta\nu$ (Sec. 2.2). The estimated transition frequency ν is used to determine the probe points $\nu \pm \delta\nu/2$. Interrogations of the atomic transition yield the excitation probabilities p^+ and p^-. (b) The difference $e = p^+ - p^-$ is used as an error signal which shows a zero crossing on resonance. By applying feedback to the estimated transition frequency ν the error signal is driven there over many iterations.

where ν^0_beat is a fixed value close to the value that ν^n_beat is converging towards when captured. Here, the control loop consists of a proportional part with gain $g_1^\mathrm{IR} \approx 0.4$, a first-order integrator with $g_2^\mathrm{IR} \approx 0.25$, and a second-order integrator with $g_3^\mathrm{IR} \approx 0.003$. The choice of gain values and integrator were optimised using simulations such that for long time scales the noise is transferred to the frequency measured on the frequency comb.

In Fig. 6.4 the OADEV of various control loops is shown for a dataset of about 5.5 h with only minor gaps and for a probe time of $t_\mathrm{p} = 15\,\mathrm{ms}$ for all the Zeeman components. At short timescales the system's instability is dominated by the servo response. After the servo time constant of about 30 s the laser becomes stabilised to the atomic transitions. The estimated frequencies for the individual Zeeman transitions does not converge for long time scales due to magnetic field drifts. The black dashed line is the approximate frequency fluctuations of the most sensitive transitions (ν_1 and ν_4) for the magnetic field instability of around 0.15 nT at the relevant timescales (Fig. 5.5). The mean frequency of all transition does average indefinitely as it represents an in-loop signal. The instability of ν_Beat scales with $\tau^{-1/2}$ for time beyond the servo time constant, indicative of white frequency noise as expected from QPN. For long time scales, a drift of around 20 Hz per day is indicated due to the instability of Si2. This can be overcome by comparing it to another optical clock which provides a more stable optical frequency at long timescales. A analysis of the performance and comparison to

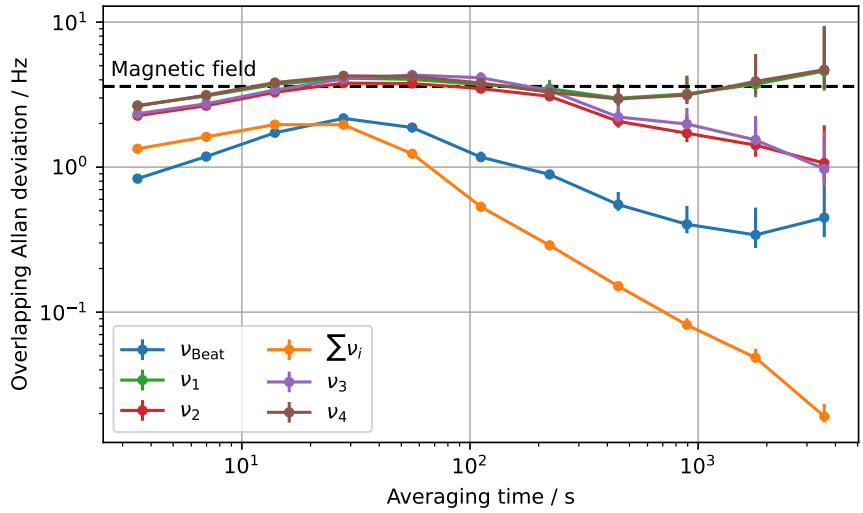

Figure 6.4: Overlapping Allan deviation of the locked clock laser. The lock consists of various stages. In the first stage the laser is locked to the four Zeeman components given in Fig. 5.4. The estimated transition frequencies, averaged over the two counter-propagating directions, ν_i do not average down for long timescales due to magnetic field fluctuations. Their instabilities show a varying noise floor due to different sensitivity to magnetic field noise and differences in excitation probability. The blacked dashed line shows the estimated instability from magnetic field instability of the most sensitive transitions (ν_1 and ν_4). The mean of all transitions is stabilised by a second control loop giving feedback to the offset between frequency comb and clock laser. This makes it an in-loop signal which averages down indefinitely and leads to the τ^{-1} scaling. The beat with the frequency comb ν_{Beat} is a representation of the quantum projection noise for long timescales up to several 1000 s where the drift of the Si2 cavity (Matei et al., 2017) becomes visible. Lines are interpolation between the points.

simulations is given in Appendix C which reproduce the experimental results within reasonable assumptions.

For clock operation, a probe time of $t_{\mathrm{p}} = 15\,\mathrm{ms}$ was employed for all transitions. In general for Rabi interrogation, a lower instability is achieved when t_{p} exceeds the excited-state lifetime, which is 10 ms for Ar^{13+}. This comes at the cost of a decreased excitation rate due to spontaneous decay (Peik et al., 2006). The loss of contrast is particularly relevant for the non-closed transitions interrogated (transitions 2 and 3 in Fig. 5.4), where population is lost due to decay to a dark state. Experimentally, a 25 % lower contrast is observed for these transitions compared to the closed transitions. The decrease in contrast increases the chance of losing lock to the transition, e.g. during a sudden change of the magnetic field. It was found that $t_{\mathrm{p}} = 15\,\mathrm{ms}$ is the maximal probe time for stable operation.

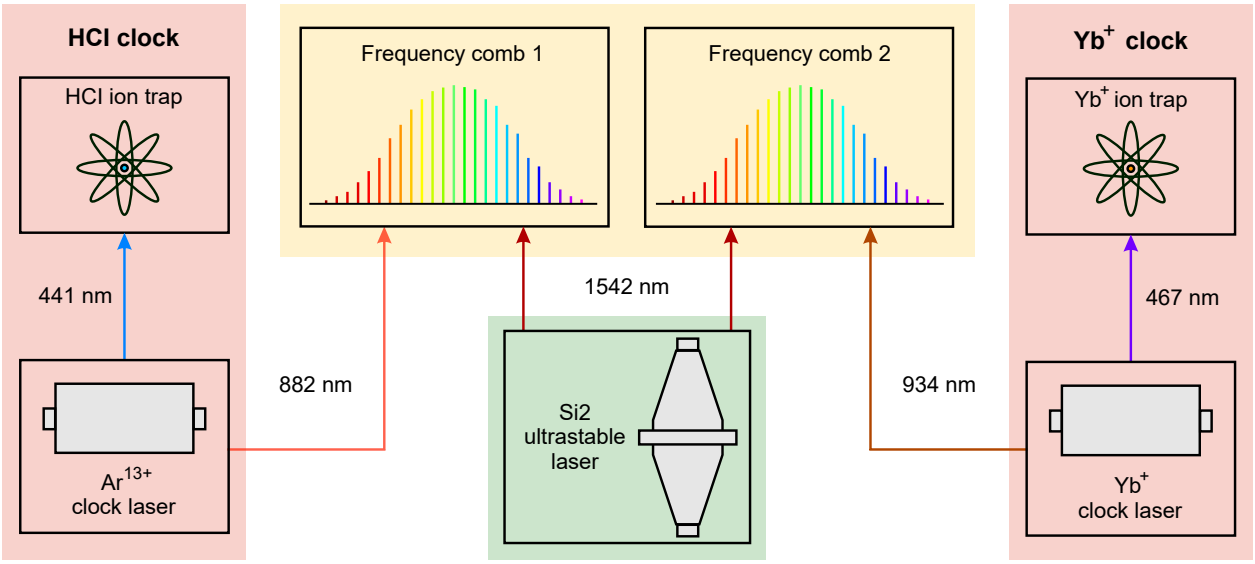

Figure 6.5: Scheme for frequency comparison. The Ar^{13+} and the $^{171}Yb^{+}$ clocks both have a clock laser interrogating their respective ions' with respective wavelengths of 441 nm and 467 nm. The ions responses are used to stabilise the lasers with parts of the fundamental light being sent to separate frequency combs. Both frequency combs are stabilised to the same laser at 1542 nm locked to the ultra-stable silicon cavity Si2 (Matei et al., 2017). At each comb this setup yields the frequency ratio between the clock laser and the Si2-stabilised laser. From this, the ratio of the clock lasers can be derived. Figure taken from King et al., 2022.

6.2 FREQUENCY RATIO MEASUREMENT

A clock comparison between the Ar^{13+} clock and another optical clock based on the electric-octupole ($E3$) transition in $^{171}Yb^{+}$ located at PTB (Huntemann et al., 2016) was performed to assess the performance of the Ar^{13+} clock. The $^{171}Yb^{+}$ clock has a fractional uncertainty of 3×10^{-18} and an instability of $1 \times 10^{-15}/\sqrt{\tau}$ (Huntemann et al., 2016; Sanner et al., 2019). The frequency comparison is performed using the scheme shown in Fig. 6.5. Each clock has an output laser beam which is stabilised to the respective optical clock transition. Each laser frequency is compared to the frequency comb spectrum. The clock laser frequency ν_i can then be derived by counting the repetition rates ν_{rep}, the carrier envelope offsets ν_{CEO} and the beat frequencies between clock lasers and the nearest tooth of the frequency comb ν_{beat}. It can be calculated through (Udem et al., 2002)

$$\nu_i = m_i \nu_{\mathrm{rep},i} + \nu_{\mathrm{CEO},i} + \nu_{\mathrm{beat},i} + \nu_{\mathrm{fix},i} \qquad i \in \{\mathrm{Ar}^{13+}, \mathrm{Yb}^{+}\} \tag{6.104}$$

where m_i is the tooth number of the frequency comb that generates the measured beat. It can be determined by measuring ν_i with a commercial wavemeter to MHz uncertainty, which is smaller than $\nu_{\mathrm{rep},i}$ or through measurements of ν_i at varying ν_{rep}. Additional fixed

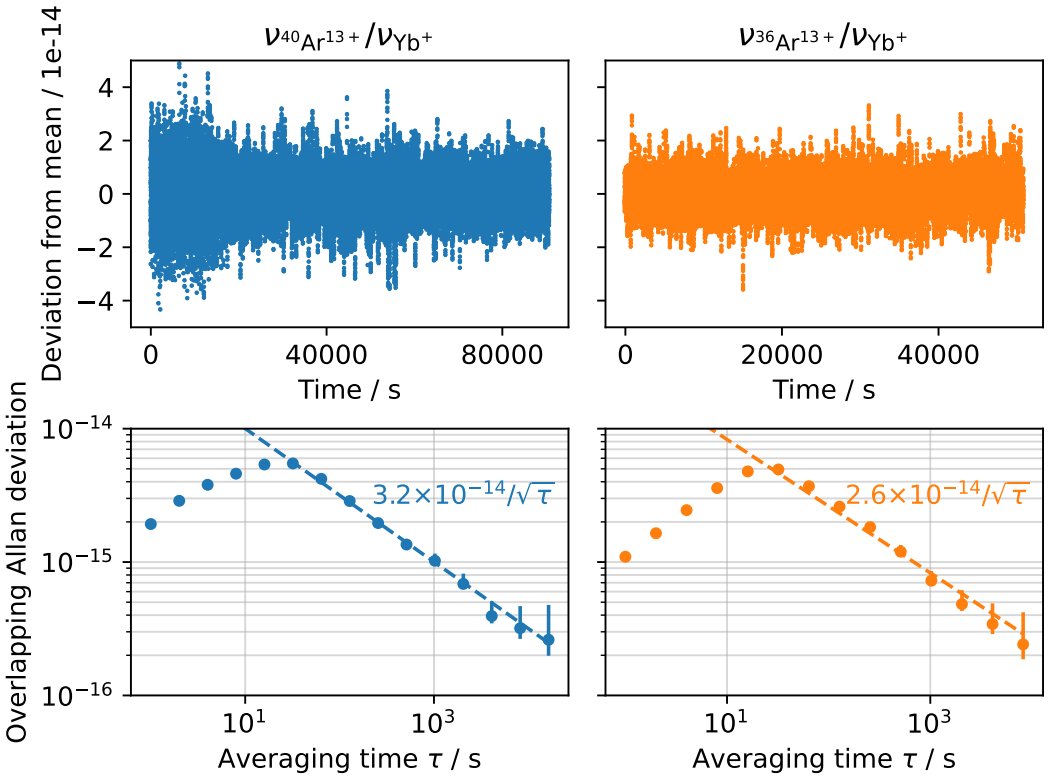

Figure 6.6: Frequency ratio measurements between Ar^{13+} and $^{171}Yb^+$. The measurement was performed for two isotopes $^{40}Ar^{13+}$ (left, blue) and $^{36}Ar^{13+}$ (right, orange) over several days. At the top the concatenated frequency trace is shown. The larger scatter in the $^{40}Ar^{13+}$ plot up to 15 000 s is caused by different gain settings compared to the remaining data trace. At the bottom the OADEV of the trace is shown. After the servo capture time of about 30 s, the $\tau^{-1/2}$ scaling coincides with the expected white frequency noise from QPN.

$\nu_{\mathrm{fix},i}$ need to be added to account for additional frequency shift e.g. from AOMs for fibre length stabilisation.

A maser-based rf reference steered towards the Cs primary standard at PTB is used to stabilise ν_{CEO} of both frequency combs. The repetition rates $\nu_{\mathrm{rep},c}$ are stabilised to the Si2 ultrastable laser (Matei et al., 2017) through a PLL of the beat between frequency combs and Si2. This is advantageous over a lock to the maser as it provides a higher stability for $\nu_{\mathrm{rep},c}$ allowing for optical-optical comparisons without limitations of the microwave clock.

In the present case, the frequency ratio of Ar^{13+} and $^{171}Yb^+$ clock laser are not directly compared as they are sent to two different frequency combs. Therefore, the frequency ratio between any clock laser and Si2 is measured, providing the intermediate result ν_i/ν_{Si2}.

In the next step, synchronous measurements of these ratios are used to derive the ratio of the two clock laser frequencies:

$$R = \left(\frac{\nu_{\mathrm{Ar}^{13+}}}{\nu_{\mathrm{Si2}}}\right) \Big/ \left(\frac{\nu_{\mathrm{Yb}^{+}}}{\nu_{\mathrm{Si2}}}\right) = \frac{\nu_{\mathrm{Ar}^{13+}}}{\nu_{\mathrm{Yb}^{+}}} \tag{6.105}$$

The advantage of this technique is that the optical clocks can be decentralised and only the light of a common ultrastable laser needs to be distributed at convenient wavelength instead of relying on a central frequency comb where all clock lasers are measured simultaneously.

The necessity of synchronous measurements usually requires a synchronisation of all involved laboratories, e.g. through a pulse-per-second signal. In the case of the Ar^{13+} clock, this is not necessary due to the employed laser stabilisation scheme, which fixes the centre frequency in the HCI laboratory for a sufficiently long averaging time (Sec. 6.1) [1].

The frequency ratio R was measured over multiple days for the two Ar^{13+} isotopes, with a total integrated time of about 100 000 s for $^{40}Ar^{13+}$ and 50 000 s for $^{36}Ar^{13+}$ after post-processing (see Appendix D). The concatenated data as well as the OADEV are given in Fig. 6.6. The OADEV shows a much larger instability compared to the expected contribution from the $^{171}Yb^{+}$ clock (Dörscher et al., 2021; Huntemann et al., 2016) and is therefore dominated by the Ar^{13+} clock. For short averaging time τ, the statistical uncertainty is dominated by the servo response to the measurement. After the servo capture time of about 30 s, the frequency ratios scale with $3.2 \times 10^{-14}/\sqrt{\tau}$ for $^{40}Ar^{13+}$ and $2.6 \times 10^{-14}/\sqrt{\tau}$ for $^{36}Ar^{13+}$. The $\tau^{-1/2}$ scaling corresponds to white noise which is an indicator of a quantum projection noise limited measurement. The lower instability for $^{36}Ar^{13+}$ was achieved due to improved state preparation by replacing the repumper laser (see Sec. 3.6.1), which reduced the dead time and increased the measurement contrast by allowing for better state preparation efficiency.

The achieved instability of $3 \times 10^{-14}/\sqrt{\tau}$ of the Ar^{13+} clock is high when compared to other state-of-the art optical clocks based on single ions (Brewer et al., 2019; Dörscher et al., 2021). A further improvement, e.g. by reducing the dead time, is limited to no better then $1 \times 10^{-14}/\sqrt{\tau}$ (Peik et al., 2006). This is mainly limited by the excited-state lifetime of only 10 ms (Lapierre et al., 2006). Therefore, an improved HCI clock should employ an atomic system with a significantly longer excited-state lifetime.

The measured R are given in Tab. 6.1. The statistical uncertainty of the frequency ratio is estimated from the OADEV by extrapolating the fitted instability to the total measurement time giving an uncertainty

1 The computers in the HCI laboratory are synchronised to the local UTC through the Network Time Protocol (NTP) to a level of tens of milliseconds. This is used to time tag data in case of intermittent issues in the HCI laboratory for data processing (Appendix D).

Measurement	Value	Relative uncertainty
$R(^{40}Ar^{13+})$	1.057 769 387 587 480 93(11)	1.1×10^{-16}
$\nu(^{40}Ar^{13+})$	679 216 462 397 957.42(11) Hz	1.6×10^{-16}
$R(^{36}Ar^{13+})$	1.057 766 462 735 187 48(13)	1.2×10^{-16}
$\nu(^{36}Ar^{13+})$	679 214 584 287 424.91(12) Hz	1.7×10^{-16}
$\nu(^{40}Ar^{13+})$ - $\nu(^{36}Ar^{13+})$	1 878 110 532.53(11) Hz	5.8×10^{-11}

Table 6.1: Measured frequency ratios (R), absolute frequencies (ν) and isotope shift. The clock comparison directly yields the frequency ratio $R = \nu(Ar^{13+})/\nu(^{171}Yb^{+})$. The absolute frequencies are derived using a previous measurement of $\nu(^{171}Yb^{+})$ by Lange et al., 2021.

	$\Delta\nu/\nu$ / 10^{-16}		σ/ν / 10^{-16}	
Shift	$^{40}Ar^{13+}$	$^{36}Ar^{13+}$	$^{40}Ar^{13+}$	$^{36}Ar^{13+}$
Statistics	0		1.0	1.3
Uncompensated paths	0		0.01	
Yb^{+} $E3$ absolute frequency	0		1.3	
Gravitational redshift	1.633		0.008	
TOTAL	1.6		1.5	1.7

Table 6.2: Uncertainties arising from the clock comparison. The shift ($\Delta\nu$) and the uncertainty (σ) of the measured absolute frequency needs to be corrected for additional shifts, which are not directly related to the Ar^{13+} clock. The uncertainty of the absolute frequency is limited approximately equally by the statistical uncertainty of the here measured frequency ratio, and the previously measured absolute frequency of $^{171}Yb^{+}$ (Lange et al., 2021). The $^{171}Yb^{+}$ absolute frequency is limited by the systematic uncertainty of the Cs primary standard.

of about 1×10^{-16}. The absolute frequency of the $^{171}Yb^{+}$ $E3$ transition has previously been measured to an uncertainty of 1.3×10^{-16} limited by the primary Cs standard (Lange et al., 2021). Using this, the absolute frequency of Ar^{13+} and the isotope shift is derived with the values also given in Tab. 6.1. The shift caused by the gravitational redshift (see Sec. 5.7) is taken into account. Another uncertainty arises from a few metres of optical paths (free-space and optical fibre) in the frequency comb setup which are not actively path-length stabilised. These have a typical excess instability of around 1×10^{-18} at the integration time of 100 000 s (Benkler et al., 2019). This is added as an estimation of the uncertainty. A summary of the shifts and uncertainty of the clock comparison is given in Tab. 6.2. The combined systematic uncertainty of the Ar^{13+} and the $^{171}Yb^{+}$ clock of 2×10^{-17} is negligible compared to the statistical uncertainty of 1×10^{-16}.

The derived result is compared to previously published values of the absolute frequency of $^{40}Ar^{13+}$ in Fig. 6.7. The measured value agrees well with most of the previous publications except for Soria Orts et al.,

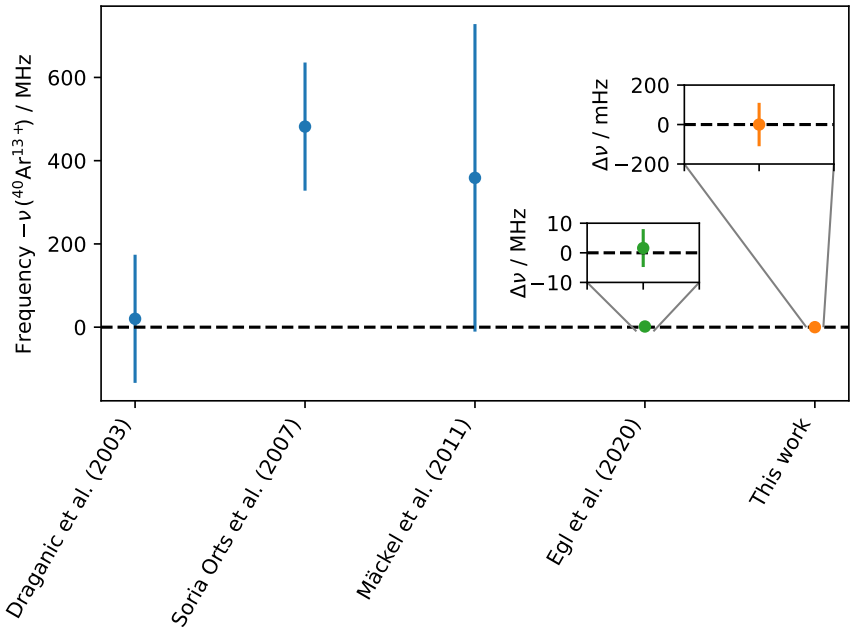

Figure 6.7: Published values of the $^{40}Ar^{13+}$ transition frequency. Measurements were predominantly performed using an EBIT (blue). Recently, a measurement using a Penning trap (green) improved the absolute frequency by more than one order of magnitude. This work (orange) improves it further by eight orders of magnitude. Details are given in the text. The values from the EBIT measurements are published as air wavelengths and have been converted to vacuum wavelength following Peck et al., 1972 with updated constants from Ciddor, 1996.

2007, which deviates by more than 3σ. This deviation was already reported by the best previous measurement (Egl et al., 2019). The improvement by eight orders of magnitude to 110 mHz from this work brings the clock transition frequency uncertainty into the regime of optical clocks and makes it one of the best known absolute transition frequencies (Baynham et al., 2018b; Lange et al., 2021; Leopardi et al., 2021; Lodewyck et al., 2016; McGrew et al., 2019; Nemitz et al., 2021; Pizzocaro et al., 2020; Schwarz et al., 2020).

The result for the isotope shift (Tab. 6.1) has an uncertainty of 110 mHz which benefits from common mode rejected of certain uncertainties. In particular, the uncertainty of the absolute frequency of the $^{171}Yb^{+}$ clock transition is strongly suppressed. The result is in good agreement and improves the best previously published value by nine orders of magnitude (Soria Orts et al., 2006). It can also be compared to theoretical predictions for the mass and field shift constants K and F (see Sec. 2.4 for definitions). The comparison of the experimental value and a recently improved theoretical prediction (King et al., 2022) is given in Tab. 6.3. The theory incorporates relativistic and QED effects for the field and mass shift (see Sec. 2.4). If only the relativistic contributions are taken into account, the prediction deviates by more

Mass shift, relativistic	1906.45 (80)
Mass shift, QED	−13.0 (36)
Field shift, relativistic	−15.9 (15)
Field shift, QED	−0.08
Total theory	1877.5 (40)
Experiment, this work	1878.110 532 51(11)
Experiment (Soria Orts et al., 2006)	1895(93)

Table 6.3: Theoretical prediction and experimental value of the isotope shift. The theory includes relativistic and QED effects (King et al., 2022) and agrees well with the experimental value. The resolved QED mass shift has previously not been observed in a many-electron system. All values are given in MHz.

than 7σ from the observed value. Agreement is achieved when the QED contributions to the mass shift, called QED nuclear recoil, are added. The QED contributions to the field shift are negligible at the theoretical uncertainties given in Tab. 6.3. Thus, this makes it the first experimental observation of the QED nuclear recoil in a many-electron system.

Higher-order standard model contributions are not included in the calculations and would lead to a deviation from Eq. (2.56). They predominantly enter through the mass shift in higher orders of (m_e/M) and were estimated to be $<$100 kHz (Yerokhin et al., 2020). This much smaller than the uncertainties of the first-order calculations and are therefore not needed to be included in Tab. 6.3.

6.3 ATOMIC PARAMETERS

Atomic parameters can be extracted from the gathered data during the clock runs. In particular, the ratio of ground- and excited-state g-factor is derived from the measurement of the Zeeman splitting as demonstrated previously (Micke et al., 2020). Similarly, the quadrupole moment Θ is estimated.

6.3.1 Ratio of g-factors

The Zeeman substates of ground- and excited-state shift due to the linear Zeeman shift as given in Eq. (5.92). This shift is linear in the magnetic field and depends on the g-factors of the involved states. From the clock data, this allows to estimate the ratio r of ground- ($g_{1/2}$) and excited-state ($g_{3/2}$) g-factor. Quadratic shifts, for example the quadrupole shift (Sec. 5.2.3) or the second-order Zeeman shift (Sec.

5.2.4.2), perturb this measurement, but are negligible at the presented statistical uncertainty.

From Eq. (5.92) it can be shown that

$$r = \frac{g_{3/2}}{g_{1/2}} = \frac{1-\rho}{3-\rho} \tag{6.106}$$

where $\rho = (\nu_4 - \nu_1) / (\nu_3 - \nu_2)$ with ν_i denoting the measured frequency of a Zeeman transition, following the numbering in Fig. 5.4. Note that only the relative frequency difference of the Zeeman components due to the linear Zeeman shift is relevant and not their absolute frequency. In the previous measurement (Micke et al., 2020), the result was limited by the drift of the magnetic field. This is mitigated here by locking to the frequency of all transitions simultaneously. A residual uncertainty is caused by magnetic field variations resulting in a servo error. This was estimated to accumulate an error of around $\pm 1\,\mathrm{mHz}$ for each Zeeman component for the measurement time of 100 000 s (Sec. 5.5). This is around two orders of magnitude smaller than the statistically limited measurement and therefore negligible.

The clock comparison data is evaluated by calculating r on a servo cycle-by-servo cycle basis with the OADEV of the data presented in Fig. 6.8. It shows that for time beyond the capture time, a scaling like $\tau^{-1/2}$ is visible indicating white frequency noise. The measured values for the two isotopes are

$$r_{40} = 2.007\,513\,7(22) \tag{6.107}$$

$$r_{36} = 2.007\,516\,9(28) \tag{6.108}$$

where the given uncertainty is dominated by the statistical uncertainty which is derived by extrapolating the fitted stability to the total amount of measured cycles. The difference $r_{40} - r_{36} = 2.5(34) \times 10^{-6}$ is consistent with the theoretical prediction of 2.2×10^{-6} (Agababaev et al., 2018, 2019).

An additional uncertainty of this measurement is caused by the magnetic field from the rf trap drive. This couples Zeeman substates within a manifold (Arnold et al., 2020; Gan et al., 2018) analogous to an a.c. Stark or a.c. Zeeman shift induced by lasers (Sec. 5.2.1 and Sec. 5.2.5). The projection of this magnetic field onto the quantisation axis has been bounded previously to be $<3\,\mu\mathrm{T}^2$ (Leopold et al., 2019). This measurement was performed at higher trap frequencies than used within this work. Due to the geometry of the trap and quantisation axis (Fig. 3.8), a similar field strength is assumed for the transverse components. Taking the above value as a conservative bound, this contributes to the uncertainty at a fractional level of 7×10^{-6}. This is included in the above given uncertainties for r.

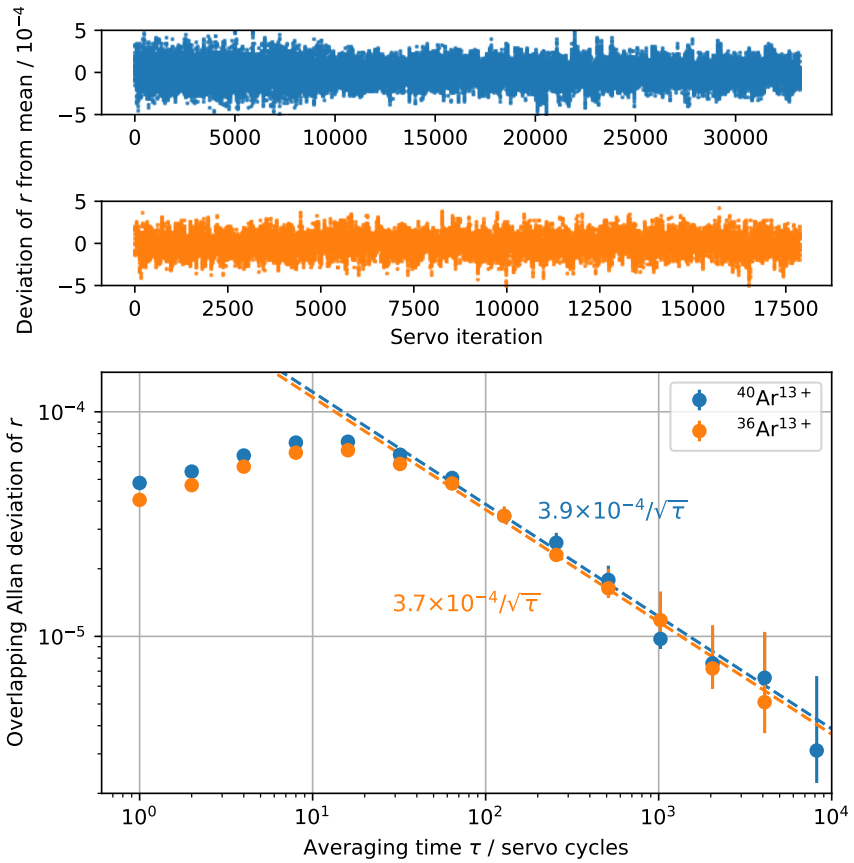

Figure 6.8: Measurement of the g-factor ratio r of Ar^{13+}. Top: time trace of the measured $r = g_{3/2}/g_{1/2}$ as a function of clock servo iteration is given for the two isotopes $^{40}Ar^{13+}$ and $^{36}Ar^{13+}$. At the bottom the corresponding OADEV is shown with a fitted instability. The averaging time τ is given in units of servo cycles. Details are given in the text.

For $^{40}Ar^{13+}$, $g_{1/2}$ has been measured using a Penning trap to an uncertainty of 1.4×10^{-9} (Arapoglou et al., 2019). Using this, $g_{3/2}$ is derived for this isotope, yielding

$$g_{3/2} = 1.332\,283\,3(15) \tag{6.109}$$

which is consistent with the previous result (Micke et al., 2020) but a four-fold improvement in uncertainty. This also confirms theoretical calculations predicting $g_{3/2}^{\text{theo}} = 1.332\,282\,5(14)$ (Agababaev et al., 2019).

6.3.2 Quadrupole moment

The measured mean frequency is free of the quadrupole shift as described by Eq. (5.90). Similar to the g-factors, a combination of Zeeman components can still be used to calculate the quadrupole moment Θ. This is achieved by comparing the mean frequency of one

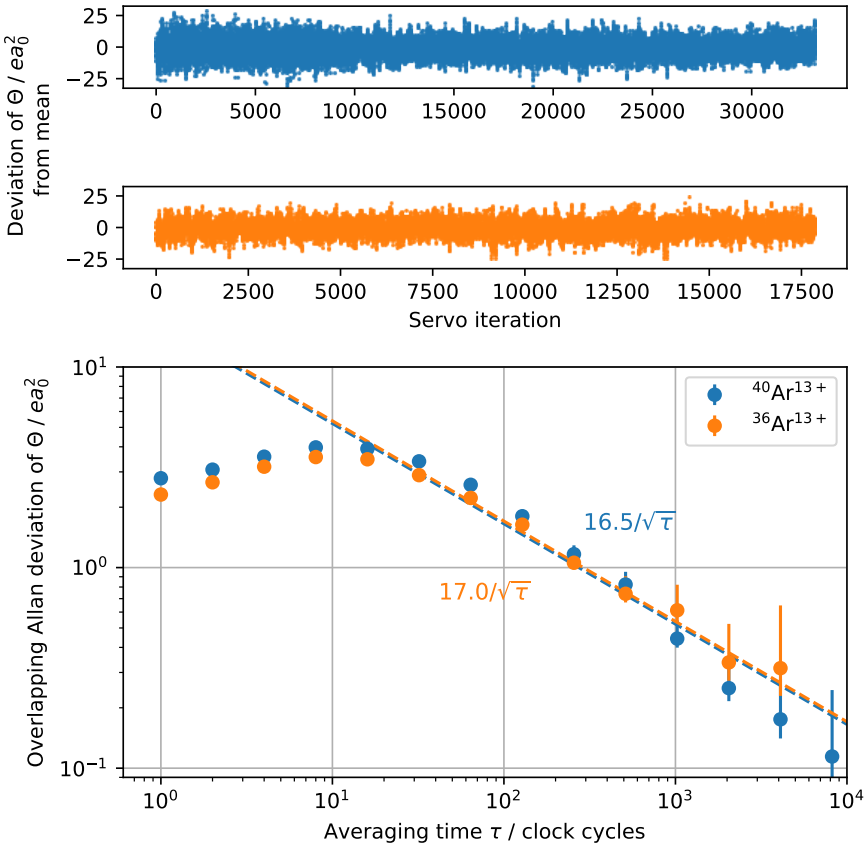

Figure 6.9: Measurement of the quadrupole moment Θ of the $^2P_{3/2}$ state in Ar^{13+}. Top: time trace of the measured quadrupole moments as a function of clock servo iteration for the two isotopes $^{40}Ar^{13+}$ and $^{36}Ar^{13+}$. Bottom: the corresponding OADEVs are shown with a fitted instability. The averaging time τ is given in units of servo cycles. Details are given in the text.

symmetric pair of Zeeman components to the other. The quadrupole moment Θ is described by

$$\Theta = \frac{h((\nu_2+\nu_3)-(\nu_1+\nu_4))}{(3\cos^2\beta - 1 - \epsilon\sin^2\beta\cos(2\alpha))}\left(\frac{\mathrm{d}E_z}{\mathrm{d}z}\right)^{-1}. \tag{6.110}$$

with the definitions of the parameters as given in Sec. 5.2.3. The electric field gradient $\mathrm{d}E_z/\mathrm{d}z$ can be calculated from the single ion motional frequency (see Eq. 5.89). Like for the g-factor, Θ is calculated on a cycle-by-cycle basis suppressing magnetic field changes in real time. An OADEV of the data shows the expected white noise behaviour for long time scales (Fig. 6.9). The resulting quadrupole moments for the two isotopes are

$$\Theta_{40} = -0.01(10)ea_0^2 \tag{6.111}$$
$$\Theta_{36} = -0.03(13)ea_0^2. \tag{6.112}$$

Species	Θ / ea_0^2
Ca^+	1.83
Sr^+	2.6
Yb^+ $E2$	1.95
Yb^+ $E3$	-0.0297
Hg^+	-0.510
Ar^{13+} (theory)	0.0235
$^{40}Ar^{13+}$ (exp.)	-0.01(10)
$^{36}Ar^{13+}$ (exp.)	-0.03(13)

Table 6.4: Quadrupole moment Θ of various optical clock ions. Singly charged systems employing states with an angular momentum $J > 1$ have typically $\Theta \approx 1$, with the exception of the Yb^+ $E3$ transition. Ar^{13+} is predicted by theory to have a similarly small value. Experimentally it was not resolved, though even the achieved bounds are smaller than all other listed systems but the Yb^+ $E3$ transition. Values are compiled from Lange et al., 2020; Ludlow et al., 2015; Müller, 2021; Yu et al., 2019. All digits are significant.

Both results are consistent with the theoretical prediction of $\Theta_{\text{theo}} = 0.0235$ (Yu et al., 2019).

To put this value into perspective, a summary for various optical clock transitions with $J > 1$ is given in Tab. 6.4. It can be seen that the Ar^{13+} clock's quadrupole moment is one of the smallest values among them. Only the value of the $^{171}Yb^+$ $E3$ transition being similar in size.

6.4 SUMMARY

The operation of an HCI clock has been demonstrated by stabilising a laser to the electric dipole-forbidden transition in Ar^{13+}. Its performance was assessed by comparing it to the established $^{171}Yb^+$ clock at PTB (Huntemann et al., 2016). An instability of $3 \times 10^{-14}/\sqrt{\tau}$ was achieved. In the future, an HCI with a longer excited-state lifetime is needed to achieve a state-of-the-art instability. The frequency ratio of Ar^{13+} and $^{171}Yb^+$ was measured to an uncertainty of 1×10^{-16} for two isotopes $^{40}Ar^{13+}$ and $^{36}Ar^{13+}$. The derived absolute frequency of $^{40}Ar^{13+}$ and the isotope shift improve upon the best previous measurements (Egl et al., 2019; Soria Orts et al., 2006) by eight and nine orders of magnitude, respectively, making them by far the most accurate values among all HCI and similar to values for neutral and singly-charged optical atomic clocks. The isotope shift was compared to the theoretical predictions and is the first experimental verification of the QED nuclear recoil in a many-electron system.

Additionally, atomic parameters were extracted from the clock data. Firstly, the ratio of ground- and excited-state g-factor was derived. Using a measurement of $g_{1/2}$ for $^{40}Ar^{13+}$ (Arapoglou et al., 2019) allowed to derive $g_{3/2}$ for this isotope. The measured values agree well with the theoretical predictions (Agababaev et al., 2018, 2019). Secondly, the quadrupole moment Θ was constrained, showing that it is one of the smallest among operational optical clocks employing

states with $J > 1$, which also confirmed theoretical predictions (Yu et al., 2019).

7 OPTICAL DIPOLE FORCE

Identification of optical transitions in HCI has so far been performed by initially using fluorescence data from an EBIT to determine the transition frequency with an uncertainty of no better than 150 MHz (Draganić et al., 2003; Mäckel et al., 2011; Rehbehn et al., 2021). From there, higher resolution spectroscopy can be performed in Penning traps with an achieved uncertainty of 10 MHz (Egl et al., 2019). Alternative to Penning traps, coherent laser spectroscopy using QLS in Paul traps can be performed with Hz-level precision (Micke et al., 2020). This works well for a sufficiently strong transition, with a lifetime on the order of 10 ms and has been demonstrated in our laboratory for Ar^{13+} and recently Ca^{14+}. Transitions with a longer lifetime are not directly observable in fluorescence measurements using EBITs and can therefore only be identified using Ritz-Rydberg combinations (Bekker et al., 2019), necessitating specific level structures (see also Sec. 9.1). If a Ritz-Rydberg combination is not possible, experimental searches are guided by *ab initio* atomic structure calculations with THz (or worse) uncertainties (Allehabi et al., 2022; Berengut et al., 2012a; Porsev et al., 2020; Yu et al., 2018). Such uncertainties are too large to enable direct searches with QLS within an experimentally feasible amount of time. For example, for an excited-state lifetime on the order of 10 s, a Rabi linewidth of 10 kHz is realistic for moderate laser powers of about 1 mW. With an experimental cycle time of 20 ms and 10 repetitions it would take more than 200 days to scan 1 THz[1].

Another issue is that initially internal state preparation of the HCI is not possible. The population distribution of a newly loaded HCI is determined by the electronic decay paths of the HCI when extracted from the EBIT and therefore largely random. Not every transition can thus be excited. Furthermore, for $M1$ transitions with a typical lifetime of about 10 ms, spontaneous decay occurs frequently when exciting the transition, which can pump the ion to a dark state. An exception to this are systems with a single ground state like Ca^{14+} or systems where the angular momentum of the excited state (F_e) is higher than in the ground state (F_g). This leads, for e.g. $M1$ transitions like in

1 This assumes that a carrier excitation can be detected. For QLS, excitation of a motional sideband is necessary which reduces the Rabi linewidth by the Lamb-Dicke parameter η. In the presented experiments, typically $\eta = 0.1$.

Ar^{13+}, to a closed transition $|F_g, m_g = \pm F_g\rangle \rightarrow |F_e, m_e = \pm F_g \pm 1\rangle$[2]. In other systems with $F_e < F_g$ such a transition does not exist. This is for example the case in certain S- and Se-like systems with the ground state $^3P_2$ and the excited state $^3P_1$ (Sec. 9.1). Thus any electronic excitation has a significant branching ratio to Zeeman substates other than the initial one. Spontaneous decay from a probed excited state has then a high chance of pumping the HCI to a different ground state, which is dark to the probe laser.

Additional search techniques are therefore necessary to enable laser spectroscopy of a large class of transitions in HCI. One technique which could be useful to mitigate these issues is an optical-dipole force (ODF) which can provide much broader signals for a given laser power than Rabi interrogation, while preserving the initial state (Hume et al., 2011; Wolf et al., 2016).

In this chapter, the theoretical description of ODF is given in Sec. 7.1 and the achievable signal width is compared to Rabi excitation. In Sec. 7.2, the ODF is experimentally demonstrated on the Ar^{13+} clock transition. The last section discuss limitations to the achievable signal width using ODF.

7.1 THEORY

The ODF works by driving stimulated Raman transitions on the motional states mediated by the electronic transition in the HCI. The coupling strength depends on the detuning of the lasers from the electronic transition and can therefore be used to search for it. The generated motional excitation is detected using the logic ion $^9Be^+$, similar to QLS. In the following, the ODF for a Ar^{13+}-$^9Be^+$ two-ion crystal is discussed as an example, though it is applicable to many HCI.

The ODF is generated by using two counter-propagating laser beams which have a common detuning Δ from the optical transition in Ar^{13+} (Fig. 7.1). The detuning Δ is chosen to be much larger than the linewidth of the transition such that the excited state is not populated. Additionally, one of the beams is detuned by δ, which is set to the frequency of one of the the motional modes along the beam direction, i.e. $\delta = \omega_z$. Here ω_z is either the IP or OP mode in the two-ion crystal for a beam with a projection onto the z-axis. This leads to a standing light wave with an intensity modulation at the motional frequency which drives transitions between Fock states (Fig. 7.1(a)). It is assumed

2 The closed transition is only visible if the corresponding ground state is populated, which is not guaranteed. The choice of magnetic field, motional frequencies and laser power can facilitate jumps in the Zeeman manifold of the ground state through off-resonant scattering. This increases the chance of detecting the transition. Nonetheless, there is no guarantee that the necessary ground state is populated.

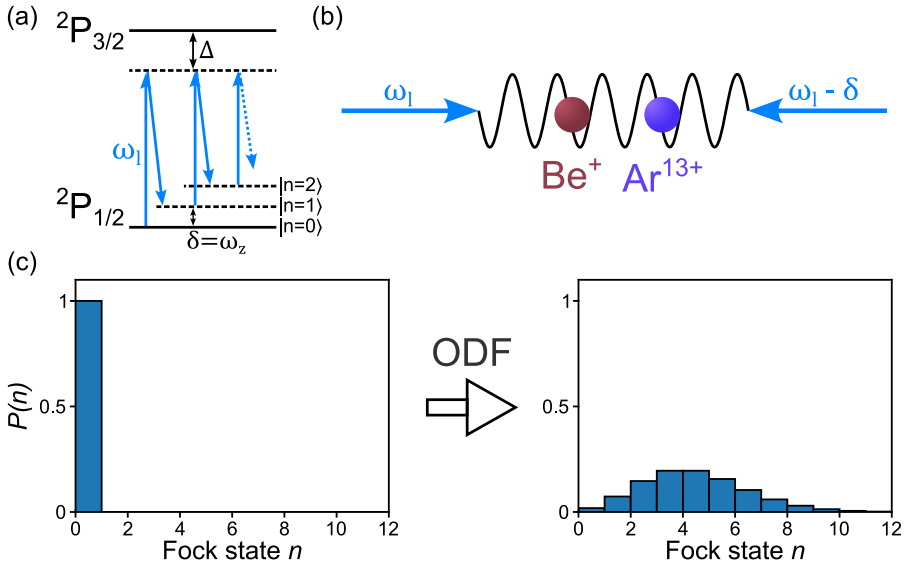

Figure 7.1: Schematic drawing of the application of an optical dipole force (ODF). (a) Involved level structure of the Ar^{13+}. The $^2P_{1/2}$ ground and $^2P_{3/2}$ excited states are coupled by two lasers with frequency ω_l at a detuning of Δ much larger than the linewidth. One of the beams is additionally detuned by $\delta = \omega_z$ where ω_z is chosen to be one of the motional frequencies. This drives stimulated Raman transitions between motional states without exciting the electronic transition. (b) The ODF is generated by applying two counter-propagating lasers. This leads to a travelling optical lattice with frequency δ. (c) Probability $P(n)$ to find the system in the Fock state n. The initially ground-state cooled mode has all Fock state population in the ground state. The ODF displaces this to a coherent state, spread across various Fock states.

that the ODF only couples to the Ar^{13+}. The neglected far off-resonant coupling to $^9Be^+$ will be addressed in Sec. 7.3.2.

When an ODF pulse is applied to the ground-state cooled Ar^{13+}-$^9Be^+$ system it displaces the motional state to a coherent state $|\alpha\rangle$ (Fig. 7.1(c)) with the Fock states n following the distribution (Hume et al., 2011)

$$P(n) = e^{-|\alpha|^2} \frac{|\alpha|^{2n}}{n!}. \tag{7.113}$$

with

$$|\alpha| = \frac{\eta t_p \Omega_1 \Omega_2}{4|\Delta|}, \tag{7.114}$$

where η is the Lamb-Dicke parameter, t_p is the interrogation time, and Ω_1 and Ω_2 are the on-resonant Rabi frequencies for the two interrogating beams when interacting with the optical transition (Fig. 7.1(a)). Note that the above equations are only valid in the far off-resonant case, i.e. $\Omega_{1,2} \ll \Delta$.

The motional excitation generated by the ODF can be detected on the $^9Be^+$ by driving a first-order RSB transition in a QLS-like scheme (Sec. 2.2.3). This reveals all population that was excited from the ground state to a higher Fock state. The first option to drive the RSB transition

is to use a stimulated Raman transition. This couples to all occupied Fock states, which have varying on-resonant Rabi frequencies (Eq. (2.43)). Since the displaced state occupies many Fock state (Eq. (7.113)), this leads to a dephasing of their contributions and results in a signal that decays to an excitation probability of around 0.5. To achieve a higher signal-to-noise ratio, the RSB transition can alternatively be probed using rapid adiabatic passage (RAP), which is robust to the differing Rabi frequencies. This is achieved by slowly varying the Rabi frequency $\Omega(t)$ with the condition $\dot{\Omega}/\Omega \ll \Omega$, leading to an adiabatic transfer of the population between the coupled states (Gebert et al., 2016, 2018; Wunderlich et al., 2007). This allows to faithful map the motional excitation to the electronic state of the $^9Be^+$, where it can be detected. Rapid adiabatic passage is employed in this chapter.

Overall, the sequence consists of initial ground state cooling ($P_{\text{init}}(n = 0) = 1$), motional excitation with an ODF pulse and subsequent readout using a first-order RSB transition driven by RAP. The excitation probability for this is given by (Eq. (7.113))

$$P_{\text{exc}} = 1 - P(0) = 1 - \exp\left[-\left(\frac{\eta t_{\text{p}} \Omega_1 \Omega_2}{4|\Delta|}\right)^2\right]. \tag{7.115}$$

For the here proposed application, to search for an unknown transition, the absolute detuning Δ from resonance needs to be scanned. Thus, it useful to estimate the detuning $\Delta_{1/2}^{\text{ODF}}$, where $P_{\text{exc}} = 0.5$, since this corresponds to a signal width and might be used as the step size when searching for an unknown transition. It is given by

$$\left|\Delta_{1/2}^{\text{ODF}}\right| = \frac{\eta t_{\text{p}} \Omega_1 \Omega_2}{4\sqrt{\ln(2)}}. \tag{7.116}$$

It depends on the probe time t_{p} and can therefore be broadened by increasing it. Note that this equation is only valid as long as $\left|\Delta_{1/2}^{\text{ODF}}\right| \gg \Omega_{1,2}$, which is not true for all probe times t_{p}.

This can be compared to the Rabi lineshape given in Eq. (2.34). For Rabi excitation, it is assumed that a QLS-like sequence is used, i.e. a first-order motional sideband transition on the HCI's electronic state is driven to transfer the electronic excitation to the $^9Be^+$ for detection. To simplify the estimation, the oscillatory term in Eq. (2.34) is neglected which leaves the envelope $\eta\Omega_{\text{R}}/\sqrt{(\eta\Omega_{\text{R}})^2 + \Delta^2}$. This used as an approximation as it is the upper bound for the excitation for all probe times. As an estimator the detuning $\Delta_{1/2}^{\text{Rabi}}$ for an excitation probability of 0.5 is used:

$$\left|\Delta_{1/2}^{\text{Rabi}}\right| = \sqrt{3}\eta\Omega_{\text{R}}. \tag{7.117}$$

For the comparison, we assume that an equal amount of total laser power is available, i.e. $\Omega_1 = \Omega_2 = \Omega_R/\sqrt{2} = \Omega$. Then, the ratio of the signal widths of the two methods can be written as

$$\left| \frac{\Delta_{1/2}^{\mathrm{ODF}}}{\Delta_{1/2}^{\mathrm{Rabi}}} \right| \approx 0.5\Omega t_p. \tag{7.118}$$

This shows that for $t_p \gtrsim 2/\Omega$ the ODF provides a detectable signal for larger detuning then Rabi excitation, which can be further broadened by increasing t_p.

As an example, assume a Rabi frequency of $\Omega/2\pi = 10\,\mathrm{kHz}$. For a probe time of $t_p = 10\,\mathrm{ms}$, the ODF leads to a 300-fold broadening at the cost of 10 ms longer experimental cycle time. Limitations to the achievable broadening are discussed in Sec. 7.3.

7.2 IMPLEMENTATION

In following the above described detection scheme is tested on the optical $M1$ transition of $^{36}Ar^{13+}$. First, the implementation of RAP is described in Sec. 7.2.1. In the subsequent Sec. 7.2.2, ODF is experimentally tested and compared to the theoretical predictions.

7.2.1 Rapid adiabatic passage

Rapid adiabatic passage is implemented on the stimulated Raman transition of the $^9Be^+$ following the approach given by Wunderlich et al., 2007. For this, the laser frequency is swept across the transition while the amplitude is modulated simultaneously. These two modulations can be separated to the two Raman beams $^9Be^+$(Fig. 3.1). Thus, the frequency modulation is applied to the red Raman laser which is linearly swept across the resonance frequency ω_0 in a range $\omega_0 - \delta_{\mathrm{RAP}}$ to $\omega_0 + \delta_{\mathrm{RAP}}$. Simultaneously, the amplitude of the blue Raman (Fig. 3.1) is modulated following a Blackman pulse shape (Sec. 3.7).

Experimentally, $\delta_{\mathrm{RAP}} = 50\,\mathrm{kHz}$ was found to achieve good results for a temporal length of the pulse of $t_{\mathrm{RAP}} = 200\,\mu\mathrm{s}$. As a test the BSB transition of the OP motional mode is driven using RAP for two cases. Firstly, after Doppler cooling and secondly after additional ground-state cooling. The population transfer as a function of t_{RAP} is shown in Fig. 7.2(a). The difference in excitation probability between the two cases is attributed to population in Fock states close to zero-crossings of the Rabi frequency, where the adiabaticity criterion is violated. Nonetheless, it shows that in the Doppler cooled case an excitation probability > 0.5 is achieved despite the occupation of many Fock states.

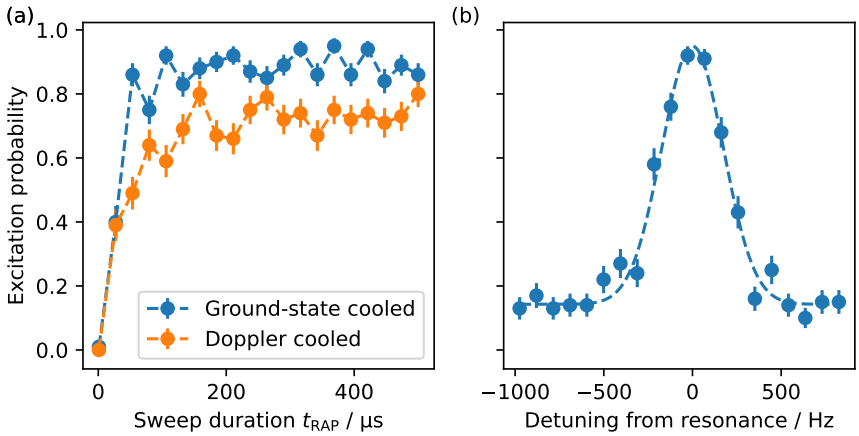

Figure 7.2: Rapid adiabatic passage and measurement of the axial motional frequency. (a) Rapid adiabatic passage applied to the BSB transition with $\delta_{RAP} = 50\,\text{kHz}$ and for varying pulse length t_{RAP}. Shown are the results after Doppler cooling and with additional ground-state cooling. When only Doppler cooling, the signal saturates around 75 %. After ground-state cooling a excitation probability of around 90 % is achieved, likely limited by a combination of state detection error, incomplete ground-state cooling and off-resonant scattering of the employed Raman beams. The difference is attributed to population close to zero-crossings in the Rabi frequency which does not satisfy the adiabaticity condition in the case of Doppler cooling. (b) Measurement of the OP mode motional frequency using a displacement generated by an oscillating electric field with varying frequency. The displaced state is mapped to the $^9Be^+$ electronic state through RAP on the RSB. The dashed line is a fit of a Gaussian function as a guide to the eye. The length of the probe pulse was 3 ms. The increased background comes from anomalous heating.

An application of RAP using a coherent state $|\alpha\rangle$ of an Ar^{13+}-$^9Be^+$ two-ion crystal is shown in Fig. 7.2(b). The displacement was generated by an oscillating voltage applied to an electrode in the vacuum chamber (Carruthers et al., 1965; Heinzen et al., 1990; Wolf et al., 2019). The oscillation frequency is varied across the frequency of the OP motional mode, showing a clear resonance where expected. This provides an easy and fast way of measuring the motional frequencies with high precision and shows that the implemented RAP can achieve a contrast $> 90\,\%$ for coherent states.

7.2.2 Displacement

The purpose of ODF is to detect a previously unknown transition. For a demonstration of the expected signal, the known clock transition of $^{36}Ar^{13+}$ is used. Owing to the long beamline used for HCI transfer, it is not possible to use two counter-propagating beams along the z-axis in the setup. Instead, one beam is aligned along the z-axis while the second beam is tilted by 15° in y_{Lab}-direction (Sec. 3.6.4). This leads

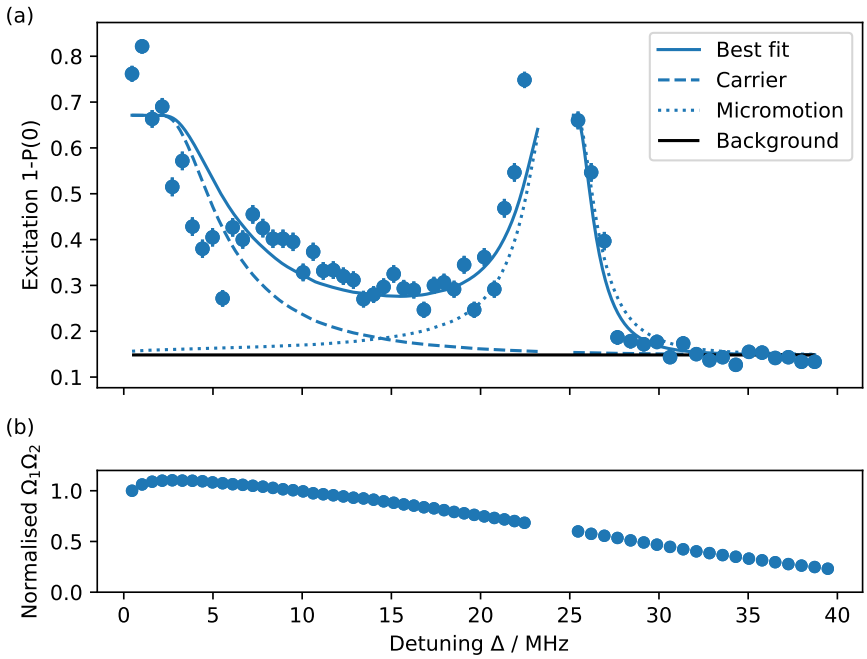

Figure 7.3: Excitation from an ODF as a function of detuning from resonance. An ODF pulse of length 7 ms is used to displace the motional state. The fit function is given in Eq. (7.121) with details provided in the main text. It was assumed that the Ar^{13+} is in the $\left|m_J = +\frac{1}{2}\right\rangle$ state for all times. The scaling factor $\zeta = 1.08(2)$ agrees reasonably well with the theoretical prediction of 1. Additionally, the contributions from the carrier (dashed) and micromotion (dotted) transitions are shown. Deviations from theory are attributed to on-resonant effects not described by Eq. (7.121). The background excitation of 15 % corresponds to the asymptotic behaviour for $\Delta = +\infty$ and is attributed to imperfect ground-state cooling and anomalous heating.

to reduced coupling of this beam to the motional mode by a factor $\cos(15°) \approx 0.97$ which will be neglected in the following discussions, as it has only a small effect on the results. For the displacement, the axial OP mode is chosen. The on-resonant Rabi frequency $\Omega_{1,2}$ for different Zeeman transitions is experimentally calibrated by performing Rabi oscillations and using $\Omega = \pi/t_\pi$ (Sec. 2.2). The measured resonant Rabi frequencies are given in Tab. 7.1 for a laser power of about 1 mW per beam.

The measured on-resonant Rabi frequencies are only valid for a specific detuning Δ. For deviations from resonance, variations of the AOM diffraction efficiencies occur and $\Omega_{1,2}$ becomes a function of Δ. Thus, the laser power is determined by measuring it at the end of each experimental cycle by generating an additional laser pulse and reading in a dedicated photodiode signal. The average photodiode signal is used to rescale the on-resonant Rabi frequency $\Omega \propto \sqrt{P}$. The normalised scaling of $\Omega_1(\Delta)\Omega_2(\Delta)$ is shown in Fig. 7.3(b).

	$\left\|^2\mathrm{P}_{1/2}, m_J\right\rangle \rightarrow \left\|^2\mathrm{P}_{3/2}, m_J\right\rangle$	$(\Omega_1/2\pi)$ / kHz	$(\Omega_2/2\pi)$ / kHz
(1)	$\left\|-\frac{1}{2}\right\rangle \rightarrow \left\|-\frac{3}{2}\right\rangle$	48.7(1)	22.9(4)
(2)	$\left\|\frac{1}{2}\right\rangle \rightarrow \left\|-\frac{1}{2}\right\rangle$	28.1(1)	13.2(3)
(3)	$\left\|-\frac{1}{2}\right\rangle \rightarrow \left\|-\frac{1}{2}\right\rangle$	32.8(1)	17.2(3)
(4)	$\left\|\frac{1}{2}\right\rangle \rightarrow \left\|\frac{1}{2}\right\rangle$	32.8(1)	17.2(3)
(5)	$\left\|-\frac{1}{2}\right\rangle \rightarrow \left\|\frac{1}{2}\right\rangle$	28.1(1)	29.5(4)
(6)	$\left\|\frac{1}{2}\right\rangle \rightarrow \left\|\frac{3}{2}\right\rangle$	48.6(1)	51.1(8)

Table 7.1: Rabi frequencies for ODF measurements. The values were extracted from measuring the interrogation time to achieve a π rotation t_π through Rabi excitation of the carrier transitions (1), (3), and (6) for the two beams independently. The remaining values were calculated using the corresponding Clebsch-Gordan coefficients. The laser power was monitored using a photodiode which is highly linear across the accessed range and the values are rescaled to the same laser power used at $\Delta = 0$ in Fig. 7.3. Difference for the various transitions come from polarisation imbalances and varying Clebsch-Gordan coefficients.

The global detuning Δ of the laser from the unperturbed $^2\mathrm{P}_{1/2} \rightarrow {}^2\mathrm{P}_{3/2}$ transition is varied and a typical signal is shown in Fig. 7.3. No data was taken close to the MM sideband where on-resonant effects become relevant, which are not covered by the employed model. A particularity of the employed setup is the large axial MM (Sec. 5.1.3) which is also visible in the data through a second resonance. To account for this and for the multiple Zeeman components of Ar^{13+}, Eq. (7.115) is extended to

$$P_{\mathrm{exc}} = 1 - P(0) = 1 - \exp\left[-\sum_{i=1,2,3} \beta_i \left(\frac{1}{\Delta_i} - \frac{\rho}{\Delta_i - \Omega_{\mathrm{rf}}}\right)^2\right] \tag{7.119}$$

where it was assumed that the Ar^{13+} is in one of the two ground states $\left|^2\mathrm{P}_{1/2}, m_J = \pm 1/2\right\rangle$ and that no quantum jumps between them occur. The sum adds up the contributions from the three transitions that are associated with a fixed ground state, which assumes no interference between different Zeeman components. The relative strength of carrier to MM sideband is described by $\rho = \Omega_{\mathrm{MM}}/\Omega_{\mathrm{carrier}} \approx 0.85$ which is known from micromotion measurements (see Sec. 5.1.3). The negative sign of the MM contribution is caused by an additional π phase shift of the MM sideband when compared to the carrier transition, where each laser beam contributes a $\pi/2$ phase shift (Keller et al., 2015; Leibfried et al., 2003). The detuning from resonance Δ_i consists of the laser detuning from the mean frequency of the Zeeman components and the linear Zeeman shift. The sum adds up the contributions from the Zeeman components with the factor

$$\beta_i = t_{\mathrm{p}} \eta \frac{\Omega_{1,i}(\Delta)\Omega_{2,i}(\Delta)}{4} \tag{7.120}$$

Probe time	$\left\|m_J = -\frac{1}{2}\right\rangle$	$\left\|m_J = +\frac{1}{2}\right\rangle$
3 ms	2.01(5)	1.38(4)
7 ms	1.32(3)	1.08(2)
12 ms	0.99(2)	0.81(2)

Table 7.2: Fitted ζ for various interrogation times and both ground states $\left|^2\mathrm{P}_{1/2}, \mathbf{m_J} = \pm\mathbf{1/2}\right\rangle$. Overall a reasonable agreement between theoretical prediction and experimental result is achieved for at least one of the two ground states. The provided uncertainties comes from fitting and experimental uncertainties. Details are given in the main text.

calculated from the experimentally measured resonant Rabi frequencies Ω_i.

For fitting of Eq. (7.119), a global fit factor ζ is used to scale the contributions from the different Zeeman components and therefore describes the ratio of experimental displacement to theoretical prediction. Furthermore, an offset (B) and an amplitude scaling (A) are included to account for experimental imperfections:

$$P_{\mathrm{fit}} = A\left\{1 - \exp\left[-\zeta \sum_{i=1,2,3} \beta_i \left(\frac{1}{\Delta_i} - \frac{\rho}{\Delta_i - \Omega_{\mathrm{rf}}}\right)^2\right]\right\} + B. \quad (7.121)$$

The result for an interrogation time of $t_\mathrm{p} = 7\,\mathrm{ms}$ is shown in Fig. 7.3. The fit describes the data well and deviations from the experimental signal are mostly found close to resonance, where resonant effects not included in the model contribute. The deviation around 5 MHz coincides with the radial modes, which have a small projection onto one of the ODF beams. This could lead to resonant excitation of the internal state, leading to a deviation of the expected signal.

Nevertheless, motional excitation is observable up to the MM sideband. The individual contributions from the carrier and MM sideband are also indicated in Fig. 7.3. This shows that even with no MM, motional excitation is expected up to $\Delta/2\pi \approx 10\,\mathrm{MHz}$. In the absence of MM, the carrier signal would increase, broadening the signal further. For Rabi excitation, an excitation signal $> 20\,\%$ would only be visible for $\Delta/2\pi < 10\,\mathrm{kHz}$ for a comparable Rabi frequency.

The scaling of the signal with the probe time t_p is demonstrated by measurements performed for probe time of 3 ms, 7 ms, and 12 ms. The resulting ζ is given in Tab. 7.2. For each probe time, two values of ζ are given, each assuming that the Ar^{13+} was in one of the two ground states during the measurements as no optical pumping was applied. The results agree reasonably well with the theoretical prediction of $\zeta = 1$ for at least one of the two ground state. The discrepancies could be from features in the experimental data that are not included in the model (Fig. 7.3). Additional effects include the heating rate that is only modelled by an background offset, but might contribute in

a more complex way to the signal by disturbing the motional state distribution. Another effect are quantum jumps between the ground states.

7.3 LIMITATIONS

The use of ODF is limited mainly by two contributions. Firstly, when scanning for an unknown transition for a long time, the axial motional mode frequency ω_z drifts and thus the two ODF beams are not resonant to the motional frequency anymore which can reduce the efficiency of the excitation. Secondly, background signals arise from two distinct sources, namely (1) heating which affects the motional state distribution and competes with the displacement, as well as (2) background coupling of the ODF lasers to the $^9Be^+$ ion. These two background effects increase the offset and this the quantum projection noise, which reduces the signal-to-noise ratio.

7.3.1 Axial motional mode frequency stability

The frequency of the OP motional mode ω_z varies over time due to fluctuations of the supplied dc voltage for trapping. For the optimal signal in ODF, the frequency difference of the two beams needs to be equal to the motional frequency ω_z. Any deviation from this leads to a reduction in signal.

To assess the stability of our trap frequency, we measure the axial motional frequency $\omega_z/2\pi \approx 1\,\mathrm{MHz}$, for a single $^9Be^+$ by locking to the motional transition using two-point sampling (Fig. 6.3). For excitation of the motional mode, an oscillating voltage at around ω_z is applied, resulting in a signal similar to what is shown in Fig. 7.2(b).

The data for almost 60 000 s of measurement are shown in Fig. 7.4 alongside its overlapping Allan deviation. The short term stability of the lock is below 10 Hz up to an averaging time of above 1000 s. For longer times a drift is visible with a rate of about 230 Hz per day which could be related to a temperature dependence of the dc voltage supply or thermal relaxation of the trap geometry. For the first 500 s in Fig. 7.4(a), a larger drift rate is visible. This might be due to changes to the dc and rf trapping voltages slightly heating up the system. Such changes are performed since initial loading of a single $^9Be^+$ is conducted at different motional frequencies than spectroscopy to increase the loading rate.

The trapping voltages used for spectroscopy of an Ar^{13+}-$^9Be^+$ crystal are different from theonce used for a single $^9Be^+$. Converting the observed drift rate to a voltage drift, yields 4 mV per day. This converts for the axial OP mode to a drift around 500 Hz per day at the typically employed trap settings.

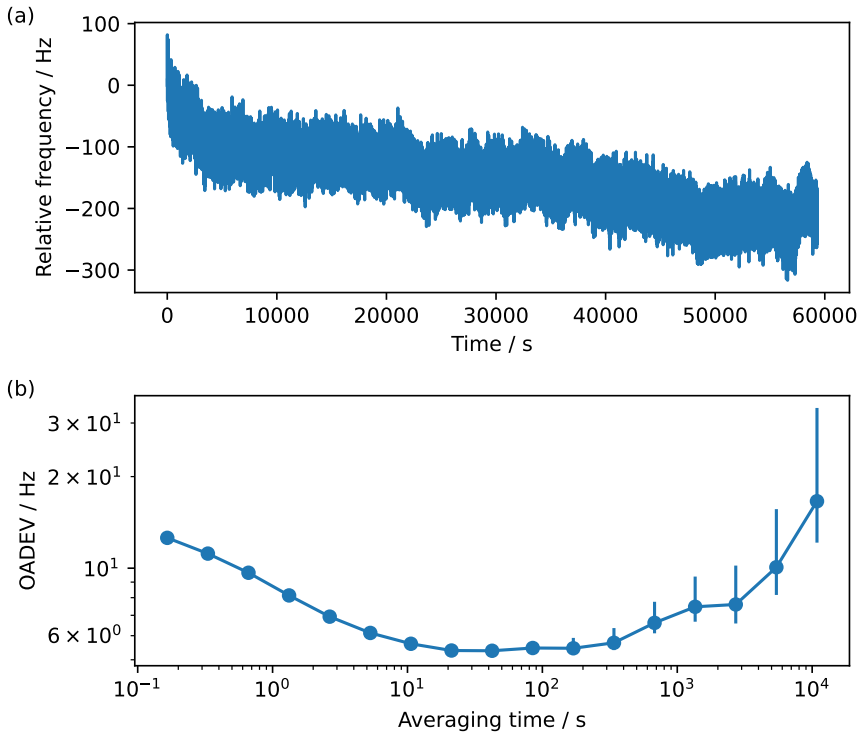

Figure 7.4: Stability of the axial motional mode frequency of a single $^9\mathbf{Be}^+$. The single ion axial motional frequency is $\omega_z/2\pi$ =1 MHz. The data was taken by locking to the motional resonance similar to what is shown in Fig. 7.2(b). (a) Time trace of the measured frequency. (b) Corresponding overlapping Allan deviation (OADEV).

The drift rate needs to be compared to the lineshape of the ODF signal as a function of the relative detuning $\delta^{\mathrm{rel}} = \delta - \omega_z$ from the motional resonance. This is described by (McCormick et al., 2019)

$$P_{\mathrm{exc}}(\delta^{\mathrm{rel}}) = 1 - P(0) = 1 - \exp\left[-2\left(\frac{|\alpha|}{\delta^{\mathrm{rel}} t_{\mathrm{p}}}\right)^2 \left(1 - \cos\left(\delta^{\mathrm{rel}} t_{\mathrm{p}}\right)\right)\right]. \tag{7.122}$$

It therefore directly depends on the resonant ($\delta = 0$) displacement $|\alpha|$ (Eq. (7.114)) and the probe time t_{p}.

A useful value is the linewidth $\delta^{\mathrm{rel}}_{1/2}$ that will occur when scanning the global detuning Δ to search for an unknown transition. For this, a step size of Δ needs to be chosen, which is taken to be the detuning $\Delta^{\mathrm{ODF}}_{1/2}$ where $P_{\mathrm{exc}}(\Delta^{\mathrm{ODF}}_{1/2}) = 0.5$ (see Eq. (7.116)). Then, $\delta^{\mathrm{rel}}_{1/2}$ can numerically be derived from Eq. (7.122) and is well approximated by

$$\delta^{\mathrm{rel}}_{1/2}/2\pi \approx \frac{1.47}{t_{\mathrm{p}}}. \tag{7.123}$$

For a probe time of $t_p = 10\,\text{ms}$, this yields $\delta_{1/2}^{\text{rel}} \approx 147\,\text{Hz}$. Therefore, a recalibration multiple times a day is necessary to maintain an optimal signal for such an interrogation time.

7.3.2 Background signals

The ODF probe time is limited by the heating rate Γ_h as it also affects the Fock state distribution and therefore competes with the ODF displacement. This is apparent, as even without any displacement, the population in the ground state will reduce as it is distributed towards higher Fock states. The increased background signal for longer porbe times reduces the signal-to-noise ratio, making detection of a weak signal difficult.

The signal from a thermal state, assuming initially a perfectly ground-state cooled state and only contributions from anomalous heating is given by (Leibfried et al., 2003)

$$P_{\text{exc}}^{\text{heat}} = 1 - P(0) = \frac{1}{1 + \Gamma_h t}. \tag{7.124}$$

For example, presume that a background signal of 20 % excitation is acceptable. For a heating rate $\Gamma_h = 10\,\text{s}^{-1}$, this would be reached after 25 ms, i.e. the probe time is limited to $t_p \leq 25\,\text{ms}$.

The application of ODF is further limited by background coupling of the laser to the far-off resonant dipole-allowed transition in $^9\text{Be}^+$. The ratio of displacement of $^9\text{Be}^+$ and HCI from the same ODF beams is given by

$$\frac{\alpha_{\text{HCI}}}{\alpha_{\text{Be}}} \approx \frac{\Delta_{\text{Be}}}{\Delta_{\text{HCI}}} \frac{\tau_{\text{Be}} \omega_{\text{Be}}^3}{\tau_{\text{HCI}} \omega_{\text{HCI}}^3} \tag{7.125}$$

where τ_i and ω_i are the lifetime and transition frequency of the transitions the ODF couples dominantly to for the respectively denoted ions. They are used to rescale the on-resonant Rabi frequency $\Omega_i^2 \propto \omega_i^3/\tau_i$ using Fermi's golden rule. Note that this description treats the $^9\text{Be}^+$ as a two level system, which is only a simplification. In the far-off resonant case here, all relevant transitions need to be summed over for an accurate assessment.

As an example, Eq. (7.125) can be estimate for the investigated Ar^{13+}-$^9\text{Be}^+$ crystal. This yields $\alpha_{\text{HCI}}/\alpha_{\text{Be}} \approx 60$ for $\Delta_{\text{HCI}}/2\pi = 10\,\text{MHz}$, where $\tau_{\text{Be}} \approx 8\,\text{ns}$ and $\omega_{\text{Be}}/2\pi \approx 958\,\text{THz}$ were used. While this makes it not relevant for the presented experimental results, it becomes relevant in searches for more narrow transitions.

When searching for a transition in an HCI, the step width needs to be chosen such that at least during one step the signal from the HCI can be distinguished from the background from $^9\text{Be}^+$. Here, we use Ni^{12+} as an example to estimate the maximum scanning step size. Sulphur-like Ni^{12+} has an optical transition at 498 nm with a lifetime

of $\tau_{\mathrm{HCI}} \approx 20\,\mathrm{s}$ (Liang et al., 2021). This system is further discussed in Sec. 9.1. Demanding $\alpha_{\mathrm{HCI}} > \alpha_{\mathrm{Be}}$, leads to

$$\Delta_{\mathrm{HCI}} < 600\ \mathrm{kHz}. \tag{7.126}$$

This poses a comparatively low bound on the step size which scales further down for states with longer lifetime.

This background signal is not a fundamental limit as it, in principle, can be removed by applying an additional displacement with an opposite phase to α_{Be}. This could for example be achieved through an oscillating voltage, instead of ODF. Another factor which needs to be taken into account, at the point where α_{Be} becomes significant, is that the two ions are spatially separated and are experiencing different laser phases at a given time (Wolf et al., 2016). This leads to interference effects, which can be controlled through choice of the ion-ion distance.

7.4 SUMMARY

Insufficient knowledge of the transition frequency of ultranarrow optical transitions in HCI makes it experimentally infeasible to directly search for them using QLS. Additionally, many level structures require optical pumping to have a reliable ground-state population, which is not possible without knowing the transition frequency to a high accuracy. A useful technique to deal with this is the initial-state preserving ODF. In this chapter, it was experimentally demonstrated that ODF allows to broaden an $M1$ transition to 10 MHz linewidths with moderate laser powers making it a potential useful technique for narrow transition searching. Effects which limit the achievable broadening were introduced and discussed.

Part III

CONCLUSIONS AND OUTLOOK

8 SUMMARY

The establishment of optical clocks based on highly charged ions (HCI) has been a long sought goal due to their favourable properties (Kozlov et al., 2018). Over recent years, many of the initial hindrances have been resolved, beginning with the extraction, isolation and sympathetic cooling of individual HCI (Schmöger et al., 2015a,b). Subsequently, quantum logic spectroscopy (Schmidt et al., 2005) was applied to coherently interrogate a dipole-forbidden transition in an HCI with Hz-level resolution (Micke et al., 2020).

Within the here presented work, the first optical clock based on an HCI has been demonstrated. First, the outstanding issue of modes that are only weakly-cooled by the logic ion (Kozlov et al., 2018; Wübbena et al., 2012) was investigated. An algorithmic cooling scheme, similar to QLS, was developed to cool the modes to the ground state. The weak coupling is further exploited to preserve this over extended periods of time, making it suitable for clock operation (King et al., 2021). A characterisation of the experimental setup yielded a fractional systematic uncertainty of 2×10^{-17} (King et al., 2022), similar to many operational optical clocks. The main limitation (excess micromotion) is a technical issue which can be improved to a level below 10^{-18} by employing an improved ion trap. The next largest shift, the probe-laser induced a.c. Zeeman shift, has an uncertainty of 2×10^{-18}. Established techniques can be applied to suppress this to a negligible level. The remaining uncertainties are estimated to be below 10^{-18}. This paves the way for an HCI based optical clock which can compete with the state-of-the-art (Brewer et al., 2019; Huntemann et al., 2016; McGrew et al., 2018) at or below 10^{-18} systematic uncertainty.

Clock operation of the HCI setup was demonstrated by comparing the frequency of the electric-dipole forbidden transition in Ar^{13+} to the well-known frequency of the electric-octupole transition in $^{171}Yb^{+}$. The achieved instability of $3 \times 10^{-14}/\sqrt{\tau}$ is limited by the 10 ms excited state lifetime of the HCI clock and significant improvements can only be achieved by employing an HCI with a longer excited-state lifetime. The frequency ratio was measured for at least 50 000 s for two isotopes ($^{40}Ar^{13+}$ and $^{36}Ar^{13+}$), yielding a statistical uncertainty of 1×10^{-16} in both cases. From this, the absolute frequency of $^{40}Ar^{13+}$ was derived and improved by eight orders of magnitude compared to the best previously published value, making it one of the most precisely known absolute frequencies. Similarly, the isotope shift was improved by nine orders of magnitude, revealing for the first time the QED nuclear recoil effect in a many-electron system (King et al., 2022).

For the future, an HCI with a longer excited-state lifetime $>1\,\mathrm{s}$ is necessary to achieve the statistical uncertainty of state-of-the-art optical clocks, enabling measurements at the limit of the systematic uncertainty. While many such transitions have theoretically been investigated and proposed, only few have been experimentally observed in fluorescence measurements (Bekker et al., 2019). In the absence of this, *ab initio* atomic structure calculations guide searches. Their uncertainty is often too large for identification of the transition using QLS within a feasible timescale. Additionally, optical pumping of the HCI's electronic state is in general not possible before the transition is known with high accuracy.

Therefore, new detection schemes are necessary to make experimental identification possible for a large variety of systems. One technique, using an optical dipole force, was experimentally demonstrated for the magnetic-dipole transition in Ar^{13+}, broadening it by more than two orders of magnitude compared to Rabi excitation. This technique also preserves the initial state, which negates the need for pumping of the internal state.

The applied techniques in this work are universal and so far no fundamental restriction for an optical clock based on an HCI has been identified. This enables a large variety of HCI to be studied as optical clocks, most notably those beneficial for tests of new physics.

9 FUTURE APPLICATIONS OF HCI

With the demonstration of an HCI-based optical clock, a large variety of systems becomes available to metrological applications and for tests of fundamental physics. In the following chapter, some challenges and applications are discussed. Section 9.1 discusses some illustrative examples of ultra-narrow optical transitions in HCI that are within experimental reach. Usage of isotope shifts in HCI to search for new physics using a so-called King plot is presented in Sec. 9.2. The possibility of searching for variations of the fine-structure constant are addressed in Sec. 9.3. Finally, the possibility of an XUV clock is considered in Sec. 9.4.

9.1 CANDIDATES FOR HCI CLOCKS

The limiting feature of the Ar^{13+} clock is the excited-state lifetime of 10 ms (Lapierre et al., 2006). This leads to an instability no better than $1 \times 10^{-14}/\sqrt{\tau}$ for a single Ar^{13+}, even when the dead time can be reduced to a negligible level (Peik et al., 2006). With this instability, it would require multiple years of averaging to approach a statistical uncertainty of 10^{-18}. This can be improved by employing multiple Ar^{13+} ions (Eq. (1.3)), with known algorithms for interrogation (Cui et al., 2022; Schulte et al., 2016). The downside of this approach is that the increased number of motional modes requires longer cooling times to maintain a systematic uncertainty at the 10^{-18} level, in particular due to additional weakly-coupled radial modes (Sec. 4.2). The corresponding increase in dead time likely negates the $\sqrt{N}$-gain from the increased number of Ar^{13+} ions.

Other single ion optical clocks have achieved instabilities of $1 \times 10^{-15}/\sqrt{\tau}$ (Brewer et al., 2019; Sanner et al., 2019) by employing longer probe times, which reaches a statistical uncertainty of 10^{-18} within two weeks of averaging. Therefore, an HCI with a clock transition with excited-state lifetime > 1 s is needed to fully establish HCI-based optical clocks. For this, $M1$ transitions are not suitable as, in the optical regime, they have millisecond-lifetimes. Thus, $E2$ (or higher order) transitions are necessary.

Various candidates have been proposed for this purpose in the literature (Kozlov et al., 2018). Some of these are based on level-crossing transitions, which are particularly sensitive to fundamental physics (Bekker et al., 2019; Berengut et al., 2011; Porsev et al., 2020), but they are experimentally and theoretically hard to control due to

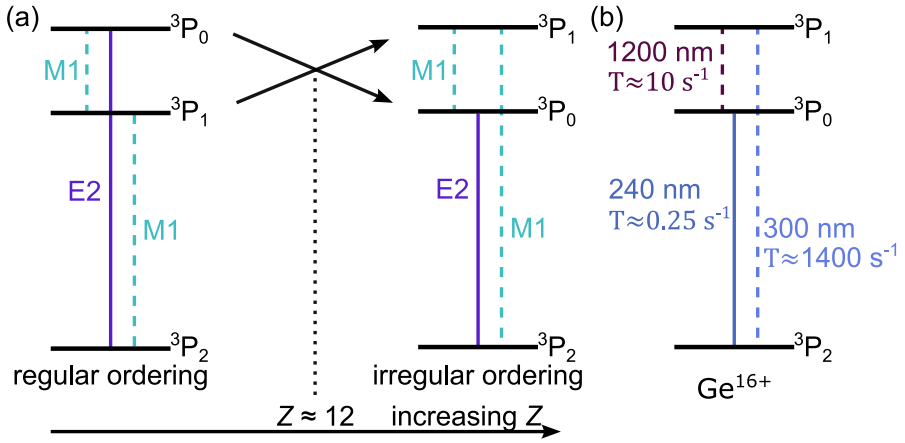

Figure 9.1: Sulphur-like systems. (a) The lowest states of Sulphur-like (S-like) systems are the ^{3}P manifold. For charge states $Z \leq 12$, they exhibit normal ordering (left), where all states can decay to lower lying states through $M1$ transitions with millisecond-lifetimes. For $Z > 12$, the irregular ordering occurs and the $^3P_0$ state can only decay through an $E2$ transition to the ground-state $^3P_2$. This provides a long-lived (> 1 s) clock state (Allehabi et al., 2022). (b) Level structure of S-like Ge^{16+}. Given are the wavelengths and transition rates T. The available magnetic-dipole transitions are at optical wavelengths, which can be observed using an EBIT and a grating spectrometer. Then, Ritz-Rydberg combination can be used to derive the clock transition that has a predicated excited-state lifetime of 4 s. Levels are not to scale. Level structure was taken from Kramida et al., 2021, transition rates from Allehabi et al., 2022; Biémont et al., 1986.

the complexity of the electronic structures. It might be more advisable to investigate simpler electronic structures first, e.g. fine-structure transitions (Allehabi et al., 2022; Yu et al., 2018; Yudin et al., 2014). Here, we will discuss the exemplary case of fine-structure transitions in Sulphur-like systems as well as general comments on the charge-to-mass ratio guiding investigations towards a state-of-the-art optical clock based on an HCI.

9.1.1 Sulphur-like systems

Sulphur-like (S-like) systems possess fine-structure transitions that are promising candidates for optical clocks. Their simple level structures make them also an instructive example showing some challenges for experimental searches of ultra-narrow transitions and potential solutions. The here proposed search schemes are not limited to S-like systems and might find more general applications in similar level structures.

The lowest lying level of S-like systems is the ^{3}P manifold with a level structure depending on the charge state Z as illustrated in Fig. 9.1(a). For low charge states, they exhibit energy ordering monotonic in J (*regular*), i.e. $E\left(^3P_0\right) > E\left(^3P_1\right) > E\left(^3P_2\right)$. This switches to energy ordering non-monotonic in J (*irregular*), i.e. $E\left(^3P_1\right) > E\left(^3P_0\right) > E\left(^3P_2\right)$

for $Z > 12$ (Allehabi et al., 2022). The irregular ordering exhibits a clock transition where the excited $^3P_0$ state can only decay through an electric-quadrupole ($E2$)-transition to the ground state $^3P_2$. The available $m_J = 0 \rightarrow m_J' = 0$ transition is beneficial, as it is to first-order magnetic field insensitive, though it should be noted that the $^3P_2$ state has a non-vanishing quadrupole moment. To cancel the quadrupole shift, it is necessary to average over multiple Zeeman components, like in Ar^{13+} (Sec. 5.2.3), or to probe with varying magnetic field directions (Itano, 2000; Lange et al., 2020). In the following, two specific S-like systems, Ge^{16+} and Ni^{12+}, are discussed.

The first system, Ge^{16+}, has been theoretically investigated by Allehabi et al., 2022 showing many favourable properties for an HCI clock. The electronic structure has an irregular energy ordering of the ^3P-manifold (Fig. 9.1(b)). The clock state $^3P_0$ has a predicted lifetime of 4 s, which is too weak to be directly observable in fluorescence measurements using an EBIT. Instead, a Ritz-Rydberg combination is possible, as both the $^3P_1 \rightarrow {}^3P_0$ and $^3P_2 \rightarrow {}^3P_1$ transition are sufficiently strong optical transitions that can be detected with a grating spectrometer. The Ritz-Rydberg formula for the clock transition is then

$$\nu\left({}^3P_2 \rightarrow {}^3P_0\right) = \nu\left({}^3P_2 \rightarrow {}^3P_1\right) - \nu\left({}^3P_1 \rightarrow {}^3P_0\right), \tag{9.127}$$

where ν is the frequency of the denoted transition. If this has been used to identify the clock with an uncertainty of around 1 GHz, direct detection becomes feasible using ODF (Chapter 7). A downside of Ge^{16+} is that spontaneous emission of the $^3P_1$ state decays with a probability of around 1 % to the $^3P_0$ state. This limits the options of using the $^3P_2 \rightarrow {}^3P_1$ for manipulation of the internal state, as will be discussed below for the case of Ni^{12+}. Instead, it might be useful to repump the clock state through the $^3P_0 \rightarrow {}^3P_1$ transition, where the $^3P_1$ state spontaneously decays to the ground state.

The more interesting S-like system is Ni^{12+}, which has theoretically been investigated by Yu et al., 2018. The level structure is shown in Fig. 9.2. It has regular energy ordering and thus the lowest lying transition is the $M1$-allowed $^3P_2 \rightarrow {}^3P_1$ transition, henceforth called logic transition. The $^3P_0$ clock state lies only ≈ 15 THz above the $^3P_1$ state. This small energy difference suppresses the $^3P_0 \rightarrow {}^3P_1$ transition rate to $0.02\,s^{-1}$ (Liang et al., 2021; Yu et al., 2018), which can be neglected for practical purposes. Through this, the clock transition $^3P_2 \rightarrow {}^3P_0$ is induced. The availability of a clock and separate logic transition in a single system provides appealing opportunities.

The logic transition is an $M1$-allowed transition with a lifetime of 6.5 ms (Yu et al., 2018). Therefore, it can be investigated in a similar way to what has been demonstrated for Ar^{13+}. This provides a stepping stone towards the much weaker clock transition. Once control over the logic transition is established, it can be used to perform fast quantum logic operations, e.g. to optically pump the internal

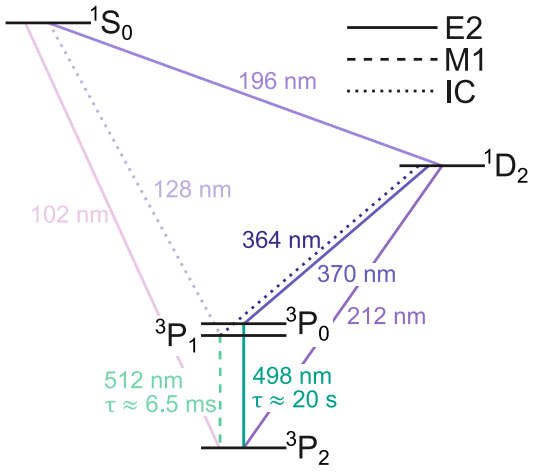

Figure 9.2: Level structure of Ni^{12+}. Shown are all transitions connecting to the ^3P-states with a wavelength >100 nm. Dashed lines indicate *M*1-allowed transitions, while full lines indicate *E*2 transitions. The dotted lines represent intercombination (IC) transitions. Levels are not to scale. Date was taken from Kramida et al., 2021 and Yu et al., 2018.

state (Micke et al., 2020), measure micromotion, apply algorithmic ground-state cooling (Sec. 4.2) or implement quantum non-demolition measurements (Hume et al., 2007). The $^3P_0$ clock state is predicted to have a lifetime of 20 s and the clock transition is expected to exhibit many of the favourable properties of HCI, like a small polarisability and a small quadrupole moment of the $^3P_2$ state (Yu et al., 2018).

The optical spectrum of highly charged Ni has experimentally been investigated within an EBIT using a Czerny-Turner spectrometer by Liang et al., 2021. There, the $^3P_2 \rightarrow {}^3P_1$ logic transition in Ni^{12+} was observed with an uncertainty of 2.3 GHz. This transition can further be narrowed using the initial-state preserving ODF (Chapter 7), where an signal width above 1 MHz is feasible (Chapter 7). This allows detection within a few hours, before employing QLS to coherently control the internal state. The $^3P_2 \rightarrow {}^3P_0$ clock transition is too weak to be detected directly from within a plasma confined inside an EBIT. Ritz-Rydberg combination from other optical lines is not possible due to a lack of sufficiently strong optical transitions connected to the $^3P_0$ clock state (see Fig. 9.2). Theoretical predictions of the transition frequency have currently an uncertainty of ≈ 3 THz (Kramida et al., 2021; Liang et al., 2021; Yu et al., 2018). Even for an unrealistic linewidth of 1 MHz for the clock transition, months of continuous searching are necessary for a direct search employing ODF or QLS.

Therefore, a search scheme using RAP for excitation of the clock transition (Lacour et al., 2007; Noel et al., 2012) in combination with a quantum non-demolition detection on the logic transition (Hume et al., 2007) is proposed. To excite the clock transition, the clock laser is scanned across the expected frequency. For a suitable scanning speed, this leads to adiabatic transfer from the ground to the excited state when crossing the clock transition. The excitation probability of the

clock state using RAP depends on the scanning speed ξ (in units of Hz/s), as (Lacour et al., 2007; Noel et al., 2012)

$$P_e = 1 - \exp\left[\frac{-\Omega^2}{4\xi}\right] \tag{9.128}$$

where it was assumed that laser noise is much smaller than the on-resonant Rabi frequency[1] Ω. To get an excitation probability $P_e > 0.5$, the scanning speed should be $\xi < \Omega^2/(4\ln 2)$. For realistic laser parameters, an on-resonant Rabi frequency $\Omega/(2\pi) = 10\,\mathrm{kHz}$ is achievable, leading to $\xi \lesssim 1.4\,\mathrm{GHz\,s^{-1}}$. With the maximum scanning speed, a 6 THz range is scanned across in about 70 min, though the range needs to be scanned across multiple times to account for the imperfect excitation probability. Assuming that ten scans are performed, a total of 12 h is necessary. A higher laser power reduces this time as the scanning speed scales linearly with it.

To detect the excitation to the clock state, the logic transition can be used as a sensor. For this, it is probed with QLS or the initial-state preserving ODF. If the clock state is excited, the logic transition can no longer be excited. The long excited-state lifetime allows usage of a quantum non-demolition measurement (Hume et al., 2007), reducing the detection error to negligible levels. The detection adds additional time which should be less than 10 % of the above estimate.

With this scheme a detection of the clock state should be possible within an experimentally feasible time. Not included in the estimation is additional time needed for the state detection as well as for technical challenges like tuning a clock laser over such a large frequency range. This scheme can also readily be applied to similar electronic structures, where a logic transitions is available additionally to the clock transition.

9.1.2 Charge-to-mass ratio

The charge-to-mass ratios of the spectroscopy ion (SI) and the logic ion (LI) in the presented experiments differ by a factor ≈ 3. This leads to largely decoupled motional modes in radial direction which were addressed with algorithmic ground-state cooling (Sec. 4.2). This technique is universal and can be applied to any system with similar weak coupling. Alternatively, a close match of charge-to-mass ratio of SI and LI lead to sufficient coupling such that the radial modes can be sympathetically cooled through the LI (Kozlov et al., 2018). Studies of the intermittent regime between strong and weak coupling have not been performed though no fundamental problems are apparent.

1 Laser noise leads to a reduced maximal excitation probability down to 50 % but permits a larger ξ. For a laser locked as described in Sec. 3.6.3, the laser noise is expected to be negligible for the estimated Rabi frequency.

Another effect is that the heating rates scale quadratically with the charge state, making high charge states unfavourable. This can be counteracted by employing an HCI with a large mass, as this suppresses the heating rate inversely and motional shifts in general. For example, the proposed transitions in $^{250}Cf^{15+}$, $^{250}Cf^{16+}$, and $^{250}Cf^{17+}$ (Berengut et al., 2012b; Porsev et al., 2020) would be six times less sensitive to motional shifts than $^{40}Ar^{13+}$. While a high charge state leads to increased heating rates, it also suppresses many external-field shifts, which scale inversely with Z (Berengut et al., 2012a). Therefore to fully exploit the favourable properties of HCI, a significant charge state is necessary. A balance between increased heating rates and suppressed external field shifts might thus provide the lowest possible uncertainty.

9.2 ISOTOPE SHIFTS FOR KING PLOTS

In recent years, measurements of isotope shifts came into focus as a way to test fundamental physics (Berengut et al., 2018; Delaunay et al., 2017b; Fichet, 2018; Flambaum et al., 2018; Frugiuele et al., 2017). The theoretical prediction of the isotope shift is currently far from the experimentally achieved results. Even in the here presented case of a system with only five electrons, the experiment surpasses theory by more than seven orders of magnitude in uncertainty. For systems with more electrons, the calculations are more complex and accurate predictions are out of reach. Additionally, limited knowledge of the nuclear charge radii R, contributes about 40 % (or 1.5 MHz) of the uncertainty in the calculated isotope shift in Ar^{13+} (King et al., 2022). To circumvent both issues, a so-called King plot can be used (King, 1963), where a linear relationship between isotope shifts of two transitions in a given element is expected.

For this, the isotope shift of a transition α in a given element is measured for isotope B relative to a reference isotope A. Equation (2.56) describes this and is rewritten as the so-called modified isotope shift (Yerokhin et al., 2020)

$$\Delta n_B^\alpha := \frac{\Delta\nu_{A,B}^\alpha}{\mu_{i,j}} = K_\alpha + \frac{r_B}{\mu_B} F_\alpha \tag{9.129}$$

where $\mu_B^{-1} = \left(\frac{m_e}{M_A} - \frac{m_e}{M_B}\right)$ is the inverse mass factor. It is calculated from the nuclear masses which are available in literature with typical relative uncertainties around 10^{-9} for stable isotopes (Wang et al., 2021). The difference in charge radii $r_B = \left(\frac{R_A^2}{\lambda\!\!\!^{-2}_C} - \frac{R_B^2}{\lambda\!\!\!^{-2}_C}\right)$ is known less accurately, as the charge radii $R_{A,B}$ are available only with a typical relative uncertainty of around 10^{-4} (Angeli et al., 2013).

Therefore, to eliminate r_B, an additional transition β can be measured such that

$$\Delta n_B^\beta = \left(K_\beta - \frac{F_\beta}{F_\alpha} K_\alpha\right) + \frac{F_\beta}{F_\alpha} \Delta n_B^\alpha. \tag{9.130}$$

This gives a linear relationship between the modified isotope shifts Δn_B^α and Δn_B^β without any additional knowledge of the atomic structure. By measuring at least three isotopes B_i relative to the reference isotope A, the isotope-independent constants K and F can be extracted and the linearity tested. Observed non-linearities can come from higher-order effects neglected in Eq. (2.56) (Flambaum et al., 2018; Yerokhin et al., 2020) or are an indication of new physics (Delaunay et al., 2017b). The higher-order effects can partially be cancelled by employing more than two transitions allowing for more accurate probing (Berengut et al., 2020). Since the amount of narrow transitions in neutral and singly-charged atoms are limited, HCI are interesting as they provide a complementary set of narrow, optical transitions.

Neutral and singly-charged Yb provide many narrow transitions where isotope shifts have been measured by various groups. There, non-linearities with a significance up to 240σ were observed (Hur et al., 2022; Ono et al., 2022), though it was shown that the majority of the non-linearity is not related to new physics but is likely from the deformation of the nucleus (Allehabi et al., 2021; Hur et al., 2022). To improve this, a better understanding of the nuclear effects in Yb is necessary.

Contrary to this, Ca is much lighter than Yb and has a spherical nucleus, providing a system with different characteristics. Five stable, even Ca isotopes (40, 42, 44, 46, 48) exist and the isotope shifts for two S−D transitions in Ca^+ have already been measured with an uncertainty below 30 Hz (Knollmann et al., 2019; Solaro et al., 2020). While a suitable optical transition in neutral Ca exists (Wilpers et al., 2007), no isotope shifts are available in literature. Alternatively, transitions in highly charged Ca can be utilised, where many have been experimentally identified for Ca^{11+} through Ca^{16+} (Rehbehn et al., 2021). The proposed P−P transitions are similar to the investigated transition in Ar^{13+}. Thus they are expected to be measurable in the existing setup with a projected sub-Hertz uncertainty.

9.3 VARIATIONS OF THE FINE-STRUCTURE CONSTANT

The exceptional uncertainties that are achieved with optical clocks and the extreme properties of HCI allow both of them to be used to test fundamental physics. Thus, the combination of both fields promises the possibility to search for new physics in so far unexplored

regimes. An example for testing of fundamental physics is searching for variations of fundamental constants, which is predicted by various theories beyond the standard model (Calmet et al., 2015; Dent et al., 2008; Martins, 2017; Stadnik et al., 2015; Uzan, 2011). Here, we will discuss the specific case of variations of the fine-structure constant α.

A variation of α would manifest in a variation of the transition frequency $\delta\nu$ of a given electronic transitions. This is related by

$$\frac{\delta\nu}{\nu} = K\frac{\delta\alpha}{\alpha} \tag{9.131}$$

where K is the sensitivity of the probed transition. If two transitions with different K are compared, a variation of α would become visible in variations of the frequency ratio (Rosenband et al., 2008). Using this, the most stringent constraints have come from the comparison of the $^{171}Yb^+$ $E2$ and $E3$ clock transitions over multiple years. This yielded temporal variation of $1.0(1.1) \times 10^{-18}$ per year (Lange et al., 2021)[2], consistent with no variation. The transitions have a sensitivity of $K_{E2} \approx 1$ and $K_{E3} \approx -5$, respectively (Flambaum et al., 2009), making this comparison one of the most sensitive one of all clock combinations.

Highly charged ion are prospective candidates to further improve this sensitivity as specific level-crossing transitions have even larger predicted sensitivities $K > 10$ (Berengut et al., 2010; Berengut et al., 2011; Dzuba et al., 2015). Some of the proposed transitions in HCI are given in Tab. 9.1. The calculation of the level structure close to a level crossing is difficult as it occurs due to an accidental near-degeneracy of electronic configurations (Berengut et al., 2010), which leads to uncertainties of around 10 % in the predicted energies. This, combined with the complex electronic structure makes identification using fluorescence spectroscopy difficult and has so far only been achieved in Pr^{9+} (Bekker et al., 2019).

For an optical clock, the complex electronic structure of the involved states is notable. In particular the high angular momentum makes experimental control difficult due to the large number of Zeeman sub-states, requiring extensive pumping of the electronic states. Another issue is the lack of isotopes without nuclear spin ($I = 0$) for some species, e.g. Ir and Pr, which introduces hyperfine structure, further complicating the electronic structure.

9.4 AN EXTREME ULTRAVIOLET CLOCK

State-of-the art single ion optical clocks achieve a statistical uncertainty of around $1 \times 10^{-15}/\sqrt{\tau}$ (Brewer et al., 2019; Sanner et al., 2019),

2 In a recent preprint by the same group, an improved limit of $1.8(2.5) \times 10^{-19}$ per year has been reported (Filzinger et al., 2023)

Species	Transition	K	Wavelength / nm
Pr^{9+} $E2$*	$^3P_0 \rightarrow {}^3F_2$	5.3	408
Pr^{9+} $E3$*	$^3P_0 \rightarrow {}^3G_3$	6.3	452
Ir^{17+}	$^3F_4 \rightarrow {}^1S_0$	145	1978
Ir^{17+}	$^3F_4 \rightarrow {}^3H_6$	−22	283
Cf^{15+}	$^2F_{5/2} \rightarrow {}^4I_{9/2}$	57	812
Sm^{14+}	$^3H_4 \rightarrow {}^3F_3$	−66	2600

Table 9.1: Level-crossing transitions and their sensitivity K to variations of the fine structure constant α. Given are some examples for proposed transitions in HCI with large K. Transitions marked with (*) have experimentally been identified, the uncertainty on the other transitions is typically around 10 %. Further proposed transitions can be found in a recent review by Kozlov et al., 2018 and references therein. Values are taken from Bekker et al., 2019; Berengut et al., 2011; Dzuba et al., 2015; Safronova et al., 2014.

as only a single emitter is employed and due to technical limits of the probe laser coherence. An increase in transition frequency can improve this (Eq. 1.3). Transitions in the extreme ultraviolet (XUV) might therefore be the next step to improve single ion clocks. This became conceivable with the advent of XUV frequency combs, which transfer an optical frequency comb to the XUV regime through high harmonic generation while the coherence is preserved (Gohle et al., 2005; Jones et al., 2005). These systems have since reached a photon energy above 100 eV (wavelength < 12 nm) (Carstens et al., 2016).

The ionisation potential of most neutral and singly charged systems are near-optical and therefore no XUV transitions are available. This is not the case for HCI, where the higher binding energy facilitates many XUV transitions. Consequently, this enables fluorescence spectroscopy of electric dipole-allowed XUV transitions excited by free-electron lasers (Epp et al., 2007). Similar as in optical clocks are electric dipole-forbidden transitions in HCI prospective candidates for an XUV clock (Kozlov et al., 2018). The largest obstacle at the moment is the requirements on the phase noise of the XUV frequency comb. The dominant phase noise comes from the fundamental light, which is quadratically amplified with the harmonic order (Benko et al., 2014). It has been argued that the achievable tooth linewidth in the XUV is limited by the pulse-by-pulse phase jitter and that current stabilisation technology allows for a megahertz tooth linewidth at best (Corsi et al., 2017). This is far too broad for metrological applications and further technical development would be necessary.

Efforts towards an XUV clock are currently ongoing in a related experiment to this work at the Max Planck Institute for Nuclear Physics in Heidelberg (Nauta et al., 2021; Stark et al., 2021).

9.5 SUMMARY

The detection of ultra-narrow optical transitions in HCI remains challenging though for the discussed electric-quadrupole transitions in S-like systems, it is within experimental reach. These are sufficiently narrow to compete with state-of-the-art optical clocks. The application of HCI for tests of fundamental physics is straightforward by employing them for isotope shifts (Rehbehn et al., 2021). This can be done in systems similar to Ar^{13+}, which allows for transfer of many of the established techniques and is currently ongoing. Other tests, like measurements of a potential variation of the fine structure constant α, are promising but require further work for identification and control of the electronic structures close to level crossings (Berengut et al., 2011). Finally, the development of a XUV clock employing HCI has the potential to overcome the statistical limitations of single ion optical clocks, though open questions regarding the phase noise of XUV frequency combs remain.

Part IV

APPENDIX

A HEATING RATE MEASUREMENT

Heating rates of the motional modes of an Ar^{13+}-$^{9}Be^{+}$ two-ion crystal are measured as they induce a second-order Doppler shift (Sec. 5.1.2). For this, the motional mode of interest is ground-state cooled first. Then the system is allowed to heat up for a variable amount of time before measuring the mean phonon number (Turchette et al., 2000) using sideband thermometry (see Eq. (4.66)). For the interrogation, either the Raman transition in $^{9}Be^{+}$ (axial modes and radial IP modes) or QLS of the HCI (radial OP modes) is used. When employing QLS, the axial modes are actively cooled during the wait time through the $^{9}Be^{+}$ to avoid detrimental effects to the quantum-logic readout. For the axial modes and the radial out-of-phase modes measurement, ground-state cooling is achieved using resolved-sideband cooling on the $^{9}Be^{+}$. For the radial in-phase modes measurement, algorithmic ground-state cooling is employed (see Sec. 4.2).

Sideband thermometry requires a thermal distribution to be valid, which for this type of measurements is valid as the heating rate quickly drives the state population to a thermal state (Chen et al., 2017; James, 1998b). The measured temperature as a function of wait time are shown in Fig. A.1 and Fig. A.2 for $^{40}Ar^{13+}$ and $^{36}Ar^{13+}$ respectively. To determine Γ_h, a linear function is fitted to the data.

The presented results are about two to three times lower than what has been reported before for a two-ion crystal in this system (Micke et al., 2020), and similar improvements have been achieved for the single ion heating rate compared to previous measurements (Leopold et al., 2019). This is due to various improvements to the rf and dc voltage supplies for the Paul trap, including installation of baluns in the rf and dc circuitry to prevent ground loops, additional filtering and better shielded cables.

The large difference in heating rate between OP and IP modes in radial direction (x/y) is mostly due to the single ion heating rate scaling quadratically with the charge state Z (Eq. (5.77)) leading to much larger heating rates for HCI. Since the x- and y-modes are only weakly coupled (see Sec. 4.2), this effect is pronounced, though it is partially counteracted by the increase in motional frequency. By accounting for difference in charge and mass of the ions, the heating rate scaling (α_h) with the motional frequency $\omega^{-\alpha_h}$ can be deduced. This yields $\alpha_h \approx 1.2$ to $\alpha_h \approx 1.7$ depending on the motional mode and isotope. Further investigations are hindered as the applied rf power is limited due to technical reasons. Understanding of electric-field noise scaling is an active field of research and will not be discussed here, as

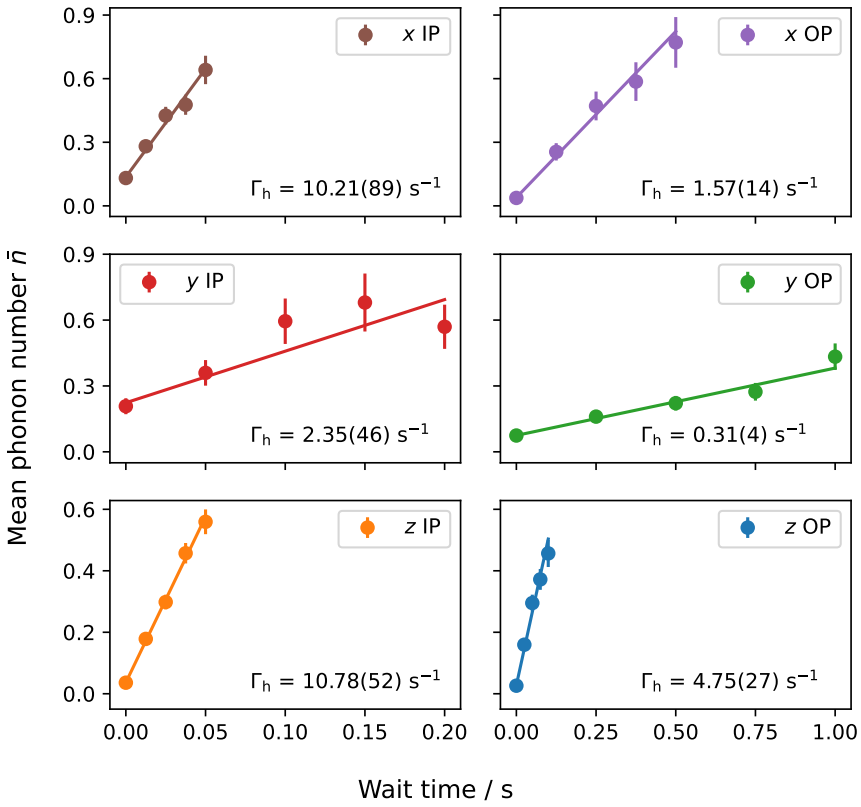

Figure A.1: Heating rates of $^{40}Ar^{13+}$. The mean phonon number ($\bar{n}$) of a given motional mode is measured after a variable wait time. This yields the heating rate Γ_h for all motional modes of the $^{40}Ar^{13+}$-$^{9}Be^{+}$ two-ion crystal. Mind the different time scales in the left and right column. Details are given in the main text. Abbreviations: IP: in-phase, OP: out-of-phase.

the data is insufficient to draw any conclusions. For a recent review of the topic see Brownnutt et al., 2015.

An interesting result is that the heating rates in the x-direction are up to five times larger than in y-direction. From Eq. (2.11) it can be seen that the motional frequency in x-direction only depends on the rf voltage, while in y-direction the dc potential also contributes. Naïvely, this would imply that the y-mode should have an additional noise contribution, which is contrary to the observed heating rates. A possible explanation is the geometric orientation of the modes, where the x-mode lies along the line connecting the dc blades (see Fig. 2.1). Differential noise between the dc blades would lead to a dipole predominantly affecting the x-mode, while the y-mode is only affected by the higher-order quadrupole. Attempts to filter the dc voltages further outside of vacuum did not show any improvement, implying that the differential noise is originating in-vacuum, e.g. by crosstalk of the long wires. Improved filtering close to the Paul trap could reveal if this is the source.

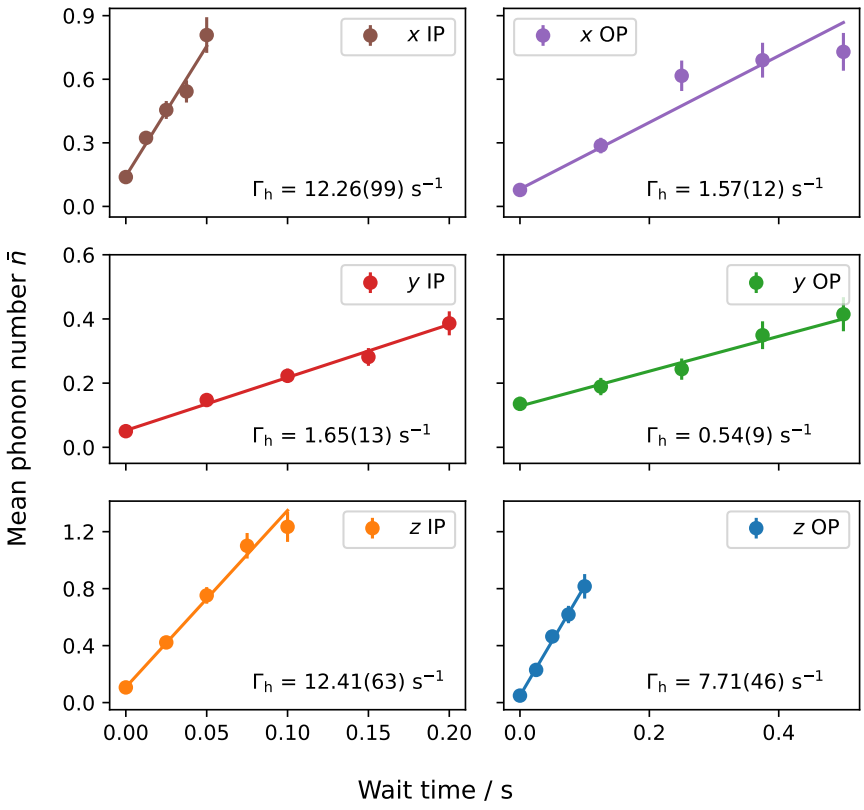

Figure A.2: Heating rates of $^{36}Ar^{13+}$. The mean phonon number ($\bar{n}$) of a given motional mode is measured after a variable wait time. This yield the heating rate Γ_h for all motional modes of the $^{36}Ar^{13+}$-$^{9}Be^{+}$ two-ion crystal. Mind the different time scales in the left and right column. Details are given in the main text. Abbreviations: IP: in-phase, OP: out-of-phase.

B THIRD-ORDER PERTURBATION THEORY OF THE ION MOTION

Commonly a second-order expansion of the Coulomb interaction of a two-ion crystal is used to describe the coupled motion. This leads to a harmonic motion as shown in Sec. 2.1.3. Higher order expansions contribute less to the overall motion but they can introduce mixing terms for different spatial dimensions.

Assuming a two-ion crystal aligned along the z-axis, Eq. (2.22) can be expanded further around the equilibrium position $\vec{x}^0$ of the two ions

$$\begin{aligned}\frac{1}{r} \approx \frac{1}{d} - \frac{(x_1-x_2)^2}{2d^3} - \frac{(y_1-y_2)^2}{2d^3} + \frac{(z_1-z_2)^2}{d^3} \\ + \frac{(z_1-z_2)^3}{2d^4} + \frac{x_1^2(z_1-z_2)+x_2^2(z_1-z_2)}{2d^4} \\ + \frac{y_1^2(z_1-z_2)+y_2^2(z_1-z_2)}{2d^4} + ...\end{aligned} \tag{B.132}$$

with the same definitions as used in Sec. 2.1.3. The first line has already been discussed in Sec. 2.1.3 and will not be discussed here again. In essence, it leads to coupling of the two ions in each spatial dimension though no mixing of different directions occurs at this order.

The transformation into the coupled eigensystem is linear and as there is no mixing, the third order terms, when treated as a perturbation, are proportional to z^3, x^2z, and y^2z. This leads to additional modes of the motion at the frequencies

$$x: \quad \omega_x \pm \omega_z \tag{B.133}$$

$$y: \quad \omega_y \pm \omega_z \tag{B.134}$$

$$z: \quad 2\omega_{x/y} \tag{B.135}$$

where ω_u can be either the IP or OP mode.

C INSTABILITY ANALYSIS

The expected instability σ of the Ar^{13+} clock can be estimated analytically and numerically based on the experimental parameters. In the following this will be examined and indications are found that for a laser linewidth of about 10 Hz. The discussion is restricted to $^{40}Ar^{13+}$ as more data is available for this isotope.

In an ideal case, the instability using Rabi excitation is described by (Peik et al., 2006)

$$\sigma(\tau) = \sqrt{\frac{p}{2}\left(1-\frac{p}{2}\right)}\frac{\Delta\nu}{p\nu_0}\sqrt{\frac{T_c}{\tau}}, \tag{C.136}$$

where τ is the averaging time, p is the peak excitation, $\Delta\nu \approx 53$ Hz is the full width at half maximum (FWHM) linewidth, $\nu_0 \approx 679.216$ THz is the transition frequency, and $T_c \approx 55$ ms is the total cycle time including state preparation, clock interrogation, and state detection. The excitation probability at the probe points is recorded during clock operation and is experimentally determined to be $p_{1,4} \approx 0.5$ for transition 1 and 4, and $p_{2,3} \approx 0.4$ for transition 2 and 3 with the numbering given in Fig. 5.4. The lower excitation probability of transition 2 and 3 is attributed to decay of their excited state to a dark state, which does not occur for the closed transitions 1 and 4 (see Fig. 5.4). With these numbers an instability of better than $2 \times 10^{-14}/\sqrt{\tau}$ is expected, which is lower than the achieved $3.2 \times 10^{-14}/\sqrt{\tau}$. In the following, some reasons for this are discussed.

The first effect not included in Eq. (C.136) is the heating rate, which affects QLS efficiency. Ground-state cooling occurs before the clock pulse, where for simplicity it is assumed that all population is in the motional ground state ($P(n=0, t=0) = 1$). After the probe pulse, the heating rate $\Gamma_h \approx 5\,s^{-1}$ reduces the motional ground-state population to (Eq. 2.55)

$$P(0, t_p) = \frac{1}{1+\Gamma_h t_p} \approx 0.93 \tag{C.137}$$

which has two relevant, distinct effects. Firstly, it leads to a background signal of $8-9\,\%$, where the finite temperature after ground-state cooling is accounted for in addition to the heating rate. Secondly, the quantum-logic transfer is affected, as the population outside the ground state contributes significantly less to the overall signal. Both of these effects combined lead to a lower signal-to-noise ratio during interrogation. It can be counteracted by actively ground-state cooling the motional mode during the clock pulse using resolved-sideband

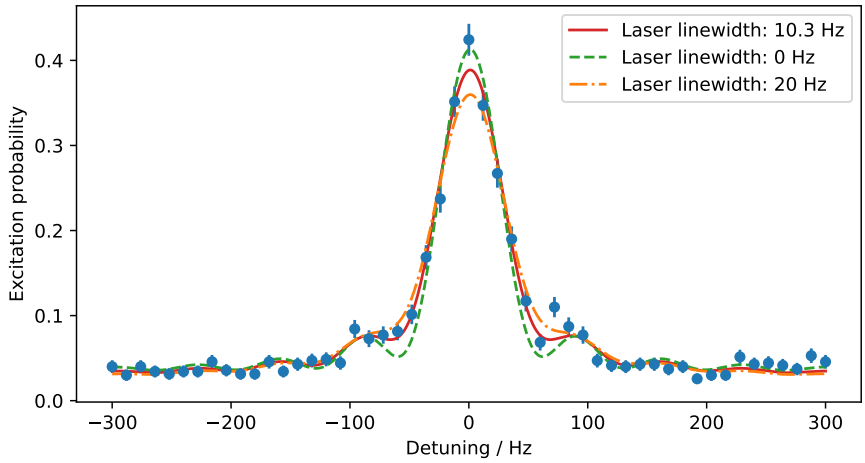

Figure C.1: Lineshape for Rabi interrogation of Ca^{14+}. The transition was probed for $t_p = 15\,\text{ms}$ with an on-resonant Rabi frequency $\Omega \approx \pi/t_p$. During the interrogation, the axial modes of the two-ion crystal were actively ground-state cooled using resolved-sideband cooling on the $^9Be^+$. The lineshape is calculated using the optical Bloch equations including the excited-state lifetime of 10.9 ms. The frequency noise on the laser is modelled as white frequency noise (Peik et al., 2006). For fitting to the experimental data (blue dots), the laser linewidth, an amplitude scaling factor and an background offset are free parameters. The best fit (red) yields a laser linewidth of 10.3(18) Hz with a reduced chi-squared $\chi^2_{\text{red}} = 1.17$. For comparison, the result for fixed laser linewidths of 0 Hz (green, dashed, $\chi^2_{\text{red}} = 1.96$) and 20 Hz (orange, dotted, $\chi^2_{\text{red}} = 1.62$) are shown.

cooling on the $^9Be^+$. This is possible to achieve without inducing an a.c. Stark shift of the clock transition due to the low polarisability of the HCI (Sec. 5.2.1). Additional ground-state cooling after the clock interrogation is also possible but would require milliseconds, which reduces the contrast as the excited state decays with its lifetime of only 9.6 ms.

Another influence is the finite laser linewidth. To estimate the laser linewidth, scans across the transitions are used. The measured lineshape depends on the laser linewidth and are modelled by numerically solving the optical Bloch equations where the excited-state lifetime of 9.6 ms and the finite laser linewidth, modelled as white laser frequency noise, are included (Peik et al., 2006). For Ar^{13+}, the linewidth can be bounded to be below 20 Hz by comparing experimental lineshapes to numerically derived ones. Lower bounds are challenging as all transitions are affected by the magnetic field instability, making the result ambiguous.

As an alternative, a laser used to interrogate the $^3P_0 \rightarrow {}^3P_1$ transition in highly charged Ca^{14+} at 570 nm with an excited-state lifetime of 10.9 ms is investigated as it is employed in current experiments (Wilzewski, 2023). The usage of Ca^{14+} has the advantage that the magnetic-field insensitive $m_J = 0 \rightarrow m'_J = 0$ transition can be probed,

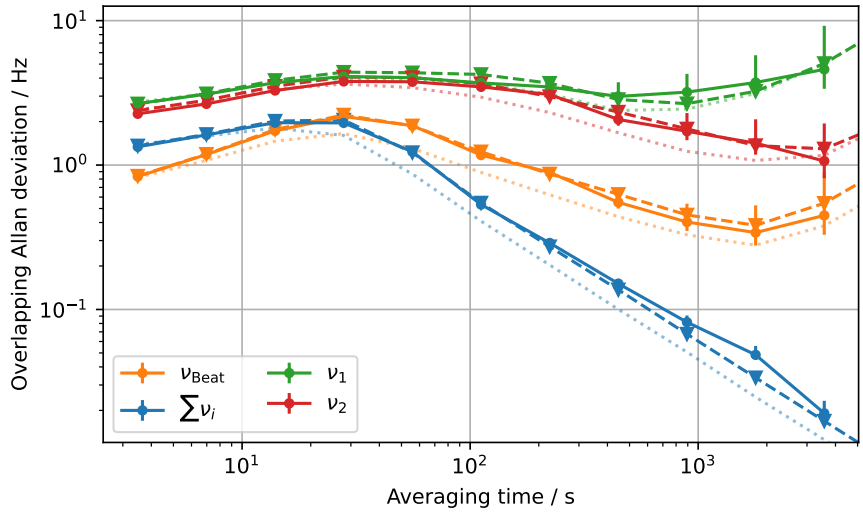

Figure C.2: Comparison between simulated and experimental clock operation. The experimental data (circles, full line) from $^{40}Ar^{13+}$ which is also given in Fig. 6.4 is shown. It is compared to simulations, which are performed as described in the main text. Either a 0 Hz (dotted line) or 10 Hz (triangles, dashed line) laser linewidth are assumed. Only the latter reproduces the experimental data. The overlapping Allan deviations were calculate from 20 000 s of experimental and 350 000 s of simulated frequency data for each laser linewidth.

removing the largest ambiguity when compared to Ar^{13+}. The locking scheme of this clock laser is similar to the here presented clock laser (Sec. 3.6.3) with the only difference being that a pre-stabilisation cavity with a much higher finesse is employed. The beam delivery to the ion has been reused from Ar^{13+} and is therefore identical (Fig. 3.6). Comparing experimental lineshapes of this transition to numerical derived ones, yields a best fit for a laser linewidth of 10.3(18) Hz as shown in Fig. C.1. For comparisons a negligible linewidth and a laser linewidth of 20 Hz are shown, which a potential deviate from the experimental data. Due to the high similarity between the setups, a similar linewidth is conceivable for the Ar^{13+} clock laser.

Finally, the clock operation of Ar^{13+} is simulated and is compared to the experimental data. In the simulation, the ion response is assumed to have ideal quantum projection noise (Itano et al., 1993). The lineshape is derived from numerical integration of the optical Bloch equations, where a laser linewidth is added additionally to decoherence from the excited-state lifetime of 9.6 ms. The laser linewidth was assumed to be either negligible or 10 Hz. The probe time is set to the experimental value of $t_\mathrm{p} = 15$ ms and the on-resonant Rabi frequency is set to $\Omega = \pi/t_\mathrm{p}$. The lineshape is offset by 0.08 to account for background from heating rates, and an amplitude factor is chosen such that the simulated mean excitation is close to experimentally recorded values. Further, a magnetic field flicker floor of 0.11 nT, a

magnetic field drift rate of 7 nT per day, and a laser drift rate of 12 Hz per day are included. These three parameters are close to experimentally expected values, but were fine-tuned by hand to reproduce the experimental data. Their exact value mostly affects the instability of the individual transitions (magnetic field) and the long term drift (laser drift), but does not affect the more important white noise limit of the clock output ν_{Beat} at intermittent timescales 100–1000 s.

The result of the simulation is compared to the experiment through their overlapping Allan deviations, which is shown in Fig. C.2. The simulation reproduces the experimental data well for a laser linewidth of 10 Hz. Neglecting the laser linewidth leads to large deviations. Despite this, it cannot unambiguously be shown that this assumption is true with the available data. It is also possible that other line broadening effects lead to the apparent laser linewidth, e.g. larger than expected low-frequency vibrations of the cryogenic system (Micke et al., 2019). To resolve this, a direct measurement of the laser linewidth is desirable, which can be achieved by comparing it to an independent ultra-stable laser.

D DATA PROCESSING

Within the frequency chain, in many cases, two independent tracking oscillators are employed for the Ar^{13+} experiment. Their free-running frequencies are oppositely detuned from their reference and different gain settings are employed. They are counted independently with a sampling frequency of 1 s and their counted frequencies typically agree at the mHz level. A cycle slip is detected by comparing the two counted frequencies and applying a 0.1 Hz threshold on their difference. This is smaller than the 1 Hz jump that occurs for a 2π cycle slip. In some cases only a single frequency counter was used. Then, the counted frequencies were compared to their fixed, nominal frequency and a 0.1 Hz threshold was applied to detect faults. This is between 5 and 100 larger than the maximally observed fluctuations during normal operation. Additionally, the down modulated beat from the frequency comb was compared to the reference frequency ν_{Ref} (Fig. 3.7) to identify spurious jumps in laser frequency due to loss of phase lock to the Si2-stabilised laser. If any deviation from the nominal values were observed, the data was removed with an additional 2 s before the fault to account for synchronisation differences between different laboratories as well as 30 s afterwards, which corresponds to the servo response time.

Additionally, unexpected large changes of the magnetic field lead in some cases to loss of servo lock to one or multiple of the Zeeman components. Such events were manually identified and data was removed in its vicinity.

CURRICULUM VITAE

Personal data

Name	Lukas Josef Spieß
Year of birth	1993
Place of birth	Wangen im Allgäu
Nationality	German

Employment

02/2017 – 05/2017	Student assistant, Ruprecht-Karls-Universität Heidelberg
10/2015 – 01/2016	Student assistant, Ruprecht-Karls-Universität Heidelberg

Education

02/2019 – today	PhD student QUEST - Institute for experimental quantum metrology, Physikalisch-Technische Bundesanstalt, Braunschweig Group of Prof. Dr. Piet O. Schmidt
10/2016 – 10/2018	Master of Science in physics Ruprecht-Karls-Universität Heidelberg Master thesis: „Setup of a vibration-suppressed cryogenic system for a RF ion trap with minimum micromotion“ Group of PD Dr. José R. Crespo López-Urrutia
10/2013 – 10/2016	Bachelor of Science in physics Ruprecht-Karls-Universität Heidelberg Bachelor thesis: „Computer simulations on cellular Potts model“ Group of Prof. Dr. Ulrich Schwarz
06/2013	Abitur, Edith-Stein Schule, Ravensburg

Publications

Authors contributing equally are marked in bold.

- **S. A. King**, **L. J. Spieß**, P. Micke, A. Wilzewski, T. Leopold, E. Benkler, R. Lange, N. Huntemann, A. Surzhykov, V. A. Yerokhin, J. R. Crespo López-Urrutia, and P. O. Schmidt (2022). "An optical atomic clock based on a highly charged ion." *Nature* 611, pp. 43–47. DOI: 10.1038/s41586-022-05245-4

- S. A. King, L. J. Spieß, P. Micke, A. Wilzewski, T. Leopold, J. R. Crespo López-Urrutia, and P. O. Schmidt (2021). "Algorithmic Ground-State Cooling of Weakly Coupled Oscillators Using Quantum Logic." *Physical Review X* 11, p. 041049. DOI: 10.1103/PhysRevX.11.041049

- J. Stark, C. Warnecke, S. Bogen, S. Chen, E. A. Dijck, S. Kühn, M. K. Rosner, A. Graf, J. Nauta, J.-H. Oelmann, L. Schmöger, M. Schwarz, D. Liebert, L. J. Spieß, S. A. King, T. Leopold, P. Micke, P. O. Schmidt, T. Pfeifer, and J. R. Crespo López-Urrutia (2021). "An ultralow-noise superconducting radio-frequency ion trap for frequency metrology with highly charged ions." *Review of Scientific Instruments* 92, p. 083203. DOI: 10.1063/5.0046569

- **P. Micke**, **T. Leopold**, **S. A. King**, E. Benkler, L. J. Spieß, L. Schmöger, M. Schwarz, J. R. C. López-Urrutia, and P. O. Schmidt (2020). "Coherent laser spectroscopy of highly charged ions using quantum logic." *Nature* 578, pp. 60–65. DOI: 10.1038/s41586-020-1959-8

- P. Micke, J. Stark, S. A. King, T. Leopold, T. Pfeifer, L. Schmöger, M. Schwarz, L. J. Spieß, P. O. Schmidt, and J. R. Crespo López-Urrutia (2019). "Closed-cycle, low-vibration 4 K cryostat for ion traps and other applications." *Review of Scientific Instruments* 90, p. 065104. DOI: 10.1063/1.5088593

Braunschweig, May 15, 2023

ACKNOWLEDGMENTS

The results of this thesis would not have been possible without the contributions of many people.

First I would like to thank my supervisor Piet O. Schmidt, who despite his tight schedule, was always available when necessary. Your expertise and vision for the project are invaluable. I also appreciate the trust we were granted to independently explore the experiment. Also thanks to Ekkehard Peik and Klemens Hammerer to be examiners at my PhD Defense, and David Leibrandt for agreeing to referee this thesis.

A special thanks to Steven King, who managed to project for many years. Without your vast knowledge regarding anything with clocks and lasers non of this would have been possible. Your enthusiasm was always motivating and I have learnt more from you than I could have imagined beforehand. Thanks also to the original team members Peter Micke and Tobias Leopold, who built large parts of the setup. While our work together was limited, I learnt many things from you. Also thanks to the new team, Alexander Wilzewski, Malte Wehrheim, and Shuying Chen, who have taken over seamless and are producing nice results. Thanks to you for all the enjoyable time in out of the lab.

Thanks to José R. Crespo Urrutia-López and his group at the MPIK in Heidelberg. Despite the limited amount of meetings that were possible, it was always a pleasure to meet with you. I am sure that your setup will continue to generate amazing results and that the collaboration will continue to be fruitful.

Thanks also to the other projects in Laue-Bau with their current and former members. The iQLOC I and II teams, Johannes Kramer, Fabian Dawel, Marek Hild, Lennart Pelzer, Ludwig Krinner, and Kai Dietze as well as the Difcos team, Fabian Wolf, Max Zawierucha, and Till Rehmert. Thanks to TIQE, Henning Hahn, Giorgio Zarantonello, Nico Pulido-Mateo, Hardik Mendpara, and Markus Duwe with whom we shared the responsibility for the Be^+ lasers. You did not only lend large amounts of equipment but also provided many (non-)scientific discussions.

Thanks to Andrey Surzhykov for explaining many theoretical concepts in a way that an experimentalist could grasp them. Your various calculations, especially your isotope shift calculations together with Vladimir Yerokhin, were invaluable for the impact of the project.

My thanks to Erik Benkler for his continuous work on the frequency combs, their maintenance and the surrounding infrastructure. This was invaluable for laser stabilisation and for clock comparison. The frequency comparison would not have been possible without the

work and expertise of the Yb^+ clock team, Richard Lange and Nils Huntemann.

For the proof reading I thank Steven, Lennart, Alex, and Malte and especially Shuying who spent endless hours reading this thesis. You have spotted many issues and unclear descriptions which helped improve the thesis a lot.

Thanks for the help with administrative issues to Sandra Ludwig, Sina Bußmann, and Birgit Ohlendorf. Your help was invaluable for many of the bureaucratic problems. For technical support, building management and work safety I would like to thank Leroy Paulmann and Andre Uhde and for help with any electronic issue, I thank David Weber and Lasse Anders. You provided many devices central to the experimental system.

Finally, thanks to my family and friends for the continuous support. You provided me welcome balance by providing non-scientific distractions at home and elsewhere.

BIBLIOGRAPHY

Agababaev, V. A., D. A. Glazov, A. V. Volotka, D. V. Zinenko, V. M. Shabaev, and G. Plunien (2018). "Ground-state g factor of middle-Z boronlike ions." *Journal of Physics: Conference Series* 1138, p. 012003. DOI: 10.1088/1742-6596/1138/1/012003 (cit. on pp. 110, 113).

Agababaev, V. A., D. A. Glazov, A. V. Volotka, D. V. Zinenko, V. M. Shabaev, and G. Plunien (2019). "g factor of the $[(1s)^2(2s)^22p]^2P_{3/2}$ state of middle-Z boronlike ions." *X-Ray Spectrometry* 1-6. DOI: 10.1002/xrs.3074 (cit. on pp. 36, 110, 111, 113).

Akerman, N. and R. Ozeri (2018). "Atomic combination clocks." *New Journal of Physics* 20, p. 123026. DOI: 10.1088/1367-2630/aaf4cb (cit. on p. 86).

Allan, D. (1987). "Time and Frequency (Time-Domain) Characterization, Estimation, and Prediction of Precision Clocks and Oscillators." *IEEE Transactions on Ultrasonics, Ferroelectrics, and Frequency Control* 34, pp. 647–654. DOI: 10.1109/T-UFFC.1987.26997 (cit. on p. 4).

Allehabi, S. O., S. M. Brewer, V. A. Dzuba, V. V. Flambaum, and K. Beloy (2022). "High-accuracy optical clocks based on group-16-like highly charged ions." *Physical Review A* 106, p. 043101. DOI: 10.1103/PhysRevA.106.043101 (cit. on pp. 115, 134, 135).

Allehabi, S. O., V. A. Dzuba, V. V. Flambaum, and A. V. Afanasjev (2021). "Nuclear deformation as a source of the nonlinearity of the King plot in the Yb^+ ion." *Physical Review A* 103, p. L030801. DOI: 10.1103/PhysRevA.103.L030801 (cit. on p. 139).

Angeli, I. and K. P. Marinova (2013). "Table of experimental nuclear ground state charge radii: An update." *Atomic Data and Nuclear Data Tables* 99, pp. 69–95. DOI: 10.1016/j.adt.2011.12.006 (cit. on p. 138).

Arapoglou, I., A. Egl, M. Höcker, T. Sailer, B. Tu, A. Weigel, R. Wolf, H. Cakir, V. A. Yerokhin, N. S. Oreshkina, V. A. Agababaev, A. V. Volotka, D. V. Zinenko, D. A. Glazov, Z. Harman, C. H. Keitel, S. Sturm, and K. Blaum (2019). "g-factor of Boronlike Argon $^{40}Ar^{13+}$." *Physical Review Letters* 122, p. 253001. DOI: 10.1103/PhysRevLett.122.253001 (cit. on pp. 36, 111, 113).

Arnold, K. J., R. Kaewuam, S. R. Chanu, T. R. Tan, Z. Zhang, and M. D. Barrett (2020). "Precision Measurements of the $^{138}Ba^+$ $6s^2S_{1/2} - 5d^2D_{5/2}$ Clock Transition." *Physical Review Letters* 124, p. 193001. DOI: 10.1103/PhysRevLett.124.193001 (cit. on p. 110).

Arnold, K. J., R. Kaewuam, A. Roy, T. R. Tan, and M. D. Barrett (2018). "Blackbody radiation shift assessment for a lutetium ion clock." *Nature Communications* 9, pp. 1–6. DOI: 10.1038/s41467-018-04079-x (cit. on p. 85).

Barontini, G., L. Blackburn, V. Boyer, F. Butuc-Mayer, X. Calmet, J. R. Crespo López-Urrutia, E. A. Curtis, B. Darquié, J. Dunningham, N. J. Fitch, E. M. Forgan, K. Georgiou, P. Gill, R. M. Godun, J. Goldwin, et al. (2022). "Measuring the stability of fundamental constants with a network of clocks." *EPJ Quantum Technology* 9, p. 12. DOI: 10.1140/epjqt/s40507-022-00130-5 (cit. on p. 9).

Bauch, A., S. Weyers, D. Piester, E. Staliuniene, and W. Yang (2012). "Generation of UTC(PTB) as a fountain-clock based time scale." *Metrologia* 49, p. 180. DOI: 10.1088/0026-1394/49/3/180 (cit. on p. 48).

Baynham, C. F. A., E. A. Curtis, R. M. Godun, J. M. Jones, P. B. R. Nisbet-Jones, P. E. G. Baird, K. Bongs, P. Gill, T. Fordell, T. Hieta, T. Lindvall, M. T. Spidell, and J. H. Lehman (2018a). "Measurement of differential polarizabilities at a mid-infrared wavelength in $^{171}Yb^{+}$." *arXiv:1801.10134 [physics.atom-ph]*. DOI: 10.48550/ARXIV.1801.10134 (cit. on p. 84).

Baynham, C. F. A., R. M. Godun, J. M. Jones, S. A. King, P. B. R. Nisbet-Jones, F. Baynes, A. Rolland, P. E. G. Baird, K. Bongs, P. Gill, and H. S. Margolis (2018b). "Absolute Frequency Measurement of the Optical Clock Transition in with an Uncertainty of Using a Frequency Link to International Atomic Time." *Journal of Modern Optics* 65, pp. 585–591. DOI: 10.1080/09500340.2017.1384514 (cit. on pp. 96, 108).

Beeks, K., T. Sikorsky, T. Schumm, J. Thielking, M. V. Okhapkin, and E. Peik (2021). "The thorium-229 low-energy isomer and the nuclear clock." *Nature Reviews Physics* 3, pp. 238–248. DOI: 10.1038/s42254-021-00286-6 (cit. on p. 7).

Beiersdorfer, P., A. L. Osterheld, J. H. Scofield, J. R. Crespo López-Urrutia, and K. Widmann (1998). "Measurement of QED and Hyperfine Splitting in the $2s_{1/2}$- $2p_{3/2}$ X-Ray Transition in Li-like $^{209}Bi^{80+}$." *Physical Review Letters* 80, pp. 3022–3025. DOI: 10.1103/PhysRevLett.80.3022 (cit. on p. 10).

Bekker, H., A. Borschevsky, Z. Harman, C. H. Keitel, T. Pfeifer, P. O. Schmidt, J. R. C. López-Urrutia, and J. C. Berengut (2019). "Detection of the 5p – 4f orbital crossing and its optical clock transition in Pr^{9+}." *Nature Communications* 10, p. 5651. DOI: 10.1038/s41467-019-13406-9 (cit. on pp. 8, 115, 132, 133, 140, 141).

Benkler, E., B. Lipphardt, T. Puppe, R. Wilk, F. Rohde, and U. Sterr (2019). "End-to-end topology for fiber comb based optical frequency

transfer at the 10^{-21} level." *Opt. Express* 27, pp. 36886–36902. DOI: 10.1364/OE.27.036886 (cit. on p. 107).

Benko, C., T. K. Allison, A. Cingöz, L. Hua, F. Labaye, D. C. Yost, and J. Ye (2014). "Extreme ultraviolet radiation with coherence time greater than 1 s." *Nature Photonics* 8, pp. 530–536. DOI: 10.1038/nphoton.2014.132 (cit. on p. 141).

Berengut, J., V. Dzuba, and V. Flambaum (2010). "Enhanced Laboratory Sensitivity to Variation of the Fine-Structure Constant using Highly Charged Ions." *Physical Review Letters* 105, p. 120801. DOI: 10.1103/PhysRevLett.105.120801 (cit. on p. 140).

Berengut, J. C., V. A. Dzuba, V. V. Flambaum, and A. Ong (2011). "Electron-Hole Transitions in Multiply Charged Ions for Precision Laser Spectroscopy and Searching for Variations in α." *Physical Review Letters* 106, p. 210802. DOI: 10.1103/PhysRevLett.106.210802 (cit. on pp. 8, 9, 133, 140–142).

Berengut, J. C., V. A. Dzuba, V. V. Flambaum, and A. Ong (2012a). "Highly charged ions with $E1$, $M1$, and $E2$ transitions within laser range." *Physical Review A* 86, p. 022517. DOI: 10.1103/PhysRevA.86.022517 (cit. on pp. 8, 9, 83, 85, 88, 115, 138).

Berengut, J. C., V. A. Dzuba, V. V. Flambaum, and A. Ong (2012b). "Optical Transitions in Highly Charged Californium Ions with High Sensitivity to Variation of the Fine-Structure Constant." *Physical Review Letters* 109, p. 070802. DOI: 10.1103/PhysRevLett.109.070802 (cit. on p. 138).

Berengut, J. C., D. Budker, C. Delaunay, V. V. Flambaum, C. Frugiuele, E. Fuchs, C. Grojean, R. Harnik, R. Ozeri, G. Perez, and Y. Soreq (2018). "Probing New Long-Range Interactions by Isotope Shift Spectroscopy." *Physical Review Letters* 120, p. 091801. DOI: 10.1103/PhysRevLett.120.091801 (cit. on p. 138).

Berengut, J. C., C. Delaunay, A. Geddes, and Y. Soreq (2020). "Generalized King linearity and new physics searches with isotope shifts." *Physical Review Research* 2, p. 043444. DOI: 10.1103/PhysRevResearch.2.043444 (cit. on p. 139).

Berkeland, D. J., J. D. Miller, J. C. Bergquist, W. M. Itano, and D. J. Wineland (1998). "Minimization of ion micromotion in a Paul trap." *Journal of Applied Physics* 83, pp. 5025–5033. DOI: 10.1063/1.367318 (cit. on pp. 13, 14, 16, 80).

Biémont, E. and J. E. Hansen (1986). "Forbidden Transitions in $3p^4$ and $4p^4$ Configurations." *Physica Scripta* 34, p. 116. DOI: 10.1088/0031-8949/34/2/005 (cit. on p. 134).

Bothwell, T., D. Kedar, E. Oelker, J. M. Robinson, S. L. Bromley, W. L. Tew, J. Ye, and C. J. Kennedy (2019). "JILA SrI optical lattice clock

with uncertainty of 2×10^{-18}." *Metrologia* 56, p. 065004. DOI: 10.1088/1681-7575/ab4089 (cit. on p. 5).

Boulder Atomic Clock Optical Network (BACON) Collaboration* (2021). "Frequency Ratio Measurements at 18-Digit Accuracy Using an Optical Clock Network." *Nature* 591, pp. 564–569. DOI: 10.1038/s41586-021-03253-4 (cit. on pp. 7, 97).

Bourdeauducq, S., whitequark, R. Jördens, D. Nadlinger, Y. Sionneau, and F. Kermarrec (2021). "ARTIQ." DOI: 10.5281/zenodo.6619071 (cit. on p. 48).

Boykin, P. O., T. Mor, V. Roychowdhury, F. Vatan, and R. Vrijen (2002). "Algorithmic cooling and scalable NMR quantum computers." *Proceedings of the National Academy of Sciences of the United States of America* 99, p. 3388. DOI: 10.1073/pnas.241641898 (cit. on p. 63).

Breit, G. (1958). "Theory of Isotope Shift." *Reviews of Modern Physics* 30, pp. 507–516. DOI: 10.1103/RevModPhys.30.507 (cit. on p. 29).

Brewer, S. M., J.-S. Chen, A. M. Hankin, E. R. Clements, C. W. Chou, D. J. Wineland, D. B. Hume, and D. R. Leibrandt (2019). "$^{27}Al^+$ Quantum-Logic Clock with a Systematic Uncertainty below 10^{-18}." *Physical Review Letters* 123, p. 033201. DOI: 10.1103/PhysRevLett.123.033201 (cit. on pp. 5, 26, 47, 74, 80, 85, 97, 106, 131, 133, 140).

Brownnutt, M., M. Kumph, P. Rabl, and R. Blatt (2015). "Ion-trap measurements of electric-field noise near surfaces." *Reviews of Modern Physics* 87, pp. 1419–1482. DOI: 10.1103/RevModPhys.87.1419 (cit. on pp. 61, 77, 146).

Bullard, E. C. (1955). "An Atomic Standard of Frequency and Time Interval: Definition of the Second of Time." *Nature* 176, pp. 282–282. DOI: 10.1038/176282a0 (cit. on p. 3).

Calmet, X. and M. Keller (2015). "Cosmological evolution of fundamental constants: From theory to experiment." *Modern Physics Letters A* 30, p. 1540028. DOI: 10.1142/S0217732315400283 (cit. on p. 140).

Campbell, C. J., A. G. Radnaev, A. Kuzmich, V. A. Dzuba, V. V. Flambaum, and A. Derevianko (2012). "Single-Ion Nuclear Clock for Metrology at the 19th Decimal Place." *Physical Review Letters* 108, p. 120802. DOI: 10.1103/PhysRevLett.108.120802 (cit. on p. 8).

Carruthers, P. and M. M. Nieto (1965). "Coherent States and the Forced Quantum Oscillator." *American Journal of Physics* 33, pp. 537–544. DOI: 10.1119/1.1971895 (cit. on p. 120).

Carstens, H., M. Högner, T. Saule, S. Holzberger, N. Lilienfein, A. Guggenmos, C. Jocher, T. Eidam, D. Esser, V. Tosa, V. Pervak, J. Limpert, A. Tünnermann, U. Kleineberg, F. Krausz, and I. Pupeza (2016). "High-harmonic generation at 250 MHz with photon energies

exceeding 100 eV." *Optica* 3, pp. 366–369. DOI: 10.1364/OPTICA.3.000366 (cit. on p. 141).

CGPM (1967). *Treizième conférence générale des poids et mesures* (cit. on p. 3).

Che, H., K. Deng, Z. T. Xu, W. H. Yuan, J. Zhang, and Z. H. Lu (2017). "Efficient Raman sideband cooling of trapped ions to their motional ground state." *Physical Review A* 96, p. 013417. DOI: 10.1103/PhysRevA.96.013417 (cit. on p. 29).

Chen, J.-S., S. M. Brewer, C. W. Chou, D. J. Wineland, D. R. Leibrandt, and D. B. Hume (2017). "Sympathetic Ground State Cooling and Time-Dilation Shifts in an $^{27}Al^+$ Optical Clock." *Physical Review Letters* 118, p. 053002. DOI: 10.1103/PhysRevLett.118.053002 (cit. on pp. 29, 65, 75, 77, 97, 145).

Chou, C. W., D. B. Hume, J. C. J. Koelemeij, D. J. Wineland, and T. Rosenband (2010a). "Frequency Comparison of Two High-Accuracy Al^+ Optical Clocks." *Physical Review Letters* 104, p. 070802. DOI: 10.1103/PhysRevLett.104.070802 (cit. on pp. 6, 25, 89).

Chou, C. W., D. B. Hume, T. Rosenband, and D. J. Wineland (2010b). "Optical Clocks and Relativity." *Science* 329, pp. 1630–1633. DOI: 10.1126/science.1192720 (cit. on p. 73).

Chou, C.-w., C. Kurz, D. B. Hume, P. N. Plessow, D. R. Leibrandt, and D. Leibfried (2017). "Preparation and coherent manipulation of pure quantum states of a single molecular ion." *Nature* 545, pp. 203–207. DOI: 10.1038/nature22338 (cit. on p. 26).

Ciddor, P. E. (1996). "Refractive index of air: new equations for the visible and near infrared." *Applied optics* 35, pp. 1566–1573. DOI: 10.1364/AO.35.001566 (cit. on p. 108).

Cohen-Tannoudji, C., B. Diu, and F. Laloë (1977). *Quantum Mechanics, Volume 1*. New York, NY: Wiley (cit. on p. 19).

Corsi, C., I. Liontos, M. Bellini, S. Cavalieri, P. Cancio Pastor, M. Siciliani de Cumis, and R. Eramo (2017). "Ultimate Limit in the Spectral Resolution of Extreme Ultraviolet Frequency Combs." *Physical Review Letters* 118, p. 143201. DOI: 10.1103/PhysRevLett.118.143201 (cit. on p. 141).

Cui, K., J. Valencia, K. T. Boyce, E. R. Clements, D. R. Leibrandt, and D. B. Hume (2022). "Scalable Quantum Logic Spectroscopy." *Physical Review Letters* 129, p. 193603. DOI: 10.1103/PhysRevLett.129.193603 (cit. on p. 133).

Davis, J., P. Dubé, and A. C. Vutha (2019). "Improved estimate of the collisional frequency shift in Al^+ optical clocks." *Physical Review*

Research 1, p. 033137. DOI: 10.1103/PhysRevResearch.1.033137 (cit. on p. 92).

Degenhardt, C., T. Nazarova, C. Lisdat, H. Stoehr, U. Sterr, and F. Riehle (2005). "Influence of Chirped Excitation Pulses in an Optical Clock With Ultracold Calcium Atoms." *IEEE Transactions on Instrumentation and Measurement* 54, pp. 771–775. DOI: 10.1109/TIM.2004.843388 (cit. on pp. 92, 93).

Delaunay, C., C. Frugiuele, E. Fuchs, and Y. Soreq (2017a). "Probing new spin-independent interactions through precision spectroscopy in atoms with few electrons." *Physical Review D* 96, p. 115002. DOI: 10.1103/PhysRevD.96.115002 (cit. on p. 30).

Delaunay, C., R. Ozeri, G. Perez, and Y. Soreq (2017b). "Probing atomic Higgs-like forces at the precision frontier." *Physical Review D* 96, p. 093001. DOI: 10.1103/PhysRevD.96.093001 (cit. on pp. 138, 139).

Denker, H., N. Lindenthal, L. Timmen, and S. Weyers (2014). "Report on leveling and GNSS results for stations on the PTB campus." *Internal report* (cit. on p. 95).

Denker, H. and L. Timmen (2022). "Ergebnisse des Nivellements an der PTB am 12.07.2022." *Internal report* (cit. on p. 95).

Dent, T., S. Stern, and C. Wetterich (2008). "Unifying cosmological and recent time variations of fundamental couplings." *Physical Review D* 78, p. 103518. DOI: 10.1103/PhysRevD.78.103518 (cit. on p. 140).

Derevianko, A., V. A. Dzuba, and V. V. Flambaum (2012). "Highly Charged Ions as a Basis of Optical Atomic Clockwork of Exceptional Accuracy." *Physical Review Letters* 109, p. 180801. DOI: 10.1103/PhysRevLett.109.180801 (cit. on p. 9).

Diedrich, F., J. C. Bergquist, W. M. Itano, and D. J. Wineland (1989). "Laser Cooling to the Zero-Point Energy of Motion." *Physical Review Letters* 62, pp. 403–406. DOI: 10.1103/PhysRevLett.62.403 (cit. on p. 29).

Dörscher, S., N. Huntemann, R. Schwarz, R. Lange, E. Benkler, B. Lipphardt, U. Sterr, E. Peik, and C. Lisdat (2021). "Optical frequency ratio of a $^{171}Yb^{+}$ single-ion clock and a ^{87}Sr lattice clock." *Metrologia* 58, p. 015005. DOI: 10.1088/1681-7575/abc86f (cit. on pp. 7, 106).

Draganić, I., J. Crespo López-Urrutia, R. DuBois, S. Fritzsche, V. Shabaev, R. Orts, I. Tupitsyn, Y. Zou, and J. Ullrich (2003). "High Precision Wavelength Measurements of QED-Sensitive Forbidden Transitions in Highly Charged Argon Ions." *Physical Review Letters* 91, p. 183001. DOI: 10.1103/PhysRevLett.91.183001 (cit. on pp. 8, 10, 35, 115).

Droste, S., C. Grebing, J. Leute, S. M. F. Raupach, A. Matveev, T. W. Hänsch, A. Bauch, R. Holzwarth, and G. Grosche (2015). "Characterization of a 450 km baseline GPS carrier-phase link using an optical fiber link." *New Journal of Physics* 17, p. 083044. DOI: 10.1088/1367-2630/17/8/083044 (cit. on p. 7).

Dubé, P., A. A. Madej, Z. Zhou, and J. E. Bernard (2013). "Evaluation of systematic shifts of the $^{88}Sr^{+}$ single-ion optical frequency standard at the 10^{-17} level." *Physical Review A* 87, p. 023806. DOI: 10.1103/PhysRevA.87.023806 (cit. on p. 86).

Dzuba, V. A., M. S. Safronova, U. I. Safronova, and V. V. Flambaum (2015). "Actinide ions for testing the spatial α-variation hypothesis." *Physical Review A* 92, p. 060502. DOI: 10.1103/PhysRevA.92.060502 (cit. on pp. 140, 141).

Edlén, B. (1943). "Die Deutung der Emissionslinien im Spektrum der Sonnenkorona." *Zeitschrift fur Astrophysik* 22, p. 30 (cit. on p. 9).

Egl, A., I. Arapoglou, M. Höcker, K. König, T. Ratajczyk, T. Sailer, B. Tu, A. Weigel, K. Blaum, W. Nörtershäuser, and S. Sturm (2019). "Application of the Continuous Stern-Gerlach Effect for Laser Spectroscopy of the $^{40}Ar^{13+}$ Fine Structure in a Penning Trap." *Physical Review Letters* 123, p. 123001. DOI: 10.1103/PhysRevLett.123.123001 (cit. on pp. 10, 35, 108, 113, 115).

Epp, S. W., J. R. C. López-Urrutia, G. Brenner, V. Mäckel, P. H. Mokler, R. Treusch, M. Kuhlmann, M. V. Yurkov, J. Feldhaus, J. R. Schneider, M. Wellhöfer, M. Martins, W. Wurth, and J. Ullrich (2007). "Soft X-Ray Laser Spectroscopy on Trapped Highly Charged Ions at FLASH." *Physical Review Letters* 98, p. 183001. DOI: 10.1103/PhysRevLett.98.183001 (cit. on pp. 10, 141).

Eschner, J., G. Morigi, F. Schmidt-Kaler, and R. Blatt (2003). "Laser cooling of trapped ions." *J. Opt. Soc. Am. B* 20, pp. 1003–1015. DOI: 10.1364/JOSAB.20.001003 (cit. on p. 68).

Essen, L. and J. V. L. Parry (1955). "An Atomic Standard of Frequency and Time Interval: A Cæsium Resonator." *Nature* 176, pp. 280–282. DOI: 10.1038/176280a0 (cit. on p. 3).

Fichet, S. (2018). "Quantum Forces from Dark Matter and Where to Find Them." *Physical Review Letters* 120, p. 131801. DOI: 10.1103/PhysRevLett.120.131801 (cit. on p. 138).

Filzinger, M., S. Dörscher, R. Lange, J. Klose, M. Steinel, E. Benkler, E. Peik, C. Lisdat, and N. Huntemann (2023). "Improved limits on the coupling of ultralight bosonic dark matter to photons from optical atomic clock comparisons." *arXiv:2301.03433 [physics.atom-ph]*. DOI: 10.48550/ARXIV.2301.03433 (cit. on p. 140).

Flambaum, V. V. and V. A. Dzuba (2009). "Search for variation of the fundamental constants in atomic, molecular, and nuclear spectra." *Canadian Journal of Physics* 87, pp. 25–33. DOI: 10.1139/p08-072 (cit. on p. 140).

Flambaum, V. V., A. J. Geddes, and A. V. Viatkina (2018). "Isotope shift, nonlinearity of King plots, and the search for new particles." *Physical Review A* 97, p. 032510. DOI: 10.1103/PhysRevA.97.032510 (cit. on pp. 138, 139).

Franzen, A. (2006). *Component Libary*. http://www.gwoptics.org/ComponentLibrary/. Published according to http://creativecommons.org/licenses/by-nc/3.0/ (cit. on pp. 6, 42, 43, 45, 47, 101).

Frugiuele, C., E. Fuchs, G. Perez, and M. Schlaffer (2017). "Constraining new physics models with isotope shift spectroscopy." *Physical Review D* 96, p. 015011. DOI: 10.1103/PhysRevD.96.015011 (cit. on p. 138).

Gan, H. C. J., G. Maslennikov, K.-W. Tseng, T. R. Tan, R. Kaewuam, K. J. Arnold, D. Matsukevich, and M. D. Barrett (2018). "Oscillating-magnetic-field effects in high-precision metrology." *Physical Review A* 98, p. 032514. DOI: 10.1103/PhysRevA.98.032514 (cit. on pp. 89, 90, 97, 110).

Gebert, F., Y. Wan, F. Wolf, J. C. Heip, and P. O. Schmidt (2016). "Detection of motional ground state population of a trapped ion using delayed pulses." *New Journal of Physics* 18, p. 013037. DOI: 10.1088/1367-2630/18/1/013037 (cit. on p. 118).

Gebert, F., Y. Wan, F. Wolf, J. C. Heip, and P. O. Schmidt (2018). "Corrigendum: Detection of motional ground state population using delayed pulses." *New Journal of Physics* 20, p. 029501. DOI: 10.1088/1367-2630/aaaafd (cit. on p. 118).

Ghosh, P. K. (1995). *Ion Traps*. Clarendon Press (cit. on p. 13).

Gill, P. (2011). "When should we change the definition of the second?" *Philosophical Transactions of the Royal Society A: Mathematical, Physical and Engineering Sciences* 369, pp. 4109–4130. DOI: 10.1098/rsta.2011.0237 (cit. on p. 5).

Gillaspy, J. D. (2001). "Highly charged ions." *Journal of Physics B: Atomic, Molecular and Optical Physics* 34, R93–R130. DOI: 10.1088/0953-4075/34/19/201 (cit. on p. 9).

Gohle, C., T. Udem, M. Herrmann, J. Rauschenberger, R. Holzwarth, H. A. Schuessler, F. Krausz, and T. W. Hänsch (2005). "A frequency comb in the extreme ultraviolet." *Nature* 436, pp. 234–237. DOI: 10.1038/nature03851 (cit. on p. 141).

Gorman, D. J., P. Schindler, S. Selvarajan, N. Daniilidis, and H. Häffner (2014). "Two-mode coupling in a single-ion oscillator via parametric resonance." *Physical Review A* 89, p. 062332. DOI: 10.1103/PhysRevA.89.062332 (cit. on p. 61).

Grotian, W. (1939). "Zur Frage der Deutung der Linien im Spektrum der Sonnenkorona." *Naturwissenschaften* 27, pp. 214–214. DOI: 10.1007/BF01488890 (cit. on p. 9).

Gruber, L., J. Holder, J. Steiger, B. Beck, H. DeWitt, J. Glassman, J. McDonald, D. Church, and D. Schneider (2001). "Evidence for Highly Charged Ion Coulomb Crystallization in Multicomponent Strongly Coupled Plasmas." *Physical Review Letters* 86, pp. 636–639. DOI: 10.1103/PhysRevLett.86.636 (cit. on p. 10).

Guena, J., M. Abgrall, D. Rovera, P. Laurent, B. Chupin, M. Lours, G. Santarelli, P. Rosenbusch, M. E. Tobar, R. Li, K. Gibble, A. Clairon, and S. Bize (2012). "Progress in atomic fountains at LNE-SYRTE." *IEEE Transactions on Ultrasonics, Ferroelectrics, and Frequency Control* 59, pp. 391–409. DOI: 10.1109/TUFFC.2012.2208 (cit. on p. 5).

Hachisu, H., M. Fujieda, S. Nagano, T. Gotoh, A. Nogami, T. Ido, S. Falke, N. Huntemann, C. Grebing, B. Lipphardt, C. Lisdat, and D. Piester (2014). "Direct comparison of optical lattice clocks with an intercontinental baseline of 9000 km." *Optics Letters* 39, pp. 4072–4075. DOI: 10.1364/OL.39.004072 (cit. on p. 7).

Hahn, H. (2019). "Two-qubit microwave quantum logic gate with $^{9}Be^{+}$ ions in scalable surface-electrode ion traps." PhD Thesis. Leibniz Universität Hannover (cit. on pp. 40–42).

Hankin, A. M., E. R. Clements, Y. Huang, S. M. Brewer, J.-S. Chen, C. W. Chou, D. B. Hume, and D. R. Leibrandt (2019). "Systematic uncertainty due to background-gas collisions in trapped-ion optical clocks." *Physical Review A* 100, p. 033419. DOI: 10.1103/PhysRevA.100.033419 (cit. on p. 92).

Hannig, S., J. Mielke, J. A. Fenske, M. Misera, N. Beev, C. Ospelkaus, and P. O. Schmidt (2018). "A highly stable monolithic enhancement cavity for second harmonic generation in the ultraviolet." *Review of Scientific Instruments* 89, p. 013106. DOI: 10.1063/1.5005515 (cit. on pp. 42, 49).

Hannig, S., L. Pelzer, N. Scharnhorst, J. Kramer, M. Stepanova, Z. T. Xu, N. Spethmann, I. D. Leroux, T. E. Mehlstäubler, and P. O. Schmidt (2019). "Towards a transportable aluminium ion quantum logic optical clock." *Review of Scientific Instruments* 90, p. 053204. DOI: 10.1063/1.5090583 (cit. on p. 25).

Harris, F. J. (1978). "On the use of windows for harmonic analysis with the discrete Fourier transform." *Proceedings of the IEEE* 66, pp. 51–83. DOI: 10.1109/PROC.1978.10837 (cit. on p. 50).

Heavner, T. P., E. A. Donley, F. Levi, G. Costanzo, T. E. Parker, J. H. Shirley, N. Ashby, S. Barlow, and S. R. Jefferts (2014). "First accuracy evaluation of NIST-F2." *Metrologia* 51, p. 174. DOI: 10.1088/0026-1394/51/3/174 (cit. on p. 5).

Heinzen, D. J. and D. J. Wineland (1990). "Quantum-limited cooling and detection of radio-frequency oscillations by laser-cooled ions." *Physical Review A* 42, pp. 2977–2994. DOI: 10.1103/PhysRevA.42.2977 (cit. on p. 120).

Hobein, M., A. Solders, M. Suhonen, Y. Liu, and R. Schuch (2011). "Evaporative Cooling and Coherent Axial Oscillations of Highly Charged Ions in a Penning Trap." *Physical Review Letters* 106. DOI: 10.1103/PhysRevLett.106.013002 (cit. on p. 10).

Hobson, R., W. Bowden, S. A. King, P. E. G. Baird, I. R. Hill, and P. Gill (2016). "Modified hyper-Ramsey methods for the elimination of probe shifts in optical clocks." *Physical Review A* 93, p. 010501. DOI: 10.1103/PhysRevA.93.010501 (cit. on pp. 92, 97).

Hosoya, T., M. Miranda, R. Inoue, and M. Kozuma (2015). "Injection locking of a high power ultraviolet laser diode for laser cooling of ytterbium atoms." *Review of Scientific Instruments* 86, p. 073110. DOI: 10.1063/1.4927132 (cit. on p. 44).

Hou, P.-Y., J. J. Wu, S. D. Erickson, D. C. Cole, G. Zarantonello, A. D. Brandt, A. C. Wilson, D. H. Slichter, and D. Leibfried (2022). "Coherently Coupled Mechanical Oscillators in the Quantum Regime." *arXiv:2205.14841 [quant-ph]*. DOI: 10.48550/ARXIV.2205.14841 (cit. on p. 61).

Howe, D., D. Allan, and J. Barnes (1981). "Properties of Signal Sources and Measurement Methods." *Thirty Fifth Annual Frequency Control Symposium*, pp. 669–716. DOI: 10.1109/FREQ.1981.200541 (cit. on p. 4).

Huang, Y., H. Guan, P. Liu, W. Bian, L. Ma, K. Liang, T. Li, and K. Gao (2016). "Frequency Comparison of Two $^{40}Ca^{+}$ Optical Clocks with an Uncertainty at the 10^{-17} Level." *Physical Review Letters* 116, p. 013001. DOI: 10.1103/PhysRevLett.116.013001 (cit. on p. 6).

Huang, Y., B. Zhang, M. Zeng, Y. Hao, Z. Ma, H. Zhang, H. Guan, Z. Chen, M. Wang, and K. Gao (2022). "Liquid-Nitrogen-Cooled Ca^{+} Optical Clock with Systematic Uncertainty of 3×10^{-18}." *Physical Review Applied* 17, p. 034041. DOI: 10.1103/PhysRevApplied.17.034041 (cit. on p. 6).

Huang, Y., H. Zhang, B. Zhang, Y. Hao, H. Guan, M. Zeng, Q. Chen, Y. Lin, Y. Wang, S. Cao, K. Liang, F. Fang, Z. Fang, T. Li, and K. Gao (2020). "Geopotential measurement with a robust, transportable Ca^+ optical clock." *Physical Review A* 102, p. 050802. DOI: 10.1103/PhysRevA.102.050802 (cit. on p. 96).

Hume, D., T. Rosenband, and D. Wineland (2007). "High-Fidelity Adaptive Qubit Detection through Repetitive Quantum Nondemolition Measurements." *Physical Review Letters* 99, p. 120502. DOI: 10.1103/PhysRevLett.99.120502 (cit. on pp. 136, 137).

Hume, D. B., C. W. Chou, D. R. Leibrandt, M. J. Thorpe, D. J. Wineland, and T. Rosenband (2011). "Trapped-Ion State Detection through Coherent Motion." *Physical Review Letters* 107, p. 243902. DOI: 10.1103/PhysRevLett.107.243902 (cit. on pp. 116, 117).

Huntemann, N., B. Lipphardt, M. Okhapkin, C. Tamm, E. Peik, A. V. Taichenachev, and V. I. Yudin (2012). "Generalized Ramsey Excitation Scheme with Suppressed Light Shift." *Physical Review Letters* 109, p. 213002. DOI: 10.1103/PhysRevLett.109.213002 (cit. on pp. 92, 97).

Huntemann, N., C. Sanner, B. Lipphardt, C. Tamm, and E. Peik (2016). "Single-Ion Atomic Clock with 3×10^{-18} Systematic Uncertainty." *Physical Review Letters* 116, p. 063001. DOI: 10.1103/PhysRevLett.116.063001 (cit. on pp. 5, 97, 99, 104, 106, 113, 131).

Hur, J., D. P. L. Aude Craik, I. Counts, E. Knyazev, L. Caldwell, C. Leung, S. Pandey, J. C. Berengut, A. Geddes, W. Nazarewicz, P.-G. Reinhard, A. Kawasaki, H. Jeon, W. Jhe, and V. Vuletić (2022). "Evidence of Two-Source King Plot Nonlinearity in Spectroscopic Search for New Boson." *Physical Review Letters* 128, p. 163201. DOI: 10.1103/PhysRevLett.128.163201 (cit. on p. 139).

Itano, W. M. (2000). "External-field shifts of the $^{199}Hg^+$ optical frequency standard." *Journal of Research of NIST* 105, pp. 829–837. DOI: 10.6028/jres.105.065 (cit. on pp. 83, 86, 135).

Itano, W. M., J. C. Bergquist, J. J. Bollinger, J. M. Gilligan, D. J. Heinzen, F. L. Moore, M. G. Raizen, and D. J. Wineland (1993). "Quantum projection noise: Population fluctuations in two-level systems." *Physical Review A* 47, pp. 3554–3570. DOI: 10.1103/PhysRevA.47.3554 (cit. on pp. 4, 51, 153).

Itano, W. M., J. C. Bergquist, J. J. Bollinger, and D. J. Wineland (1995). "Cooling methods in ion traps." *Physica Scripta* 1995, p. 106. DOI: 10.1088/0031-8949/1995/T59/013 (cit. on p. 28).

Itano, W. M. and D. J. Wineland (1982). "Laser cooling of ions stored in harmonic and Penning traps." *Physical Review A* 25, pp. 35–54. DOI: 10.1103/PhysRevA.25.35 (cit. on p. 68).

James, D. F. V. (1998a). "Quantum dynamics of cold trapped ions with application to quantum computation." *Applied Physics B: Lasers and Optics* 66, pp. 181–190. DOI: 10.1007/s003400050373 (cit. on pp. 17, 18).

James, D. F. V. (1998b). "Theory of Heating of the Quantum Ground State of Trapped Ions." *Physical Review Letters* 81, p. 317. DOI: 10.1103/PhysRevLett.81.317 (cit. on pp. 77, 78, 145).

Jian, B., J. Bernard, M. Gertsvolf, and P. Dubé (2022). "Improved absolute frequency measurement of the strontium ion clock using a GPS link to the SI second." *Metrologia* 60, p. 015007. DOI: 10.1088/1681-7575/aca615 (cit. on p. 6).

Jones, R., K. Moll, M. Thorpe, and J. Ye (2005). "Phase-Coherent Frequency Combs in the Vacuum Ultraviolet via High-Harmonic Generation inside a Femtosecond Enhancement Cavity." *Physical Review Letters* 94, p. 193201. DOI: 10.1103/PhysRevLett.94.193201 (cit. on p. 141).

Kazda, M., V. Gerginov, N. Huntemann, B. Lipphardt, and S. Weyers (2016). "Phase Analysis for Frequency Standards in the Microwave and Optical Domains." *IEEE Transactions on Ultrasonics, Ferroelectrics, and Frequency Control* 63, pp. 970–974. DOI: 10.1109/TUFFC.2016.2515759 (cit. on p. 93).

Keller, J., T. Burgermeister, D. Kalincev, J. Kiethe, and T. E. Mehlstäubler (2016). "Evaluation of trap-induced systematic frequency shifts for a multi-ion optical clock at the 10^{-19} level." *Journal of Physics: Conference Series* 723, p. 012027. DOI: 10.1088/1742-6596/723/1/012027 (cit. on p. 80).

Keller, J., H. L. Partner, T. Burgermeister, and T. E. Mehlstäubler (2015). "Precise determination of micromotion for trapped-ion optical clocks." *Journal of Applied Physics* 118, p. 104501. DOI: 10.1063/1.4930037 (cit. on pp. 16, 122).

Kielpinski, D., B. E. King, C. J. Myatt, C. A. Sackett, Q. A. Turchette, W. M. Itano, C. Monroe, D. J. Wineland, and W. H. Zurek (2000). "Sympathetic cooling of trapped ions for quantum logic." *Physical Review A* 61, p. 032310. DOI: 10.1103/PhysRevA.61.032310 (cit. on pp. 17, 18).

Kien, F. L., J. Liang, K. Hakuta, and V. Balykin (2004). "Field intensity distributions and polarization orientations in a vacuum-clad subwavelength-diameter optical fiber." *Optics Communications* 242, pp. 445–455. DOI: https://doi.org/10.1016/j.optcom.2004.08.044 (cit. on p. 90).

King, S. A., T. Leopold, P. Thekkeppatt, and P. O. Schmidt (2018). "A self-injection locked DBR laser for laser cooling of beryllium ions."

Applied Physics B 124, p. 214. DOI: 10.1007/s00340-018-7080-0 (cit. on p. 41).

King, S. A., L. J. Spieß, P. Micke, A. Wilzewski, T. Leopold, E. Benkler, R. Lange, N. Huntemann, A. Surzhykov, V. A. Yerokhin, J. R. Crespo López-Urrutia, and P. O. Schmidt (2022). "An optical atomic clock based on a highly charged ion." *Nature* 611, pp. 43–47. DOI: 10.1038/s41586-022-05245-4 (cit. on pp. 30, 36, 73, 99, 104, 108, 109, 131, 138).

King, S. A., L. J. Spieß, P. Micke, A. Wilzewski, T. Leopold, J. R. Crespo López-Urrutia, and P. O. Schmidt (2021). "Algorithmic Ground-State Cooling of Weakly Coupled Oscillators Using Quantum Logic." *Physical Review X* 11, p. 041049. DOI: 10.1103/PhysRevX.11.041049 (cit. on pp. 26, 63, 64, 131).

King, W. H. (1963). "Comments on the Article "Peculiarities of the Isotope Shift in the Samarium Spectrum"." *Journal of the Optical Society of America* 53, pp. 638–639. DOI: 10.1364/JOSA.53.000638 (cit. on pp. 29, 138).

Knapp, D., R. Marrs, S. Elliott, E. Magee, and R. Zasadzinski (1993). "A high-energy electron beam ion trap for production of high-charge high-Z ions." *Nuclear Instruments and Methods in Physics Research Section A: Accelerators, Spectrometers, Detectors and Associated Equipment* 334, pp. 305–312. DOI: https://doi.org/10.1016/0168-9002(93)90790-O (cit. on p. 8).

Knollmann, F. W., A. N. Patel, and S. C. Doret (2019). "Part-per-billion measurement of the $4^2S_{1/2} \rightarrow 3^2D_{5/2}$ electric quadrupole transition isotope shifts between $^{42,44,48}Ca^+$ and $^{40}Ca^+$." *Physical Review A* 100, p. 022514. DOI: 10.1103/PhysRevA.100.022514 (cit. on p. 139).

Kozlov, M. G., M. S. Safronova, J. R. Crespo López-Urrutia, and P. O. Schmidt (2018). "Highly charged ions: Optical clocks and applications in fundamental physics." *Reviews of Modern Physics* 90, p. 045005. DOI: 10.1103/RevModPhys.90.045005 (cit. on pp. 8–10, 18, 55, 131, 133, 137, 141).

Kraemer, S., J. Moens, M. Athanasakis-Kaklamanakis, S. Bara, K. Beeks, P. Chhetri, K. Chrysalidis, A. Claessens, T. E. Cocolios, J. M. Correia, H. De Witte, R. Ferrer, S. Geldhof, R. Heinke, N. Hosseini, et al. (2022). "Observation of the radiative decay of the ^{229}Th nuclear clock isomer." *arXiv:2209.10276 [nucl-ex]*. DOI: 10.48550/ARXIV.2209.10276 (cit. on p. 7).

Kramida, A., Y. Ralchenko, J. Reader, and NIST ASD Team (2021). NIST Atomic Spectra Database(ver. 5.9), [Online]. URL: https://physics.nist.gov/asd [2023, January 10]. National Institute of Standards and Technology, Gaithersburg, MD. (Cit. on pp. 84, 134, 136).

Lacour, X., S. Guérin, L. P. Yatsenko, N. V. Vitanov, and H. R. Jauslin (2007). "Uniform analytic description of dephasing effects in two-state transitions." *Physical Review A* 75, p. 033417. DOI: 10.1103/PhysRevA.75.033417 (cit. on pp. 136, 137).

Lange, R., N. Huntemann, J. M. Rahm, C. Sanner, H. Shao, B. Lipphardt, C. Tamm, S. Weyers, and E. Peik (2021). "Improved Limits for Violations of Local Position Invariance from Atomic Clock Comparisons." *Physical Review Letters* 126, p. 011102. DOI: 10.1103/PhysRevLett.126.011102 (cit. on pp. 6, 107, 108, 140).

Lange, R., N. Huntemann, C. Sanner, H. Shao, B. Lipphardt, C. Tamm, and E. Peik (2020). "Coherent Suppression of Tensor Frequency Shifts through Magnetic Field Rotation." *Physical Review Letters* 125, p. 143201. DOI: 10.1103/PhysRevLett.125.143201 (cit. on pp. 113, 135).

Lapierre, A., J. R. Crespo López-Urrutia, J. Braun, G. Brenner, H. Bruhns, D. Fischer, A. J. González Martínez, V. Mironov, C. Osborne, G. Sikler, R. Soria Orts, H. Tawara, J. Ullrich, V. M. Shabaev, I. I. Tupitsyn, and A. Volotka (2006). "Lifetime measurement of the Ar XIV $1s^2 2s^2 2p^2 P^o_{3/2}$ metastable level at the Heidelberg electron-beam ion trap." *Physical Review A* 73, p. 052507. DOI: 10.1103/PhysRevA.73.052507 (cit. on pp. 35, 106, 133).

Leibfried, D., R. Blatt, C. Monroe, and D. Wineland (2003). "Quantum dynamics of single trapped ions." *Review of Modern Physics* 75, pp. 281–324. DOI: 10.1103/RevModPhys.75.281 (cit. on pp. 13, 19, 22, 23, 26, 122, 126).

Leopardi, H., K. Beloy, T. Bothwell, S. M. Brewer, S. L. Bromley, J.-S. Chen, S. A. Diddams, R. J. Fasano, Y. S. Hassan, D. B. Hume, D. Kedar, C. J. Kennedy, D. R. Leibrandt, A. D. Ludlow, W. F. McGrew, et al. (2021). "Measurement of the $^{27}Al^+$ and ^{87}Sr absolute optical frequencies." *Metrologia* 58, p. 015017. DOI: 10.1088/1681-7575/abd040 (cit. on p. 108).

Leopold, T., S. A. King, P. Micke, A. Bautista-Salvador, J. C. Heip, C. Ospelkaus, J. R. Crespo López-Urrutia, and P. O. Schmidt (2019). "A cryogenic radio-frequency ion trap for quantum logic spectroscopy of highly charged ions." *Review of Scientific Instruments* 90, p. 073201. DOI: 10.1063/1.5100594 (cit. on pp. 11, 16, 33, 37, 40, 51, 75, 77, 79, 80, 83, 89, 110, 145).

Leopold, T. (2018). "A cryogenic ion trap system for quantum logic spectroscopy of highly charged ions." PhD Thesis. Leibniz Universität Hannover (cit. on pp. 15, 23, 24, 29, 33–35, 37, 38, 40, 46, 51, 61, 62, 78, 83).

Lett, P. D., W. D. Phillips, S. L. Rolston, C. E. Tanner, R. N. Watts, and C. I. Westbrook (1989). "Optical molasses." *Journal of the Optical*

Society of America B 6, pp. 2084–2107. DOI: 10.1364/JOSAB.6.002084 (cit. on p. 26).

Levi, F., D. Calonico, C. E. Calosso, A. Godone, S. Micalizio, and G. A. Costanzo (2014). "Accuracy evaluation of ITCsF2: a nitrogen cooled caesium fountain." *Metrologia* 51, p. 270. DOI: 10.1088/0026-1394/51/3/270 (cit. on p. 5).

Liang, S.-Y., T.-X. Zhang, H. Guan, Q.-F. Lu, J. Xiao, S.-L. Chen, Y. Huang, Y.-H. Zhang, C.-B. Li, Y.-M. Zou, J.-G. Li, Z.-C. Yan, A. Derevianko, M.-S. Zhan, T.-Y. Shi, and K.-L. Gao (2021). "Probing multiple electric-dipole-forbidden optical transitions in highly charged nickel ions." *Physical Review A* 103, p. 022804. DOI: 10.1103/PhysRevA.103.022804 (cit. on pp. 127, 135, 136).

Lin, Y., D. R. Leibrandt, D. Leibfried, and C.-w. Chou (2020). "Quantum entanglement between an atom and a molecule." *Nature* 581, pp. 273–277. DOI: 10.1038/s41586-020-2257-1 (cit. on p. 25).

Lindenfels, D. von, M. Wiesel, D. A. Glazov, A. V. Volotka, M. M. Sokolov, V. M. Shabaev, G. Plunien, W. Quint, G. Birkl, A. Martin, and M. Vogel (2013). "Experimental access to higher-order Zeeman effects by precision spectroscopy of highly charged ions in a Penning trap." *Physical Review A* 87, p. 023412. DOI: 10.1103/PhysRevA.87.023412 (cit. on p. 89).

Lindenfels, D.-F. F. v. (2015). "Experimental Studies of Highly Charged Ions in a Penning Trap for the Measurement of Electron Magnetic Moments by Double-Resonance Spectroscopy." eng. PhD Thesis. Heidelberg: Ruprecht-Karls-Universität Heidelberg. DOI: 10.11588/heidok.00019835 (cit. on pp. 88, 89).

Lisdat, C., G. Grosche, N. Quintin, C. Shi, S. M. F. Raupach, C. Grebing, D. Nicolodi, F. Stefani, A. Al-Masoudi, S. Dörscher, S. Häfner, J.-L. Robyr, N. Chiodo, S. Bilicki, E. Bookjans, et al. (2016). "A clock network for geodesy and fundamental science." *Nature Communications* 7, p. 12443. DOI: 10.1038/ncomms12443 (cit. on p. 7).

Lodewyck, J., S. Bilicki, E. Bookjans, J.-L. Robyr, C. Shi, G. Vallet, R. Le Targat, D. Nicolodi, Y. Le Coq, J. Guéna, M. Abgrall, P. Rosenbusch, and S. Bize (2016). "Optical to microwave clock frequency ratios with a nearly continuous strontium optical lattice clock." *Metrologia* 53, pp. 1123–1130. DOI: 10.1088/0026-1394/53/4/1123 (cit. on pp. 96, 108).

Ludlow, A. D., M. M. Boyd, J. Ye, E. Peik, and P. O. Schmidt (2015). "Optical atomic clocks." *Reviews of Modern Physics* 87, pp. 637–701. DOI: 10.1103/RevModPhys.87.637 (cit. on p. 113).

Ma, L.-S., P. Jungner, J. Ye, and J. L. Hall (1994). "Delivering the same optical frequency at two places: accurate cancellation of phase noise

introduced by an optical fiber or other time-varying path." *Optics Letters* 19, pp. 1777–1779. DOI: 10.1364/OL.19.001777 (cit. on pp. 43–45).

Mäckel, V., R. Klawitter, G. Brenner, J. R. Crespo López-Urrutia, and J. Ullrich (2011). "Laser Spectroscopy on Forbidden Transitions in Trapped Highly Charged Ar^{13+} Ions." *Physical Review Letters* 107, p. 143002. DOI: 10.1103/PhysRevLett.107.143002 (cit. on pp. 10, 35, 115).

Mäckel, V., R. Klawitter, G. Brenner, J. R. Crespo López-Urrutia, and J. Ullrich (2013). "Laser spectroscopy of highly charged argon at the Heidelberg electron beam ion trap." en. *Physica Scripta* T156, p. 014004. DOI: 10.1088/0031-8949/2013/T156/014004 (cit. on p. 35).

Martins, C. J. A. P. (2017). "The status of varying constants: a review of the physics, searches and implications." *Reports on Progress in Physics* 80, p. 126902. DOI: 10.1088/1361-6633/aa860e (cit. on p. 140).

Matei, D. G., T. Legero, S. Häfner, C. Grebing, R. Weyrich, W. Zhang, L. Sonderhouse, J. M. Robinson, J. Ye, F. Riehle, and U. Sterr (2017). "1.5 μm Lasers with Sub-10 mHz Linewidth." *Physical Review Letters* 118, p. 263202. DOI: 10.1103/PhysRevLett.118.263202 (cit. on pp. 45, 46, 103–105).

McCormick, K. C., J. Keller, D. J. Wineland, A. C. Wilson, and D. Leibfried (2019). "Coherently displaced oscillator quantum states of a single trapped atom." *Quantum Science and Technology* 4, p. 024010. DOI: 10.1088/2058-9565/ab0513 (cit. on p. 125).

McGrew, W. F., X. Zhang, R. J. Fasano, S. A. Schäffer, K. Beloy, D. Nicolodi, R. C. Brown, N. Hinkley, G. Milani, M. Schioppo, T. H. Yoon, and A. D. Ludlow (2018). "Atomic clock performance enabling geodesy below the centimetre level." *Nature* 564, p. 87. DOI: 10.1038/s41586-018-0738-2 (cit. on pp. 5, 131).

McGrew, W. F., X. Zhang, H. Leopardi, R. J. Fasano, D. Nicolodi, K. Beloy, J. Yao, J. A. Sherman, S. A. Schäffer, J. Savory, R. C. Brown, S. Römisch, C. W. Oates, T. E. Parker, T. M. Fortier, and A. D. Ludlow (2019). "Towards the optical second: verifying optical clocks at the SI limit." *Optica* 6, pp. 448–454. DOI: 10.1364/OPTICA.6.000448 (cit. on pp. 6, 108).

Mehlstäubler, T. E., G. Grosche, C. Lisdat, P. O. Schmidt, and H. Denker (2018). "Atomic clocks for geodesy." *Reports on Progress in Physics* 81, p. 064401. DOI: 10.1088/1361-6633/aab409 (cit. on p. 95).

Merkel, B., K. Thirumalai, J. E. Tarlton, V. M. Schäfer, C. J. Ballance, T. P. Harty, and D. M. Lucas (2019). "Magnetic field stabilization system

for atomic physics experiments." *Review of Scientific Instruments* 90, p. 044702. DOI: 10.1063/1.5080093 (cit. on p. 40).

Micke, P., S. Kühn, L. Buchauer, J. R. Harries, T. M. Bücking, K. Blaum, A. Cieluch, A. Egl, D. Hollain, S. Kraemer, T. Pfeifer, P. O. Schmidt, R. X. Schüssler, C. Schweiger, T. Stöhlker, S. Sturm, R. N. Wolf, S. Bernitt, and J. R. Crespo López-Urrutia (2018). "The Heidelberg compact electron beam ion traps." *Review of Scientific Instruments* 89, p. 063109. DOI: 10.1063/1.5026961 (cit. on pp. 8, 33, 36).

Micke, P., T. Leopold, S. A. King, E. Benkler, L. J. Spieß, L. Schmöger, M. Schwarz, J. R. C. López-Urrutia, and P. O. Schmidt (2020). "Coherent laser spectroscopy of highly charged ions using quantum logic." *Nature* 578, pp. 60–65. DOI: 10.1038/s41586-020-1959-8 (cit. on pp. 11, 25, 26, 35–37, 42, 51, 63, 109–111, 115, 131, 136, 145).

Micke, P., J. Stark, S. A. King, T. Leopold, T. Pfeifer, L. Schmöger, M. Schwarz, L. J. Spieß, P. O. Schmidt, and J. R. Crespo López-Urrutia (2019). "Closed-cycle, low-vibration 4 K cryostat for ion traps and other applications." *Review of Scientific Instruments* 90, p. 065104. DOI: 10.1063/1.5088593 (cit. on pp. 11, 33, 37–39, 92, 154).

Micke, P. (2020). "Quantum Logic Spectroscopy of Highly Charged Ions." PhD Thesis. Leibniz Universität Hannover (cit. on pp. 16, 33, 51).

Monroe, C., D. M. Meekhof, B. E. King, S. R. Jefferts, W. M. Itano, D. J. Wineland, and P. Gould (1995). "Resolved-sideband Raman cooling of a bound atom to the 3D zero-point energy." *Physical Review Letters* 75, pp. 4011–4014. DOI: 10.1103/PhysRevLett.75.4011 (cit. on p. 28).

Morigi, G. (2003). "Cooling atomic motion with quantum interference." *Physical Review A* 67, p. 033402. DOI: 10.1103/PhysRevA.67.033402 (cit. on p. 34).

Müller, R. A. (2021). *Private communication* (cit. on pp. 86, 113).

Nauta, J., J. Nauta, J. Nauta, J.-H. Oelmann, J.-H. Oelmann, A. Borodin, A. Ackermann, P. Knauer, I. S. Muhammad, R. Pappenberger, T. Pfeifer, T. Pfeifer, J. R. C. López-Urrutia, and J. R. C. López-Urrutia (2021). "XUV frequency comb production with an astigmatism-compensated enhancement cavity." *Optics Express* 29, pp. 2624–2636. DOI: 10.1364/OE.414987 (cit. on p. 141).

Nemitz, N., T. Gotoh, F. Nakagawa, H. Ito, Y. Hanado, T. Ido, and H. Hachisu (2021). "Absolute Frequency of ^{87}Sr at 1.8×10^{-16} Uncertainty by Reference to Remote Primary Frequency Standards." *Metrologia* 58, p. 025006. DOI: 10.1088/1681-7575/abc232 (cit. on p. 108).

Noel, T., M. R. Dietrich, N. Kurz, G. Shu, J. Wright, and B. B. Blinov (2012). "Adiabatic passage in the presence of noise." *Physical Review A* 85, p. 023401. DOI: 10.1103/PhysRevA.85.023401 (cit. on pp. 136, 137).

Ono, K., Y. Saito, T. Ishiyama, T. Higomoto, T. Takano, Y. Takasu, Y. Yamamoto, M. Tanaka, and Y. Takahashi (2022). "Observation of Nonlinearity of Generalized King Plot in the Search for New Boson." *Physical Review X* 12, p. 021033. DOI: 10.1103/PhysRevX.12.021033 (cit. on p. 139).

Pagett, C. J. H., P. H. Moriya, R. Celistrino Teixeira, R. F. Shiozaki, M. Hemmerling, and P. W. Courteille (2016). "Injection locking of a low cost high power laser diode at 461 nm." *Review of Scientific Instruments* 87, p. 053105. DOI: 10.1063/1.4947462 (cit. on p. 44).

Peck, E. R. and K. Reeder (1972). "Dispersion of Air∗." *Journal of the Optical Society of America* 62, pp. 958–962. DOI: 10.1364/JOSA.62.000958 (cit. on p. 108).

Peik, E. and C. Tamm (2003). "Nuclear laser spectroscopy of the 3.5 eV transition in Th-229." *Europhysics Letters (EPL)* 61, pp. 181–186. DOI: 10.1209/epl/i2003-00210-x (cit. on p. 7).

Peik, E., T. Schneider, and C. Tamm (2006). "Laser frequency stabilization to a single ion." *Journal of Physics B: Atomic, Molecular and Optical Physics* 39, pp. 145–158. DOI: 10.1088/0953-4075/39/1/012 (cit. on pp. 93, 101–103, 106, 133, 151, 152).

Piester, D., A. Bauch, J. Becker, E. Staliuniene, and C. Schlunegger (2008). "On measurement noise in the European TWSTFT network." *IEEE Transactions on Ultrasonics, Ferroelectrics and Frequency Control* 55, pp. 1906–1912. DOI: 10.1109/TUFFC.882 (cit. on p. 7).

Pizzocaro, M., F. Bregolin, P. Barbieri, B. Rauf, F. Levi, and D. Calonico (2020). "Absolute Frequency Measurement of the $^1S_0$–$^3P_0$ Transition of ^{171}Yb with a Link to International Atomic Time." *Metrologia* 57, p. 035007. DOI: 10.1088/1681-7575/ab50e8 (cit. on p. 108).

Porsev, S. G., U. I. Safronova, M. S. Safronova, P. O. Schmidt, A. I. Bondarev, M. G. Kozlov, I. I. Tupitsyn, and C. Cheung (2020). "Optical clocks based on the Cf^{15+} and Cf^{17+} ions." *Physical Review A* 102, p. 012802. DOI: 10.1103/PhysRevA.102.012802 (cit. on pp. 8, 115, 133, 138).

Pyka, K., N. Herschbach, J. Keller, and T. E. Mehlstäubler (2014). "A high-precision segmented Paul trap with minimized micromotion for an optical multiple-ion clock." *Applied Physics B* 114, pp. 231–241. DOI: 10.1007/s00340-013-5580-5 (cit. on p. 97).

Rasmusson, A. J., M. D'Onofrio, Y. Xie, J. Cui, and P. Richerme (2021). "Optimized pulsed sideband cooling and enhanced thermometry

of trapped ions." *Physical Review A* 104, p. 043108. DOI: 10.1103/PhysRevA.104.043108 (cit. on pp. 29, 65, 75, 77).

Rehbehn, N.-H., M. K. Rosner, H. Bekker, J. C. Berengut, P. O. Schmidt, S. A. King, P. Micke, M. F. Gu, R. Müller, A. Surzhykov, and J. R. C. López-Urrutia (2021). "Sensitivity to New Physics of Isotope-Shift Studies Using the Coronal Lines of Highly Charged Calcium Ions." *Physical Review A* 103, p. L040801. DOI: 10.1103/PhysRevA.103.L040801 (cit. on pp. 8, 115, 139, 142).

Riedel, F., A. Al-Masoudi, E. Benkler, S. Dörscher, V. Gerginov, C. Grebing, S. Häfner, N. Huntemann, B. Lipphardt, C. Lisdat, E. Peik, D. Piester, C. Sanner, C. Tamm, S. Weyers, et al. (2020). "Direct comparisons of European primary and secondary frequency standards via satellite techniques." *Metrologia* 57, p. 045005. DOI: 10.1088/1681-7575/ab6745 (cit. on p. 7).

Riehle, F. (2004). *Frequency standards: basics and applications*. Weinheim: Wiley-VCH. DOI: 10.1002/3527605991 (cit. on pp. 5, 10, 19, 20).

Riehle, F. (2015). "Towards a redefinition of the second based on optical atomic clocks." *Comptes Rendus Physique* 16, pp. 506–515. DOI: https://doi.org/10.1016/j.crhy.2015.03.012 (cit. on p. 5).

Riehle, F., P. Gill, F. Arias, and L. Robertsson (2018). "The CIPM list of recommended frequency standard values: guidelines and procedures." *Metrologia* 55, p. 188. DOI: 10.1088/1681-7575/aaa302 (cit. on p. 6).

Riley, W. J. (2008). *Handbook of Frequency Stability Analysis*. Tech. rep. Gaithersburg, MD: National Institute of Standards and Technology, NIST SP 1065. DOI: 10.6028/NIST.SP.1065 (cit. on p. 4).

Riley, W. J. (2016). *Stable32*. https://www.wriley.com/ (cit. on p. 4).

Roos, C. F., M. Chwalla, K. Kim, M. Riebe, and R. Blatt (2006). "'Designer atoms' for quantum metrology." *Nature* 443, pp. 316–319. DOI: 10.1038/nature05101 (cit. on p. 86).

Rosenband, T., D. B. Hume, P. O. Schmidt, C. W. Chou, A. Brusch, L. Lorini, W. H. Oskay, R. E. Drullinger, T. M. Fortier, J. E. Stalnaker, S. A. Diddams, W. C. Swann, N. R. Newbury, W. M. Itano, D. J. Wineland, and J. C. Bergquist (2008). "Frequency Ratio of Al^+ and Hg^+ Single-Ion Optical Clocks; Metrology at the 17^{th} Decimal Place." *Science* 319, pp. 1808–1812. DOI: 10.1126/science.1154622 (cit. on pp. 58, 93, 140).

Rosenband, T. P., W. M. Itano, P. O. Schmidt, D. Hume, J. Koelemeij, J. C. Bergquist, and D. J. Wineland (2006). "Blackbody radiation shift of the $^{27}Al^+$ $^1S_0$ - $^3P_0$ transition." Proc. EFTF Conf., Braunschweig, (cit. on p. 84).

Safronova, M. S., V. A. Dzuba, V. V. Flambaum, U. I. Safronova, S. G. Porsev, and M. G. Kozlov (2014). "Highly Charged Ions for Atomic Clocks, Quantum Information, and Search for α variation." *Physical Review Letters* 113, p. 030801. DOI: 10.1103/PhysRevLett.113.030801 (cit. on p. 141).

Sailer, T., V. Debierre, Z. Harman, F. Heiße, C. König, J. Morgner, B. Tu, A. V. Volotka, C. H. Keitel, K. Blaum, and S. Sturm (2022). "Measurement of the bound-electron g-factor difference in coupled ions." *Nature* 606, pp. 479–483. DOI: 10.1038/s41586-022-04807-w (cit. on p. 30).

Sanner, C., N. Huntemann, R. Lange, C. Tamm, and E. Peik (2018). "Autobalanced Ramsey Spectroscopy." *Physical Review Letters* 120, p. 053602. DOI: 10.1103/PhysRevLett.120.053602 (cit. on pp. 92, 97).

Sanner, C., N. Huntemann, R. Lange, C. Tamm, E. Peik, M. S. Safronova, and S. G. Porsev (2019). "Optical clock comparison for Lorentz symmetry testing." *Nature* 567, pp. 204–208. DOI: 10.1038/s41586-019-0972-2 (cit. on pp. 5, 6, 104, 133, 140).

Schiller, S. (2007). "Hydrogenlike Highly Charged Ions for Tests of the Time Independence of Fundamental Constants." *Physical Review Letters* 98, p. 180801. DOI: 10.1103/PhysRevLett.98.180801 (cit. on pp. 9, 10).

Schmidt, P. O., T. Rosenband, C. Langer, W. M. Itano, J. C. Bergquist, and D. J. Wineland (2005). "Spectroscopy Using Quantum Logic." *Science* 309, pp. 749–752. DOI: 10.1126/science.1114375 (cit. on pp. 10, 19, 25, 131).

Schmöger, L., M. Schwarz, T. M. Baumann, O. O. Versolato, B. Piest, T. Pfeifer, J. Ullrich, P. O. Schmidt, and J. R. C. López-Urrutia (2015a). "Deceleration, precooling, and multi-pass stopping of highly charged ions in Be^+ Coulomb crystals." *Review of Scientific Instruments* 86, p. 103111. DOI: 10.1063/1.4934245 (cit. on pp. 10, 36, 131).

Schmöger, L., O. O. Versolato, M. Schwarz, M. Kohnen, A. Windberger, B. Piest, S. Feuchtenbeiner, J. Pedregosa-Gutierrez, T. Leopold, P. Micke, A. K. Hansen, T. M. Baumann, M. Drewsen, J. Ullrich, P. O. Schmidt, and J. R. C. López-Urrutia (2015b). "Coulomb crystallization of highly charged ions." *Science* 347, pp. 1233–1236. DOI: 10.1126/science.aaa2960 (cit. on pp. 10, 36, 131).

Schmöger, L. (2013). "Ein elektrodynamisches System für den Transfer hochgeladener Ionen in eine Paulfalle." Diploma Thesis. Ruprecht-Karls-Universität Heidelberg (cit. on p. 36).

Schnatz, H., B. Lipphardt, J. Helmcke, F. Riehle, and G. Zinner (1996). "First Phase-Coherent Frequency Measurement of Visible Radiation." *Physical Review Letters* 76, pp. 18–21. DOI: 10.1103/PhysRevLett.76.18 (cit. on p. 3).

Schneider, D., D. A. Church, G. Weinberg, J. Steiger, B. Beck, J. McDonald, E. Magee, and D. Knapp (1994). "Confinement in a cryogenic penning trap of highest charge state ions from EBIT." *Review of Scientific Instruments* 65, pp. 3472–3478. DOI: 10.1063/1.1144525. eprint: https://doi.org/10.1063/1.1144525 (cit. on p. 10).

Schulte, M., N. Lörch, I. D. Leroux, P. O. Schmidt, and K. Hammerer (2016). "Quantum Algorithmic Readout in Multi-Ion Clocks." *Physical Review Letters* 116, p. 013002. DOI: 10.1103/PhysRevLett.116.013002 (cit. on p. 133).

Schwarz, M., O. O. Versolato, A. Windberger, F. R. Brunner, T. Ballance, S. N. Eberle, J. Ullrich, P. O. Schmidt, A. K. Hansen, A. D. Gingell, M. Drewsen, and J. R. C. López-Urrutia (2012). "Cryogenic linear Paul trap for cold highly charged ion experiments." *Review of Scientific Instruments* 83, pp. 083115–083115–10. DOI: doi:10.1063/1.4742770 (cit. on p. 10).

Schwarz, R., S. Dörscher, A. Al-Masoudi, E. Benkler, T. Legero, U. Sterr, S. Weyers, J. Rahm, B. Lipphardt, and C. Lisdat (2020). "Long term measurement of the ^{87}Sr clock frequency at the limit of primary Cs clocks." *Physical Review Research* 2, p. 033242. DOI: 10.1103/PhysRevResearch.2.033242 (cit. on pp. 5, 6, 96, 108).

Seelig, P., S. Borneis, A. Dax, T. Engel, S. Faber, M. Gerlach, C. Holbrow, G. Huber, T. Kühl, D. Marx, K. Meier, P. Merz, W. Quint, F. Schmitt, M. Tomaselli, et al. (1998). "Ground State Hyperfine Splitting of Hydrogenlike ^{207}Pb^{81+} by Laser Excitation of a Bunched Ion Beam in the GSI Experimental Storage Ring." *Physical Review Letters* 81, pp. 4824–4827. DOI: 10.1103/PhysRevLett.81.4824 (cit. on p. 8).

Seiferle, B., L. v. d. Wense, P. V. Bilous, I. Amersdorffer, C. Lemell, F. Libisch, S. Stellmer, T. Schumm, C. E. Düllmann, A. Pálffy, and P. G. Thirolf (2019). "Energy of the 229 Th nuclear clock transition." *Nature* 573, pp. 243–246. DOI: 10.1038/s41586-019-1533-4 (cit. on p. 7).

Shabaev, V. M. (1998). "QED theory of the nuclear recoil effect in atoms." *Physical Review A* 57, pp. 59–67. DOI: 10.1103/PhysRevA.57.59 (cit. on p. 30).

Siegman, A. E. (1986). *Lasers*. University Science Books (cit. on p. 44).

Sikorsky, T., J. Geist, D. Hengstler, S. Kempf, L. Gastaldo, C. Enss, C. Mokry, J. Runke, C. E. Düllmann, P. Wobrauschek, K. Beeks, V. Rosecker, J. H. Sterba, G. Kazakov, T. Schumm, and A. Fleischmann

(2020). "Measurement of the ^{229}Th Isomer Energy with a Magnetic Microcalorimeter." *Physical Review Letters* 125, p. 142503. DOI: 10.1103/PhysRevLett.125.142503 (cit. on p. 7).

Solaro, C., S. Meyer, K. Fisher, J. C. Berengut, E. Fuchs, and M. Drewsen (2020). "Improved Isotope-Shift-Based Bounds on Bosons beyond the Standard Model through Measurements of the $^2D_{3/2} - ^2D_{5/2}$ Interval in Ca^+." *Physical Review Letters* 125, p. 123003. DOI: 10.1103/PhysRevLett.125.123003 (cit. on p. 139).

Soria Orts, R., J. R. Crespo López-Urrutia, H. Bruhns, A. J. González Martínez, Z. Harman, U. D. Jentschura, C. H. Keitel, A. Lapierre, H. Tawara, I. I. Tupitsyn, J. Ullrich, and A. V. Volotka (2007). "Zeeman splitting and g factor of the $1s^22s^22p\ ^2P_{3/2}$ and $^2P_{1/2}$ levels in Ar^{13+}." *Physical Review A* 76, p. 052501. DOI: 10.1103/PhysRevA.76.052501 (cit. on pp. 35, 107).

Soria Orts, R., Z. Harman, J. R. C. López-Urrutia, A. N. Artemyev, H. Bruhns, A. J. G. Martínez, U. D. Jentschura, C. H. Keitel, A. Lapierre, V. Mironov, V. M. Shabaev, H. Tawara, I. I. Tupitsyn, J. Ullrich, and A. V. Volotka (2006). "Exploring Relativistic Many-Body Recoil Effects in Highly Charged Ions." *Physical Review Letters* 97, p. 103002. DOI: 10.1103/PhysRevLett.97.103002 (cit. on pp. 30, 36, 108, 109, 113).

Stadnik, Y. V. and V. V. Flambaum (2015). "Can Dark Matter Induce Cosmological Evolution of the Fundamental Constants of Nature?" *Physical Review Letters* 115, p. 201301. DOI: 10.1103/PhysRevLett.115.201301 (cit. on p. 140).

Stark, J., C. Warnecke, S. Bogen, S. Chen, E. A. Dijck, S. Kühn, M. K. Rosner, A. Graf, J. Nauta, J.-H. Oelmann, L. Schmöger, M. Schwarz, D. Liebert, L. J. Spieß, S. A. King, T. Leopold, P. Micke, P. O. Schmidt, T. Pfeifer, and J. R. Crespo López-Urrutia (2021). "An ultralow-noise superconducting radio-frequency ion trap for frequency metrology with highly charged ions." *Review of Scientific Instruments* 92, p. 083203. DOI: 10.1063/5.0046569 (cit. on p. 141).

Steinel, M., H. Shao, M. Filzinger, B. Lipphardt, M. Brinkmann, A. Didier, T. E. Mehlstäubler, T. Lindvall, E. Peik, and N. Huntemann (2022). "Evaluation of a $^{88}Sr^+$ optical clock with a direct measurement of the blackbody radiation shift and determination of the clock frequency." *arXiv:2212.08687 [physics.atom-ph]*. DOI: 10.48550/ARXIV.2212.08687 (cit. on p. 6).

Stenholm, S. (1986). "The semiclassical theory of laser cooling." *Review of Modern Physics* 58, pp. 699–739. DOI: 10.1103/RevModPhys.58.699 (cit. on pp. 27, 28, 68, 78).

Stepanova, M. (2014). "Laser frequency stabilization for quantum logic experiments with single trapped $^{9}Be^{+}$ ions." Bachelor Thesis. Leibniz Universität Hannover (cit. on p. 42).

Stöhlker, T., H. Reich, K. Beckert, F. Bosch, A. Gallus, H. Eickhoff, B. Franzke, T. Kandler, O. Klepper, C. Kozhuharov, G. Menzel, P. H. Mokler, F. Nolden, H. T. Prinz, P. Spädtke, et al. (1997). "First experiment with decelerated bare uranium ions conducted at the ESR storage ring." *Hyperfine Interactions* 108, pp. 29–38. DOI: 10.1023/A:1012669503724 (cit. on p. 8).

Szymaniec, K., S. N. Lea, K. Gibble, S. E. Park, K. Liu, and P. Głowacki (2016). "NPL Cs fountain frequency standards and the quest for the ultimate accuracy." *Journal of Physics: Conference Series* 723, p. 012003. DOI: 10.1088/1742-6596/723/1/012003 (cit. on p. 5).

Timmen, L. (2018). "Absolute gravity measurements at station PTB Braunschweig "alte Gleiswaage" with the Hannover gravity meter FG5X-220 in June 2018." *Internal report* (cit. on p. 95).

Turchette, Q. A., Kielpinski, B. E. King, D. Leibfried, D. M. Meekhof, C. J. Myatt, M. A. Rowe, C. A. Sackett, C. S. Wood, W. M. Itano, C. Monroe, and D. J. Wineland (2000). "Heating of trapped ions from the quantum ground state." *Physical Review A* 61, p. 063418. DOI: 10.1103/PhysRevA.61.063418 (cit. on pp. 65, 77, 78, 145).

Udem, T., R. Holzwarth, and T. W. Hänsch (2002). "Optical frequency metrology." *Nature* 416, pp. 233–237. DOI: 10.1038/416233a (cit. on pp. 3, 104).

Ullmann, J., Z. Andelkovic, C. Brandau, A. Dax, W. Geithner, C. Geppert, C. Gorges, M. Hammen, V. Hannen, S. Kaufmann, K. Konig, Y. A. Litvinov, M. Lochmann, B. Maass, J. Meisner, et al. (2017). "High precision hyperfine measurements in Bismuth challenge bound-state strong-field QED." *Nature Communications* 8. DOI: 10.1038/ncomms15484 (cit. on p. 10).

Ushijima, I., M. Takamoto, M. Das, T. Ohkubo, and H. Katori (2015). "Cryogenic optical lattice clocks." *Nature Photonics* 9, pp. 185–189. DOI: 10.1038/nphoton.2015.5 (cit. on pp. 5, 6, 97).

Uzan, J.-P. (2011). "Varying constants, Gravitation and Cosmology." *Living Reviews in Relativity* 14 (cit. on p. 140).

Wan, Y., F. Gebert, F. Wolf, and P. O. Schmidt (2015). "Efficient sympathetic motional-ground-state cooling of a molecular ion." *Physical Review A* 91, p. 043425. DOI: 10.1103/PhysRevA.91.043425 (cit. on pp. 23, 29, 77).

Wang, M., W. Huang, F. Kondev, G. Audi, and S. Naimi (2021). "The AME 2020 atomic mass evaluation (II). Tables, graphs and refer-

ences*." *Chinese Physics C* 45, p. 030003. DOI: 10.1088/1674-1137/abddaf (cit. on p. 138).

Werth, G., V. N. Gheorghe, and F. G. Major (2009). *Charged Particle Traps II*. Springer Berlin Heidelberg. DOI: 10.1007/978-3-540-92261-2 (cit. on p. 13).

Weyers, S., V. Gerginov, M. Kazda, J. Rahm, B. Lipphardt, G. Dobrev, and K. Gibble (2018). "Advances in the accuracy, stability, and reliability of the PTB primary fountain clocks." *Metrologia* 55, p. 789. DOI: 10.1088/1681-7575/aae008 (cit. on p. 5).

Wilpers, G., C. W. Oates, S. A. Diddams, A. Bartels, T. M. Fortier, W. H. Oskay, J. C. Bergquist, S. R. Jefferts, T. P. Heavner, T. E. Parker, and L. Hollberg (2007). "Absolute frequency measurement of the neutral ^{40}Ca optical frequency standard at 657 nm based on microkelvin atoms." *Metrologia* 44, p. 146. DOI: 10.1088/0026-1394/44/2/005 (cit. on p. 139).

Wilzewski, A. (2023). *Private communication* (cit. on p. 152).

Windberger, A., J. R. Crespo López-Urrutia, H. Bekker, N. S. Oreshkina, J. C. Berengut, V. Bock, A. Borschevsky, V. A. Dzuba, E. Eliav, Z. Harman, U. Kaldor, S. Kaul, U. I. Safronova, V. V. Flambaum, C. H. Keitel, P. O. Schmidt, J. Ullrich, and O. O. Versolato (2015). "Identification of the Predicted 5s-4f Level Crossing Optical Lines with Applications to Metrology and Searches for the Variation of Fundamental Constants." *Physical Review Letters* 114, p. 150801. DOI: 10.1103/PhysRevLett.114.150801 (cit. on p. 10).

Wineland, D. J., J. C. Bergquist, J. J. Bollinger, R. E. Drullinger, and W. M. Itano (2002). "Quantum Computers and Atomic Clocks." *Proceedings of the 6th Symposium on Frequency Standards and Metrology*. University of St Andrews, Fife, Scotland, pp. 361–368. DOI: 10.1142/9789812777713_0040 (cit. on pp. 10, 24, 25).

Wineland, D. J., W. M. Itano, J. C. Bergquist, and R. G. Hulet (1987). "Laser-cooling limits and single-ion spectroscopy." *Physical Review A* 36, pp. 2220–2232. DOI: 10.1103/PhysRevA.36.2220 (cit. on p. 26).

Wineland, D. J., C. Monroe, W. M. Itano, D. Leibfried, B. E. King, and D. M. Meekhof (1998). "Experimental issues in coherent quantum-state manipulation of trapped atomic ions." *Journal of Research of the National Institute of Standards and Technology* 103, pp. 259–328. DOI: 10.6028/jres.103.019 (cit. on pp. 13, 19, 63, 66).

Wolf, F., C. Shi, J. C. Heip, M. Gessner, L. Pezzè, A. Smerzi, M. Schulte, K. Hammerer, and P. O. Schmidt (2019). "Motional Fock states for quantum-enhanced amplitude and phase measurements with trapped ions." *Nature Communications* 10, p. 2929. DOI: 10.1038/s41467-019-10576-4 (cit. on p. 120).

Wolf, F., Y. Wan, J. C. Heip, F. Gebert, C. Shi, and P. O. Schmidt (2016). "Non-destructive state detection for quantum logic spectroscopy of molecular ions." *Nature* 530, pp. 457–460. DOI: 10.1038/nature16513 (cit. on pp. 25, 116, 127).

Wübbena, J. B., S. Amairi, O. Mandel, and P. O. Schmidt (2012). "Sympathetic cooling of mixed-species two-ion crystals for precision spectroscopy." *Physical Review A* 85, p. 043412. DOI: 10.1103/PhysRevA.85.043412 (cit. on pp. 17, 18, 55, 59, 131).

Wunderlich, C., T. Hannemann, T. Körber, H. Häffner, C. Roos, W. Hänsel, R. Blatt, and F. Schmidt-Kaler (2007). "Robust state preparation of a single trapped ion by adiabatic passage." *Journal of Modern Optics* 54, pp. 1541–1549. DOI: 10.1080/09500340600741082 (cit. on pp. 118, 119).

Yerokhin, V. A., R. A. Müller, A. Surzhykov, P. Micke, and P. O. Schmidt (2020). "Nonlinear isotope-shift effects in Be-like, B-like, and C-like argon." *Physical Review A* 101, p. 012502. DOI: 10.1103/PhysRevA.101.012502 (cit. on pp. 30, 109, 138, 139).

Yu, Y.-m. and B. K. Sahoo (2018). "Selected highly charged ions as prospective candidates for optical clocks with quality factors larger than 10^{15}." *Physical Review A* 97, p. 041403. DOI: 10.1103/PhysRevA.97.041403 (cit. on pp. 8, 115, 134–136).

Yu, Y.-m. and B. K. Sahoo (2019). "Investigating ground-state fine-structure properties to explore suitability of boronlike S^{11+}-K^{14+} and galliumlike Nb^{10+}-Ru^{13+} ions as possible atomic clocks." *Physical Review A* 99, p. 022513. DOI: 10.1103/PhysRevA.99.022513 (cit. on pp. 84–86, 113, 114).

Yudin, V. I., A. V. Taichenachev, and A. Derevianko (2014). "Magnetic-Dipole Transitions in Highly Charged Ions as a Basis of Ultraprecise Optical Clocks." *Physical Review Letters* 113, p. 233003. DOI: 10.1103/PhysRevLett.113.233003 (cit. on pp. 8, 134).

Yudin, V. I., A. V. Taichenachev, C. W. Oates, Z. W. Barber, N. D. Lemke, A. D. Ludlow, U. Sterr, C. Lisdat, and F. Riehle (2010). "Hyper-Ramsey spectroscopy of optical clock transitions." *Physical Review A* 82, p. 011804. DOI: 10.1103/PhysRevA.82.011804 (cit. on pp. 92, 97).

Yudin, V., A. Taichenachev, O. Prudnikov, M. Basalaev, V. Pal'chikov, M. von Boehn, T. Mehlstäubler, and S. Bagayev (2023). "Probe-Field-Ellipticity-Induced Shift in an Atomic Clock." *Physical Review Applied* 19, p. 014022. DOI: 10.1103/PhysRevApplied.19.014022 (cit. on p. 90).

Zhiqiang, Z., K. J. Arnold, R. Kaewuam, and M. D. Barrett (2022). "$^{176}Lu^{+}$ clock comparison at the 10^{-18} level via correlation spec-

troscopy." *arXiv:2212.04652 [quant-ph]*. DOI: 10.48550/ARXIV.2212.04652 (cit. on p. 6).

Zubova, N. A., A. V. Malyshev, I. I. Tupitsyn, V. M. Shabaev, Y. S. Kozhedub, G. Plunien, C. Brandau, and T. Stöhlker (2016). "Isotope shifts of the $2p_{3/2}$-$2p_{1/2}$ transition in B-like ions." *Physical Review A* 93, p. 052502. DOI: 10.1103/PhysRevA.93.052502 (cit. on pp. 30, 36).